SOLAR FLARES AS NATURAL PARTICLE ACCELERATORS: A HIGH-ENERGY VIEW FROM X-RAY OBSERVATIONS AND THEORETICAL MODELS

Wei Liu
NASA Goddard Space Flight Center

To my wife
Li Jin

Figure 1: Artistic view of *RHESSI* observing the Sun from a near-earth orbit. *RHESSI* is a NASA Small Explorer mission designed to investigate particle acceleration and explosive energy release in solar flares. Since its launch on 2002 February 5, *RHESSI* has been providing scientists with unprecedented data revealing new physics and challenging existing theories. This mission inspired the work that eventually led to the production of this book [Courtesy of *RHESSI* Team].

Front cover picture — A full Sun image showing a flare near disk center and an eruptive prominence on the west limb.

Contents

Preface **ix**

Acknowledgements **xi**

1 Introduction **1**
1.1 Solar Flare Observations and Models 1
1.2 Stochastic Particle Acceleration Model 2
1.3 Hard X-ray Observations and *RHESSI* Instruments 4
1.4 Introduction to This Book 5
1.4.1 *RHESSI* Observations 5
1.4.2 Combining the Fokker-Planck and Hydrodynamic Codes 6

2 Statistical Study of *RHESSI* Limb Flares **8**
2.1 Introduction 8
2.2 Data Reduction and Analysis 9
2.2.1 Sample Selection Criteria 9
2.2.2 Imaging 11
2.2.3 Imaging Spectra and Light Curves 11
2.3 Case Study Results 12
2.3.1 Single Loop Flares 12
2.3.2 Multiple Loop Flares 14
2.3.3 Miscellaneous Types 15
2.4 Statistical Results 18
2.4.1 Imaging Spectroscopy 18
2.4.2 Statistics of the Relative Fluxes: FPs vs. LTs 20
2.5 Flare Statistics and Selection Biases 20
2.6 Summary and Discussion 22

3 Flare Reconnection Model: 2003-11-03 X3.9 Flare **23**
3.1 Introduction 23
3.2 Observations and Data Analysis 24
3.2.1 Source Structure and Motion 25
3.2.2 Imaging Spectroscopy 27
3.3 Summary and Discussion 30

4 Double Coronal Source: 2002-04-30 M1.4 Flare **33**
4.1 Introduction . . . 33
4.2 Observations and Data Analysis . . . 35
4.2.1 Source Structure: Energy Dependence . . . 37
4.2.2 Source Structure: Temporal Evolution . . . 39
4.2.3 Spectral Evolution . . . 42
4.3 Interpretation and Discussion . . . 46
4.3.1 Energy Dependence of Source Structure . . . 46
4.3.2 Temporal Evolution of Source Structure . . . 48
4.3.3 Spectral Characteristics . . . 49
4.4 Summary and Discussion . . . 50

5 Conjugate HXR Footpoints: 2003-10-29 X10 Flare **53**
5.1 Introduction . . . 53
5.2 Observations and Data Analysis . . . 55
5.2.1 *RHESSI* Light Curves and Images . . . 56
5.2.2 Imaging Spectroscopy of Footpoint and Loop-top Sources . . . 59
5.2.3 Multiwavelength Images . . . 62
5.3 Two-phase Unshearing Motions of HXR Footpoints . . . 62
5.4 Temporal Correlations of Conjugate Footpoints . . . 66
5.4.1 Spectral Correlations . . . 66
5.4.2 Spatial Correlations . . . 70
5.4.3 Magnetic Field Correlation . . . 70
5.4.4 Correlations Among Spectral, Spatial, and Magnetic Field Parameters 71
5.4.5 Implications of Various Correlations . . . 72
5.5 HXR Footpoint Asymmetries . . . 73
5.5.1 Magnetic Mirroring . . . 74
5.5.2 Column Density . . . 75
5.5.3 Magnetic Mirroring and Column Density Combined . . . 78
5.5.4 Other Transport Effects and FP Asymmetries . . . 79
5.5.5 Acceleration-induced Asymmetry . . . 80
5.6 Summary and Discussion . . . 82

6 Chromospheric Evaporation: 2003-11-13 M1.7 Flare **85**
6.1 Introduction . . . 85
6.2 Observations and Data Analyses . . . 86
6.2.1 Source Structure and Evolution . . . 89
6.2.2 Spectral Analysis . . . 97
6.2.3 The Neupert Effect . . . 98
6.3 Loop Density Derivation . . . 104
6.4 Summary and Discussion . . . 107

7 Modeling Impulsive Phase Solar Flares **109**
7.1 Introduction . . . 109
7.2 Simulation Models . . . 111
7.2.1 Stochastic Acceleration Model . . . 111
7.2.2 Particle Transport and Radiation Model . . . 115
7.2.3 NRL Hydrodynamic Model . . . 117
7.2.4 Combining the Particle and Hydrodynamic Codes . . . 118
7.3 Simulation Result . . . 122
7.3.1 Case R: Reference Calculation . . . 123
7.3.2 Case A: Fiducial Run with SA Model . . . 125
7.3.3 Case B: Variable Electron Spectrum . . . 134
7.3.4 Case C: Harder Electron Spectrum . . . 139
7.3.5 Case D: Smaller Normalization . . . 139
7.3.6 Comparing The Cases: A Summary . . . 145
7.4 Summary and Discussion . . . 147

8 Testing the Neupert Effect **149**
8.1 Energy Budget and the Neupert Effect . . . 149
8.2 Case R: Reference Calculation . . . 151
8.2.1 History of Energy Budget . . . 151
8.2.2 Neupert Effect Test . . . 153
8.3 Cases A-D: Combined HD & Particle Calculation . . . 157
8.3.1 Case A: Fiducial Run with SA Model . . . 157
8.3.2 Case B: Variable Electron Spectrum . . . 159
8.3.3 Case C: Harder Electron Spectrum . . . 160
8.3.4 Case D: Smaller Normalization . . . 160
8.4 Summary and Discussion . . . 163

9 Hydrodynamic Simulation of the Decay Phase **166**
9.1 Introduction . . . 166
9.2 Model of Suppression of Conduction and Plasma Heating . . . 167
9.3 Numerical Results . . . 168
9.3.1 Case A: No Heating or Suppression of Conduction . . . 170
9.3.2 Case B: Heating Only . . . 172
9.3.3 Case C: Suppression of Conduction Only . . . 173
9.3.4 Case D: Heating and Suppression of Conduction . . . 174
9.3.5 Comparing Cases A-D . . . 176
9.4 Summary and Discussion . . . 179

10 Concluding Remarks **180**
10.1 Summary and Conclusions . . . 180
10.1.1 Hard X-ray Observations . . . 180
10.1.2 Combined Fokker-Planck and Hydrodynamic Modeling . . . 183
10.2 Future Work . . . 184

Appendices **187**

A *RHESSI* Data Analysis Tools **187**
A.1 Imaging Spectroscopy Flow Chart . . . 187
A.2 Notes for Imaging Spectroscopy . . . 190
A.3 Spectral Analysis for 2002-04-30 M1.4 Flare . . . 192
A.3.1 Spatially Integrated Spectra . . . 192
A.3.2 Spatially Resolved (Imaged) Spectra . . . 195
A.4 Effects of Pulse Pileup . . . 196
A.4.1 Pileup Effects for 2003-11-13 M1.7 Flare . . . 197
A.4.2 Pileup Effects on Imaging Spectroscopy for 2003-10-29 X10 Flare . . 198
A.5 *RHESSI* Simulation Tool and Its Applications . . . 200

B Notes for Analyzing 2003-10-29 X10 Flare **202**
B.1 Coalignment of Images from Different Instruments . . . 202
B.2 Derivation of Footpoint Fluxes from Asymmetric Column Densities . . . 204
B.3 Estimation of Column Densities in Loop Legs . . . 205

C Coulomb Loss and Diffusion in Warm Plasmas **208**
C.1 Coulomb Loss in Warm Plasmas . . . 208
C.2 Coulomb Diffusion in Warm Plasmas . . . 210
C.3 Implementation of Coulomb Loss and Diffusion . . . 211
C.4 Thermalization Test of Injected Distribution . . . 214

List of **215**
Tables . . . 215
Figures . . . 216

Bibliography **219**

Index **227**
Author Index . . . 227
Subject Index . . . 229

Preface

It is well-known that the Sun is vital to the Earth and human beings because it supplies all the energy we need to survive. Another role that the Sun plays had escaped our attention until recent decades and the advent of space exploration. The Sun not only affects the terrestrial climate, but it also controls the conditions in space, the so-called "space weather", through solar activity. Solar flares, discovered in 1859, are one of the most spectacular phenomena of solar activity. They are natural accelerators that can boost particles to nearly the speed of light. These energetic particles, when arriving in near-earth space, can damage satellites and do harm to astronauts. Solar flares have thus stirred renewed interest of solar and space physicists. They provide a unique laboratory for studying particle acceleration mechanisms in general and investigating solar activity for space weather forecast purposes in particular. Understanding solar flares has other far-reaching implications, and can shed light on flares occurring elsewhere in the universe, such as those on other stars and accretion disks and near black holes.

A rich literature exists describing various aspects of solar flares. This includes several flare-dedicated books: *Solar Flares* by Švestka (1976), *The Physics of Solar Flares* by Tandberg-Hanssen & Emslie (1988), and *Particle Acceleration and Kinematics in Solar Flares* by Aschwanden (2002), and a few space mission motivated conference proceedings: *Solar Flares – A Monograph from Skylab Solar Workshop II* edited by Sturrock (1980), *Energetic Phenomena on the Sun – The Solar Maximum Mission Flare Workshop Proceedings* edited by Kundu & Woodgate (1986), and the upcoming *Solar Flares at High Energy – A RHESSI-inspired Monograph* edited by Dennis, Emslie, Hudson, & Lin (2008). The comprehensive textbook *Physics of the Solar Corona* by Aschwanden (2004) also includes extensive material on solar flares.

Advances in our knowledge of solar flares have been driven by multiwavelength observations obtained by space-borne and ground-based instruments over decades, particularly hard X-rays (HXRs) recorded by *Solar Maximum Mission* (*SMM*), *Hinotori*, *Yohkoh*, and *Compton Gamma Ray Observatory* (*CGRO*). In February 2002 NASA's *Reuven Ramaty High Energy Solar Spectroscopic Imager* (*RHESSI*) was launched. Unprecedented data poured in and new physics waited to be discovered. It was *RHESSI*'s scientific promise that motivated me to devote my PhD research to high-energy physics of solar flares. This led to the production of the materials presented in this work, which includes primarily my dissertation completed in late 2006 at Stanford University. In early 2008, after being approached by the German publisher Verlag Dr. Müller who proposed to publish my dissertation as a monograph, I made necessary revisions (Chapters 4 and 5) and additions (Appendices) based on my postdoctoral research at NASA Goddard Space Flight Center.

The main theme of this book is the investigation of the macro and micro physics of acceleration and transport of particles in solar flares, and their thermal and nonthermal radiative signatures. We have employed a two-pronged approach that relies on both data interpretation and numerical modeling, between which we attempt to bridge with physical concepts and first principles. With the goal to confirm or disprove theoretical models, we draw heavily on results from *RHESSI* HXR observations (Chapters 2–6), because HXRs provide the most useful information on the properties of accelerated electrons. This is complemented by combined Fokker-Planck and hydrodynamic simulations (Chapters 7–9) in an effort to improve our modeling capabilities and to explain new observations.

Our investigation started with a statistical study of limb flares with an emphasis on imaging spectroscopy of loop-top and footpoint X-ray sources (Chapter 2). This survey led to serendipitous discoveries of new physics in four individual flares: (1) the 2003 November 03 X3.9 flare showing correlated loop-top and footpoint source motions (Chapter 3), (2) the 2002 April 30 M1.4 flare exhibiting a rarely observed double coronal X-ray source as evidence of magnetic reconnection (Chapter 4), (3) the 2003 October 29 X10 flare with conjugate footpoints showing unshearing motions, various correlations, and asymmetric characteristics (Chapter 5), and (4) the 2003 November 13 M1.7 flare showing chromospheric evaporation signatures in HXRs (Chapter 6).

Motivated by these *RHESSI* observations, we devoted our modeling efforts to combining the Stanford stochastic acceleration (Fokker-Planck) model with the Naval Research Laboratory flux tube (hydrodynamic) model. As the first successful one of its kind, this combined model simulates, in a self-consistent manner, the interplay of the particle acceleration, transport, and radiation effects, and the atmospheric response to energy deposition by nonthermal electrons during the impulsive phase (Chapter 7). The empirical Neupert effect is tested with a more rigorous calculation of energy contents from this model than previous works (Chapter 8). We also examine the effects of suppression of conduction and/or heating in the presence of hydrodynamic flows during the decay phase (Chapter 9). We conclude this book by recapitulating our main findings, offering a prognosis for future investigation (Chapter 10), and providing a comprehensive description of *RHESSI* data analysis techniques used in this research and other technical details (Appendixes A–C).

This book therefore differs from others in existing literature in the sense that it provides a balanced treatment of observations and models. It is aimed at graduate students or early-career researchers who are acquainted with the basis physics, but need a jump start to grasp the latest development in high-energy aspects of solar flares. Younger readers are referred to the books of Tandberg-Hanssen & Emslie (1988), Aschwanden (2004), and others for an introduction to the required physical context.

Greenbelt, Maryland, May 2008 *Wei Liu*

Acknowledgements

The author wishes to thank many individuals who have, in one way or another, contributed to the production of this book. I am most indebted to Prof. Vahé Petrosian, my PhD adviser at Stanford University. Without his continuous motivation, invaluable support, intellectual guidance, and help of various kinds, my dissertation and this volume could barely be accomplished. I am indebted to Drs. Brian Dennis and Gordon Holman, my current postdoctoral supervisors, for their crucial inputs to my work at NASA Goddard Space Flight Center. I am grateful to Prof. Philip Scherrer, my research adviser in my early years at Stanford and a member of my dissertation committee, who provided me with generous support and a great deal of help in many ways. His critical comments on my dissertation in the late stage of writing were especially appreciated. I thank other committee members, Profs. Peter Sturrock, Tsuneyoshi Kamae, and Robert Wagoner for their comments that helped improve my dissertation. I would like to thank my previous adviser, Prof. You Qiu Hu at University of Science and Technology of China, who sparked my interest in the fascinating field of solar physics and taught me MHD simulation skills. I am deeply grateful to Dr. Boon Chye Low for his motivation of my interest in CMEs and solar MHD, and for his long-term support and help.

I would like to acknowledge contributions to my research from colleagues. Dr. Siming Liu offered many critical ideas from a theoretical point of view to the *RHESSI* observations and he originally noted the interesting features in the 2003 November 13 M1.7 flare (Chapter 6). Yan-Wei Jiang performed spectral fitting for the statistical study of imaging spectroscopy (Chapter 2) and for other flares (Chapters 3 and 6). William East contributed to the programming task of implementing Coulomb collisions with warm-plasma into the acceleration portion of the $\mathcal{F}$*lare* code (Appendix C). Drs. Haisheng Ji and Chang Liu provided imaged X-ray fluxes and Hα image fits files, respectively, for the 2003 October 29 X10 flare (Chapter 5).

I would like to thank Dr. John Mariska for generously providing his hydrodynamic code and for his timely help with flare simulations; I thank Dr. Peng Li for discussions in this regard. I am thankful to Dr. Vladimir Airapetian, my collaborator, for his insight of extending my simulation work to exoplanetary auroras. I thank Dr. Gordon Hurford for helpful discussions on imaging techniques, and Prof. Robert Lin for his leadership that ensured the successful *RHESSI* mission. I am particularly thankful to Dr. Thomas R. Metcalf, who tragically passed away recently, for his indispensable help with the PIXON imaging technique. I thank Sam Krucker, Jim McTiernan, Kim Tolbert, David Smith, Richard Schwartz, Edward Schmahl, Rick Pernak, Linhui Sui, Amir Caspi, Steven Christe, Ryan Milligan, Merrick Berg, Chau Dang, Andy Gopie, and other *RHESSI* team members

for discussions and help of various kinds.

I am particularly grateful to Dr. Xue Pu Zhao for his motivation and guidance for my CME studies and heliospheric research. I sincerely thank Prof. Shi Tsan Wu for his advice and motivation for numerical MHD simulations of CMEs; I thank Drs. Tianxi Zhang and Weiping Guo for their help with the numerical code. I thank Drs. Yang Liu and Todd Hoeksema for help with analyzing WSO and *SOHO* MDI magnetic field data. I also thank Drs. Junwei Zhao, Sasha Kosovichev, Laurent Gizon, Aaron Birch, Tom Duvall, and Jesper Schou for discussions of helioseismology and various help (particularly on IDL); I thank Keh-Cheng Chu and Jeneen Sommers for their help with computing issues. I thank Drs. Simon Plunkett for help with analyzing *SOHO* LASCO CME data, Mei Zhang for comments and suggestions for my early CME simulations, Henrik Lundstedt for discussions on CME predictions and wavelet analysis of magnetic field time-series data, Nariaki Nitta for discussions on CME observations, and Drs. Tongjiang Wang, George Fisher, Janet Luhmann, Yan Li, Yuhong Fan, and Sarah Gibson for helpful discussions on various topics.

I also thank my Stanford fellow students Michael Dorris, Chi Yung (Stephen) Ng, and David Sowards-Emmerd for help with Linux, Latex, C++, and scientific computing in general, and Stephen Healey, Cheng Zheng, Adam Mantz, Mustafa Amin, Eric Morganson, Jane Li, and many others, who brought passion and fun to the astronomy program. I thank our administrative staff Carol Krueger (GSFC), Dana Volponi, Margaret Stehle, Violet Catindig, Maria Frank, Kathline Guan, and Elva Carbajal (Stanford) for dealing with logistical issues. I thank my friends Dunwei Wang, Zheng Wang, Yanping Pan, Ruixue Liu, Xiuping Xie, Yulin Chen, Zhaohua Yang, Arito Nishimori, Kyungyun Shin, Yao Chen, Zhigang Peng, Xianglei Huang, Yun Chen, Feng Deng, Yan Xu, Tongsheng Xia, Yi Zhou, and many others too numerous to list here for their friendship and various help.

Data analysis in this research utilized the *RHESSI* software package developed and maintained by the *RHESSI* team members; the map structure developed by Dr. Dominic Zarro was used to produce the heliographic figures presented in this work; we also used many general tools in the IDL *Solar SoftWare* (SSW) package contributed by the solar physics community at large and maintained by Dr. Samuel Freeland. This work was supported in part by NASA grants NAG5-12111 and NAG5 11918-1, and NSF grant ATM 03-12344 at Stanford University, and in part by the NASA Postdoctoral Program at the Goddard Space Flight Center, administered by Oak Ridge Associated Universities through a contract with NASA.

I wish to acknowledge the most helpful support provided by the publisher, Verlag Dr. Müller (VDM), in particular for editorial help from Mr. Chiponda Chimbelu. I also thank GSFC summer student Shea Hess Webber for her kind help with proofing the manuscript.

Special thanks goes to my wife, Li Jin, whom this book is dedicated to, and to my parents, Tianxuan Liu and Youfang Zhang, who have provided me with love and a great deal of support over decades.

Chapter 1

Introduction

Acceleration of particles and the consequent transport and radiation effects are ubiquitous in astrophysical plasmas, such as those responsible for cosmic ray particles, gamma-ray bursts, and flares on accretion disks near compact objects (e.g., black holes and X-ray binaries). Solar flares serve as one of the most suitable laboratories to study particle acceleration and related high-energy processes, because of the proximity of the Sun and abundant observations available. The primary goal of this research is to understand particle acceleration mechanisms in general, and how these mechanisms operate in solar flares in particular.

1.1 Solar Flare Observations and Models

Solar flares are one of the two most energetic phenomena on the Sun (the other being coronal mass ejections, CMEs), involving up to some 10^{32} ergs or more energy released on a timescale of a few minutes to tens of minutes (cf., solar luminosity of 3.8×10^{33} ergs s^{-1}). The first flare ever observed was an emission burst in white-light discovered on 1859 September 01 by R. C. Carrington and R. Hodgson independently. Since then, flare observations have been accumulated over a century in many other wavelengths, including Hα, radio waves, as well as X-rays and gamma-rays in recent decades.

Theoretical investigations of solar flares have lagged behind. Among the earliest flare models were those proposed by Carmichael (1964), Sturrock (1966), Hirayama (1974), and Kopp & Pneuman (1976). These 2-D models, in one way or another, involve magnetic reconnection (Sweet, 1958; Parker, 1963; Petschek, 1964) with an inverted "Y"- or an "X"-shaped topology, in a (vertical) current sheet, which can be produced by a preceding CME or magnetic flux emergence from below the photosphere. Advances in recent decades have improved on these early models, but the basic picture remains the same.

In the currently widely accepted scenario, the basic physical processes involved and the observational signatures are as follows. Magnetic reconnection, as the primary energy release mechanism occurring in the corona, leads to plasma heating and particle acceleration. Some particles escape along the open magnetic field lines into the interplanetary space, with electrons producing various radio bursts and some electrons (Wang et al., 2006; Krucker et al., 2007) and ions (Krucker & Lin, 2000) being detected at 1 AU. Other particles escape along the newly reconnected closed magnetic loop to lower layers of the atmosphere.

Electrons, while spiraling along magnetic field lines, can produce microwave bursts via synchrotron radiation. These electrons, in the meanwhile, lose their energy through Coulomb collisions with the ambient plasma, primarily in the transition region and chromosphere where the density is sufficiently high, and produce *thick-target* (Brown, 1971; Petrosian, 1973) hard X-rays (HXRs) via bremsstrahlung. This results in the so-called footpoint (FPs; Hoyng et al., 1981; Sakao, 1994; Petrosian et al., 2002) emission observed at HXR energies. Accelerated ions, while colliding with background particles, can excite nuclear reactions and produce gamma-ray emission (e.g., Ramaty & Murphy, 1987; Hurford et al., 2003).

The released energy, which is carried by particles and/or thermal conduction and transferred to lower atmospheres, can heat the chromosphere rapidly. The resulting overpressure in the over-heated chromosphere can drive a mass flow upward along the loop at a speed of a few hundred km s^{-1}, which can be observed as blue-shifted chromospheric emission lines. The mass motion fills the flaring loop with a hot plasma, giving rise to the loop structure seen in soft X-ray (SXR) and gradual evolution of SXR flux. This process, termed *chromospheric evaporation* by Neupert (1968), was proposed to explain the empirical temporal relationship of the derivative of the SXR flux and the microwave or HXR light curve, i.e., the Neupert effect (Hudson, 1991), which is observed in some (but not all) flares (Dennis & Zarro, 1993).

Consequent energy redistribution in the lower layers of the atmosphere, on the other hand, can produce ribbons seen in Hα and occasionally in white-light (e.g., Hudson et al., 2006) for the brightest flares. As time proceeds, reconnection develops to higher altitudes in the inverted-Y shaped configuration, and the two HXR FPs and Hα ribbons are usually seen move away from each other, in a direction more or less perpendicular to the magnetic neutral line. This gives the standard picture of a two-ribbon flare.

1.2 Stochastic Particle Acceleration Model

There are two most important unresolved questions regarding the physics of solar flares. The first is how energy is released, which involves details of the magnetic reconnection process. The other is how particles are accelerated, which is the main goal of this book, and we focus on acceleration of electrons here.

In general, there are three types of acceleration commonly quoted for solar flares (and other astrophysical plasmas). (1) **Direct electric field acceleration** (e.g., Holman, 1985; Benka & Holman, 1994) can boost a particle to high energies simply via the Coulomb force from the electric field and may operate in the current sheet or in the reconnection site, but it is difficult to maintain a large-scale coherent DC electric field. (2) **Shock or first-order Fermi acceleration** (e.g., Tsuneta & Naito, 1998) can energize particles by making them repeatedly pass through the shock front back and forth and this mechanism may be present in the fast shock produced by the super-magnetosonic outflow jet from the reconnection region. However, it would be difficult to reflect the particles in the upstream region. (3) **Stochastic (second-order Fermi) acceleration** by turbulence or plasma waves is the most likely mechanism for solar flares (Petrosian, 1994, 1996), compared with the shortcomings of the other two mechanisms (although they may also be operating to some extent).

The **stochastic acceleration (SA)** mechanism has been studied and advanced by many authors for solar flares with various purposes (e.g. Ramaty, 1979; Ramaty & Murphy, 1987; Hamilton & Petrosian, 1992; Miller et al., 1996; Park et al., 1997; Petrosian & Liu, 2004), and for astrophysical environments (e.g., around black holes, Liu et al., 2004b, 2006b). The SA model is supported by remote HXR observations and by *in situ* measurements of interplanetary particles. In particular, Liu, Petrosian, & Mason (2004a, 2006c) have shown that the enhanced ^{3}He over ^{4}He ions observed by the *Advanced Composition Explorer* (*ACE*) spacecraft can be accounted for by the preferential resonance interactions of ^{3}He with turbulence.

In the SA model, the basic picture is as follows (see Fig. 1.1, *left panel*). As a consequence of magnetic reconnection, large-scale turbulence or plasma waves are generated at/near the reconnection region. Turbulence then cascades to small scales, and accelerates particles and heats the plasma via resonance wave-particle interactions in a region near/at the top of the flaring loop. The accelerated particles produce in the acceleration region the *thin-target* HXR loop-top (LT) source (Masuda 1994), which was one of the major discoveries of the *Yohkoh* mission. Some particles are trapped in the acceleration region due to scattering by turbulence, some escape down to lower atmospheres to produce the *thick-target* FP emission, and others escape up into interplanetary space along open field lines as mentioned above.

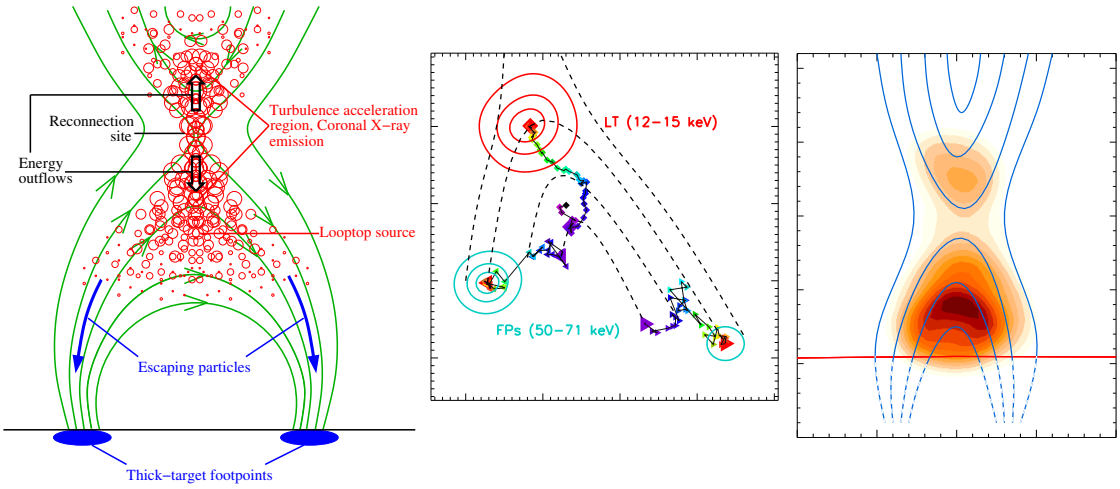

Figure 1.1: *Left:* Sketch of the stochastic acceleration model (Hamilton & Petrosian, 1992; Park & Petrosian, 1995; Petrosian & Liu, 2004) proposed for solar flares. The curves are magnetic field lines in a possible configuration; the open circles represent turbulence or plasma waves that are generated during magnetic reconnection. *Middle:* Temporal evolution of the LT and FP HXR sources of the 2003 November 03 X10 flare (see Chapter 3). The symbols indicate the source centroids and the gray scale from dark to bright shows time at 20 s intervals, with contours for the last interval. The dashed curves connect schematically the FP and LT sources for different times showing the expected evolution for the model on the left. *Right:* Image of the 2002 April 30 M1.4 flare (see Chapter 4), showing an elongated LT source with two distinct peaks as expected from the model on the left. The horizontal line indicates the solar limb which occulted the FPs and the curves (added by hand) represent the magnetic field lines. Both the middle and right panels are rotated from their original orientations for ease of viewing.

The stochastic acceleration process can be described by the Fokker-Planck equation,

$$\frac{\partial f}{\partial t} = \frac{\partial}{\partial E}\left[D(E)\frac{\partial f}{\partial E}\right] + \frac{\partial}{\partial E}\{[A(E) - \dot{E}_L]f\} - \frac{f}{T_{\rm esc}(E)} + Q(E)\,, \tag{1.1}$$

where $f \equiv f(t, E)$ is the electron distribution function, $E = \gamma - 1$ (γ being the Lorentz factor) is the electron kinetic energy in units of $m_e c^2$, $D(E)$ and $A(E)$ are the energy diffusion and systematic acceleration coefficients, $T_{\rm esc}$ is the particle escape time, $Q(E)$ is the total injection flux of electrons into the acceleration region that acts as source term in the equation. $\dot{E}_L = \dot{E}_{\rm Coul} + \dot{E}_{\rm synch}$ is the absolute value of the net systematic energy loss rate, which is a combination of Coulomb loss $\dot{E}_{\rm Coul}$ and synchrotron loss $\dot{E}_{\rm synch}$. The central task of such a model is to determine the resonance condition for a particle (with a given momentum and pitch angle) and a given turbulence spectrum, and thus obtain the coefficients $D(E)$, $A(E)$, and $T_{\rm esc}$.

The subsequent particle transport in the flare loop can be described with a similar diffusion equation, with the addition of the magnetic mirroring effect and pitch angle scattering. A unified code, called *$\mathcal{F}$lare*, that can calculate the particle acceleration and transport, together with bremsstrahlung radiation, has been developed (Petrosian, Donaghy, & Llyod 2001), on the basis of previous advances accumulated over two decades (Leach, 1984; McTiernan, 1989; Lu, 1989; Hamilton, 1990; Park, 1996). This code was used in the theoretical modeling part of this book (see Chapter 7).

1.3 Hard X-ray Observations and *RHESSI* Instruments

HXRs (and gamma-rays) observed during the impulsive phase of flares provide the most direct information on the spectrum of accelerated particles and give us clues to the acceleration mechanisms. A power-law distribution (with an index of δ) of electrons, for example, can produce a power-law HXR spectrum with a photon index of $\gamma \simeq \delta \pm 1$ from a thin- and thick-target sources, respectively.

Observations by HXR instruments on board earlier missions,[1] including *Orbiting Solar Observatory-5* and -7, *International Sun-Earth Explorer* (*ISEE*)-3, *Solar Maximum Mission* (*SMM*), *Hinotori*, *Compton Gamma Ray Observatory* (*CGRO*), and *Yohkoh*, have advanced our understanding on this subject (see the review by Aschwanden, 2004). The currently active *Reuven Ramaty High Energy Solar Spectroscopic Imager* (*RHESSI*) mission with its superior capabilities (Lin et al., 2002) has proven that it can make a more accurate determination of temporal, spectral and spatial evolution of flares (see the *RHESSI* dedicated *Solar Physics* Vol. 210, 2002 and *Astrophysical Journal Letters* Vol. 595, No. 2, 2003).

RHESSI is a NASA small explorer (SMEX) mission, designed to study particle acceleration and energy release in solar flares (and some non-solar science, Lin et al. 2002). It has an array of nine large-volume (300 $\rm cm^3$) coaxial germanium detectors (Smith et al., 2002), with a total collecting area of $\sim 150\,\rm cm^2$. This provides an energy resolution down to $\sim 1\,$keV and an energy coverage of 3 keV–17 MeV. Its imaging capability is enabled by the Rotating Modulation Collimator (RMC) system and the spacecraft spin at 15 rpm ($\sim 4\,$s period). Each of the nine subcollimators consists of two grids, 1.55 m apart, with the

[1] See Aschwanden (2004, p. 552) for a complete list of previous HXR instruments.

germanium detector equipped behind the rear grid. During a flare, each photon arriving at the detector is tagged with its arrival time and energy. Then the spatial information is recovered through the image reconstruction procedure at the time of data analysis on the ground, which is realized by Fourier transform of the time series data of energy tagged counts, i.e., the modulation pattern (Hurford et al., 2002). Such a unique imaging system produces an angular resolution of $2.3''$ in its 1° field of view (covering the full Sun). The temporal resolution can reach $\sim 2\,\mathrm{s}$ for detailed images and tens of ms for basic images.

Since its launch, *RHESSI* has provided us with unprecedented details of solar flares, some of which are serendipitous (e.g., Liu, W. et al., 2006) and some of which pose new challenges to theoretical models (e.g., Sui & Holman, 2003; Hurford et al., 2003). We will present some of such observations in this book.

1.4 Introduction to This Book

The main theme of this book is the investigation of the micro and macro physics of the acceleration and transport of particles (electrons[2]) in solar flares, and their thermal and nonthermal radiative signatures. To reach this objective, we took a two-prong attack, using HXR data analysis and theoretical modeling, both couched in the framework of the SA model. Our data analysis concentrated on HXR images and spectra observed by *RHESSI* during the impulsive phase of flares. Our modeling efforts was devoted to combining the SA model and the *Flare* code with a hydrodynamic (HD) model (Mariska, Emslie, & Li, 1989) to study the interplay of the particle acceleration, transport, and radiation effects and the atmospheric response to the energy deposition by accelerated electrons.

1.4.1 *RHESSI* Observations

During 1970s and 1980s, HXR imagers on board early missions, such as *SMM* and *Hinotori*, revealed the FP emission which supports the thick-target model (Brown, 1971; Petrosian, 1973) for solar flares. In early 1990s, the *Yohkoh* mission discovered the HXR LT source (Sakao, 1994; Masuda, 1994), which marked a milestone in flare research and provided further evidence for the stochastic acceleration model (e.g., Hamilton & Petrosian, 1992). *RHESSI*, with its superior capabilities, can provide more accurate temporal, spatial, and spectral information of the LT and FP (and other possible) sources and thus help improve theoretical models. Obtaining such information of individual sources and offering appropriate physical interpretations is the main task of the observational part of this book.

In the SA model, the LT emission comes directly from the accelerated electrons (thin target) and the FP emission is produced by escaping electrons in a thick target region. The fluxes and spectra of the two sources are related and can thus be used to constrain the SA model parameters. We have carried out a preliminary statistical study of 29 *limb* flares, which have minimal projection effects, and obtained the relative spectra and fluxes of the LT and FP sources. We find a large difference between the average values of the LT and FP spectral indexes, which, together with other statistical results, will be presented in *Chapter 2*. This statistical study have also paved the path to identify four interesting flares

[2] Acceleration of protons and other ions is another aspect of solar flare energetics, and is beyond the scope of this work.

for in-depth investigations, each of which presents *evidence* of particular aspects as well as imposes *challenges* for the classical reconnection model of solar flares.

In the classical flare model, as mentioned earlier, magnetic reconnection takes place at lower altitudes first and progresses to higher overlying loops as time proceeds. In this picture, one would expect that the FPs move apart while the LT source moves up with time. We will show in *Chapter 3* an excellent example (the 2003 November 03 X3.9 flare, see Fig. 1.1, *middle*) of such a picture. In the following two chapters, we will focus on the LT and the FP emission respectively.

In the common 2-D reconnection picture, outflow jets of high speed plasmas are present in opposite directions along the current sheet. Accelerated particles and heated plasmas are expected to be present in both directions as well. As we can see in Figure 1.1 (*right panel*), an M1.4 flare occurring on 2002 April 30 exhibits a double-source structure in the corona, which suggests that reconnection takes place in between. Analysis of the images and spectra of this flare will be presented in *Chapter 4*.

We now turn our attention from coronal (LT) emission to chromospheric (FP) emission. As noted earlier HXR observations can provide useful information about the electron spectrum, while magnetic field measurements of the flare region can give clues to magnetic reconnection development. Combining both observations, if available, can improve our understanding of flares. As we will see in *Chapter 5*, the 2003 October 29 X10 flare, which occurred near the disk center and thus had minimal projection effects for line-of-sight magnetic field measurement, provided us such an excellent opportunity.

In *Chapter 6*, we will, again, examine both LT and FP emissions. The 2003 November 13 M1.7 flare shows some unusual spatial evolution and provides direct evidence for chromospheric evaporation. We find that emission from the legs of the loop dominates at intermediate energies and the emission centroids move from the FPs to the LT as time proceeds. This suggests an increase of loop density, possibly as a consequence of chromospheric evaporation. However, some observed source morphologies and their evolution cannot be accounted for by previous modeling efforts. Therefore, simulations with more realistic physical conditions are required to explain the results as well as the particle acceleration & transport and plasma heating processes.

1.4.2 Combining the Fokker-Planck and Hydrodynamic Codes

Motivated by the *RHESSI* observations mentioned above, we have embarked on an investigation of combining the Fokker-Planck $\mathcal{F}$*lare* code with the Naval Research Laboratory (NRL) flux tube hydrodynamic (HD) model (Mariska, Emslie, & Li 1989). Aside from the observational incentive, the theoretical motivation comes as follows.

There are basically two faces of a solar flare — one concerns energetic particles and their transport and radiation effects, and the other concerns the hydrodynamic evolution of the plasma in the flare loop. These two aspects are actually coupled together in a circular chain. Particles, on the one hand, lose their energy via Coulomb collisions and heat the background plasma, which causes chromospheric evaporation that changes the density and temperature distribution in the loop. In turn, such changes affect the particle acceleration and transport processes and influence the spectrum of the accelerated particles. The energy deposition rate (by particles) will also be altered and fed back to the hydrodynamics of the

background plasma.

Due to the complexity of the subject, however, people tend to decouple these processes and study one at a time while assuming some simple forms for the others. For particle acceleration and transport, as mentioned earlier, one of the main streams of studies solves the Fokker-Planck equation and keeps track of the particle distribution function (e.g., Leach 1984; McTiernan 1989), assuming a *static* background atmosphere. For the hydrodynamics, a majority of efforts (e.g., Fisher et al., 1985c,b) are put into 1-D numerical HD simulations, assuming the plasma can only move along the magnetic field line, which is a valid assumption for a magnetic field dominated (low-β) plasma. In such simulations, some form of a *simple* (e.g., power-law) electron distribution is usually assumed and results from simplified analytical solutions are used to provide the heating rate.

A more realistic and self-contained treatment of both particles and gas dynamics is thus desired. We have started such an investigation and engineered the two codes (as mentioned above) to work together, which possesses the potential to advance our understanding of solar flares significantly. We have used the newly combined code to examine the atmospheric response to the energy deposition of electrons with a spectrum predicted by the SA model (Petrosian & Liu, 2004). Our approach and result will be presented in *Chapter 7*.

From the same simulations, we have also examined the empirical Neupert effect with more rigorous (than previous works, e.g., by Veronig et al. 2005) calculations of the energy contents and thermal and nonthermal X-ray radiation. This study will be presented in *Chapter 8*.

As an extension of our studies on the flare impulsive phase, we will present in *Chapter 9* a simulation of the decay phase. The goal here is to test the effects of suppression of conduction and/or heating, presumably produced by turbulence (at a lower level during the decay phase), in the presence of HD *flows*. Our earlier analytical investigation (Jiang et al., 2006) of the problem assumed a hydrostatic atmosphere which is an approximation, and rigorously speaking, not quite realistic. Our result confirms the earlier conclusion that suppression of conduction and/or heating is required to explain the X-ray observations and suggests that an even larger factor of suppression would be needed.

Finally, in *Appendixes A–C*, we will provide a comprehensive description of the *RHESSI* data analysis procedures employed here, an account of the techniques used for analyzing HXR FP asymmetries, and a note on the improvement of the current SA model by inclusion of Coulomb collisions with a warm/hot background plasma.

Chapter 2

Statistical Study of Limb Flares Observed by *RHESSI* : Imaging and Imaging Spectroscopy

2.1 Introduction

Observations of solar flares by low spectral and spatial resolution instruments can give us only the light curve and a crude spectrum of the whole flare which may consist of many distinct sources with different characteristics. The discovery of distinct looptop (LT) sources (Sakao, 1994; Masuda, 1994) in addition to the normal footpoint (FP) sources, made by the *Yohkoh* satellite, has provided further evidence for the stochastic acceleration model (Petrosian & Donaghy, 1999; Petrosian et al., 2002) which was shown to be consistent with the broadband spectra of several solar flares (Park et al. 1997). As suggested by this and other models, these different sources should have different electron spectra determined by the physical condition at the acceleration site. Statistical studies of FP-to-LT flux ratios have been conducted for *Yohkoh* flares (Petrosian et al., 2002; Tomczak & Ciborski, 2007).

The exceptional imaging spectroscopic capacity of *RHESSI* (Lin et al. 2002), combined with its excellent time resolution, provides us a multi-dimensional picture of solar flares, which can set stringent constraints on the model parameters and will eventually improve our understanding of the relevant physical processes.

One important aspect of such constraints can be obtained from the spectral correlation of the FP and LT sources. In the stochastic acceleration model the LT emission comes directly from the accelerated electrons (thin target) while the FP emission is produced by the escaping electrons in a thick target region. The flux and spectra of the two sources are related. The exact relation depends on various acceleration mechanism and plasma parameters but very roughly the FP to LT X-ray flux ratio at photon energy E can be written as (see Petrosian & Donaghy 1999 and eq. [7.23]) $I_{FP}/I_{LT} \simeq \tau_{\rm loss}(E)/T_{\rm esc}(E)$, where $\tau_{\rm loss} = E/\dot{E}_L$ is the electron energy loss time at the LT (due to Coulomb collision at low energies and synchrotron loss at high energies), and the energy dependence of the escape time $T_{\rm esc}$ (see, e.g., eq. [7.20]) depends on the details of the acceleration process in the LT region. This means that the relative spectra can constrain the plasma and acceleration

model parameters. At low energies, for example, $\tau_{\rm loss} \propto E^{3/2}$ (since $\dot{E}_{\rm Coul} \propto 1/\beta$, see eq. [7.3]), and thus the functional form of $T_{\rm esc}(E)$ can be directly obtained from the observed flux ratio.

A statistical study of the relative spectra of different sources is thus required to obtain such observational constraints with sufficient statistical confidence. We carefully selected a sample of 29 limb flares, which may provide some statistical information on LT and FP emissions. Battaglia & Benz (2006) recently reported a similar study of five *RHESSI* flares. A larger sample of events has not been practically feasible in the past, given the evolving *RHESSI* instrument calibration and software on the early stage of the mission (launched 2002), but we look forward to expanding our sample in the future.

We present in this chapter images, light curves of the LT and FP sources of the sample flares, as well as their imaging spectroscopy. We describe the flare selection criteria and the imaging procedure in §2.2. Results from case studies of typical events are given in §2.3. Statistics of various parameters is presented in §2.4 and §2.5. Finally we conclude this chapter with §2.6. Discussions on miscellaneous data analysis techniques used in this study are given in Appendices §A.1 and §A.2.

2.2 Data Reduction and Analysis

2.2.1 Sample Selection Criteria

We searched through the online *RHESSI* flare list (from February 12, 2002 through April 18, 2004[1]) for appropriate limb flares, using criteria similar to those introduced by Masuda (1994) and used by Petrosian et al. (2002), which are:

- Heliocentric longitude ≥ 70 degrees. This provides sufficient angular separation between FP and LT sources. The heliocentric (x, y) coordinates in the *RHESSI* flare list[2] were converted to heliographic (longitude, latitude) coordinates[3]. For flares whose locations are not available in the list, we obtained the locations by making full disk *RHESSI* images, usually in the 12–25 keV energy channel about the peak time, and used the position of the brightest pixel as the flare location.

- Peak count rate ≥ 30 per second per detector in the 12–25 keV channel, allowing sufficient count statistics and thus good image quality.

We then carefully examined the sample flares satisfying these criteria and eliminated those with strong particle events, severe pileup or decimation, or poor data quality. There are 29 flares included in our final sample, which are listed in Table 2.1. The heliographic locations (*left*) and the distribution of the peak count rate (*right*) at 12–25 keV are shown Figure 2.1. For each sample event, we performed imaging spectroscopy and light curve study as follows.

[1]The analysis presented here was initiated back in 2003 using the *RHESSI* software existing then. New flares were added to the latest sample as of April 18, 2004. The software has been improved since then and thus may give slightly different results.

[2]see http://hesperia.gsfc.nasa.gov/hessidata/dbase/hessi_flare_list.txt

[3]We used xy2lonlat.pro in the *Solar SoftWare* package to do the conversion. For flare locations off the limb, the corresponding positions projected back to the limb were used. These flares may have a longitude greater than 90° (see Table 2.1), because the solar pole is not aligned in the plane of the sky.

Table 2.1: List of (22 + 7 = 29) flare events included in this study.

Flare ID (ymmdd#)	Peak time (UT)	Disk position	NOAA AR #	GOES class	Peak Count	Highest E-band (keV)	Image spec. (Y/N)	Notes
2022003	11:06:18	N13W73?	-	C7.5	656	50-100		3 FPs, no LT?
2032819	17:58:18	S04W90	-	C7.6	200	25-50		one source (LT)?
2041509	23:12:26	N21W77	9893?	M1.2	816	25-50		complex^T
2051706	07:38:10	N13E89?	-	M1.5	1328	25-50		2 LTs?
2051909	21:46:22	S23E78	-	C4.7	84	25-50		source not well def.
2062904	09:29:46	S17E79	-	C2.0	352	12-25		single loop
2072301	00:30:06	S13E74	0039	X4.8	57379	800-7000	Y	complex^T
2072307	12:21:42	S19E78	-	C2.9	240	25-50		complex^T?
2080327	19:06:54	S16W83	0039	X1.0	28697	25-50		complex^T
2080602	05:18:18	N17E92	-	C2.1	108	25-50		single loop?
2081203	02:17:18	S08E86	-	C1.4	160	25-50	Y	single loop
2082336	16:10:18	S10W88	-	-	104	25-50		single loop^T
2082418	11:16:10	S05W89	0069?	-	400	25-50		complex (multi-LTs)^T?
2082803	10:59:30	S18W79	0083	C5.7	912	50-100		complex
2082809	18:10:46	N10E87	-	C6.6	784	12-25		one source (LT)
2090309	12:45:42	S08W77	0087?	C1.5	128	25-50		complex
2090608	16:27:02	S06E89	-	C9.2	752	25-50		loop not well def?
2090801	01:39:10	S11E79	0105	M1.5	1072	12-25	Y	complex
2092002	09:26:42	S25E75	0126	M1.8	1520	800-7000	Y	single loop
2111410	11:09:38	S15E71	0195?	C5.5	352	50-100		2 FPs
2112532	21:50:30	S13W89	-	C?	72	25-50		single loop
3021411	09:17:18	N12W88	-	M1.2	1072	25-50		one source
added 05/2004:								
2042101	01:30:30	S15W91	9906	X1.5	59298	800-7000	Y	complex (multi-LTs, 2-FPs)
2090708	17:41:22	S12E88	-	-	240	25-50	Y	complex (multi-LTs, 2-FPs)
3102405	02:35:34	S19E83	-	-	1587	50-100	Y	complex (multi-LTs, 2-FPs)
3110316	09:51:38	N09W77	-	X3.9	13808	300-800	Y	single loop
3110319	15:31:14	S15W72	-	-	3032	25-50	Y	complex (multi-loop, 3-FPs)
3111313	04:59:14	N02E87	0501	M1.7	1328	50-100	Y	single loop
4010604	06:25:30	N05E89	-	-	2288	800-7000	Y	complex (multi-LTs, 2-FPs)

Note — The first 22 events were selected from the period from 12-Feb-2002 through 02-May-2003; the new 7 events were from the period through 18-Apr-2004. (1) Peak counts (counts/s) are in the 12–25 keV energy band. (2) "Image spec." — Y (yes) marks a total of 11 events whose LT and FP spectra have been obtained for spectral index statistics shown in Fig. 2.10. (3) "single loop": 8 events here are of this type. (4) "complex" = complex morphology or multiple loops; 13 events fall into this category. (5) "one source" = only one source was detected; 3 events have this characteristics. (6) Out of the rest 5 events, two do not have a well-defined loop (source) structure, and the other three appear to have either LT or FP (not both) sources. (7) The superscript 'T' denotes those flares with *TRACE* data available in the *RHESSI* FOV.

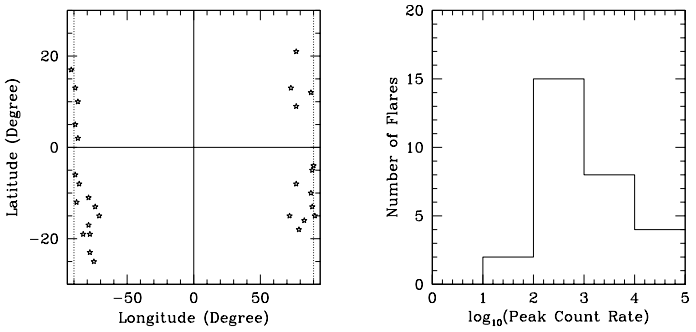

Figure 2.1: Heliographic location distribution (*left*) and histogram of the peak count rate (*right*) at 12–25 keV of the sample flares. The dotted vertical lines in the left panel marks 90° in longitude.

2.2.2 Imaging

At the time of this study, for the purpose of studying spectroscopy and light curves of individual sources using *RHESSI* data, the first step was to reconstruct images in different energy bands and/or time ranges. We describe the key points in our imaging processes below and list the details in the appendix (see § A.1).

(1) **Imaging algorithms**. Among the available *RHESSI* imaging algorithms (Hurford et al. 2002), we used Back-projection and/or CLEAN for preliminary studies, and CLEAN for light curves of individual sources as it is relatively much faster. We used much more computationally expensive PIXON for imaging spectroscopy, which is most suitable for this task because of its excellent photometry.

(2) **Integration Time Intervals.** Different time intervals were selected for different purposes. For spectroscopic images, a time interval about the peak in the 25–50 keV channel is preferred. For light curve images, we selected a time range including the rise and decay phase and divided it into a number of time bins (each bin for an image). Each time bin has an appropriate length (a multiple of the spacecraft spin period $\simeq$4 s) to allow sufficient photon counts for imaging as well as good temporal resolution. All the time bins are selected to exclude intervals with particle events, with attenuator state changes, or with decimation state changes.

(3) **Energy Bins.** For imaging spectroscopy, the energy ranges were set as follows. The lower limit of the energy range was obtained by the attenuator states: namely, about 3 keV when none of the two attenuators is in, 6 keV when one is in, and 10 keV when both are in. The upper limit goes as high as there are sufficient signals in the images. Once the energy range was obtained we divided it into logarithmically spaced bins. Two aspects were taken into account for determining the energy bin width. On the one hand, we would like to have as many as possible bins in order to obtain a sufficiently large number of data points for spectral fits, but the smallest bin width (at the low energy end) should not be smaller than 1 keV, the nominal *RHESSI* energy resolution; on the other, we would like to have broad energy bins to increase the photon count rate in each bin for better statistical S/N in images, but it is not legitimate to construct images with an arbitrarily wide[4] energy range because the instrument response varies with energy and the imaging software only take a mean energy for computing the expected instrument response (Smith et al. 2002). For light curves, we took much broader energy bins, within which images at different energies exhibit common features.

2.2.3 Imaging Spectra and Light Curves

Once images at different energies or times are obtained, we are ready to infer spectra as well as light curves of individual sources. By examining images at various energies and times, we identified FP and/or LT sources. For each source, we selected a box to enclose it and summed over all the pixel values in this box, divided by the width of the energy bin, to get the differential photon flux. If available, images from *Transition Region And Coronal Explorer* (*TRACE*) were used to help distinguish individual sources. Plotting the

[4]Smith et al. (2002) recommended that the size of a energy bin should not exceeds 1/10 of its mean energy for (spatially integrated) spectroscopy. However, this requirement might be too strict imaging spectroscopy, as one usually must use relatively broad energy bins to achieve sufficient count statistics for imaging.

flux versus energy (time) results in the spectrum (light curve) and in turn the characteristics of the spectrum (light curve) provides clues on the nature of the source. For the events in which we cannot unambiguously identify the magnetic connectivity between corresponding FP and LT sources, we summed the fluxes of all the FPs.

2.3 Case Study Results

We present in this section results from selected events falling in three morphological categories: single-loop, multiple-loop, and miscellaneous types.

2.3.1 Single Loop Flares

Out of the 29 total events, eight appear to be morphologically similar to the canonical Masuda (1994) flare, namely, a LT source connected by a single flaring loop to two FPs. PIXON images of these flares were obtained around the peak time, and other times whenever the count rate was sufficiently large to allow imaging in the 25–50 keV band. We use these images as the input for imaging spectroscopy.

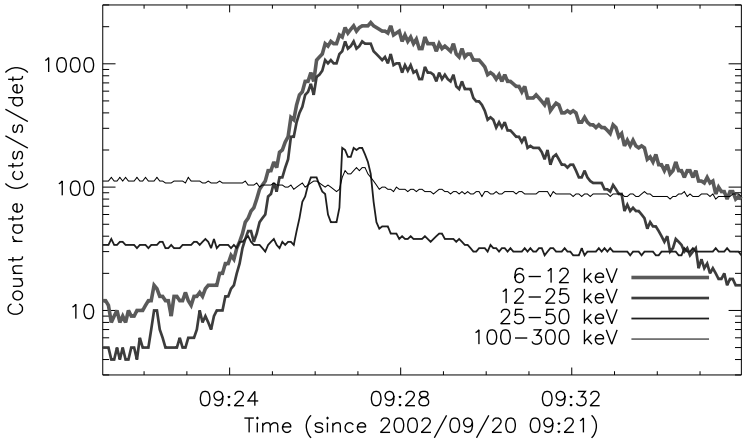

Figure 2.2: *RHESSI* light curves of the 2002 September 20 M1.8 flare (ID: 2092002).

Here we describe the 2002 September 20 flare (ID 20920020), which is a *GOES* M1.8 event observed by *RHESSI* up to 800–7000 keV. This event started at 09:22:08 UT, continued rising to a sub-peak at 09:25:59 UT in energy channel between 25 keV and 300 keV, and peaked at 09:26:42 UT nearly simultaneously in the energy channels from 6 keV through 300 keV as can be seen from the light curves in Figure 2.2. We focus on the impulsive phase here. The decay phase of this flare was studied by Jiang et al. (2006).

The HXR images were reconstructed by the PIXON algorithm using front segments of detectors 3 through 6, and detectors 8 and 9, with a minimal spatial resolution of $7''$. Figure 2.3 shows the resulting images in separate energy bands for a time interval [09:26:36, 09:27:20 UT], covering the main peak. It is clearly shown that in the 11.1–12.4 keV image a diffuse source dominates, suggesting a hot LT source. Two FP sources appear in about

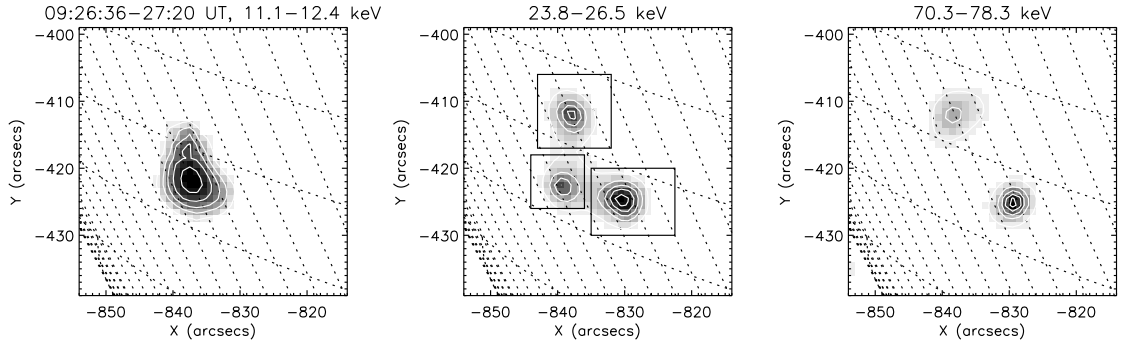

Figure 2.3: Hard X-ray images of flare 2092002 at different energies. The white contours are at the 10%, 30%, 50%, 70%, and 90% levels of the maximum of each panel. We show in the middle panel three boxes defined to enclose individual sources to infer their spectra and light curves.

23.8–26.5 keV and become more and more dominant at higher energies. Note the southern FP is much brighter than the northern one, which may be due to possible asymmetric convergence of the magnetic loop. That is, the loop may converge more rapidly approaching to the northern FP and this result in a stronger magnetic mirroring effect which suppresses the number of high-energy electrons that reach the chromosphere there. We will address asymmetric FP emission in depth later (see Chapter 5).

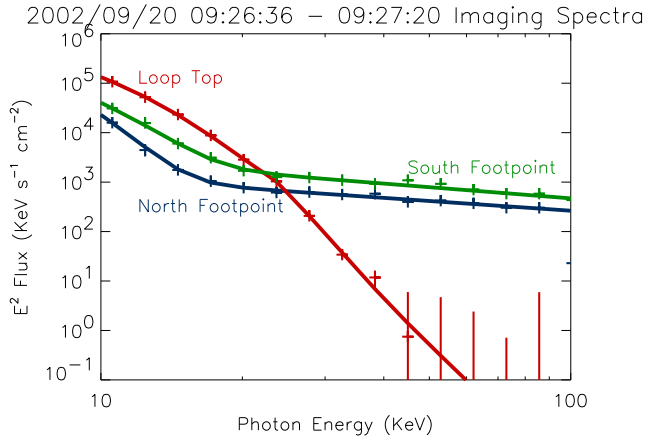

Figure 2.4: νf_ν spectra of the LT and FP sources of flare 2092002. The thick lines are fits from a thermal plus power-law model [from Jiang et al. 2003].

We used the boxes shown in Figure 2.3 (*middle*) to define the three sources and integrated the photon flux within each box to obtain the corresponding spectrum, which is shown in Figure 2.4. We (Jiang, Liu, Petrosian, & McTiernan, 2003) then fitted each spectrum with a thermal plus power-law model. The best fit suggests the LT source (fitted within 10–57 keV) has a temperature $k_{\rm B}T = 2.22\,{\rm keV}$. The two FPs have a weaker thermal component ($k_{\rm B}T = 1.31, 1.82\,{\rm keV}$) and a stronger power-law component, with an index of $\gamma = 2.65, 2.75$ for the northern and southern one, respectively.

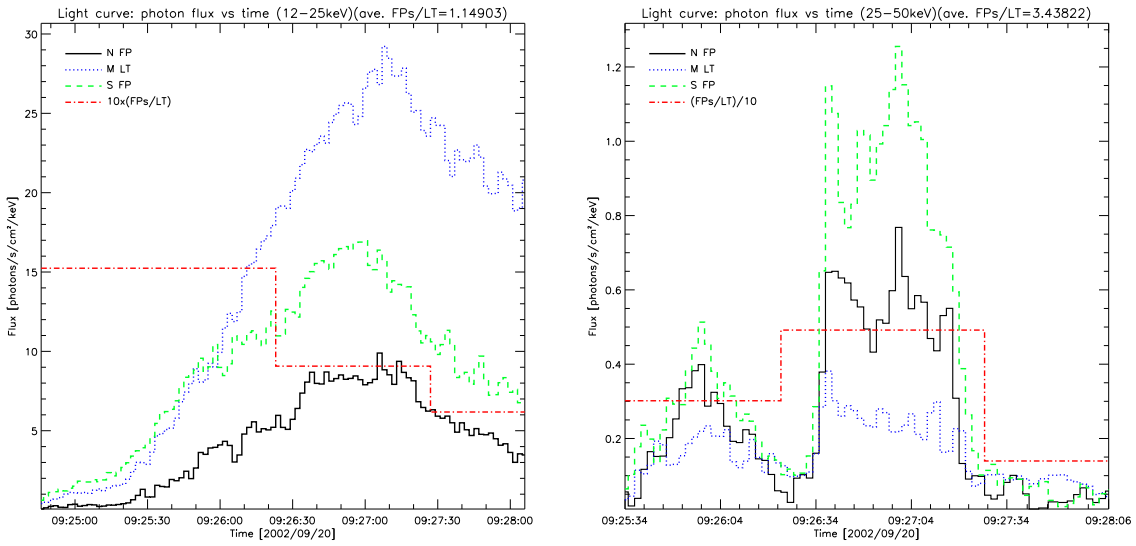

Figure 2.5: Light curves of individual FP and LT sources in the 12–25 keV (*left*) and 25–50 keV (*right*) energy band for flare 2092002. The dot-dashed, step-shaped curves show the ratio of flux of the two FPs to the LT sources, averaged over time intervals before, during, and after the peak. "N FP" refers to the northern FP, "M LT" the middle LT, "S FP" the southern FP.

We also used the boxes defined in Figure 2.2 to infer the light curves of individual sources. Figure 2.5 shows such light curves at a cadence of 2 s with about a 4 s integration time in the 12–25 keV and 25–50 keV band. The ratio of the fluxes of the two FPs combined to the LT source averaged over the rise, peak, and decay phase, respectively, is shown as the dot-dashed line. We note that the LT source dominates at 12–25 keV and its importance gradually increases with time; in contrast, the FP sources are much brighter in the 25–50 keV channel but it decreases more rapidly after the peak. We note that from the first pulse to the second (as seen at 25–50 keV), the LT emission is essentially constant at 25–50 keV band but increases substantially in the 12–25 keV band. This suggests the LP spectrum undergoes softening.

2.3.2 Multiple Loop Flares

In the selected sample, 13 flares appear to have a more complex morphology, one[5] of which was identified as a multiple-loop event, similar to those studied by Petrosian et al. (2002) during the rising phase of solar cycle 23. This event (ID: 2080327), is an X1.0 flare, occurring in AR10039 on 2002 August 03. Figure 2.6 shows the light curves (*left*), which exhibit a complex history, with multiple pulses appearing at high energies ($\gtrsim$50 keV).

Figure 2.7 shows *RHESSI* image contours at different energies superimposed on a *TRACE* 171 Å image. As is evident, the HXR source morphology is more complex than the 2092002 flare. At high energies, there are several sources (presumably FPs) located inside the limb. At low energies, the structure appears simple, with a single source (LT) appearing above

[5]The other complex events require further analysis of light curves and imaging spectroscopy, as well as multiple-wavelength observation to distinguish individual sources.

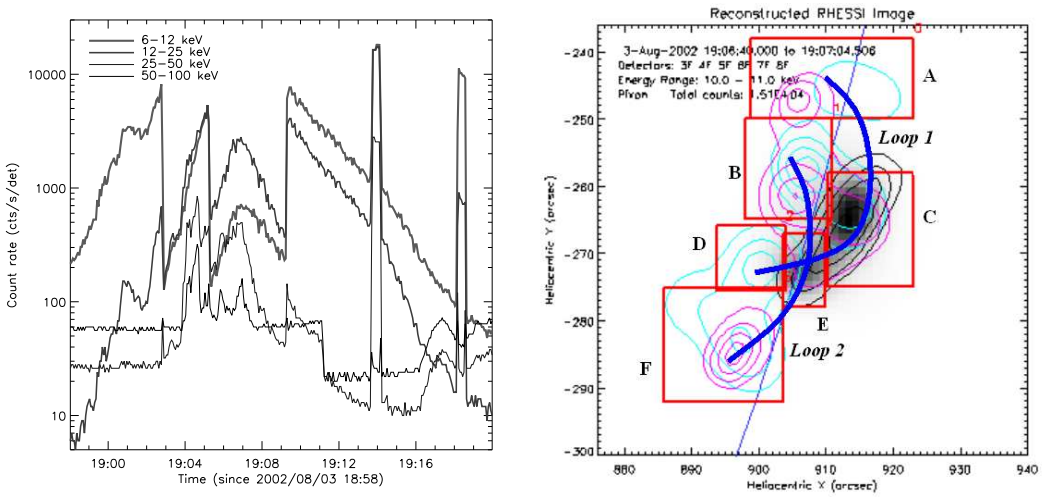

Figure 2.6: Light curves (*left*) and PIXON images, together with boxes enclosing individual sources (*right*), of the 2002 August 03 X1.0 flare (ID: 2080327). The artificial jumps of the count rates (*left*) are due to the changes of the attenuator state. The background map and the contours are images at different energies, same as those shown in Fig. 2.7. Two major flaring loops, marked with thick curves, are identified, and their corresponding LT and FP sources are assigned a letter, A, B, C, etc.

the limb. However, its elongate shape and the existence of many FP sources suggest that this simple appearance could be a projection effect and there are probably more than one LT sources (but not resolved by *RHESSI*). The *TRACE* image was recorded at a later time (19:32:37 UT) during the flare and was selected in order to show the coronal loop structure in EUV, which reveals an arcade of a series of magnetic loops. Two of these loops seem to be cospatial with the *RHESSI* sources, and based on this, we group the HXR sources in two loops, as shown in Figure 2.6 (*right*). Sources A, C, and D are of loop 1, and the others are of loop 2.

Again we obtained the light curves (Fig. 2.8) of the individual sources by integrating fluxes in the boxes (see Fig. 2.6, *right*). We note that the two loops do not contribute equally to the total emission. In the 25–50 keV band, the total flux of loop 2 is higher during the first pulse but lower in the second than that of loop 1; in the 12–25 keV channel, the LT source of loop 2 is stronger than that of loop 1 by a factor of ∼2 during the first pulse (although their total fluxes are comparable at this time), but much weaker by a factor of 4 in the second pulse (and the total flux of loop 2 is lower too). The LT emission from loop 1 dominates over others in the second (major) peak in both energy channels. In the 25–50 keV band, the total flux of loop 1 (2) increases (decrease) from the first peak to the second. This suggests that the burst of loop 1 may be initiated by its interaction with loop 2.

2.3.3 Miscellaneous Types

In six events of this sample, not both LT and FP sources are present. Based on their locations, light curves, and spectra, out of these six flares, we find that three appear to have only a LT source, one seems to have *two* LT sources (beyond the limb), and the other two seem to have only FP sources (see Table 2.1).

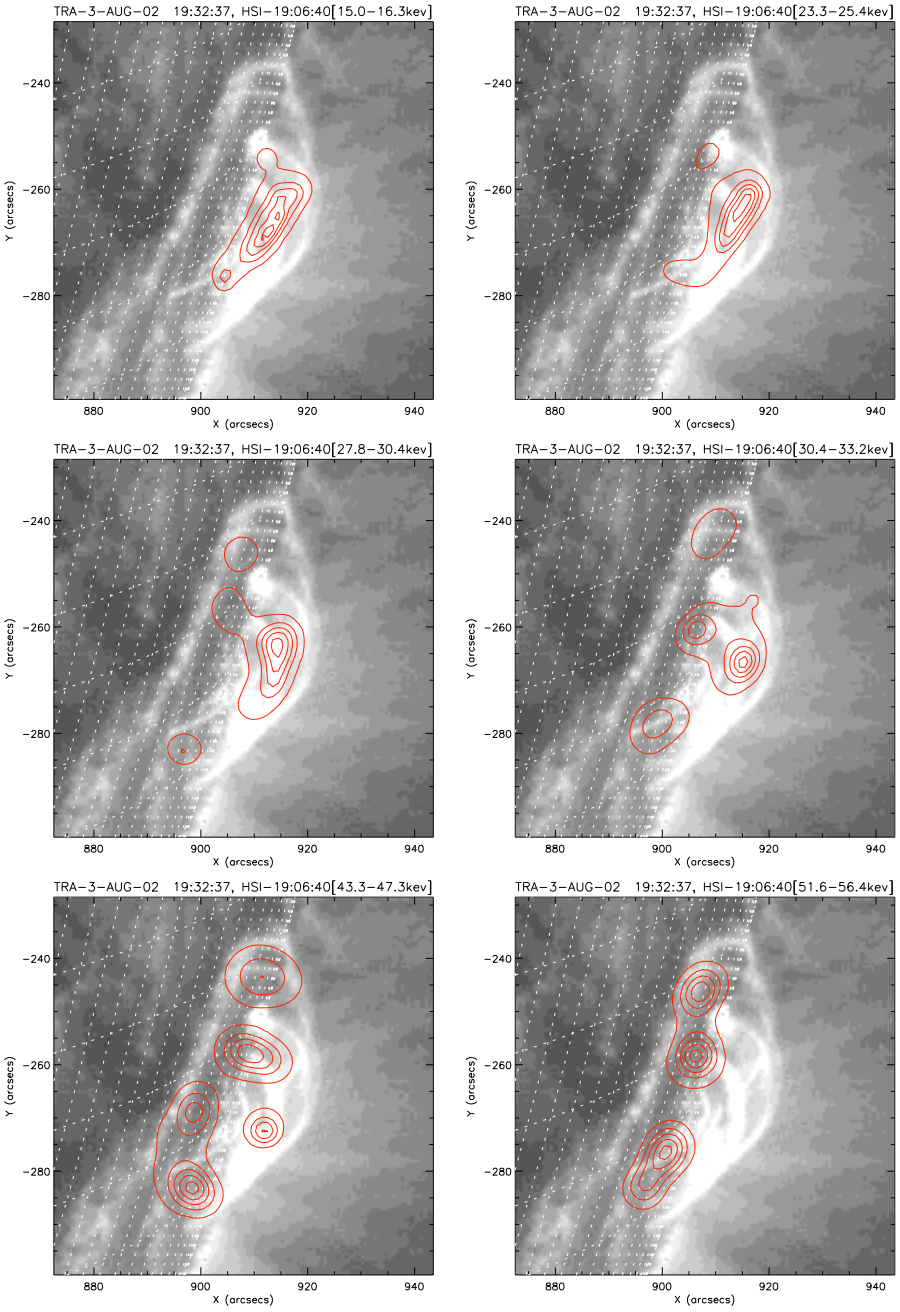

Figure 2.7: *RHESSI* HXR contours at different energies superimposed on a *TRACE* 171 Å images for flare 2080327. Heliographic grids (*dotted lines*) have a 1° spacing in both longitude and latitude.

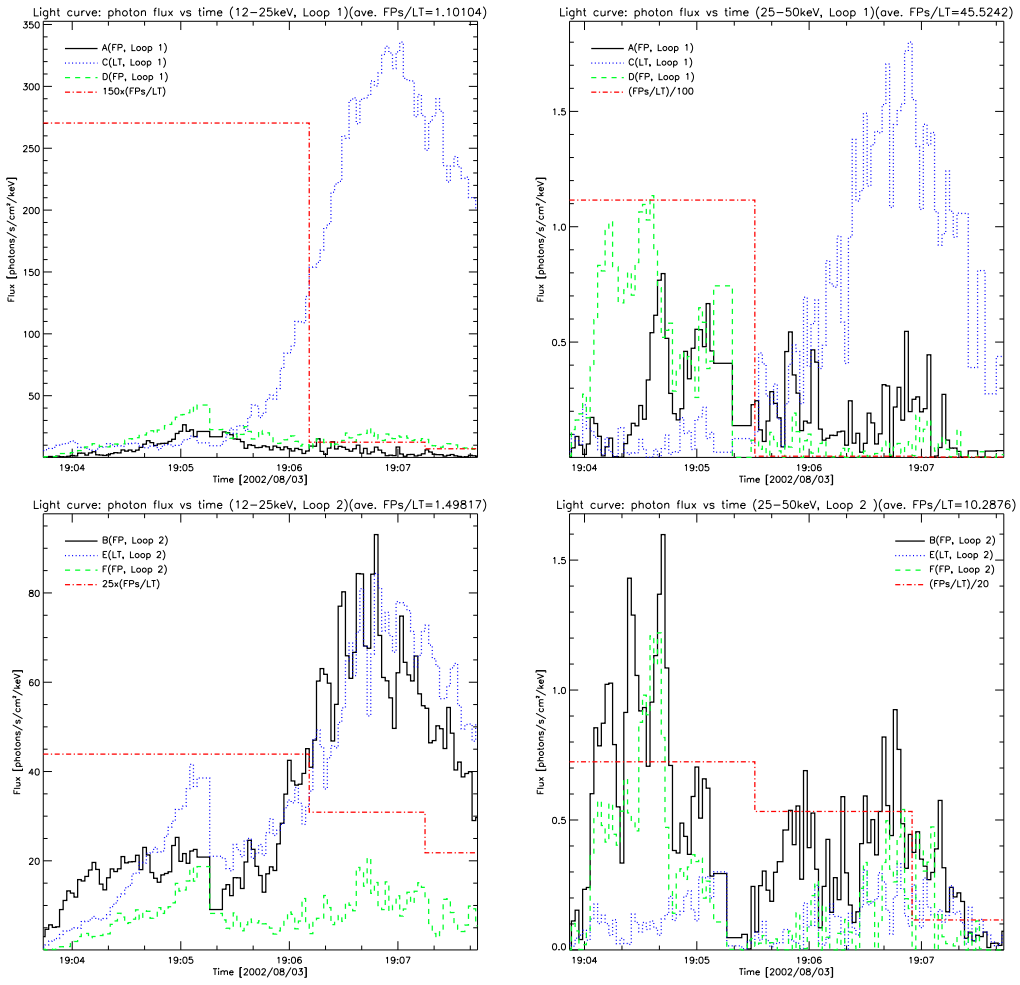

Figure 2.8: Same as Fig. 2.5, but for the two loops of flare 2080327. The upper panels are for loop 1 (see Fig. 2.6, *right*) in 12–25 keV (*left*) and 25–50 keV (*right*); the lower panels are for loop 2.

Flare 2082809 (C6.6), occurring on 2002 August 28, is a single LT source flare, without FPs detected. In the PIXON images at around the peak time, this event appears as a single source on the limb (see Fig. 2.9, *left*) in all the 13 energy bins from 10 to 54.2 keV. CLEAN images at different times also indicate a single source. Fits to the spatially integrated spectrum yield a power law index of 5.0 (steep) and a temperature of 1.9 keV, suggesting this source is a LT, presumably with its corresponding FPs being occulted behind the limb.

Flare 2111410 (2002 November 14, C5.5), does not show an appreciable LT source possibly because the LT is too faint to be detected (i.e., out the *RHESSI* dynamic range) and/or the angular separation is not sufficient between the LP and FPs, considering its low heliocentric longitude of 71°, the lowest in this sample of the 29 flares.

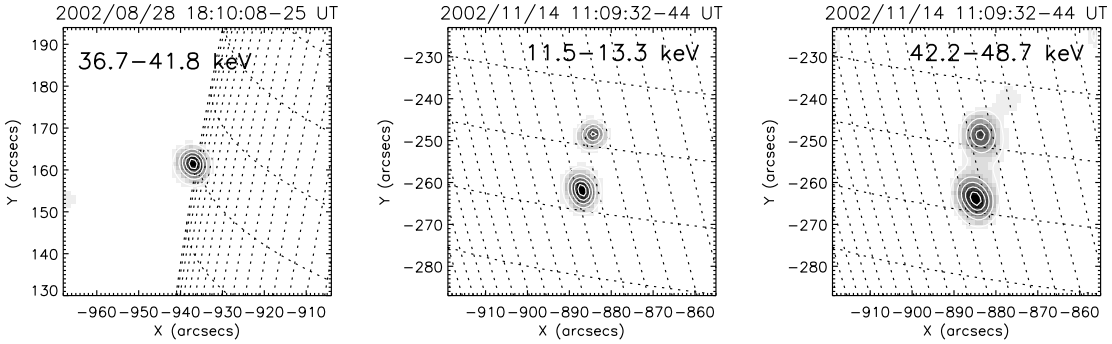

Figure 2.9: Images of flare 2082809 at 36.7–41.8 keV (*left*) and flare 2111410 at 11.5–13.3 (*middle*) and 42.2–48.7 keV (*right*).

2.4 Statistical Results

2.4.1 Imaging Spectroscopy

Figure 2.10 (*left*) shows the histogram of LT and FP spectral indexes from single power-law fits for a set of 11 limb flares (i.e., those marked with "Y" in the "Image spec." column of Table 2.1). Several flares with multiple pulses have multiple entries in the data set. In general, the LT spectra are steeper than those of the FPs. The means of the two distributions are $\bar{\gamma}_{\rm LT} = 6.84$ and $\bar{\gamma}_{\rm FP} = 3.35$ and yield a large difference of $\Delta\bar{\gamma} = 3.49$, which could be expected from the stochastic acceleration model (Petrosian & Liu 2004). Such a large difference is also seen for some of the individual flares as shown in the scatter

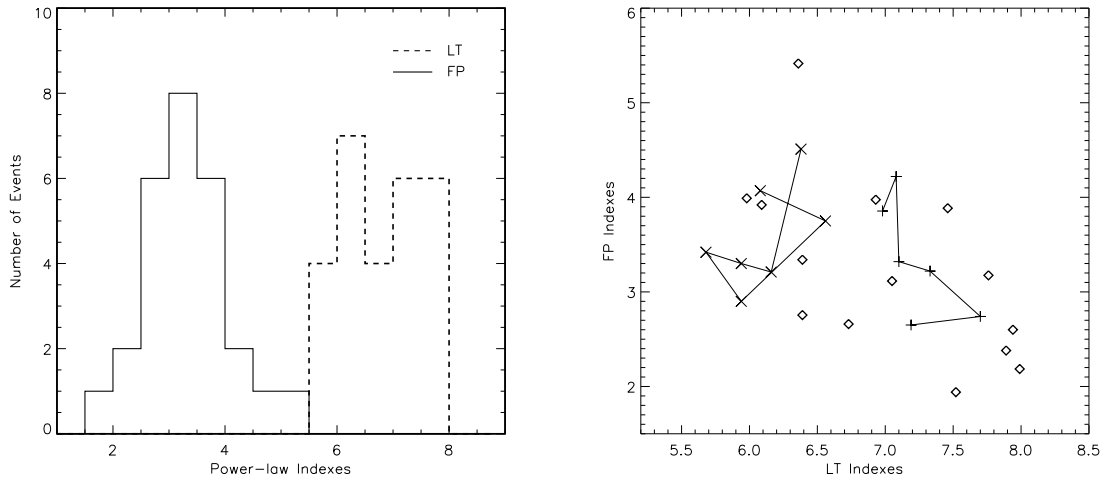

Figure 2.10: *Left*: Histogram of LT and FP spectral indexes during the impulsive peak for a sample of 11 limb flares (see Table 2.1). *Right*: The spectral indexes of the LT vs FP sources for the same sample. The data set also includes the first (*cross*) and second (*plus*) pulses of the 2003 November 03 flare (see Chapter 3), for which the data points are connected by lines.

plot on the right panel for the same flares. Note that Petrosian et al. (2002) obtained $\bar{\gamma}_{\rm LT} = 6.2 \pm 1.5$ and $\bar{\gamma}_{\rm FP} = 4.9 \pm 1.5$ from broadband *Yohkoh* data. The main difference between our and their results is that our FP spectra are harder, which can be ascribed to the different flare sample selected here and/or the higher energy and spatial resolution *RHESSI* has as compared with *Yohkoh*.

However, one would also expect some correlation between these indexes which does not seem to be present. In this figure we also show the evolution of these indexes for the 2003 November 03 X3.9 flare (see Chapter 3), whenever both the LT and FP sources can be fitted with a power law model. During the first pulse (cross signs) the spectral indexes seem to be correlated weakly, but not during the second pulse (plus signs), which appears to be still in its rising phase (see Fig. 3.3) and a weak anti-correlation is seen in the index values. The correlation expected from the simple model is clearly not present. But this is not surprising. Firstly, the actual LT and FP spectra and expressions for loss and escape

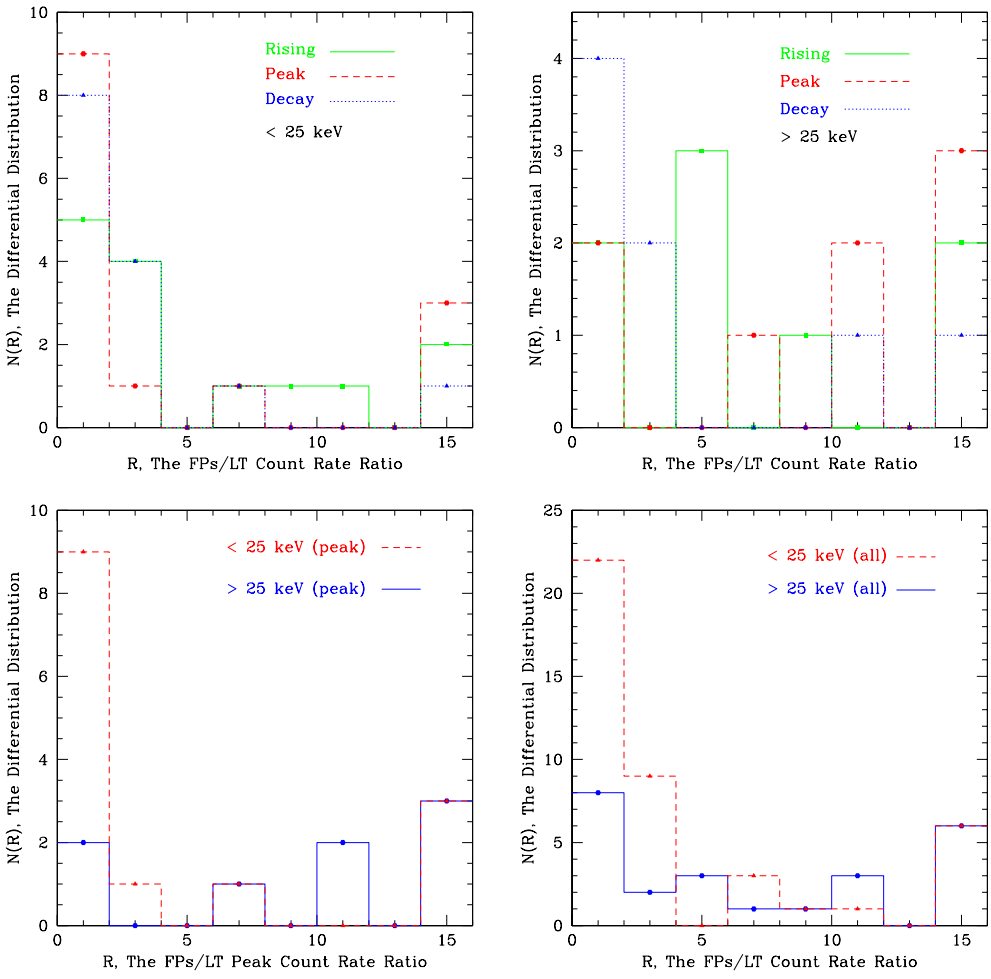

Figure 2.11: Histograms of R, the FPs to LP flux ratios at different times and energies, with a bin size of 2. The upper cutoff is set at 16, about the upper limit of *RHESSI* images, and any ratio greater than this value is counted to the last bin (note this results in the tail bump at $R = 16$).

times are more complicated (see Chapter 7). Secondly, the observed LT indexes are more representative of the spectrum at lower energy (where the spectrum is steeper) than those of the FPs. These indicate that we need to carry out more accurate data analysis and use more accurate models than the toy model given earlier.

2.4.2 Statistics of the Relative Fluxes: FPs vs. LTs

For ten of the sample flares, we have obtained the light curves of individual LT and FP sources and their flux ratios. Histograms of the FP-to-LT flux ratio are shown in Figure 2.11, which reveals the following characteristics.

1. Again, we find that the LT sources have softer spectra than the FP sources (see the *lower right* panel). At low energies ($\leq$ 25 keV), the median of flux ratio distribution is very close to one; in contrast, at high energies ($\geq$ 25 keV), the median ratio is much greater than unity and its distribution is much flatter. These results are qualitatively consistent with the theoretical calculations by Petrosian and Liu (2004).

2. At flare peak times, the LT emission dominates at low energies (with the ratio distribution concentrated close to unity) while FPs dominate at high energies (*lower left* panel).

3. During the decay phase of a flare (*upper* panels), the LT source tends to be the major contributor to the total flare emission, especially at low energies ($\leq$ 25 keV).

4. At high energies ($\geq$ 25 keV), the median of the distribution first increases (from the rise to the peak phase) and then decreases, which translates to that the relative importance of the FP emission has an up-and-down variation. This LT-FP-LT pattern is correlated with the commonly observed soft-hard-soft variation in the spatially integrated spectrum during the course of a flare, and this suggests such a spectrum variation is (at least partly) contributed by the transition between the spatial variation of the dominant emission.

2.5 Flare Statistics and Selection Biases

The study described above is appropriate for a small sample of flares. To uncover the general characteristics of flares, it is necessary to have statistical studies of the parameters (e.g. peak X-ray flux and duration) for a much larger number of flares. Here we briefly describe the background of this subject and propose an approach for a future study.

Several statistical investigations of distributions, ranges and mean values of relevant parameters, and the correlations between them have been carried out (see, e.g., Lee et al., 1993, 1995; Petrosian et al., 2002) using statistical methods developed by Efron & Petrosian (1992, 1995). Similar statistical studies were done by many others as well (e.g., Dennis, 1985; Crosby, Aschwanden, & Dennis, 1993; Dennis & Zarro, 1993).

One of the most important aspects of this kind of study is proper accounting of the selection biases. The first step here is the careful selection of the sample. The left panel of Figure 2.12 shows a representative distribution of peak count rates of *RHESSI* flares.

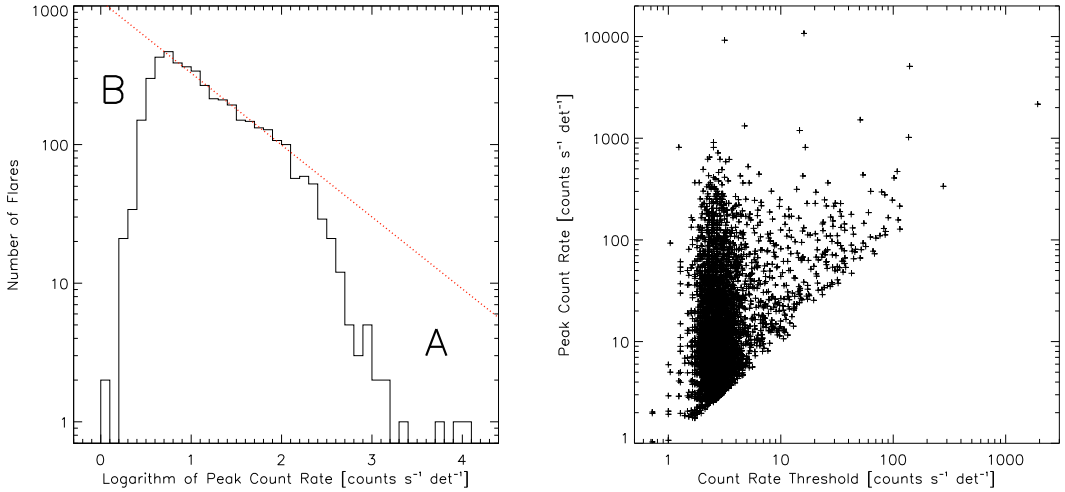

Figure 2.12: *Left*: Distribution of the *RHESSI* flares with peak count rates (in the 12–25 keV channel) greater than 4σ above the background noise and when no shutters were in, the latter of which introduces the bias at high count rates in region A that can be corrected. The bias at low count rates (region B) is due to variation of the detection threshold as shown on the *Right*, which shows the peak count rate vs. the threshold count rate for these flares. The truncation of the data below the diagonal line is obvious.

It clearly suffers from bias at high peak count rates (A) from the effects of the *RHESSI* shutters and at low peak rates (B) due to background variations. A flare usually is identified when its count rate in some channel is more than several sigmas above the background noise. This means that the threshold for detection varies from flare to flare and with the energy band due to different background. The right panel of Figure 2.12 shows the peak count rate versus the threshold count rate of the flares used in the left hand side plot. It is clear that the sample is biased against identification of weaker flares, as shown by the truncation of the data below the diagonal line, when the background level, and hence the count-rate threshold, is higher. Less obvious but no less real is the truncation above a peak rate of about 100 counts $\mathrm{s}^{-1}\mathrm{detector}^{-1}$ due to the insertion of the *RHESSI* shutters for these more intense flares. This kind of biased or truncated data can be analyzed using our statistical methods (Efron & Petrosian 1992, 1999). Several other characteristics of flare emission, e.g. duration and spectrum, also influence the sample selection process (see Lee et al. 1993, 1995), and will require similar thorough statistical treatment.

Su, Gan, & Li (2006) have recently reported a statistical study on *RHESSI* peak count rates and various (rise, decay, and duration) timescales, using data in the 12–25 keV band which was taken directly from the online flare list without proper corrections. For example, they used a simple, empirical method to account for the different attenuator states. They found a power-law index of 1.80 ± 0.02 for the peak count rates, but this may be subject to improper consideration of the instrument response and selection biases mentioned above.

In the near future, as the *RHESSI* calibration and software are improved and become more stable, we plan to carry out a similar analysis for more flares, carefully correcting various biases. The peak X-ray flux would be the first parameter to be studied. For each

flare in the *RHESSI* flare list, one should use the detector response matrix (DRM) to convert the count rate to the incident photon rate and properly subtract the background, using the *RHESSI* spectral analysis software package, Object Spectral Executive (OSPEX).. An automated tool will be developed to perform this analysis. The statistical methods quoted above will be used to correct selection biases. Similar analysis will be applied to other flare parameters, e.g. duration and total counts.

We expect to obtain the intrinsic distribution of these flare parameters and their correlation with much higher accuracy and sensitivity benefiting from the superior capabilities of *RHESSI*, and compare the results with those from earlier missions. This will provide important implications to flare energization and particle acceleration. Examples of such implications include addressing the question that whether numerous small flares play a significant role in coronal heating (Lee et al. 1993).

2.6 Summary and Discussion

We have initiated an investigation of a sample of *limb flares* observed by *RHESSI*. We used X-ray images to infer flaring loop structures and to distinguish between FP and LT sources. We analyzed the light curves and spectra of these individual sources, and presented the statistics of the spectrum indexes, as well as the FP-to-LT flux ratio during different phases of a flare. The preliminary results from a sample of 29 flares are as follows.

1. The averages of the LT and FP spectral indexes are 6.84 and 3.35, respectively, with a large difference of 3.49, which can, in principle, be used to constrain the parameters in the particle acceleration model.

2. An expected correlation between the LT and FP spectral indexes is not present in this study, suggesting that a more accurate statistical study (with a larger sample) is required and a more rigorous prediction from the particle acceleration model is needed as well.

3. At flare peak times, the LT (FP) emission dominates at low (high) energies. During the decay phase, the LT emission becomes more important than the FP emission. The LT-FP-LT variation of relative importance of HXR emission is correlated with the soft-hard-soft variation of the spatially integrated spectrum.

We have also proposed a plan for future statistical studies (in addition to expanding the sample of flares for imaging spectroscopy analysis), in which using proper statistical methods to correct data selection biases is required to uncover the intrinsic distribution of various flare parameters.

The statistical study presented here, in practice, also served as data mining to identify several interesting flares for detailed investigations. Studies of these particular events will be presented in next four chapters.

Chapter 3

Classical Flare Models and New *RHESSI* Observations: The 2003-11-03 X3.9 Flare[1]

3.1 Introduction

Since its launch *RHESSI* has observed several X-class flares and thousands of mid-class and small flares. The compactness of microflares limits our access to details of the energy release and particle acceleration processes (Krucker et al., 2002). On the other hand, large and well-resolved flares usually involve multiple loops with complex structures, and the looptop (LT) and associated footpoint (FP) sources are not readily identified and separated (Gallagher et al., 2002; Lin et al., 2003). This makes a direct comparison of theoretical models with observations a challenging task (Alexander & Metcalf, 2002; Sui et al., 2002). This task would be easier for a large flare with a simple morphology, where one can identify source positions and evolutions with certainty (Tsuneta, 1996; Tsuneta et al., 1997).

In late October and early November of 2003, *RHESSI* and other instruments observed a series of X-class flares from solar Active Regions 0486 and 0488 (reminiscence of the 1991 June flares of the previous solar cycle; Schmieder et al., 1994). Among these flares, we studied an event that occurred on November 3 in AR 0488 at heliographic coordinate N09°, W77°. Unlike other X-class flares, e.g., the 2002 April 21 flare (Gallagher et al., 2002) and the gamma-ray flare on 2002 July 23 (Lin et al., 2003), this flare shows a surprisingly simple morphology with well-defined one LT and two FP sources.

In this chapter we present a brief description of the spatial evolution of the various emission regions of this flare. As we show, this provides an excellent example of the classical solar flare model of magnetic reconnection and energy release in an inverted Y magnetic field configuration (Kopp & Pneuman, 1976; Forbes & Acton, 1996; Aschwanden, 2002), whereby reconnection in the oppositely directed field lines leads to particle acceleration near the LT. The energy release and particle acceleration processes are not well understood; nevertheless, it is expected that the reconnection will produce closed loops at lower altitudes first and progress to higher overlying loops as time advances. Consequently, the altitude of the LT

[1]The majority of the material in this chapter was published in Liu, W., Jiang, Liu, & Petrosian (2004a).

source and the separation of the two FPs should increase with time. The flare studied here shows this exact behavior.

On the other hand, we also see evidence for deviations from the simplest reconnection models. Our study indicates that the reconnecting fields could be nonuniform and may have a shearing component. In the next section, we present the observations, data analysis, and our results. Their implications are discussed in § 3.3.

3.2 Observations and Data Analysis

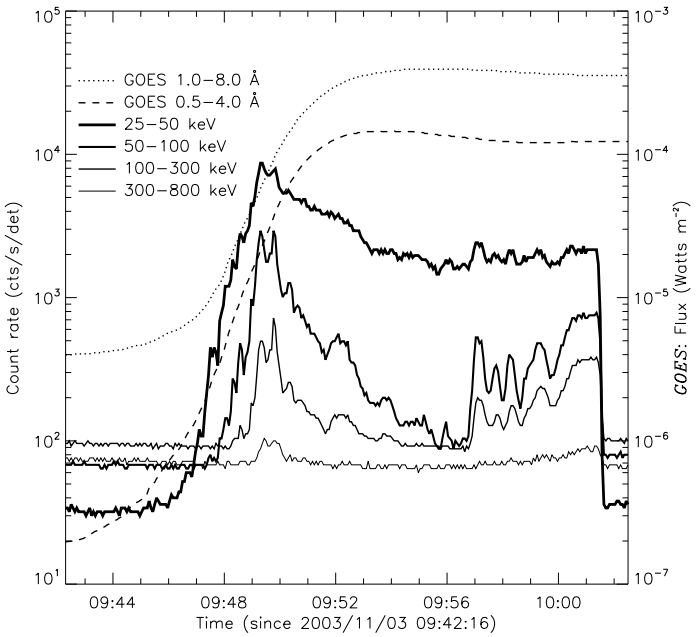

Figure 3.1: *RHESSI* count rates (counts/second/detector, averaged over 4 s intervals) and *GOES*-12 fluxes (in a 3 s cadence).

The flare under study, classified as a *GOES* X3.9-class flare, was observed by *RHESSI*, *Solar and Heliospheric Observatory* (*SOHO*), etc. Figure 3.1 shows the *RHESSI* and *GOES-12* light curves. In lower energy channels (< 25 keV), the count rates started to rise at around 09:43 UT, peaked about nine minutes later, and then began a monotonic declining phase until 10:01:20 UT when *RHESSI* entered the Earth's night region. The higher energy channel (> 50 keV) light curves exhibit two broad impulsive bursts, each of them consisting of several pulses with a more quiescent part in between, suggesting a persistent but episodic energy release process. Impulsive radio activities were also observed by the Nançay Observatory (Dauphin et al., 2006) A partial halo coronal mass ejection (CME) with a speed of ~ 1375 km s^{-1} was observed by the Large Angle and Spectrometric Coronagraph on *SOHO*.

3.2.1 Source Structure and Motion

To study the hard X-ray (HXR) source motion and structure, we obtained images at different energies in 20 s intervals from 09:46:20 through 10:01:00 UT using the CLEAN algorithm (Hurford et al., 2002) and front segments of detectors 3–8 to achieve a FWHM of $9\farcs8$ with a $0\farcs5$ pixel size. Figure 3.2 shows the HXR emission contours during the two main activity peaks. There are three sources: an LT, a northern FP (N-FP), and a southern FP (S-FP). The LT source dominates at low energies while the FPs dominate at high energies. As evident from the background pre-flare magnetogram obtained with the Michelson Doppler Imager (MDI), the N-FP is around a negative magnetic polarity region while the S-FP remains in a region of positive polarity. Note that early in the event there is a partial overlap between the N-FP and the LT source. Grids with higher spatial resolution will not help for this flare because grid 2 is in a severely degraded condition (Smith et al., 2002) and grid 1 will overresolve the sources (see Schmahl & Hurford, 2003, for technical details). A postflare (10:35:43 UT) EUV Imaging Telescope (EIT) 195 Å image (not shown) shows a loop structure that agrees well with the *RHESSI* sources.

As shown in Figure 3.2, the LT and FPs have well-defined and correlated motions, with the symbols indicating their emission centroids at different times. The white dashed straight line represents the main direction of the LT motion, which is roughly at a right angle to the solar limb. We refer to the motion along this direction as changes in altitude. The motion perpendicular to this direction might be due to asymmetry of the reconnecting loops or the LT motion along an arcade. Before the rise of the impulsive HXR emission, there is an apparent downward LT motion. This downward motion could indicate a shrinkage of newly formed loops. It may also be due to the formation of nearby sources (Krucker, Hurford, & Lin, 2003) or to projection effects should the LT source move eastward along an arcade of loops (Sato, 2001). Qualitatively similar features have been seen in several other flares (Krucker et al., 2003; Sui & Holman, 2003), suggesting that this may be a common characteristic of solar flares. However, for the remainder of the flare duration the LT source rises systematically. The apparent separation of the FP sources, whenever detectable, also increases with comparable speed. As emphasized above, this is expected in a simple continuous reconnection process that moves up to the corona, accelerating particles and energizing plasma higher up into overlying larger loops.

To analyze the FP motion quantitatively, one needs to take into account projection effects because any motion and its associated uncertainty in the east-west direction are amplified by a factor of about $\csc 77^\circ \simeq 4.4$. Motions in this direction are highly uncertain, and the motion of both FPs appears to have an east-west component. Magnetic reconnection, on the other hand, is characterized by the change in the size of newly formed loops rather than their absolute motions. Thus one may concentrate on the relative motion of the two conjugate FPs. In the insert panel of Figure 3.2, we illustrate this relative motion by fixing the S-FP at the origin of the coordinates and showing the relative locations of the N-FP. The relative motion is obviously systematic. The fact that the line tracing the location of the N-FP is not exactly aligned with the lines connecting the two FPs shows that there is another component of the relative motion introducing a small rotation of the plane containing the newly formed loop. Because this line is nearly parallel to the longitudinal line, one can ignore the projection affects. We quantify the relative motion along this line, and

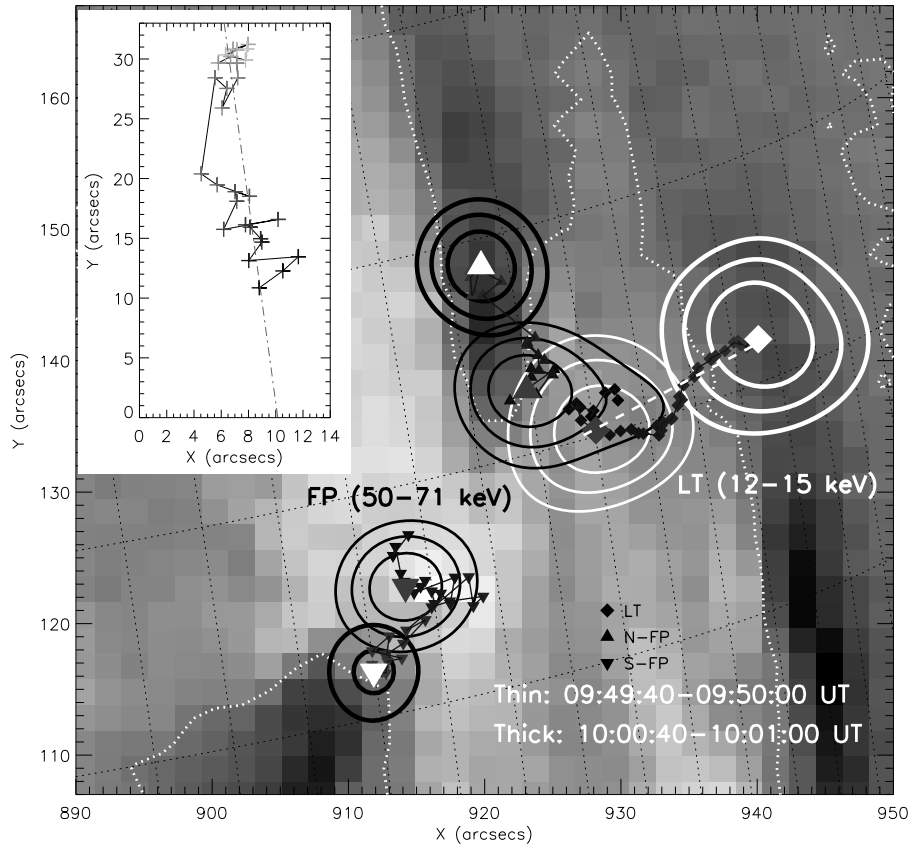

Figure 3.2: Temporal evolution of HXR source centroids, over-plotted on an MDI magnetogram (09:32:30 UT). Black line segments connect the centroids obtained from CLEAN images in successive 20 s intervals chronologically from dark (09:46:20 UT) through gray to white (10:01:00 UT). The LT (12–15 keV) centroid is the brightness-weighted source center within the 70% level contour, but each FP (50–71 keV) centroid is the peak position obtained with a 3×3 pixel parabolic fit around the brightest pixel. The white dashed straight line represents the main direction of motion of the LT source. To estimate the uncertainty in the LT centroid location, we fitted the LT data points with four straight lines within the time intervals, 09:46:20–09:49:40, 09:49:40–09:52:00, 09:52:00–09:55:20, and 09:55:20–10:01:00 UT, respectively. For each interval, following Krucker et al. (2003), the standard deviation of the offset of the data from the corresponding straight line was used as the error in the location. The insert shows the relative positions of the N-FP with respect to the S-FP, which is fixed at the origin. We attribute the motion perpendicular to the straight line to uncertainties in the locations (see text for details). Four HXR images in two time intervals, 09:49:40–09:50:00 (*inner*) and 10:00:40–10:01:00 UT (*outer*), and in two energy channels, 12–15 (*white*) and 50-71 keV (*dark*), are overplotted as contours (at 55%, 70%, 85% levels of the maximum brightness of the image), which clearly depict the LT and FPs, respectively. The centroids corresponding to these two intervals are indicated with larger symbols. The magnetogram shows the line-of-sight magnetic field in a gray scale ranging from −979 (*black*: pointing away from the observer) to +1004 Gauss (*white*). The apparent neutral lines are marked as white dotted lines [from Liu, W. et al. 2004a].

the standard deviation of the displacement (apparently) perpendicular to this line is used as an upper limit for the uncertainties of this relative motion.

Figure 3.3*b* shows this relative motion of the FPs (at 50–71 keV) along with the location of the emission centroids of the LT source in three energy bands projected onto its main direction of motion that is nearly perpendicular to the solar limb. As evident, the two motions are correlated and the two sets of data points are nearly parallel to each other indicating comparable velocities. To further investigate these motions we divide the observed flare duration into four phases: a pre-impulsive phase (before 09:48:10 UT) when there is no significant high-energy HXR emission, a rising phase (from 09:48:10 to 09:49:50 UT), a declining phase (from 09:49:50 to 09:56:50 UT), and a second active phase (from 09:56:50 to 10:01:00 UT). We then fit straight lines to each segment and determine the corresponding average velocities. The results are summarized in Table 3.1. Surprisingly, the LT velocity is highest in the declining phase, when the X-ray emission is relatively weaker (Fig. 3.3*c*). In the simplest model of reconnection of *uniform* and oppositely directed magnetic fields, one would expect the opposite correlation, i.e., a higher rate of energy release when the velocity is larger. However, this would be true if the observed HXR flux were actually proportional to the total energy release and if reconnection were indeed occurring in a uniform background plasma, neither one of which is exactly true.

Table 3.1: LT velocities and FP separation speed.

Time range	LT velocities (km/s)				FP speed(km/s)
(UT)	9-12 keV	12-15 keV	15-19 keV	19-24 keV	(50-71 keV)
09:46:20-09:48:10	-18.3 ± 3.7	-22.5 ± 4.6	-32.5 ± 4.1	-30.8 ± 4.7	— — —
09:48:10-09:49:50	3.5 ± 3.3	4.0 ± 3.0	4.7 ± 2.6	4.3 ± 2.7	29.1 ± 11.6
09:49:50-09:56:50	14.6 ± 0.4	16.5 ± 0.2	18.0 ± 0.2	20.9 ± 0.1	22.4 ± 2.5
09:56:50-10:01:00	9.3 ± 0.9	8.6 ± 0.7	6.6 ± 0.7	5.9 ± 0.5	10.4 ± 3.6

Another interesting morphological evolution is the change of the centroid of the LT source with energy. In Figure 3.4 (*left*) we show the *RHESSI* 75% contours and centroids at several energies superposed on an MDI continuum image showing sunspots. Compared with the two FPs, the LT source shows a clear and systematic displacement of the centroid of the higher energy emissions toward higher altitudes, as seen in two other flares (Sui & Holman, 2003; Gallagher et al., 2002).

To investigate what this separation of the LT centroids is related to, we looked for its correlations with other characteristics. We found an anticorrelation between the centroid separation and the high-energy (100–300 keV) count rate, which comes mainly from the FPs (3.3*d*). The continuous curve in Figure 3.4 (*right*) shows their cross-correlation function, which gives a peak correlation coefficient of -0.51 ± 0.08 with a time lag of $\Delta t = -22 \pm 39$ s. The data points (LT separation vs. HXR count rate) used for evaluating the correlation and a straight-line fit are also shown in the same figure.

3.2.2 Imaging Spectroscopy

We also analyzed the spectra of this flare. In most cases, the spatially integrated spectra from 8 to 100 keV can be fitted with a double power law (DPL) model or a thermal plus a

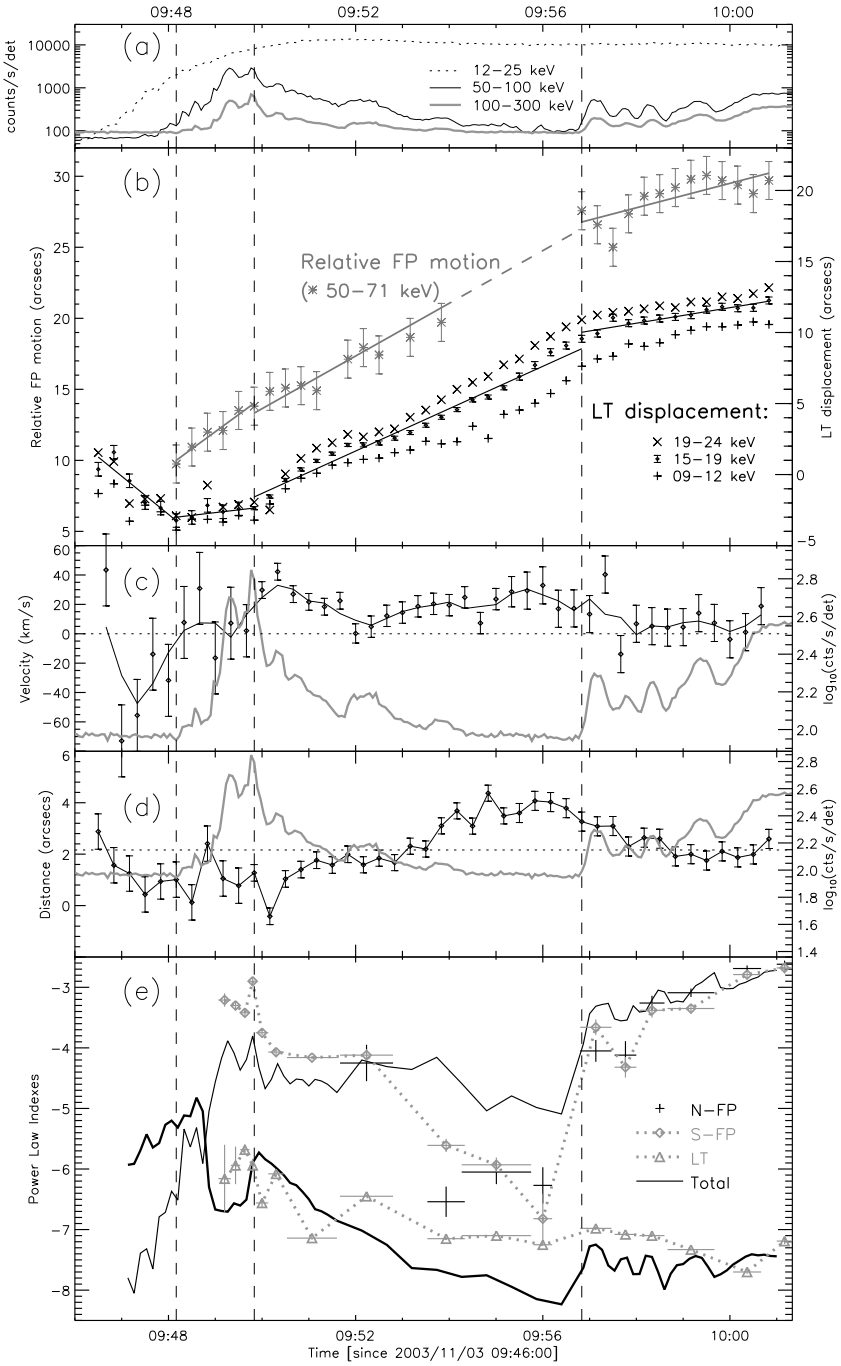

Figure 3.3: (*a*) *RHESSI* light curves. (*b*) Evolution of the displacement of the LT centroid (*right scale*) and the separation of the two FPs (*left scale*). The straight lines are fits to the data (15-19 keV for LT). The vertical dashed lines separate the four phases (see text). (*c*) LT velocity at 15–19 keV (*symbols*) and its value (*thin line*) smoothed over one minute intervals. The thick curve is the logarithmic count rate at 100–300 keV (*right scale*). (*d*) Separation of the LT centroids at 19–24 and 9–12 keV (panel *b*), together with the count rate logarithm (same as *c*), vs. time. The dotted line marks their mean. (e) Spectral indexes for various model fits. The thick and thin solid curves give the low and high energy indexes of the spatially integrated spectra. Imaging spectroscopic results are indicated by the points with 1σ vertical error bars. Horizontal error bars represent imaging integration time. [*a–d* from Liu, W. et al. 2004a].

power law (ThPL) model with similar reduced χ^2_r. The time history of the DPL parameters are shown by the solid lines in Figure 3.3*e* (The high energy index of the ThPL is nearly identical to that of the DPL). Note that during the first rising phase the spectra change from convex to concave (Holman et al., 2003), as can be seen from the intersection of the low- and high-energy indexes.

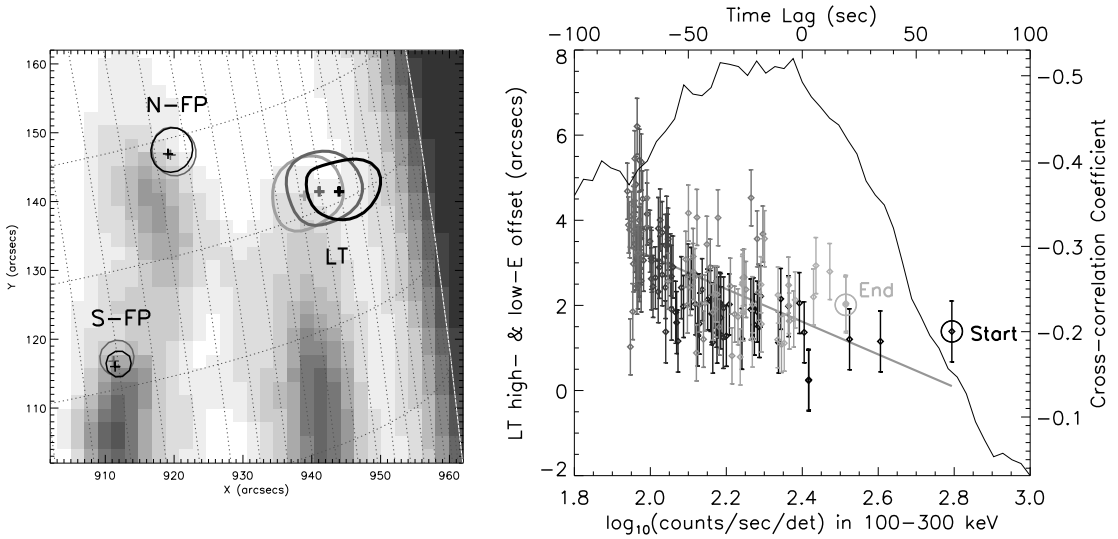

Figure 3.4: *Left: RHESSI* image contours (75%) and the corresponding brightness-weighted centroids (*plus signs*) in the interval 10:01:00–10:01:20 UT. The LT contours are for 12–14 (*light gray*), 18–21 (*gray*), and 27–31 keV (*dark gray*) and the FP contours are for 40–46 (*gray*) and 60–73 keV (*dark gray*). The background is an MDI continuum map taken at 09:36:00 UT. The dark areas inside the limb are three sunspots. *Right:* Correlation between the LT structure and the 100–300 keV (mainly FPs) light curve. The thin curve (with the top and right axis) shows the cross-correlation coefficient of the logarithm of the count rate and the separation between the 19–24 and 9–12 keV centroids of the LT source, showing a 22 ± 39 s delay relative to the light curve. The separation is similar to that shown in Fig. 3.3*d* but with a higher time resolution, obtained by imaging at a 4 s cadence (same as the light curve) with an integration time of one spacecraft spin period (~ 4 s) from 09:49:48 to 10:01:00 UT. We excluded the first two phases of the flare duration when the spatial contamination to the LT source by the N-FP is severe. The diamond symbols (with the bottom and left axis) show the LT separation vs. the logarithm of the count rate shifted by +24 s, corresponding to the peak of the correlation coefficient. The vertical error bars represent the uncertainty in the centroid separation. The darkness of the symbols represents time with the start and end point being circled. The gray thick line is a linear fit to the data with a slope of -3.84 ± 0.34 [from Liu, W. et al. 2004a].

For the purpose of imaging spectroscopy we reconstructed CLEAN images (pixel size of $1''$) with detectors 3-6 and 8 (excluding detector 7 because of its poor spectral resolution) at photon energies from 12 keV through 200 keV in 18 time intervals mostly selected at the peaks of the higher energy emission. To get the spectra of individual sources we used the component maps. For a given area, taking into account the over-sampling of the $1''$ pixel size compared to the $\sim 9''.5$ FWHM resolution (S. Krucker, private communication), the

RMS fluctuation in the residual map was used to estimate the error of the corresponding source flux. When the FPs and LT are well separated, we successfully obtained the spectra of the LT and two FP sources. Early in the event (between 09:47:48 and 09:51:37 UT) when the LT and N-FP source are partially overlapped, we first obtained the spectrum of the S-FP and the combined spectrum of the LT and N-FP. Then assuming that the two FP sources have the same spectral index and dominate at high energies (> 50 keV), we subtracted the N-FP spectrum (normalized appropriately) from the combined spectrum to obtain the LT spectrum.

In general, the spectra of the two FPs can be fitted by a single power law with very similar indexes and their fluxes are consistent within a factor of ~ 2. The LT spectrum can be fitted by a power law as well and its index is smaller than those of the FPs by > 4 units (Fig. 3.3*e*). This difference is larger than that found by Petrosian, Donaghy, & McTiernan (2002) though. On the other hand, as we have shown earlier in Chapter 2, a large difference of 3.49 between the average FP and LT spectral indexes are also found from our preliminary statistical study, which seems to be consistent with the stochastic acceleration model (Petrosian & Liu, S. 2004). (Note that the LT and FP spectra are fitted in the energy range 12-200 keV. However, the FP spectral indexes are mainly determined by data above 30 keV because data points below this energy have relatively large error bars, while most of the contribution to the LT index comes from data below 30 keV as the LT spectrum has comparably large errors above 30 keV.) There also seems to be a weak *anti-correlation* (see also Fig. 2.10) between the indexes of the LT and FP sources during the second active phase of the flare. This is not expected from simple solar flare models. Unlike other *RHESSI* flares that we have studied, in this flare a thermal model gives a poor fit to the LT spectra for most of the times (Holman et al. 2003).

The bottom panel of Figure 3.3 shows that the imaging spectroscopic results (without pileup correction which is not yet available for imaging) are roughly consistent with the spatially integrated values (which are corrected for pileup). The primary reason for the difference most likely is due to the presence of extended sources (Schmahl & Hurford, 2002) as well as some pileup effects. To investigate the pileup effect on imaging spectroscopy, we fitted the LT spectra in 12-30 keV energy range (Emslie et al., 2003), where the pileup effect is negligible and found that the power-law index changed by 10% in the worst case (livetime $\sim 77\%$) and by less than 5% at all the other times ($73\% \leq$ livetime $\leq 94\%$). The pileup correction therefore will not change the imaging spectroscopic results significantly.

3.3 Summary and Discussion

We have investigated the 2003 November 3 X3.9 flare, having a simple morphology with well-defined LT and FP sources. The high flux combined with the simple loop structure allows us to determine the spatial evolution of the LT and FP sources clearly and to compare with the simple reconnection models. Similar studies of flares have been limited to the investigation of the motion of the FPs alone (Sakao, Kosugi, & Masuda 1998; Qiu et al. 2002; Fletcher & Hudson 2002) or have dealt with complex loop structures (Krucker et al. 2003; Qiu, Lee, & Gary 2004). This has made the comparison with models more difficult. Our analysis of *RHESSI* data has yielded several new and interesting results.

1. We observe a systematic rise of the LT source and a comparable increase in the separation of the FPs as the flare proceeds. This agrees very well with the canonical solar flare model of magnetic reconnection in an inverted Y configuration. Similar behaviors have been reported previously using soft X-ray or EUV observations (Švestka et al., 1987; Tsuneta et al., 1992; Gallagher et al., 2002) during later thermal gradual phases of flares. However, these emissions are not directly related to the impulsive particle acceleration processes (Forbes & Acton, 1996).

2. The LT source seems to move more slowly during the HXR peaks than during the declining and more quiescent phases, in apparent disagreement with reconnection of *uniform* and oppositely directed field lines, where one would expect a correlation between the velocity of the LT source and the energy release rate. However, we note that the HXR flux is not a good proxy for the energy release rate, and the magnetic fields in the reconnection region are likely to be nonuniform. Stronger magnetic fields would require a smaller volume of reconnecting fields and possibly slower motion. However, in an inhomogeneous case other factors such as the geometry and Alfvén velocity variation can also come into play. This problem needs further exploration.

3. The centroid of the LT source appears to be at higher altitudes for higher photon energies. This suggests that the energy releasing process happens above the LT and that harder spectra, implying more efficient acceleration, are produced at higher altitudes. In the stochastic acceleration model by turbulence where the acceleration efficiency depends on the intensity of turbulence, this would indicate a decrease of the intensity with decreasing altitudes, presumably because of decay of turbulence away from its source at a higher altitude (Petrosian & Liu, 2004).

4. The above shift of the centroids decreases with the increase of HXR flux from the FPs. Such an anticorrelation will be difficult to produce in simple models. In the above-mentioned model, this would imply a more inhomogeneous distribution of turbulence during more active phases, because a smaller shift means a larger spatial gradient.

5. The spatially integrated spectra are fitted equally well with a double power-law model and a thermal plus power-law model.

6. The imaging spectroscopy study suggests that the LT and FP sources could be purely nonthermal. In the second active phase of the flare, there appears to be an anti-correlation between spectral indexes of the LT and FP sources and their difference can exceed 4.

Another possible explanation, in regard to No. 4 mentioned above, concerns the interplay of the heating/acceleration and cooling processes. Studies of the evolution of loops in the gradual phase indicate that cooling of the plasma confined within closed loops plays an important role in determining the observed emission morphology (Forbes & Acton 1996). If cooling is also important in the impulsive phase, one would expect that loops forming earlier have lower plasma temperatures and contribute mainly to emission at lower energies. Then the motions of the emission centroids at lower energies will be dominated by the cooling process. The motions of centroids at higher energies, however, are presumably determined

by the heating/acceleration process, a direct consequence of reconnection. When higher energy sources slow down due to the increase of reconnecting magnetic fields as discussed above, the apparent velocities of lower energy sources do not change significantly until their centroids are determined by emission from hotter plasmas at the reconnection site. The sudden decrease of the 19-24 keV centroid velocity and the relatively smooth transition of the 9-12 keV centroid motion during the onset of the second HXR burst (Fig. 3.3*b*) and the delay of the LT centroid separation relative to the light curve (Fig. 3.4, *right*) seem to support such a scenario.

A more detailed analysis of this flare including imaging spectroscopy and quantitative comparison with theoretical models will be needed to shed light on the observations presented here and distinguish between the possibilities discussed above.

Chapter 4

Double Coronal Hard and Soft X-Ray Source as Evidence of Magnetic Reconnection: The 2002-04-30 M1.4 Flare[1]

4.1 Introduction

In the classical reconnection model (e.g., Petschek, 1964) magnetic field annihilation in a current sheet produces outflows of high-speed plasma in opposite directions (see Fig. 1.1, *left panel*). This process can generate turbulence that accelerates particles and heats the background plasma stochastically (e.g., Ramaty, 1979; Hamilton & Petrosian, 1992; Park & Petrosian, 1995; Miller et al., 1996; Petrosian & Liu, 2004). Radio emission and hard and soft X-rays (HXRs and SXRs) produced by the high-energy particles and hot plasma are expected to show signatures of the two oppositely directed outflows. Specifically, one would expect to see two distinct X-ray sources, one above and one below the reconnection region (in the case of a vertical current sheet).

It is well established that many flares have SXR and HXR emission arising both from the source near the top of the loop (loop-top source; e.g., Masuda, 1994; Petrosian et al., 2002; Liu, W. et al., 2004a; Jiang et al., 2006; Battaglia & Benz, 2006, Chapter 2,) and from a pair of footpoint sources (e.g., Hoyng et al., 1981; Sakao, 1994; Sui et al., 2002; Saint-Hilaire et al., 2008). The loop-top source is believed to be near the reconnection site and produced by freshly accelerated particles and/or heated plasma. Observations of the expected two distinct X-ray sources above and below the reconnection region have rarely been reported. This may be due to limited sensitivity, dynamic range, and/or spatial resolution of the instruments, because one source may be much dimmer than the other, the two sources may be too close together to be resolved, or both may be much weaker than the footpoints.

Sui & Holman (2003) and Sui et al. (2004) reported a second coronal source that appeared above a stronger loop-top source in the 2002 April 15 flare and in another two

[1]The majority of the material in this chapter was published in Liu, W., Petrosian, Dennis, & Jiang (2008b).

homologous flares. They suggested that there was a current sheet existing between the two sources. Recently, in one of the events reported by Sui et al. (2004), Wang et al. (2007) discovered high-speed outflows revealed by Doppler shifts measured by the Solar Ultraviolet Measurements of Emitted Radiation (SUMER) instrument on board the *Solar and Heliospheric Observatory* (*SOHO*). This provides more evidence of magnetic reconnection. Veronig et al. (2006) also found a second coronal source appearing briefly in the 2003 November 3 X3.9 flare (Liu, W. et al., 2004a; Dauphin et al., 2006). Li & Gan (2007) reported another *RHESSI* flare, occurring on 2002 November 2, which shows a similar double coronal source morphology. They interpreted the two sources as thermal emission because no HXR emission was detected above 25 keV and the footpoints were occulted. In their event, however, the two sources have somewhat different temporal evolution, with the flux of the upper source peaking about 18 minutes later than that of the lower source. In radio wavelengths, Pick et al. (2005) reported a double-source structure observed in the 2002 June 2 flare with the multi-frequency Nançay radio-heliograph (432–150 MHz). Due to its low brightness and/or technical difficulties, X-ray imaging spectroscopy of the weaker coronal source was not available or has not been studied for the above *RHESSI* events (Sui & Holman, 2003; Sui et al., 2004; Veronig et al., 2006; Li & Gan, 2007).

We report here another flare with two distinct coronal X-ray sources that occurred on 2002 April 30. The brightness of the upper source relative to the lower source is larger and the upper source stays longer ($\sim$12 minutes) than those (3–5 minutes) of Sui et al. (2004). In addition, the footpoints are occulted by the solar limb, and thus the spectra of the coronal sources are not contaminated by the footpoints at high energies. This makes a stronger case for the double coronal source phenomenon and allows for more detailed analysis, including X-ray imaging spectroscopy and temporal evolution of the individual sources. Analysis of the decay phase of this flare was originally reported by Jiang et al. (2006) as an example of suppression of thermal conduction and/or continuous heating attributed to the presence of plasma turbulence. Here we extend the analysis throughout the whole course of the flare.

Early in the flare, the two coronal sources are close together and the source morphology exhibits a double cusp or "X" shape, possibly indicating where magnetic reconnection takes place. As the flare evolves, the two sources gradually separate from each other. Both sources exhibit energy-dependent structure similar to that found for the flares reported by Sui et al. (2004) and Liu, W. et al. (2004a). In general, for the lower source, higher energy emission comes from higher altitudes, while the opposite is true for the upper source. Imaging spectroscopy shows that the two sources have very similar nonthermal components and light curves. These observations suggest that the two HXR/SXR coronal sources are produced by intimately related populations of accelerated/heated electrons resulting from energy release in the same reconnection region, which most likely lies between the two sources. These are consistent with the general picture outlined above. We also find that the two sources have different thermal components, with a lower temperature and larger emission measure for the lower source. Different magnetic topologies and plasma densities of the two sources can be the causes of such differences.

We present the observations and data analysis in §4.2 and our physical interpretation in §4.3. We conclude this chapter with a brief summary and discussion in §4.4. Details of specific *RHESSI* spectral analysis techniques are provided in Appendix A.3.

4.2 Observations and Data Analysis

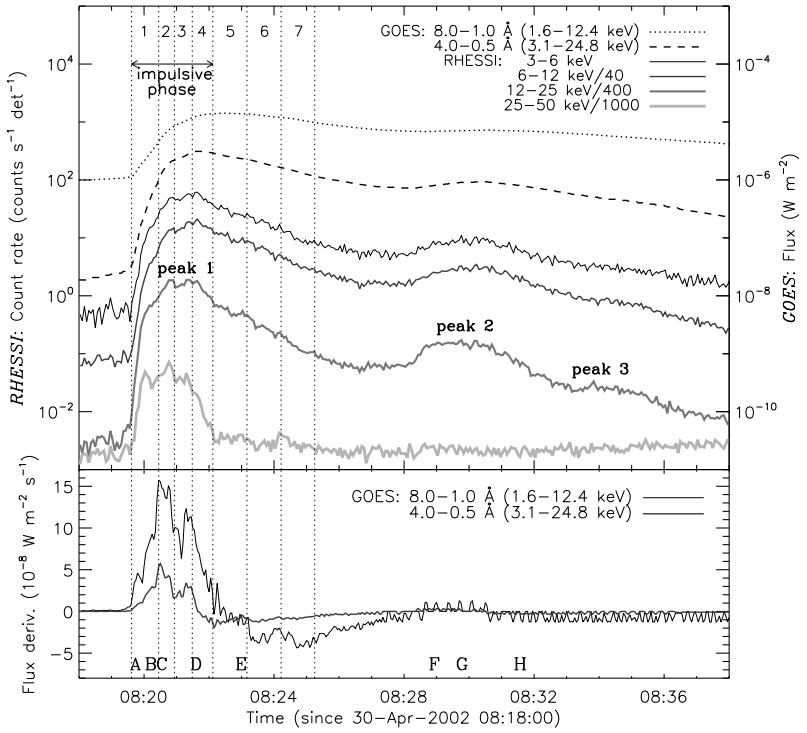

Figure 4.1: *Top*: *RHESSI* and *GOES*-10 light curves of the 2002 April 30 M1.4 flare. The *RHESSI* count rates (*left scale*) are averaged over every 4 s, with scaling factors of 1, 1/40, 1/400, and 1/1000 for the energy bands 3–6, 6–12, 12–25, and 25–50 keV, respectively. The *GOES* fluxes (*right scale*) in the bandpass of 8–1 Å (1.6–12.4 keV) and 4.0–0.5 Å (3.1–24.8 keV) are in a cadence of 3 s. The vertical dotted lines mark the seven time intervals used for imaging spectroscopy (see Figs. 4.6 and 4.7). Intervals 1–4 correspond to the impulsive phase according to the 25–50 keV light curve. Three peaks on the 12–25 keV curves are also marked. *Bottom*: Time derivatives of the *GOES* fluxes, showing the Neupert-type behavior. The capital letters (A–H) at the bottom mark the central times of the intervals of the images shown in Fig. 4.4. Note that the energy release episode of peak 2 may actually start at ∼08:25 UT when the exponential decay rate of the *RHESSI* light curves (3–25 keV) decreases and the *GOES* time derivative (8–1 Å) starts to increase [from Liu, W. et al. 2008b].

The event under study, classified as a *Geostationary Operational Environment Satellite* (*GOES*) M1.4 flare, started at 08:19 UT on 2002 April 30. Figure 4.1 (*top panel*) shows the *RHESSI* light curves in four energy bands between 3 and 50 keV together with the fluxes of the two *GOES* channels (1–8 and 0.5–4.0 Å). During the full course of the flare *RHESSI* is in the A1 attenuator state, i.e. with the thin shutters in. According to the 12–25 keV light curve, there are three peaks that are progressively weaker and softer. Above 25 keV there is no detectable count rate increase beyond the first peak that we refer to as the impulsive phase.

The temporal trend of the time derivatives (Fig. 4.1, *bottom panel*) of the *GOES* fluxes mimics that of the *RHESSI* 25–50 keV count rate. This type of correlation is known as

the Neupert effect (Neupert, 1968) and has been observed in many (but not all) flares (Dennis & Zarro, 1993; Veronig et al., 2005; Liu, W. et al., 2006). Such flares are usually observed on the solar disk where HXRs are seen from the footpoints, indicating prompt energy release and impulsive heating of the chromosphere by the nonthermal electrons. The

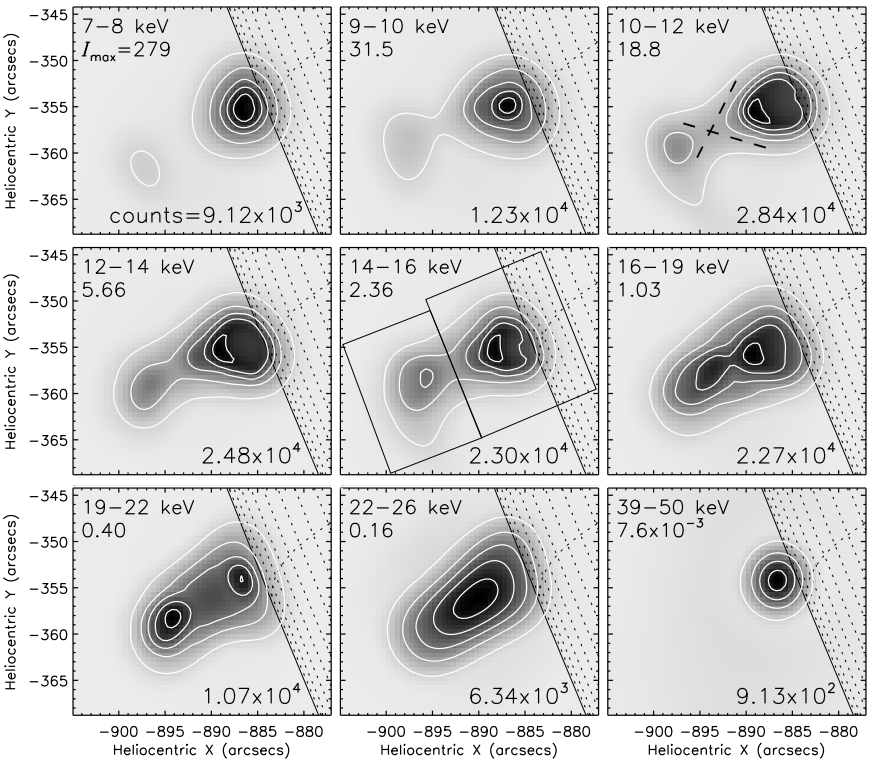

Figure 4.2: *RHESSI* PIXON images in different energy bands at 08:20:27–08:20:56 UT (interval 2 in Fig. 4.1), around the maximum of the main (first) HXR peak. We used the PIXON background model and detectors 3–6 and 8, which yield a resolution of $\sim 4.6''$ determined from the FWHM of the point-spread function obtained by simulation. Note that the PIXON algorithm, under favorable conditions, can achieve a resolution as small as a fraction (see Aschwanden et al., 2004, their §A8) of the FWHM resolution of the finest detector used ($6.8''$ for detector 3 in our case). The contour levels are 10%, 30%, 50%, 70%, and 90% of the maximum, $I_{\max}$ (shown in the upper left corner of each panel, in units of photons cm^{-2} s^{-1} arcsec^{-2}), of each individual image. The numbers in the lower right corners are the total counts accumulated by the detectors used for image reconstruction. The heliographic grid spacing is 1°. The boxes shown in the 14–16 keV panel are used to obtain the fluxes and centroids of the two sources in all the images at this time (see text). The two black dashed lines in the 10–12 keV panel forming an "X" show the possible configuration of the reconnecting magnetic field [from Liu, W. et al. 2008b].

hot and dense plasma resulting from the subsequent chromospheric evaporation (Neupert, 1968) then fills the loop and gives rise to the gradual SXR increase (see Chapter 8). In this flare, however, the footpoints are occulted by the limb (as we show below). Thus, the presence of the Neupert effect here implies that the coronal impulsive HXRs are produced by the same nonthermal electrons that further propagate down to the footpoints and drive

chromospheric evaporation there.

The spatial morphology of the flare is shown in Figure 4.2 in X-rays and in Figure 4.3 in extreme-ultraviolet (EUV). Figure 4.2 shows PIXON (Metcalf et al., 1996; Hurford et al., 2002) images at different energies integrated over the interval of 08:20:27–08:20:56 UT (marked No. 2 in Fig. 4.1) during the first HXR peak. As can be seen, this flare occurred on the east limb, and the X-ray emission at all energies (even as high as 39–50 keV) appeared above the limb, suggesting that the footpoints were occulted. This conclusion is supported by *SOHO* observations shown in Figure 4.3. The top left panel shows an EUV Imaging Telescope (EIT) 195 Å image taken at 08:22:58 UT (just 2 minutes after the *RHESSI* images in Fig. 4.3). The contours are for the *RHESSI* image at 9–10 keV shown in Figure 4.2. The *RHESSI* source is co-spatial with the brightening in the EIT image, which is clearly above the limb. The flare occurred near the region where large-scale trans-equatorial loops are rooted, presumably behind the limb. There was no brightening on the disk detected by EIT, nor was an active region seen in the *SOHO* Michelson Doppler Imager (MDI) magnetograms in the vicinity of this flare. EIT and MDI have spatial resolutions of $2.6''$ and $4''$, respectively, both better than the $6.8''$ resolution of the finest *RHESSI* detector (No. 3) used here. The top right panel of Figure 4.3 shows the MDI magnetogram at 21:20 UT, about 13 hr after the flare. At this time, NOAA AR 9934 had just appeared on the disk next to the *RHESSI* source due to the solar rotation. This suggests that the flare took place in this active region when it was still behind the limb. Because of the large size of the active region, it is difficult to determine the possible locations of the footpoints of the flare and to estimate the approximate altitudes of the coronal sources.

4.2.1 Source Structure: Energy Dependence

Let us now return to Figure 4.2 and examine in detail the energy-dependent morphology of the flare. At the lowest energy shown (7–8 keV), there are two distinct sources, which we call the lower and upper coronal sources. The centroids of both sources are above the solar limb, and the upper source is dimmer. At a slightly higher energy, 9–10 keV, the sources appear closer together and a cusp shape develops between them. This trend is more pronounced at higher energies (10–19 keV), and the two sources (particularly the lower one) seem to have a feature convex toward each other, mimicking the "X" shape of the magnetic field lines in the standard reconnection model. Meanwhile, the relative brightness of the upper source increases with energy.

The change in source altitude with energy is shown more clearly in the lower left panel of Figure 4.3. The upper coronal source shifts toward lower altitudes with increasing energy, while the lower coronal source behaves oppositely. At 16–19 keV, the two sources, while being spatially resolved, are closest together with their centroids separated by $4\farcs6 \pm 0\farcs3$ (see Fig. 4.3, *lower left*).

We can appreciate this more quantitatively by looking at the heights (above the limb) of the centroids of the upper and lower coronal sources as a function of energy. This is shown in the lower right panel of Figure 4.3. The boxes depicted in the middle panel of Figure 4.2 were used to obtain the centroid positions. The error bars were obtained from

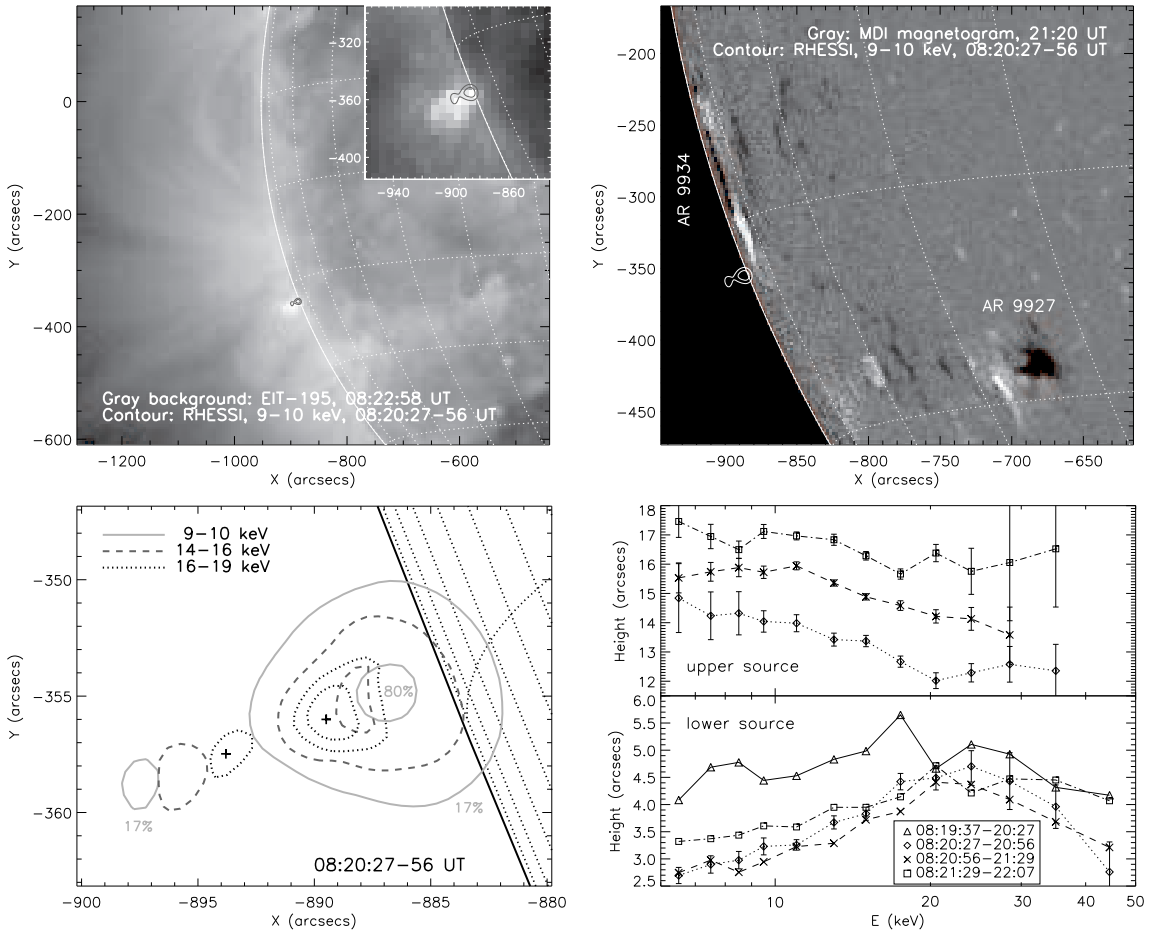

Figure 4.3: *Upper left*: *SOHO* EIT 195 Å image at 08:22:58 UT in the background, superimposed with *RHESSI* contours at 9–10 keV and 08:20:27–08:20:56 UT. The insert shows the zoomed view of the *RHESSI* source and co-spatial EIT emission (with a different gray scale for better contrast). *Upper right*: *SOHO*/MDI magnetogram taken at 21:20 UT (some 13 hr after the flare), overplotted with the same *RHESSI* 9–10 keV contours. The NOAA active regions (ARs) are labeled. The heliographic grid spacing is 10° in the two upper panels. *Lower left*: Overlay of images in contours, same as those shown in Fig. 4.2, in three energy bands as indicated in the legend. The contour levels are at 17% and 80% (9–10 keV), 47% and 90% (14–16 keV), and 80% and 90% (16–19 keV) of the maximum brightness of individual images. In each image, two contours appear in the lower coronal source, while only the lower level contour is present in the upper source because of its faintness. The two plus signs mark the centroids (separated by $4\farcs6 \pm 0\farcs3$) of the lower and upper 16–19 keV sources inside the 90% and 80% contours, respectively. The heliographic grid spacing is 1°. *Lower right*: Height above the limb of the centroids for the upper and lower coronal sources plotted as a function of energy for time intervals 1–4 marked in Fig. 4.1. Note that during the first interval, only one source is detected and is shown as the lower source. For clarity, uncertainties are shown for only one time interval for the lower source and they are similar at other times [from Liu, W. et al. 2008b].

the centroid position uncertainties in the same images reconstructed with the visibility-based forward-fitting algorithm currently available in the *RHESSI* software. The energy-dependent pattern is clearly present; that is, the centroid of the upper (lower) source shifts to lower (higher) altitudes with increasing energy. We note that, at very high energies ($\gtrsim$ 20 keV), this pattern becomes obscure (see Figs. 4.2 and 4.3), but the uncertainties in the source locations become large due to low count rates.

Three other time intervals during the first HXR peak were also analyzed, and the results are plotted in Figure 4.3, exhibiting similar patterns. At the very beginning of the flare (08:19:37–08:20:27 UT), only one source is visible, and we assign its centroid (*black triangles*) to the lower source, since it is the main source. As mentioned earlier, the second and third HXR peaks are weaker and softer, which does not allow for this kind of detailed analysis with narrow energy bins. We defer our physical interpretation of these observations to §4.3.1.

4.2.2 Source Structure: Temporal Evolution

We now change our perspective, using relatively wider energy bins as a trade-off for finer time resolution (compared with the above analysis), and examine the temporal evolution of the source structure throughout the full course of the flare.

Figure 4.4 shows the PIXON images taken at 6–9, 9–12, 12–16, and 16–25 keV at eight separate times (labeled A–H in Fig. 4.1). The morphology evolves following the general trend mentioned above. Early (08:19:28–08:20:01 UT, interval A) in the flare only a single source is visible. During the next time interval (B), the upper coronal source appears at 6–9 keV, but only a single source is evident at higher energies albeit with elongated shapes. In interval C, two distinct coronal sources appear in a dumbbell shape at all the energies. As time proceeds, both sources move to higher altitudes. This morphology is present for about 12 minutes (from 08:20 to 08:32 UT) until the declining phase of the second peak when only one source is detected, possibly because of the faintness of the upper source and the low count rate. Note that after 08:29 UT the upper source is dimmer than 20% of the maximum of the image and thus does not appear in panels G and H.

The motions of the sources can be seen more clearly from the migration of the centroids. To obtain the centroids and fluxes of the sources, we use contours whose levels are equal to within 5% of the minimum between the two sources so that the contours of the two sources are independent. The last panel in Figure 4.4 shows the evolution of the centroid positions of the two sources at 6–9 keV. During the first HXR peak (indicated by the dark arrow), the lower coronal source first shifts to lower altitudes and then ascends. This is consistent with the decrease of the loop-top height early during the flare observed in several other events (Sui & Holman, 2003; Liu, W. et al., 2004a; Sui et al., 2004). Meanwhile, the upper source generally moves upward. Such centroid motions are also present at other energies as shown in the lower right panel of Figure 4.3. The reversal of the lower source altitude seems to happen again, but is less obvious, during the second peak (marked by the gray arrow).

We can examine the same phenomenon more quantitatively by checking the height of the source centroid as a function of time at different energies. This is shown in Figure 4.5*a* for the upper (*left scale*) and lower (*right scale*) coronal sources. We find that, again, the higher energy emission comes from lower altitudes for the upper source and the lower source

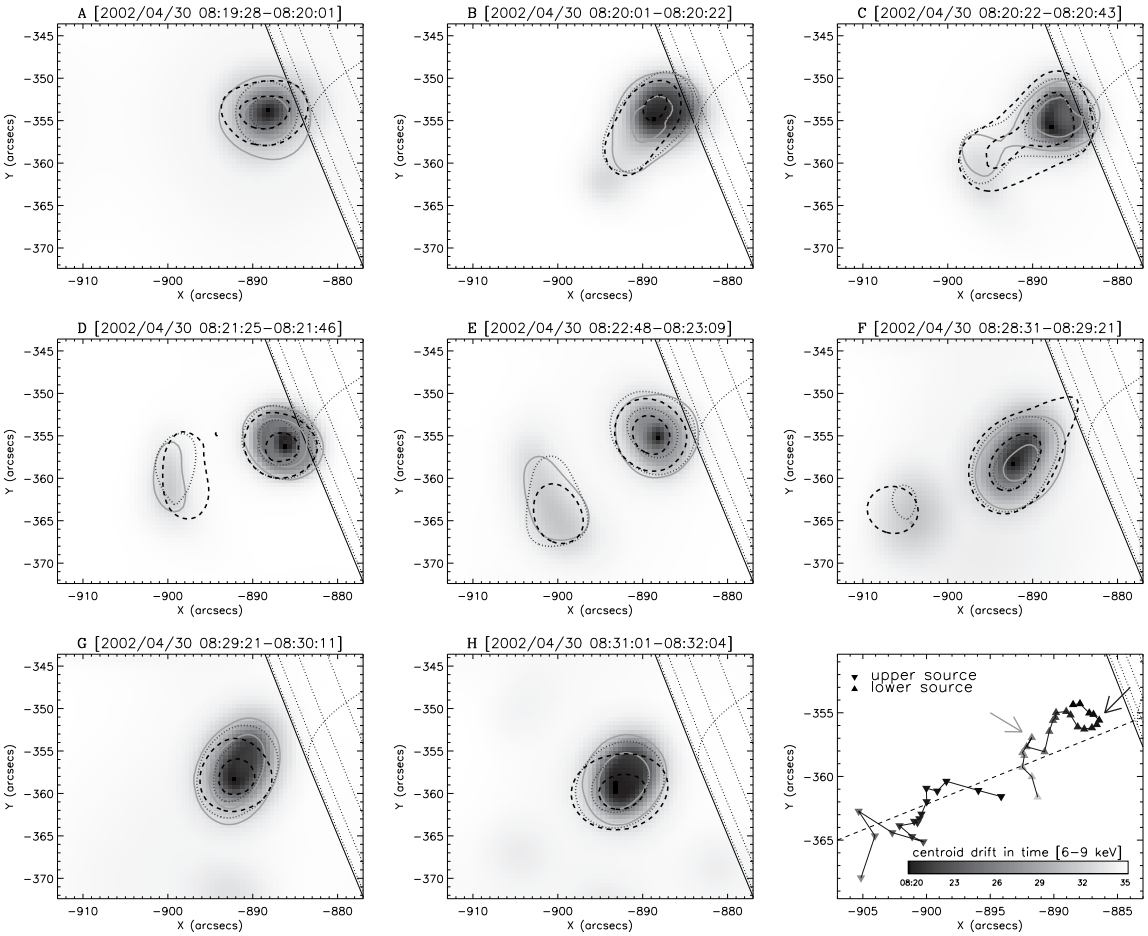

Figure 4.4: PIXON images of different energies made with detectors 3–6 and 8 at selected times (i.e., intervals A–H as marked in Fig. 4.1). In each panel, the gray-scale background is at 6–9 keV, while the solid, dotted, dashed contours (20% and 70% of the peak flux of each image) are at 9–12, 12–16, and 16–25 keV, respectively. The heliographic grid spacing is 2°. The last panel shows the locations of the centroids of the lower and upper 6–9 keV sources at different times indicated by the color bar. The dashed line indicates the radial direction (perpendicular to the limb). The dark and gray arrows point to the centroid locations at the times of the first and second HXR peaks, respectively [from Liu, W. et al. 2008b].

shows the opposite trend. The only exception (indicated by the dashed box) to this general behavior occurs for the upper source during the late declining phase of the first HXR peak and during the second and third peaks when there are large uncertainties because of low count rates.

At 6–9 keV (*asterisks*) the altitude of the lower source first *decreases* at a velocity of 10 ± 2 km s^{-1}, while the altitude of the upper source *increases* at a velocity of 52 ± 18 km s^{-1}. These are indicated by linear fits (*solid line*) during the high flux period. This happens during the rising phase (up to 08:21:14 UT) of the first HXR peak and is followed by an increase of the altitudes of the two sources with comparable velocities (15 ± 1 and

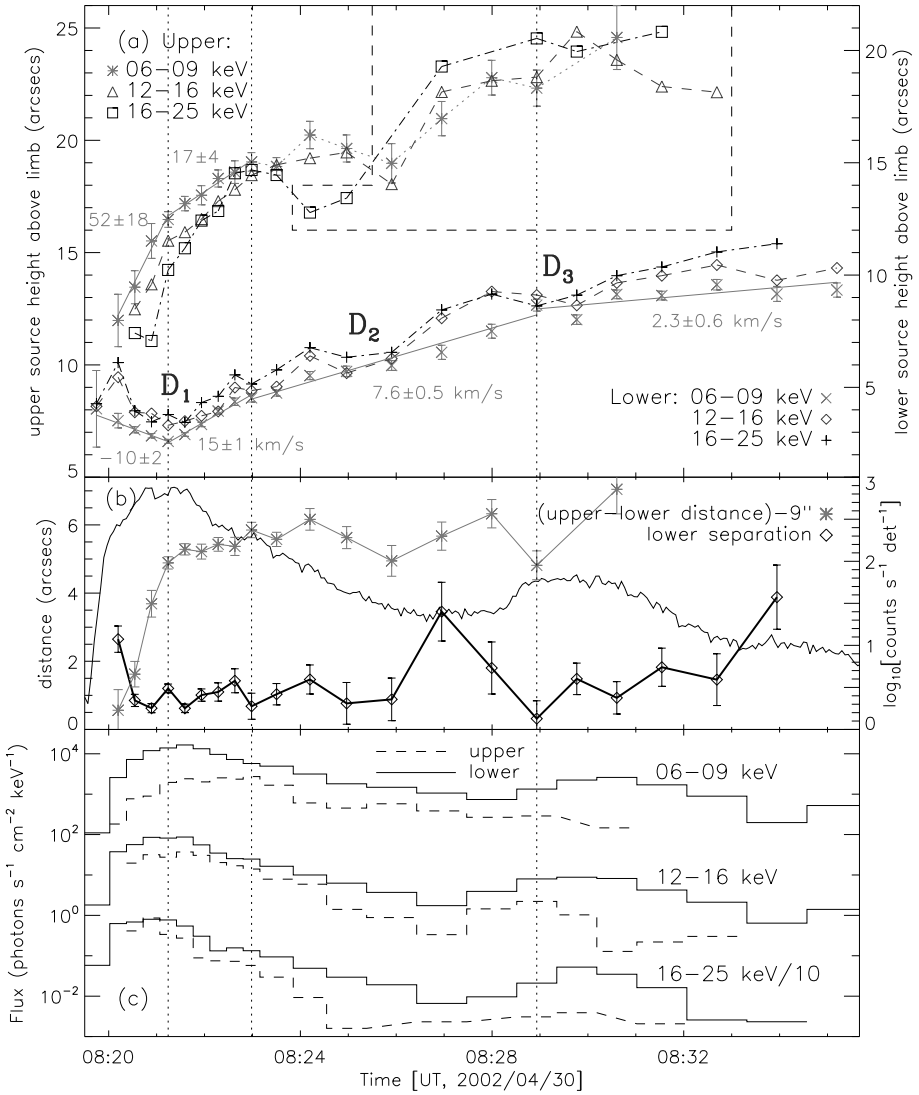

Figure 4.5: (*a*) Height (above the limb) of the centroids at different energies for the upper (*left scale*) and lower (*right scale*) coronal sources. The dotted vertical lines separate the different phases according to the motion of the lower source centroid (see text). The solid straight lines are linear fits to the data during the corresponding time intervals, with the adjacent numbers indicating the velocities of the altitude gain in units of km s^{-1}. The centroid position of the upper source has large fluctuations and uncertainties during the interval marked by the dashed box. The letters D_1, D_2, and D_3 mark the times when the altitude of the lower source decreases. (*b*) *Left scale*: Distance (*asterisks*) between the centroids of the two coronal sources at 6–9 keV and separation (*diamonds*) between the centroids of the lower source at 6–9 and 16–25 keV. The former is shifted downward by 9″. *Right scale*: Base-10 logarithm of the spatially integrated light curve (counts s^{-1} $detector^{-1}$, *thin line*) at 12–25 keV. (*c*) Light curves of the upper (*dashed line*) and lower (*solid line*) coronal sources in the energy bands of 6–9, 12–16, and 16–25 keV (divided by 10). The same contours (see text) were used to obtain these light curves and the centroid positions in panel *a* [from Liu, W. et al. 2008b].

17 ± 4 km s^{-1} for the lower and upper sources, respectively) during the early declining phase (up to 08:22:59 UT). As time proceeds, the two sources generally continue to move to higher altitudes. The velocity of the lower source drops to 7.6 ± 0.5 km s^{-1} until 08:28:56 UT, around the maximum of the second HXR peak, and then to 2.3 ± 0.6 km s^{-1} afterwards. The velocity of the upper source also decreases in general, with some fluctuations most likely due to the large uncertainties mentioned above. The relative motion of the two sources can be seen from the temporal variation of the distance between their centroids as shown in Figure 4.5*b* (*asterisks*), which undergoes a fast initial increase and then stays roughly constant at $15'' \pm 1''$ within the uncertainties.

At 12–16 (*triangles*) and 16–25 keV (*squares*), the centroids have a trend similar to those at 6–9 keV, except for the lower coronal source during the early rising phase of the first HXR peak. The initial increase of the height of the "lower"[2] source at about 08:20 UT results from the elongation (see the second panel in Fig. 4.4) of the single source, which could be a combination of the lower and upper sources that are not resolved. The following rapid decrease in height in the next time interval is a consequence of the transition from a single-source to a double-source structure as mentioned earlier. The upper source, on the other hand, rises more rapidly than at 6–9 keV during the HXR rising and early declining phases. Its velocity at 16–25 keV, for example, is 32 ± 3 km s^{-1} during the interval of 08:21:14–08:22:59 UT. This energy dependence of the rate of rise is consistent with the general trend of the loop-top source observed in several other flares (Liu, W. et al., 2004a; Sui et al., 2004). We note in passing that, in addition to the first HXR peak (marked with D_1 in Fig. 4.5), the altitudes of the lower source centroids also appear to first decrease and then increase during two other time periods (D_2 and D_3).[3] This effect is most pronounced at 12–16 and 16–25 keV.

4.2.3 Spectral Evolution

In this section we examine the relationship between the fluxes and spectra of the two coronal sources. Figure 4.5*c* shows the photon flux evolution at 6–9, 12–16, and 16–25 keV. As evident, the fluxes of the two sources basically follow the same time variation in all three energy bands. The upper coronal source, however, appears later and disappears earlier, presumably due to its faintness and the limited *RHESSI* dynamic range (∼10:1). It also peaks later at 6–9 keV.

We also conducted imaging spectroscopic analysis for each of the seven time intervals defined in Figure 4.1. The spectra of the two sources separately and the spatially integrated spectra were fitted with a single-temperature thermal spectrum plus a power-law function. One important step was to fit the spatially integrated spectra of individual detectors separately and then average the results in order to obtain the best-fit parameters and their uncertainties. Interested readers are referred to Appendix A.3 for the technical details of

[2] Again, we assign its centroid to the lower source when there is only a single source detected.

[3] D_3 coincides with the second HXR peak, and D_2 occurs around 08:25 UT, which is the possible actual start of the second energy release episode (see Fig. 4.1), when the upper source also appears to show a significant decrease in centroid altitude. Such altitude variations seem to be associated with the possible increases of energy release rate indicated by the light curves. However, compared with D_1, the features at the two later times are less definitive given the relatively fewer data points and larger uncertainties of the centroid heights.

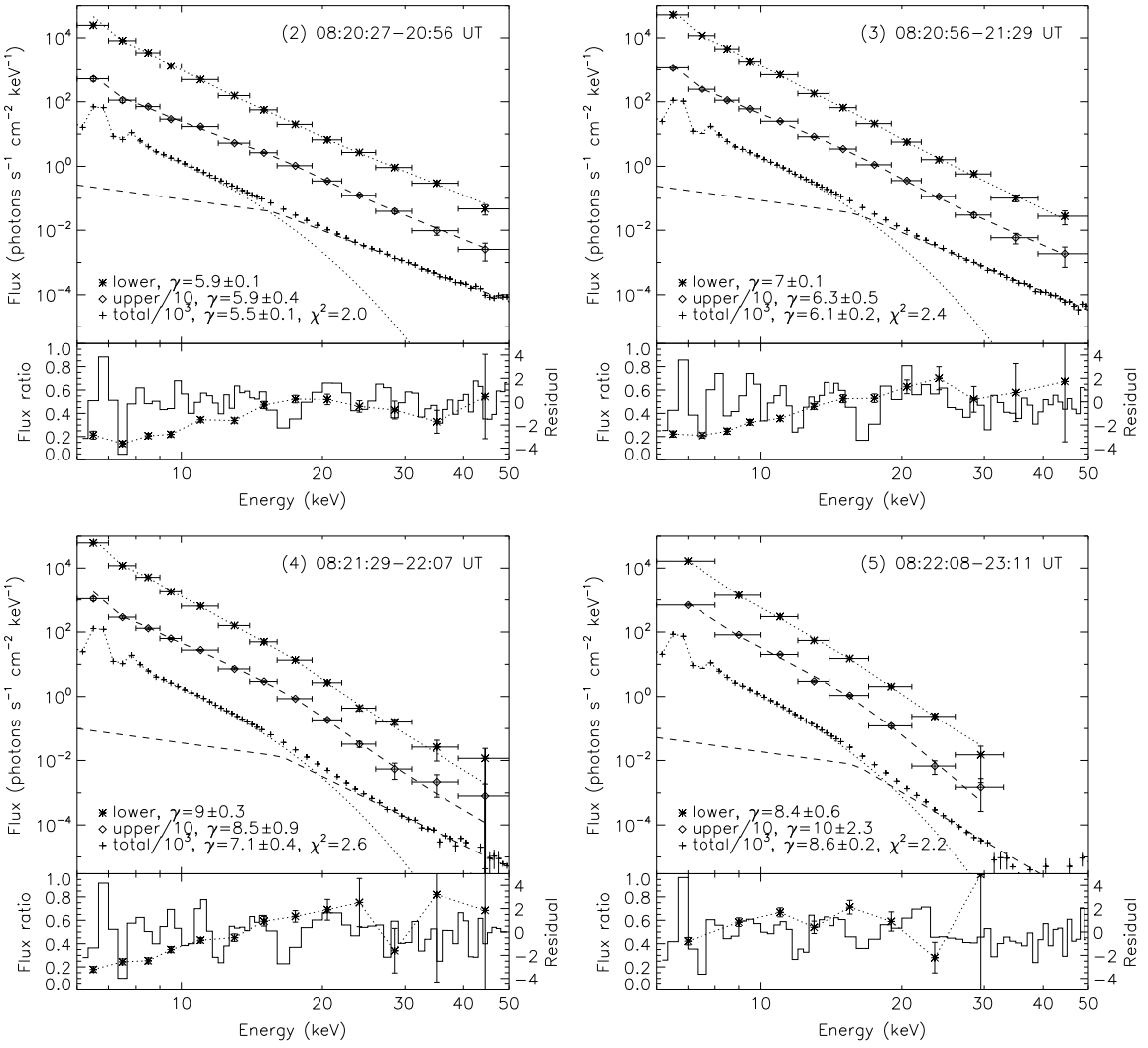

Figure 4.6: Spectra of the lower and upper coronal sources and the spatially integrated spectra (labeled as "total") at four times during the major flare peak. The numbers (2, 3, 4, and 5) in the upper-right corners correspond to the numbered time intervals shown in Fig. 4.1. The upper source's spectra and the total spectra have been shifted downward by one and three decades, respectively. The horizontal error bars represent the energy bin widths and the vertical error bars are the statistical uncertainties of the spectra. The best fit to the data with a thermal plus power-law model is shown as the dotted (dashed) line for the lower (upper) source. The thermal (*dotted line*) and power-law (*dashed line*) components of the best fit to the total spectra are also shown. The legend indicates the corresponding power-law indexes (γ) for each spectrum ($\gamma = 2$ below the low cutoff energy). The lower portion of each panel shows the ratio of the upper to lower fluxes (*asterisks*, *left scale*), and the residuals (*solid lines* lines, *right scale*) of the fit to the spatially integrated spectra, normalized to the $1\,\sigma$ uncertainty of the measured flux at each energy [from Liu, W. et al. 2008b].

the spectrum-fitting procedures used to obtain the results reported here.

A sample of the resulting spectra of four intervals is shown in Figure 4.6. Fits to the spatially integrated spectra indicate that the low-energy emission is dominated by the thermal components, while the nonthermal power-law components dominate at high energies. The two components cross each other at an energy that we call $E_{\rm cross}$. The spectra of the two coronal sources measured separately have similar slopes. In general, the ratio of the two spectra (upper source/lower source) is smaller than unity and gradually increases with energy below around $E_{\rm cross}$. This trend can also be appreciated by noting the increasing relative brightness of the upper source when energy increases as shown in Figure 4.2. This energy-dependent variation of the flux ratio means that the thermal emissions of the two sources are somewhat different not only in emission measure (EM) but also in temperature, because different EMs alone would only affect the normalizations and produce a flux ratio that is independent of energy. We also note that above $E_{\rm cross}$, the ratio stays constant within the larger uncertainties. This means that the nonthermal spectra of the two sources have similar power-law indexes (see Fig. 4.7*a*).

The reduced χ^2 values of the spatially integrated spectra are somewhat large ($\gtrsim$2), partly because we set the systematic uncertainties to be zero as opposed to the default 2%. Another reason was that we averaged the photon fluxes and best-fit parameters over different detectors that have slightly different characteristics. Thus, the averaged model may not necessarily be the best fit to the averaged data (see §A.3.1, item 9), although the χ^2 values of the fits to the individual detectors are usually close to unity. The normalized residuals exhibit some systematic (nonrandom) variations, as shown in the bottom portion of each panel of Figure 4.6. This suggests that the simple spectrum form adopted here may not represent all the details of the data. However, since we are mainly concerned with the similarities and differences between the spectra of the two coronal sources, such systematic variations would affect both spectra the same way and thus will not alter our major conclusions. More sophisticated techniques, such as the regularization method (Kontar et al., 2004), can be used to obtain better fits to the data, but they are beyond the scope of this chapter.

We now examine the temporal evolution of various spectral characteristics as shown in Figure 4.7. Let us focus on the late impulsive phase outlined by the two vertical dotted lines.[4] Again we find that the power-law indexes (Fig. 4.7*a*) of the two coronal sources are very close, with a difference of $\Delta\gamma \leq 0.7$. The two spectra undergo continuous softening during this stage, and the spatially integrated spectrum follows the same general trend.

Figures 4.7*b* and 4.7*c* show that the thermal emissions of the two sources are quite different as noted above. The lower coronal source has a larger emission measure but lower

[4]Beyond the time interval between the two vertical lines in Fig. 4.7, i.e., during the early impulsive phase (before 08:20:27 UT) and the decay phase (after 08:22:08 UT), interpretation of the spectral fitting needs to be taken with caution because of the large uncertainties due to low count rates and thus relatively poor statistics. Specifically, during certain intervals, reliable power-law components from fits to the spatially resolved spectra could not be obtained, and thus the corresponding values of the spectral index (γ) and thermal-nonthermal crossover energy ($E_{\rm cross}$) are not shown in Fig. 4.7. In addition, the averages of the best-fit parameters of the two sources differ significantly from the corresponding values of the spatially integrated spectrum. This is unexpected and may indicate that there existed an extended source with low-surface brightness and/or that the fits to the imaged spectra at these times are not reliable. Nevertheless, we show the fitting results here for completeness.

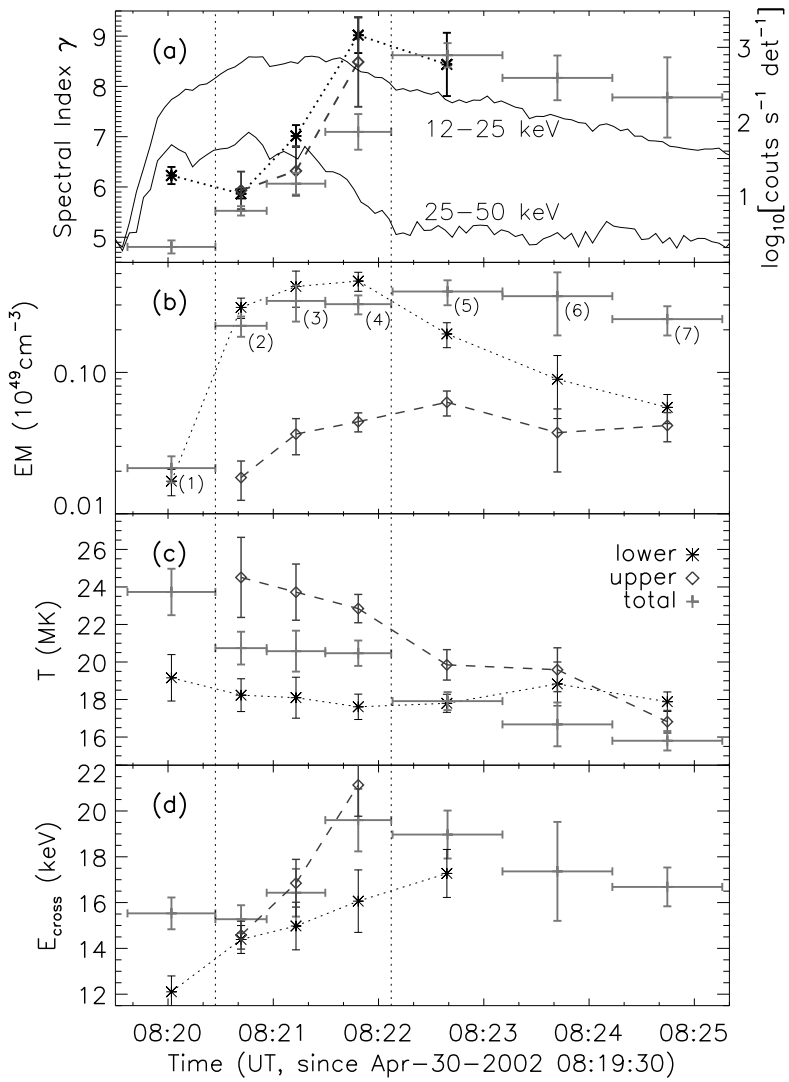

Figure 4.7: Evolution of various spectroscopic quantities of the lower (*asterisks*) and upper (*diamonds*) coronal sources and the spatially integrated emission (*plus signs*, labeled "total"). The horizontal error bars represent the widths of the time intervals of integration as labeled (1–7) in panel *b* (also in Fig. 4.1). The two vertical dotted lines mark the boundaries of the time range when both coronal sources are best imaged. This spans the late impulsive phase (see the 25–50 keV light curve). Before and after this time range the imaging spectroscopy has relatively large uncertainties (see text). (*a*) Spectral indexes (*symbols*, *left scale*) of the power-law components of the model fits, together with the 12–25 and 25–50 keV light curves (*solid lines*, *right scale*). (*b*) and (*c*) Emission measures (in $10^{49}\,\mathrm{cm}^{-3}$) and temperatures (in 10^6 K) of the thermal components of the model fits. (*d*) The crossover energy, E_{cross}, at which the thermal and power-law components are equal. Note that the values here are the upper limits of E_{cross}. This is because we assumed a $\gamma = 2$ index for the photon spectrum below the low-energy cutoff, but the power-law component may extend to low energies with a steeper index, thus lowering the values of E_{cross} [from Liu, W. et al. 2008b].

temperature than the upper source. As time proceeds, both sources undergo a temperature decrease and emission measure increase. This must be the result of the interplay of continuous heating, cooling by conduction and radiation, and heat exchange between regions of different temperatures within the emission source. Note that the temperature and emission measure of the spatially integrated spectrum, as expected, lie between those of the two sources.

We can further estimate the densities of the two sources using their EMs and approximate volumes. Assuming that the sources are spheres and using the $6.3''$ and $5.2''$ FWHM source sizes obtained from the visibility forward fitting images as the diameters, we obtained the volumes, V. We then estimated the lower limits of the densities ($n = [\mathrm{EM}/(Vf)]^{1/2}$, assuming a filling factor f of unity) of the lower and upper sources at 08:20:27–08:20:56 UT to be 2.4×10^{11} and $8.0 \times 10^{10}\,\mathrm{cm}^{-3}$, respectively.

Figure 4.7*d* shows the history of the crossover energy E_{cross}. In general, the lower source has a lower E_{cross} because of its lower temperature. The E_{cross} values of both sources increase with time because the thermal emission becomes increasingly dominant, as seen in many other flares. A physical interpretation of these observations is presented in §4.3.

4.3 Interpretation and Discussion

4.3.1 Energy Dependence of Source Structure

The energy-dependent source morphology presented in §4.2.1 (see Fig. 4.3, *lower left*) is similar to that reported by Sui & Holman (2003) and Sui et al. (2004) and interpreted as magnetic reconnection taking place between the two coronal sources. In their interpretation, plasma with a higher temperature is located closer[5] to the reconnection site than plasma with a lower temperature. This can result in higher energy emission coming from a region closer to the reconnection site while lower energy emission comes from a region farther away, provided that the emission is solely produced by *thermal* emission (free-free and free-bound) and the lower temperature plasma has a higher emission measure.

Our interpretation is somewhat different, particularly for this flare. Regardless of the emission nature (thermal or nonthermal) of the HXRs, the energy-dependent source structure here simply means *harder* (flatter) photon spectra *closer* to the reconnection site, which can give rise to a higher weighting there at high energies for the centroid calculations (see Fig. 4.8). A larger spatial gradient of the spectral hardness would lead to a larger separation of the emission centroids at two given photon energies, and a zero gradient (uniform spectrum) means no separation. As we have seen in §4.2.3, both coronal sources have substantial power-law (presumably nonthermal) tails (Fig. 4.6), which makes a purely thermal interpretation improbable. In the framework of the stochastic acceleration model (Hamilton & Petrosian, 1992; Miller et al., 1996), one expects both heating of plasma and acceleration of particles into a nonthermal tail to take place. As shown in Petrosian & Liu (2004), higher levels of turbulence tend to produce harder electron spectra or more acceleration and less

[5]Sui & Holman (2003) also suggested a possible transition at about 17 keV from the thermal flare loops to the Masuda-type above-the-loop HXR source (Masuda et al., 1994), on the basis of the sudden displacement of the loop-top source position in the 2002 April 15 flare.

heating. One expects a higher turbulence level near the X-point of the reconnection site than farther away. Consequently, there will be more acceleration and thus stronger nonthermal emission near the center, but more heating and thus stronger thermal emission farther away from the X-point. In other words, the electron spectra and thus the observed photon spectra will be harder closer to the reconnection site. This physical picture is sketched in Figure 4.9.

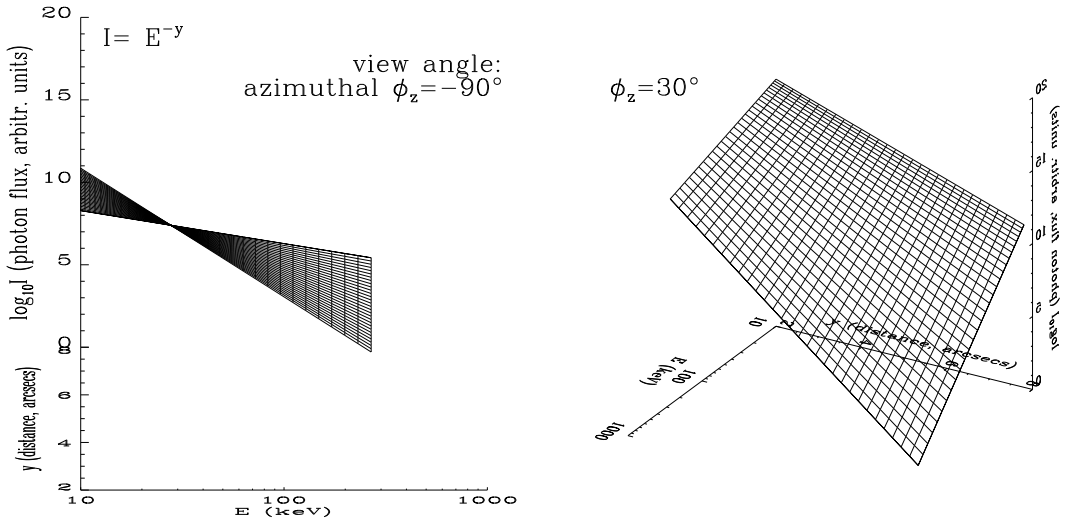

Figure 4.8: Surface plot of photon flux I as a function of energy E and distance y from the reconnection site. The selected functional form of $I = E^{-y}$, as an example, demonstrates how a spatial variation of the spectral hardness can lead to a spatial separation of emission centroids at different energies. The intersection curve of the flux surface and a plane perpendicular to the y-axis gives the spectrum at a given position y, while a cut of the surface perpendicular to the E-axis gives the spatial distribution of emission at a given energy E. The fact that the spectrum is *harder* (flatter) at smaller distances translates into that the emission profile at higher energies is concentrated *more* toward small distances. This gives rise to emission centroids at higher energies being closer to the reconnection site.

The observations here support the above scenario. As shown in Figure 4.6, below the critical energy $E_{\rm cross}$ (say, $\sim$15 keV for 08:20:27–08:20:56 UT), the emission is dominated by the thermal component, and the two sources are farther apart at lower energies (see Fig. 4.3, *lower panels*). This translates to the outer region away from the center of the reconnection site being mainly thermal emission at low energies. Above $E_{\rm cross}$, on the other hand, the power-law component dominates. The two sources being closer together at higher energies[6] thus means that the region near the center is dominated by nonthermal emission (see Fig. 4.9).[7]

We note that the small centroid separation of $4.6'' \pm 0.3''$ (Fig. 4.3, *lower left*) identifies

[6]At even higher energies ($\gtrsim$25 keV), the distance between the two sources seems to increase, but with larger uncertainties (Fig. 4.3, *lower right*). This transition, if real, may suggest that transport effects become important. This is because higher energy electrons require greater column depths to stop them, and thus they tend to produce nonthermal bremsstrahlung emission at larger distances from where they are accelerated.

[7]This argument is equivalent to the approach of obtaining detailed spectroscopy of multiple regions as small as $4''$, but this was not attempted here.

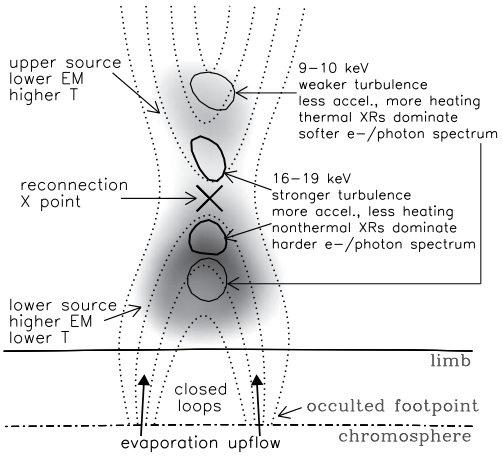

Figure 4.9: Schematic of the physical scenario (see text) superimposed on the *RHESSI* observations as a manifestation of the stochastic acceleration model illustrated in Fig. 1.1 (*left panel*). The 14–16 keV PIXON image at 08:20:27–08:20:56 UT is the gray background, overlaid with the simultaneous 9–10 (*thin*) and 16–19 keV (*thick*) contours. These are the same images shown in the lower left panel of Fig. 4.3, with their orientation rotated for demonstration purposes. The hand-drawn dotted curves represent a possible magnetic field configuration [from Liu, W. et al. 2008b].

a region within which the center of reconnection activity is located. To our knowledge, this is the smallest (3.3 ± 0.2 Mm) feature of the reconnection region yet resolved by X-ray observations on the Sun.

4.3.2 Temporal Evolution of Source Structure

Figure 4.5*b* shows the separation (*black diamonds*) between the centroids of the lower coronal source at 6–9 and 16–25 keV, together with the 12–25 keV light curve. These two curves seem to be anti-correlated such that this separation becomes smaller when the HXR flux is larger. This is consistent with that reported by Liu, W. et al. (2004a, their Fig. 1) in a much brighter (X3.9) flare where this effect was more pronounced. This trend was also present in two of the three homologous flares reported by Sui et al. (2004).

In our earlier publication (Liu, W. et al., 2004a) we suggested that the anti-correlation indicates a smaller (more homogeneous) spatial gradient of turbulence density or particle acceleration rate around the peak of the impulsive phase, owing to the presence of a higher turbulence level. Here we further note that such a spatial distribution of acceleration rate can result from the interplay of various physical processes (with different spatial distributions and timescales) that contribute to energy release, dissipation, and redistribution. Processes that can carry energy away from the acceleration region include damping of turbulence (waves), escape of accelerated particles, thermal conduction, and radiative loss. Detailed modeling is required to offer a self-contained physical explanation for the observational feature presented here.

4.3.3 Spectral Characteristics

The temporal *correlation* of the light curves (Fig. 4.5*c*) and the *similar* power-law spectral components (Figs. 4.6 and 4.7*a*) of the two coronal sources, when taken together, suggest that these HXR emissions are produced by the nonthermal electrons that are accelerated by the *same* mechanism (presumably stochastic acceleration by similar turbulence following the reconnection process. Such a correlation provides more direct evidence and a more complete picture for the interpretation outlined above in §4.3.1.

As we noted in §4.2.3, the coronal sources have quite different *thermal* emissions, with the lower source having a higher EM but lower temperature. There are several possible reasons why this can happen: (1) The lower source resides at a lower altitude where the local density may be slightly higher in the gravitationally stratified atmosphere. The difference between the heights of the two sources is on the order of 10 Mm, which is a fraction of the coronal density scale height ($\gtrsim$60 Mm, the quiet-Sun value). Thus, the density difference due to height variation is no more than about 15%. This is not sufficient to account for the large difference in density between the two sources noted earlier. (2) As shown in Figure 4.9, the two coronal sources lie below and above the X point of the reconnection region. It is most likely that the lower source is located at the top of the flaring loop that is magnetically connected to the chromosphere. This allows the chromosphere to supply dense material to the lower source along the magnetic field lines during chromospheric evaporation. The evaporated plasma, although heated, is still relatively cooler than the hot plasma near the reconnection site in the corona. (3) In addition, thermal conduction and plasma convection can readily carry heat away from the lower source down the magnetic loop to the cool chromosphere. All three reasons contribute to the higher EM and lower temperature of the lower coronal source. In contrast, the upper source may be magnetically disconnected from, or more remotely connected to, the solar surface. The lower density material of the upper source can thus be heated to a higher temperature due to the lack of a direct supply of cool material and the reduced thermal conduction to the chromosphere.

We have also noted that the *nonthermal* components of the two coronal sources have similar spectral indexes, but the upper source is weaker. The spectral indexes could not always be determined for both sources seen in other similar events (Sui & Holman, 2003; Sui et al., 2004; Veronig et al., 2006; Li & Gan, 2007), but the upper source was always the weaker of the two. Here we discuss the possibilities that can lead to the weaker nonthermal radiation of the upper source in particular and its low surface brightness in general. In the framework of the stochastic acceleration model, all the processes involved in producing the observed emission — the rate of generation of turbulence, the spectrum of turbulence, the rate of acceleration and emission — depend on the temperature, density, and the magnetic field strength and geometry. As we mentioned above, the temperature, density, and field geometry of the two coronal sources are different. The magnetic field strength most likely decreases with height. Consequently, we expect different HXR intensities from the two sources. For example, the lower plasma density in the upper source will result in lower surface brightness for both thermal and nonthermal bremsstrahlung emission. Magnetic topology can have similar effects. The electrons responsible for the upper source are likely to be on open field lines or on field lines that connect back to the chromosphere more remotely (e.g., Liu et al., 2006a) and thus produce their X-ray emission in a more spatially

diffuse region. In contrast, for the lower source, the electrons are confined in the closed loop. In addition, as noted above, chromospheric evaporation can further increase the density in the loop, enhancing the density effect mentioned here. These factors, again, lead to lower surface brightness for the upper source. Finally, the rate of acceleration or heating depends primarily on the strength of the magnetic field (Petrosian & Liu, 2004), so that the relatively weaker magnetic field of the upper source may result in slower acceleration and thus weaker nonthermal emission. A large sample of this type of flares is required to confirm or reject this explanation.

We should emphasize that since the radiating electrons in both sources are the *direct* product of the same acceleration mechanism, they share common signatures. This would explain the spectral similarity of the nonthermal emissions of the two coronal sources. The thermal X-ray–emitting plasma, however, in addition to direct heating by turbulence, involves many other *indirect* or *secondary* processes, such as cooling by thermal conduction and hydrodynamic effects (e.g., evaporation in the closed loop). Therefore, the two thermal sources exhibit relatively large differences in their temperatures and emission measures.

4.4 Summary and Discussion

We have performed imaging and spectral analysis of the *RHESSI* observations of the M1.4 flare that occurred on 2002 April 30. Two correlated coronal HXR sources appeared at different altitudes during the impulsive and early decay phases of the flare. The long duration (∼12 minutes) of the sources allows for detailed analysis, and the results support that magnetic reconnection and particle acceleration were taking place between the two sources. Our conclusions are as follows.

1. Both coronal sources exhibit energy-dependent morphology. Higher energy emission comes from higher altitudes for the lower source, while the opposite is true for the upper source (Figs. 4.2 and 4.3). This suggests that the center of magnetic reconnection is located within the small region between the sources.

2. The energy-dependent source structure (Fig. 4.3), combined with spectrum analysis (Fig. 4.6), implies that the inner region near the reconnection site is energetically dominated by nonthermal emission, while the outer region is dominated by thermal emission. This observation, in the framework of the stochastic acceleration model developed by Hamilton & Petrosian (1992) and Petrosian & Liu (2004), supports the scenario (Fig. 4.9) that a higher turbulence level and thus more acceleration and less heating are located closer to the reconnection site.

3. The light curves (Fig. 4.5*c*) and the shapes of the nonthermal spectra (Figs. 4.6 and 4.7*a*) of the two X-ray sources obtained from imaging spectroscopy are similar. This suggests that intimately related populations of electrons, presumably heated and accelerated by the same mechanism following energy release in the same reconnection region, are responsible for producing both X-ray sources.

4. The thermal emission indicates that the lower coronal source has a larger emission measure but lower temperature than the upper source (Figs. 4.7*b* and 4.7*c*). This is

ascribed to the expected different magnetic connectivities of the two sources with the solar surface and the associated different plasma densities.

5. During the rising phase of the main HXR peak, the lower source (at 6–9 keV) moves *downward* for nearly 2 minutes at a velocity of 10 ± 2 km s^{-1}, while the corresponding upper source moves *upward* at 52 ± 18 km s^{-1} (Fig. 4.5*a*). During the early HXR declining phase, the two sources move upward at comparable velocities (15 ± 1 vs. 17 ± 4 km s^{-1}) for another 2 minutes. Afterwards, both sources generally continue to move upward with gradually decreasing velocities throughout the course of the flare, with some marginally significant fluctuations.

6. For the lower source, the separation between the centroids of the emission at different energies seems to be anti-correlated with the HXR light curve (Fig. 4.5*b*), which is consistent with our earlier finding (Liu, W. et al., 2004a). In the stochastic acceleration model such a feature suggests that a stronger turbulence level (thus a larger acceleration or heating rate and a higher HXR flux) is associated with a smaller spatial gradient (i.e., more homogeneous) of the turbulence distribution or of the electron spectral hardness.

All the above conclusions fit the picture of magnetic reconnection taking place between the two sources as illustrated in Figure 4.9. This is another, yet stronger, case of a double-coronal-source morphology observed in X-rays, in addition to the five other events reported by Sui & Holman (2003), Sui et al. (2004), Veronig et al. (2006), and Li & Gan (2007).

The general variation with height of the coronal emission raises some interesting questions and provides clues to the energy release and acceleration processes. The fact that there are two sources rather than one elongated continuous source suggests that energy release takes place primarily away from the X point of magnetic reconnection. This can be explained by the following scenario. One may envision that the reconnection gives rise to an electric field that results in runaway beams of particles. This is an unstable situation and will lead to the generation of plasma waves or turbulence, which can then heat and accelerate particles some distance away from the X point.

In addition, the energy-dependent structure of each source (i.e., higher energy emission being closer to the X point) that extends over a region of $\lesssim 10''$ suggests that energy release and some particle acceleration occurs in this region. This also indicates that the turbulence level or acceleration rate decreases with distance from the X point, which results in softer electron spectra farther away from that point. In other words, this observation suggests that the usually observed loop-top source is part of the acceleration region that resides in the loop and has some spatial extent, which is consistent with the recent study reported by Xu et al. (2008). (In their cases, the second coronal source at even higher altitudes above the reconnection site were not detected presumably because of the low total intensity and/or surface brightness.)

Our conclusions do not support the idea that particles are accelerated outside the HXR source before being injected into the loop. Moreover, the observations here are contrary to the predictions of the collisional thick-target model (e.g., Brown, 1971; Petrosian, 1973), which has been generally accepted for the footpoint emission and was recently invoked by Veronig & Brown (2004) to explain the bulk coronal HXRs in two flares described by Sui

et al. (2004). In such a model one expects higher energy emission to come from larger distances from the acceleration site (e.g., see Liu, W. et al., 2006, for HXRs from the legs and footpoints of a flare loop) due to the transport effects mentioned in §4.3.1. The electron spectrum becomes progressively harder with distance (because low-energy electrons lose energy faster). This disagrees with the observations of the flare presented here and of the two flares reported by Sui et al. (2004).

We note in passing that there is a common belief that the "Masuda" type of "above-the-loop" sources (Masuda et al., 1994) constitutes a special class of HXR emission. We should point out that the "Masuda" source is most likely an extreme case of the lower coronal source observed here and of the commonly observed loop-top sources that exhibit harder spectra higher up in the corona (e.g., Sui & Holman, 2003; Liu, W. et al., 2004a; Sui et al., 2004). We also emphasize that some type of trapping is required to confine high-energy electrons in the corona while allowing some electrons to escape to the chromosphere (see Fig. 1.1, *left panel*). Coulomb collision in a high-density corona cannot explain simultaneous high-energy coronal and footpoint emission at energies as high as 33–54 keV in the Masuda case. The stochastic acceleration model, on the other hand, provides the required trapping by turbulence that can scatter particles and accelerate them at the same time (Petrosian & Liu, 2004; Jiang et al., 2006).

Finally, besides the stochastic acceleration model, other commonly cited mechanisms, such as acceleration by shocks (e.g., Tsuneta & Naito, 1998)[8] and/or DC electric fields (e.g., Holman, 1985; Benka & Holman, 1994), may or may not be able to explain the energy-dependent source structure presented here. A rigorous theoretical investigation of these models is required to evaluate their viability.

[8]In the Tsuneta & Naito (1998) model, magnetic mirroring between the two standing slow shocks, for example, could confine the accelerated electrons that can produce a HXR coronal source.

Chapter 5

Conjugate Hard X-ray Footpoints — Unshearing Motions, Correlations, and Asymmetries: The 2003-10-29 X10 Flare[1]

5.1 Introduction

As noted in §1, magnetic reconnection is believed to be the primary channel of energy release, which leads to heating of plasma and acceleration of particles in solar flares. Details of reconnection and particle acceleration, however, remain largely unknown. X-ray observations of the loop-top (LT) and footpoint (FP) sources, particularly of their spatial, temporal, and spectral properties, combined with magnetic field measurements of the flare region, can provide critical information about how and where electrons are accelerated subsequent to magnetic reconnection. In Chapter 4 we focused on emission from coronal sources, while here we turn our attention to emission from conjugate FPs.

Unshearing and/or approaching motions of double Hα kernels and/or HXR FPs were recently found in the early impulsive peaks of three flares (Ji et al., 2004, 2006, 2007). These FP motions occurred during the period when the LT source descended in altitude, similar to that reported by Sui & Holman (2003), Sui et al. (2004), and Liu, W. et al. (2004a, 2008b).The approach of FPs was also evident in two of the four events reported by Fletcher & Hudson (2002). These new observations challenge the above classical picture. Veronig et al. (2006) proposed a collapsing magnetic trap model to explain the LT descending motions, which, however, cannot explain the FP approaching motions. Ji et al. (2007) suggested that such correlated FP and LT motions result from relaxation of flare loops. The reported LT descents were usually observed in flares occurring near the solar limb where the LT height can be readily measured, but the FP motions in the east-west direction are obscured by projection effects. Flares close to disk center, like the one reported here, can give an alternative perspective.

[1]The majority of this chapter was submitted to ApJ for publication (Liu, W. et al., 2008a).

Correlations between a pair of conjugate HXR FPs are expected, since they are believed to be produced by high-energy electrons released from the same acceleration region. The relative timing of conjugate FPs was found to be simultaneous within an uncertainty of 0.1–0.3 s (Sakao, 1994) based on *Yohkoh* Hard X-Ray Telescope (HXT) *Yohkoh* observations. For double FPs in tens of flares observed by the *Ramaty High Energy Solar Spectroscopic Imager* (*RHESSI*), temporal correlations in the HXR fluxes in two wide energy bands (25–50 and 50–100 keV) with a time resolution of 8 s were identified by Jin & Ding (2007). Spectral correlations at individual HXR peaks were investigated by Saint-Hilaire et al. (2008), who found power-law indexes that differed by <0.6. This spectral index difference is similar to that found by Sakao (1994), but smaller than the values as high as 1 or 2 reported by Petrosian et al. (2002) based on analysis of *Yohkoh* HXT images.

Asymmetric FPs, i.e., conjugate FPs with different properties (HXR fluxes, magnetic field strengths, etc.) are commonly observed (e.g., Sakao, 1994). This has been ascribed to asymmetric magnetic mirroring where a brighter HXR FP is associated with a weaker magnetic field (Li et al., 1997; Aschwanden et al., 1999; Qiu et al., 2001; Li & Ding, 2004). This picture is consistent with observations at radio wavelengths where brighter microwave emission appears at the FP with the stronger magnetic field (e.g., Kundu et al., 1995; Wang et al., 1995). Exceptions to the mirroring scenario were reported by Goff et al. (2004), who found one third of 32 *Yohkoh* flares with an opposite trend, that is, the association of the brighter HXR FP with the stronger magnetic field. Falewicz & Siarkowski (2007) re-examined three exceptions in the sample of Goff et al. and attributed this opposite asymmetry to different column densities in the two legs of the flare loop, as also suggested by Emslie et al. (2003) and Liu, W. (2006). Temporal variations of the flux asymmetry were found in a *Yohkoh* flare (Siarkowski & Falewicz, 2004), and energy- and time-dependent variations were seen in a *RHESSI* flare (Alexander & Metcalf, 2002). The latter were interpreted by McClements & Alexander (2005) as a consequence of an asymmetric, energy-dependent and time-dependent injection of accelerated electrons.

Previous studies of conjugate HXR FPs, in general, suffered from limited time, spatial, and/or energy resolution and/or coverage of HXR emission, mainly restricted by the instrumental capabilities, or from lack of magnetic field measurements. We report here on a comprehensive study of the conjugate FPs in the 2003 October 29 X10 flare observed by *RHESSI* that overcomes many of the previous shortcomings. This flare provides a unique opportunity to track the spatial and spectral evolution of the double HXR FPs and their associated magnetic fields in great detail, and to study all three interrelated aspects: *unshearing motions*, *correlations*, and *asymmetries*. This flare occurred near disk center, where FP motions and line-of-sight magnetic field measurements have minimum projection effects. Its long ($\sim$20 minutes) impulsive phase and high *RHESSI* count rates up to several hundred keV allow for a detailed study of variations both in time and energy. The flare was also well observed by the *Transition Region and Coronal Explorer* (*TRACE*), the *Solar and Heliospheric Observatory* (*SOHO*), and other spacecraft and many ground-based observatories. The rich database of multiwavelength observations and a wide range of literature covering different aspects of this event (e.g., Xu et al., 2004; Krucker et al., 2005) are particularly beneficial for this in-depth study.

We present the observations and data analysis in §5.2. These include general *RHESSI* light curves and images, *RHESSI* imaging spectroscopy, and multiwavelength observations.

We investigate in §5.3 the two phases (fast and slow) of unshearing motions of the FPs and the associated LT motion. In §5.4 we explore various correlations of the FPs, particularly of their HXR fluxes, spectral shapes, spatial variations, and magnetic fields. Possible contributions to the HXR flux and spectral asymmetries are discussed in §5.5, followed by our summary in §5.6. A discussion of pulse pileup effects, technical details on coaligning images made by different instruments, a mathematical treatment of the asymmetric column density effect, and an estimate of the coronal column densities in the legs of the flare loop are given in Appendixes A.4.2, B.1, B.2, and B.3, respectively.

5.2 Observations and Data Analysis

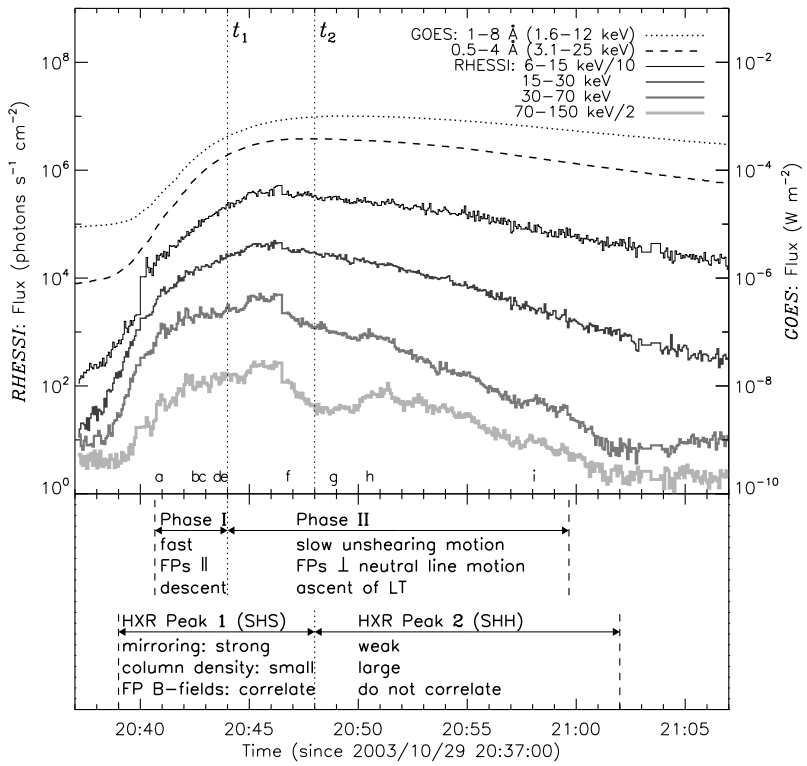

Figure 5.1: *RHESSI* and *GOES*-12 light curves of the 2003 October 29 X10 flare. The *RHESSI* fluxes (*left scale*) were obtained by spatially integrating the images of the flare region reconstructed for every consecutive 4 s interval (from Ji et al. 2008). The 6–15 and 70–150 keV curves are scaled down by factors of 10 and 2, respectively. The two channel *GOES* fluxes are on the right scale. The vertical dotted lines mark the two transitions (t_1 and t_2) denoted in the bottom panel. t_1 divides Phases I and II based on FP motions (see §5.3), and t_2 divides >70 keV HXR Peaks 1 and 2 (see §5.4.1). The letters "*a*–*i*" on the middle x-axis indicate the times of the nine images shown in Fig. 5.2. Note that both attenuators were in place (A3 state) during the time range shown here, except before 20:40 UT and during the interval of 21:03:12–21:03:40 UT, when only the thin attenuators were in (A1 state). The changes of the attenuator state were responsible for the artificial jumps of the light curves at these times. Another jump occurred at 20:46:36 UT when the front detector changed its decimation state from FD1 to FD4 (Smith et al., 2002) [from Liu, W. et al. 2008a].

We present in this section general multiwavelength and *RHESSI* X-ray observations to indicate the context for our detailed discussions to follow on the conjugate FPs. The event under study occurred in AR 10486 (W5°S18°) starting at 20:37 UT on 2003 October 29, during the so-called Halloween storms (e.g., Gopalswamy et al., 2005). It was a *Geostationary Operational Environment Satellite* (*GOES*) X10 class, white-light, two-ribbon flare, which produced strong gamma-ray line emission (Hurford et al., 2006) and helioseismic signals (Donea & Lindsey, 2005). It was associated with various other solar activity, including a fast ($\sim$2000 $\mathrm{km\,s^{-1}}$) halo coronal mass ejections (CMEs), and heliospheric consequences. This was the first white-light flare observed at the opacity minimum at 1.6 μm, which corresponds to the deepest layer of the photosphere that can be seen (Xu et al., 2004, 2006). There were strong photospheric shearing flows present near the magnetic neutral lines in this active region prior to the flare onset (Yang et al., 2004), which may be related to the unusually large amount of magnetic free energy ($\sim$6 $\times 10^{33}$ ergs; Metcalf et al. 2005) stored in this AR. By analyzing Huairou and Mees vector magnetograms, Liu et al. (2007) proposed that this flare resulted from reconnection between magnetic flux tubes having opposite current helicities. This may be connected to the soft X-ray sigmoid structure and unshearing motions of HXR FPs found by Ji et al. (2008) during the early phase of the flare. Liu & Hayashi (2006), using potential field extrapolations from the *SOHO* Michelson Doppler Imager (MDI) observations, investigated the large-scale coronal magnetic filed of AR 10486 and its high productivity of CMEs. Liu et al. (2006a) found remote brightenings more than 2×10^5 km away from the main flare site. Solar energetic particles (SEPs) were detected after this flare by *GOES* and the *Advanced Composition Explorer* (*ACE*).

Our goal in this chapter is to understand the temporal and spectral variations of the asymmetric HXR FPs and their associated magnetic fields. We thus focus on HXR observations obtained by *RHESSI* and line-of-sight photospheric magnetograms obtained by *SOHO* MDI. Vector magnetograms measured with chromospheric emission lines are more desirable for this study, as relevant magnetic mirroring may take place above the chromosphere where thick-target HXRs are produced. However, the extensive efforts required for calibrating vector magnetograms are not warranted for this study because of possibly small improvements that will not alter our conclusions. Specifically, because this flare is close to disk center (W5°S18°), line-of-sight MDI magnetograms already provide a good approximation (within 5%) of the vertical component of the photospheric magnetic field that is assumed to be proportional to the total chromospheric magnetic field strength. It would have been interesting to examine microwave images which may show opposite FP asymmetry as in HXRs (Kundu et al., 1995). However, spectrograms of this flare obtained at the Owens Valley Solar Array do not allow for image reconstruction due to poor data quality (J. Lee & C. Liu, private communication), while Nobeyama was not observing (before 6 AM, local time).

5.2.1 *RHESSI* Light Curves and Images

RHESSI had very good coverage of this event. However, HXR counts, particularly at high energies, were heavily contaminated by particles from the Earth's radiation belts during the course of the flare. Fortunately, count rates produced by these particles are unmodulated and are removed during image reconstruction (Hurford et al., 2002). Therefore, CLEAN

images were made at short time intervals for each energy bin and then spatially integrated to obtain a light curve. Such *RHESSI* light curves, as shown in Figure 5.1*a* together with *GOES* fluxes, were obtained by Ji et al. (2008) by integrating consecutive 4 s images. We find that, at low energies (<30 keV), the X-ray light curves show a single peak and an almost exponential decay after the maximum. At high energies (>70 keV), there are two peaks (Peaks 1 and 2) divided at 20:48 UT.

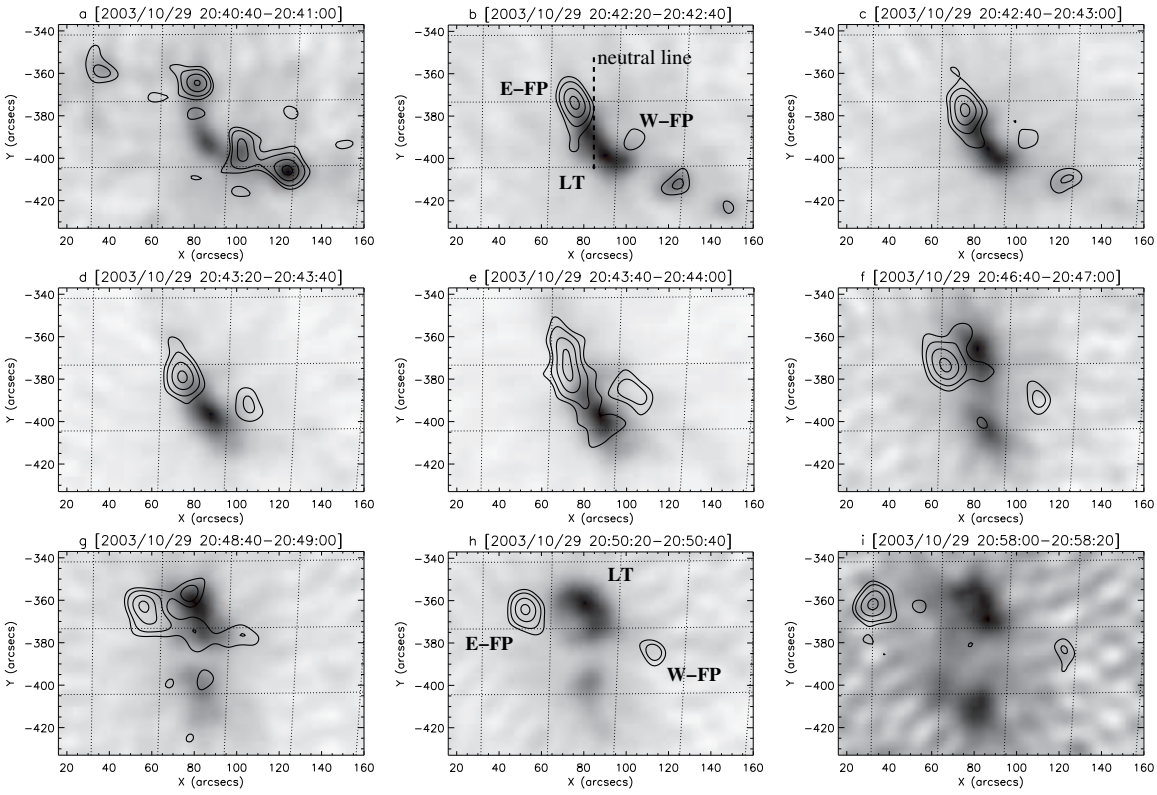

Figure 5.2: Evolution of HXR sources as seen in *RHESSI* CLEAN images made with detectors 3–8 (FWHM resolution 9.8″) in two energy bands, 12–25 keV as gray scale and 60–100 keV as contours (at 23%, 35%, 60%, and 90% of the maximum of each image). The dashed line in panel *b* shows the location of the magnetic neutral line shown in Fig. 5.6*a* that has been corrected for the solar rotation to the time of this image. The dotted lines mark the heliographic longitudes and latitudes with 2° spacing [from Liu, W. et al. 2008a].

To obtain the flare morphology and its general evolution, we focused on a time range from 20:40:40 to 20:59:40 UT beyond which the double conjugate FPs of interest (identified below) were not clearly imaged, due to complex morphology and/or low count rates. We first divided this time range into 57 consecutive 20 s intervals, except for one interval that was shortened to 12 s to avoid the decimation state change at 20:46:36 UT. We then reconstructed images in two broad energy bands, 12–25 and 60-100 keV, using the CLEAN algorithm and uniform weighting among detectors 3–8 (Hurford et al., 2002). The effective FWHM angular resolution is 9.8″.

A sample of the resulting images is shown in Figure 5.2. Early in the flare (before

20:43:20 UT, Fig. 5.2*d*), several bright points at 60–100 keV are dispersed across the image, suggesting FPs of multiple loops. Part of the 12–25 keV emission appears elongated and curved between the adjacent FPs, corresponding to the LT source(s). Toward the southwest, part of the 12–25 keV emission seems to overlap with the FP emission, possibly due to either a projection effect. As time proceeds, the FP structure seen at 60–100 keV becomes simpler, and only two distinct FPs are present (after 20:43:20 UT). They generally move away from each other. At the same time, the 12–25 keV emission gradually changes from one to two LT sources, one in the north and the other in the south.

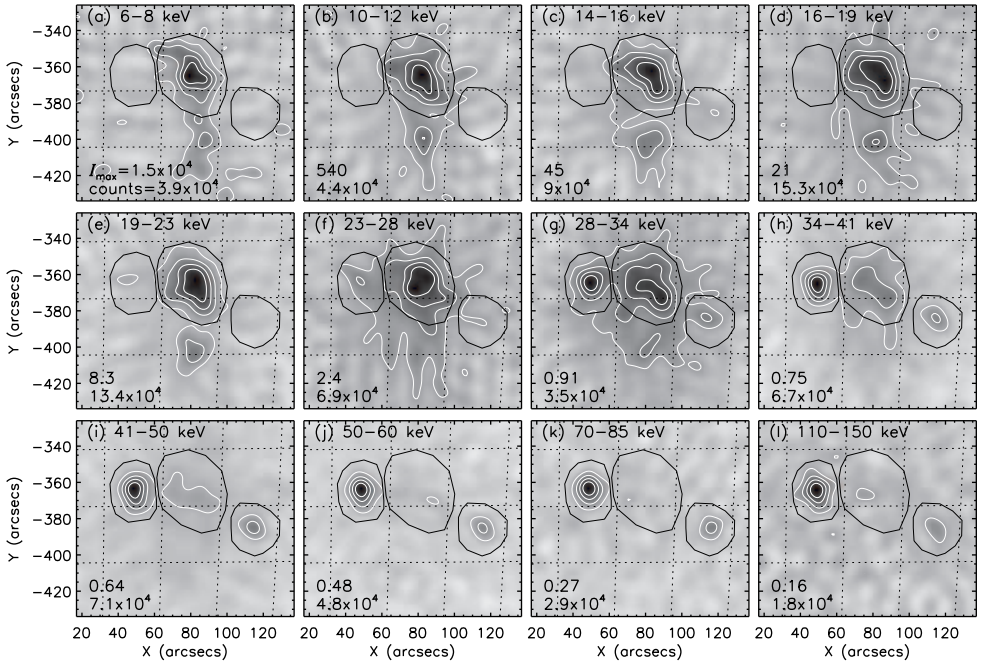

Figure 5.3: CLEAN images in different energy bins at 20:51:20–20:51:40 UT made with detectors 3–9. The contour levels are 20%, 40%, 60%, and 80% of the maximum surface brightness, $I_{\max}$ (shown in the lower left corner of each panel, in units of photons $\mathrm{cm}^{-2}\,\mathrm{s}^{-1}\,\mathrm{arcsec}^{-2}$), of each individual image. The number below $I_{\max}$ indicates the total counts accumulated by the detectors used. The heliographic grid spacing is 2°. The same three dark, hand-drawn polygons in each panel were used to obtain the fluxes of the LT and two FP sources [from Liu, W. et al. 2008a].

We identified the conjugate FPs and the corresponding LT source of interest as follows for detailed analysis: (1) At later times (after 20:43:20 UT), only two FPs are seen in each image at 60-100 keV and so they are considered conjugate. We call the FP on the eastern (left) side E-FP and the one on the western (right) side W-FP (see, e.g., Fig. 5.2*h*). (2) At earlier times when more than two FPs are present, we set forth the following selection criteria: (*a*) The source morphology of the two conjugate FPs must be consistent with the picture that they are magnetically connected through the LT source between them seen in the corresponding 12–25 keV image (see, e.g., Fig. 5.2*b*). (*b*) During the time evolution the two FPs must show continuity and consistency in position and HXR flux, which other short-lived FPs lack. Under these criteria, the selected E-FP is the brightest FP to the east of the magnetic neutral line (*thick dashed* in Figs. 5.2*b* and 5.6*a*), and W-FP is the

one to the west located nearest to the neutral line. (3) Once the conjugate FPs are found, their corresponding LT source was identified as the 12–25 keV emission that lies closest to the straight line joining the FPs. For example, at later times (see, e.g., Fig. 5.2*h*), the northern LT is selected, while the southern LT is ignored since it does not seem to have any corresponding FP emission, presumably because of its faintness that exceeds *RHESSI*'s dynamic range ($\gtrsim$10:1 for images, Hurford et al., 2002, see Appendix §A.5).

5.2.2 Imaging Spectroscopy of Footpoint and Loop-top Sources

Next, we examine the spectroscopic characteristics of the LT and FP sources and their temporal evolution. For each of the 57 consecutive 20 s intervals defined above, we reconstructed CLEAN images in 16 energy bins that are progressively wider from 6 to 150 keV. A sample of these images is shown in Figure 5.3 for 20:51:20–20:51:40 UT, where four images showing similar morphology as in neighboring energy bins are omitted. The emission is dominated by the two LT sources at low energies and the double FP sources at high energies.

The next step was to obtain photon fluxes of the sources for each time interval. For each FP source, we used a hand-drawn polygon that envelops all the 10% (of the maximum brightness of the image) contours at energies where this FP source was clearly imaged. For the corresponding LT source, we drew a polygon that encloses the 20% contours, which was selected to minimize spatial contamination from the FPs. We then read the resulting multiple-energy image cube into the standard *RHESSI* spectral analysis software (OSPEX) package. This package integrates photon fluxes inside each polygon, and uses the full detector response matrix to estimate the true incident photon spectrum. The RMS of the residual map of the CLEAN image was used to calculate the uncertainty for the photon flux in each energy bin, with proper consideration of the source area and grid spatial resolution. This imaging spectroscopy technique is detailed by Liu, W. et al. (2008b). Note that we did not use contours at a fixed level (as opposed to polygons fixed in space) to obtain the fluxes because of the complex source morphology that makes such contours vary with energy.

One important issue for this X10 flare is pulse pileup (Smith et al., 2002) that at high count rates distorts the count-rate spectrum. We have discussed in Appendix A.4.2 various effects of pileup on our analysis and the remedy that we have applied to minimize them. Although it is currently not possible to obtain accurate spectra throughout the full energy range for all sources, pileup mainly affects the LT sources in the energy range of 20–50 keV (e.g., see Figs. 5.3*h* and 5.3*k*). In other words, pileup effects are negligible for the LT sources below 20 keV and for the FP sources above 50 keV. This conclusion enabled us to confine the extent of pileup effects both in energy and in space, and yet to infer desired spectral information. We thus fitted the LT spectrum below 20 keV with an assumed isothermal model from CHIANTI ver. 5.2 (Young et al., 2003), using the coronal iron abundance of 4 times the photospheric value, to determine its temperature (T) and emission measure (EM); we fitted the FP spectrum above 50 keV with an assumed single power-law model to find its spectral index (γ) and normalization flux (I) at the reference energy of 50 keV.

Spectra of the LT and FP sources are shown in Figure 5.4*a* for the interval of 20:44:40–20:45:00 UT (during the main impulsive peak). Above 50 keV, both FP spectra have a power-law shape, with the E-FP flux being twice that of W-FP but only slightly harder. Consequently, the W-to-E ratio of the two FP spectra generally decreases with energy

(Fig. 5.4*b*) or stays constant within uncertainties. Below 20 keV the LT spectrum shows the exponential shape of isothermal bremsstrahlung emission, with the iron line feature at 6.7 keV visible. Note that below 50 keV the FP spectra may be compromised by pileup effects[2] and spatial contamination from the LT source, and likewise above 20 keV the apparent LT flux is contaminated by FP emission at the same energy and by pileup from lower energies (Fig. 5.4*a*).

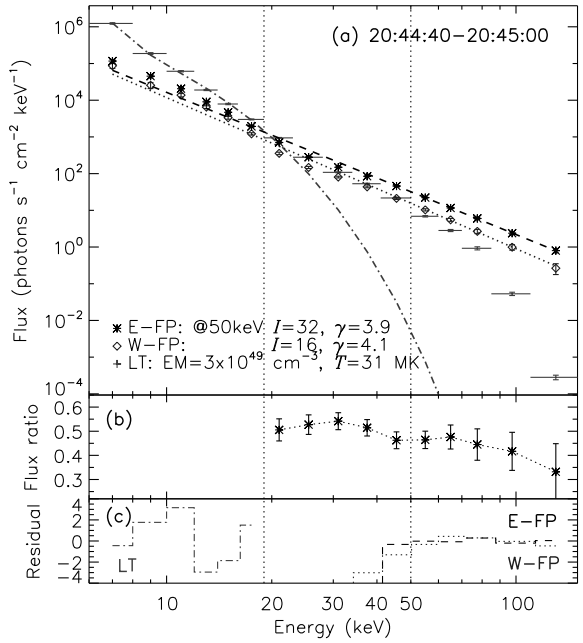

Figure 5.4: (*a*) Spatially resolved spectra of the LT and two FP sources at 20:44:40–20:45:00 UT. The horizontal bars on the LT spectrum represent the energy bin widths in the range of 6–150 keV. The dashed and dotted lines are power-law fits from 50–150 keV for E-FP and W-FP, respectively, and the dot-dashed line is a single temperature thermal fit from 6–19 keV for the LT. The legend shows the photon fluxes (I) at 50 keV and the spectral indexes (γ) for the FPs, and the emission measure (EM) and temperature (T) for the LT. (*b*) Ratio of the W-to-E FP fluxes. (*c*) Fitting residuals normalized by the 1σ uncertainties for the LT (*dot-dashed*), E-FP (*dashed*) and W-FP (*dotted*) sources [from Liu, W. et al. 2008a].

We now examine the spectral evolution of the LT source and defer that of the FP sources to §5.4.1. As shown in Figure 5.5*a*, the measured temperatures are consistent with a monotonic decrease with time, presumably due to cooling of the thermal plasma through various channels whose rate exceeds the heating rate at these times. The EM (Fig. 5.5*b*), on the other hand, increases rapidly in the first ∼5 minutes and then stays roughly constant followed by a slight decrease toward the end. The increase and decrease of the EM is likely due to chromospheric evaporation (e.g., Liu, W. et al., 2006) and/or direct coronal heating and consequent cooling of the plasma.

[2]The trend of the two FP spectra (being nearly parallel to one another) extends below 50 keV to ∼20 keV, suggesting that pulse pileup may have minimal effects on the relative spectral shapes of the FPs, and that our selection of 50 keV as the lower limit for reliable FP spectra is likely to be unnecessarily conservative.

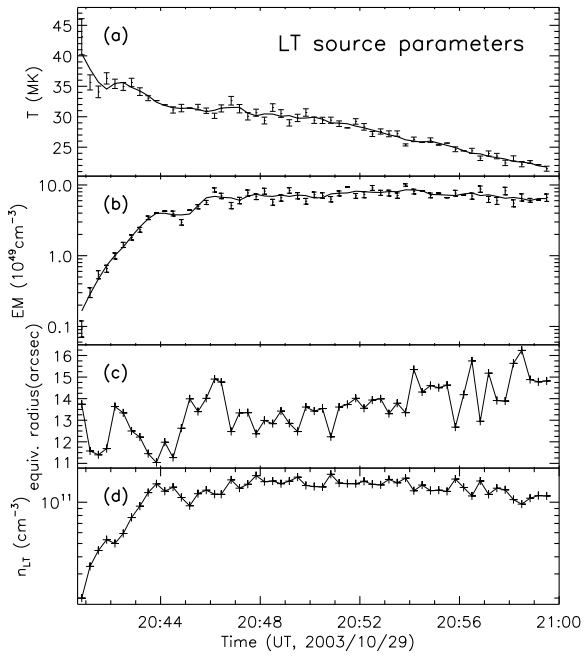

Figure 5.5: Evolution of spectroscopic parameters of the LT source. (*a*) Temperature T and (*b*) emission measure EM with 20 s integration time. The solid lines are 7-point box-car smooths of the original fitting results indicated by the symbols. (*c*) Radius r of the equivalent sphere of the LT source (see §5.2.2) and (*d*) corresponding electron number density $n_{\rm LT}$ [from Liu, W. et al. 2008a].

In order to infer the density of the LT source, we assumed that it has a spherical shape with the projected area a equal to the area inside the 50% brightness contour at 12–25 keV. We then obtained the radius $r = (a/\pi)^{1/2}$ and volume $V = 4\pi r^3/3$ of the *equivalent sphere* and the corresponding density $n_{\rm LT} = [{\rm EM}/(Vf)]^{1/2}$. In doing so we assumed a filling factor f of unity, and used the EM values smoothed with a 7-point box-car to minimize fluctuations possibly caused by the inevitable anti-correlation between T and EM during spectral fitting. The values of r and $n_{\rm LT}$ as functions of time are shown in Figures 5.5*c* and 5.5*d*, respectively. As evident, the size of the sphere stays roughly constant between $11''$–$16''$ and thus the density follows the same trend as the EM.

To obtain the spatial evolution of the double FP sources and the corresponding LT source, one can track the migration of their centroid positions with time. For each 12–25 and 60–100 keV image obtained in §5.2.1, we used contours at 50% and 90% of the maximum brightness of each LT and conjugate FP source, respectively, to locate its emission centroid. The reason for a higher contour level for the FPs (than the LT) is that the E-FP source spreads along the flare ribbon (see, e.g., Fig. 5.2*e*) and we need the brightest "kernel" to obtain the corresponding magnetic field strength averaged inside this contour (see §5.4.3). The resulting centroids at different times are superimposed on the multiwavelength images in Figure 5.6, and shown in greater detail in Figure 5.7, which we will examine in §5.3.

5.2.3 Multiwavelength Images

The following multiwavelength images were used in this analysis: magnetograms, Hα, white-light, and extreme ultraviolet (EUV). They were shifted by various amounts in the solar east-west (x) and south-north (y) directions to match the *RHESSI* aspect, believed to be accurate at the sub-arcsecond level (Fivian et al., 2002). All images were corrected for various geometric effects (solar rotation, *SOHO* L1 to Earth view, etc.) where applicable. These procedures are detailed in Appendix B.1.

A preflare *SOHO* MDI magnetogram at 20:30:35 UT is shown in Figure 5.6*a*, overlaid with the centroids of the *RHESSI* FPs at 60–100 keV obtained in §5.2.2 at 57 time intervals. E-FP is located in the negative (*dark*) polarity to the left of the general magnetic neutral line (*dashed*), while W-FP is in the positive (*white*) polarity to the right.

An Hα blue wing (6562.41 Å) image at 20:42:11 UT (Fig. 5.6*b*) displays flare ribbons in opposite magnetic polarities (cf., Fig. 5.6*a*). A *RHESSI* 60–100 keV image at the nearest time of 20:42:00–20:42:20 UT is overlaid as contours, which appear as three HXR sources on or near the three Hα kernels.[3] The strongest HXR FP source (E-FP) is cospatial with the brightest Hα emission that is located in the negative magnetic polarity, suggestive of the causal correlation between the flux of HXR-producing electrons and the heating rate of the lower atmosphere responsible for the Hα emission.[4] Note that E-FP is also associated with the major compact seismic signature, as reported by Donea & Lindsey (2005).

Comparing a *TRACE* white-light image at 20:49:49 UT shown in Figure 5.6*c* with Figure 5.6*a*, we find three large sunspots in the positive polarity to the right and three small sunspots in the negative polarity just left of the general neutral line. *RHESSI* 60–100 keV contours nearest in time are shown in gray,[5] where the double FP sources correspond to parts of the white-light flare emission (*light-gray contours* and *arrows*).

The *TRACE* 195 Å image at 20:50:42 UT in Figure 5.6*d* shows an arcade of flare loops distributed along the magnetic neutral line. Overlaid are *RHESSI* images at 12–25 keV for the LT sources and 60–100 keV for the FP sources at 20:50:40–20:51:00 UT. The former appear at the apexes of the EUV loops and the latter at the footpoints.

5.3 Two-phase Unshearing Motions of HXR Footpoints

We now examine in greater detail the motions of the HXR sources in the context of the multiwavelength observations described above. In an attempt to correct for projection effects and to obtain the true 3D loop geometry, we assumed that the centroids of the LT and two FP sources at a given time are connected by a semi-circular model loop. We then used the solar x and y coordinates of these three points in the sky plane to determine the

[3]The most south-west Hα kernel does not have a HXR counterpart, possibly due to *RHESSI*'s limited dynamic range ($\gtrsim$10:1).

[4]The weaker HXR W-FP is ahead (to the west) of the corresponding Hα kernel, which may result from direct (other than collisional) heating, or from cooling of the hot plasma previously heated by nonthermal electrons with an increasing emission measure, since Hα emission is sensitive to temperature and density. It is possible that our coalignment of the *RHESSI* and Hα images is not perfect, and the HXR image can be shifted to the left by a few arcseconds such that both E- and W-FP can lead their corresponding Hα kernels.

[5]Some weak HXR emission also appears between the two FPs, which is, most likely, an artifact caused by pulse pileup of the LT emission (see §A.4.2).

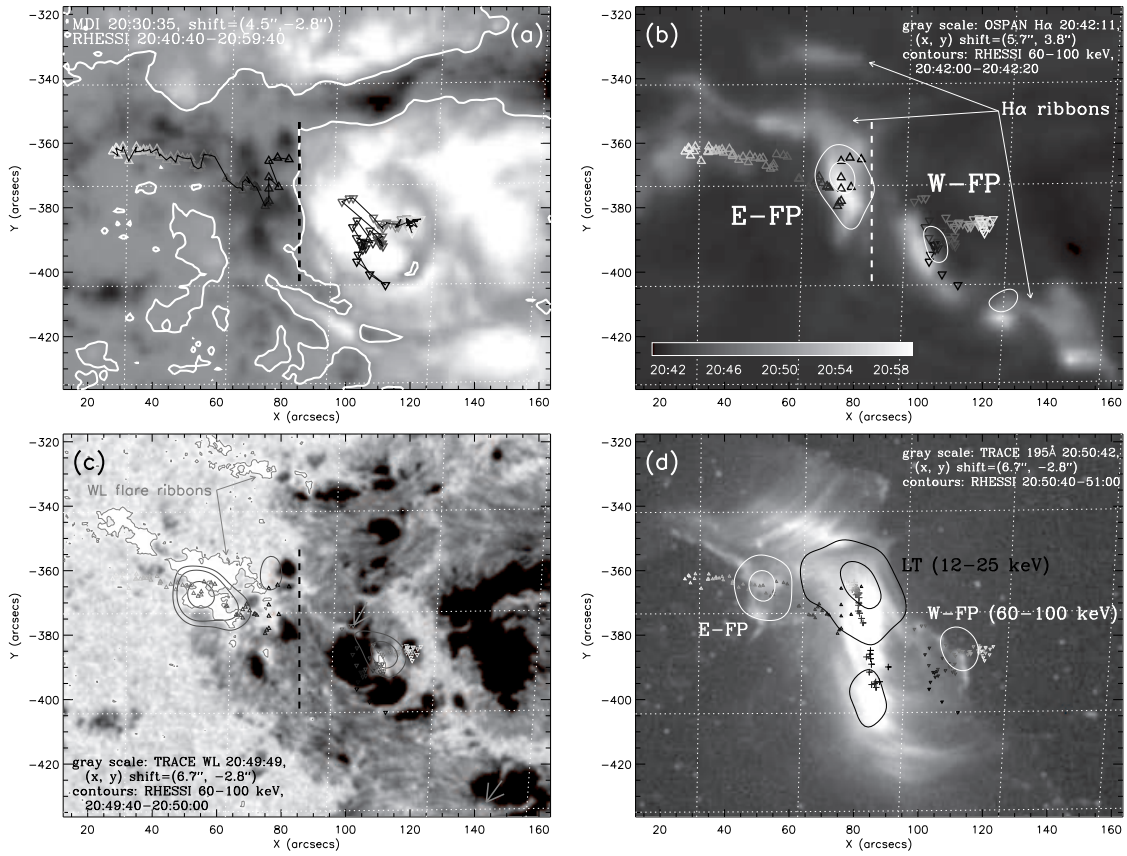

Figure 5.6: (*a*) preflare *SOHO* MDI magnetogram (centered at 20:30:35 UT with an integration time of 30 s) overlaid with magnetic neutral lines in white and *RHESSI* FP centroids as symbols. The white (dark) gray scale represents positive (negative) line-of-sight magnetic fields pointing away (toward) the observer. The vertical thick dashed line outlines the general magnetic neutral line between the two FPs, which is also shown in (*b*) and (*c*). The temporal evolution of the *RHESSI* centroid positions is indicated by the color bar in (*b*). Both the MDI magnetogram and *RHESSI* centroids were corrected for the solar differential rotation and shifted to their corresponding positions at the time of the *TRACE* image in (*d*); additional shifts of $\Delta x = 4.5'' \pm 2.0''$ and $\Delta y = -2.8'' \pm 2.0''$ were applied to the MDI map to compensate its pointing offset from *RHESSI* (see Appendix B.1). The same correction procedures were applied to (*b*), (*c*), and (*d*). (*b*) Same as (*a*) but for the Optical Solar Patrol Network (OSPAN) Hα blue wing (6562.41 Å) image taken at 20:42:11 UT showing the flare ribbons, overlaid with a concurrent *RHESSI* 60–100 keV image as gray contours (20% & 70%). (*c*) Same as (*b*) but for a *TRACE* white-light image at 20:49:49 UT and a *RHESSI* 60–100 keV image at contour levels of 20%, 30%, and 70%. The light-gray contours are at 99% of the maximum brightness of the *TRACE* image, highlighting some of the excessive white-light emission on the flare ribbons, the rest of which is marked by the two short arrows. (*d*) Same as (*b*) but for a *TRACE* 195 Å image at 20:50:42 UT, overlaid with concurrent *RHESSI* contours in dark (30% & 80%) for the LTs at 12–25 keV and in white (20% & 70%) for the FPs at 60–100 keV. The evolution of the LT (*plus signs*) and FP (*triangles*) centroids is also shown (see also Fig.5.7*a*) [from Liu, W. et al. 2008a].

size and the orientation of the semi-circle in 3D space, knowing that the FPs are located on the solar surface and the LT in the corona. A sample of the loops at selected times is shown in Figure 5.7*a*. We find that the inclination angle between the model loop and the solar surface ranges from 27° to 76°, and that the loop length ($l_{\rm total}$; see Fig. 5.7*c*) generally first decreases and then increases with a minimum at 20:43:50 UT.

The LT centroids (*plus signs*), as shown in Figure 5.7*a*, are situated at all times close to the neutral line (*dashed*) as expected, and form two clusters, one in the south and the other in the north. As time proceeds, the LT centroid appears to move from the apex of one loop to another along the arcade seen in *TRACE* 195 Å (Fig. 5.6*d*). It first gradually moves southward until 20:43:30 UT (marked by the open circle in Fig. 5.7*a*), when it starts to rapidly shift to the northern cluster and continue moving northward afterwards. This can be more clearly seen from its relative displacement projected onto the direction parallel to the north-south neutral line as a function of time shown in Figure 5.7*d* (Δy_{LT}, *dot-dashed line*).

As to the FPs, in general, E-FP first moves southward and then turns to the east, while W-FP first moves northward and then turns to the west, as indicated by two of the three thick arrows in Figure 5.7*a*. The evolution of the position of E-FP relative to W-FP (or the positional vector from W-FP to E-FP) is shown in Figure 5.7*b*. There is clearly a turning point which occurs at t_1=20:44 UT and divides the evolution of the FP positions into two phases: (1) Phase I (20:40:40–20:44:00 UT) when the two FPs generally move toward each other in a direction essentially parallel to the neutral line, (2) Phase II (20:44:00–20:59:40 UT) when the two move away from each other mainly perpendicular to the neutral line. The transition between the two phases coincides (within 30 s) with the minimum of the estimated loop length and the direction reversal of the LT motion noted above. Another signature of this two-phase division is the morphological transition at 20:43:20 UT, before which there are multiple FP sources, but only two FPs present afterwards (see Fig. 5.2). Below we describe in detail the HXR source evolution in the two phases.

We further decomposed the distance between the FPs into two components: perpendicular and parallel to the neutral line as shown in Figure 5.7*e*, where the two phases are divided by the vertical dotted line at t_1. As can be seen, the parallel distance (*asterisks*) first rapidly decreases at a velocity of 108 ± 18 km s^{-1} given by the linear fit during Phase I (covering a range of 27″ in ∼3 minutes); it then stays almost constant during Phase II with a slight increase (a range of 15″ in ∼16 minutes with 7 ± 1 km s^{-1}). In contrast, the perpendicular distance (*dashed*) has a small variation in Phase I (a range of 12″ with 15 ± 13 km s^{-1}) and increases continuously at a velocity of 51 ± 1 km s^{-1} in Phase II (range: 63″).

Next we obtained the shear angle (θ; Fig. 5.7*b*) from the normal to the neutral line (parallel to the y-axis) to the W-to-E relative positional vector, which is shown as a function of time in Figure 5.7*e* (*solid line*, *right axis*). This angle exhibits a fast decrease (from 56° to 22°) during Phase I and a slow decrease (down to 12°) during Phase II. An independent study by Ji et al. (2008) also found the same unshearing motions in two phases, which they referred to as *sigmoid* and *arcade* phases based on the X-ray morphology.

The unshearing motions of the HXR FPs indicate that the newly reconnected magnetic field lines are progressively less sheared during the flare. It can be seen that *TRACE* 195 Å loops corresponding to the HXR FPs at early times (not shown) are indeed highly sheared.

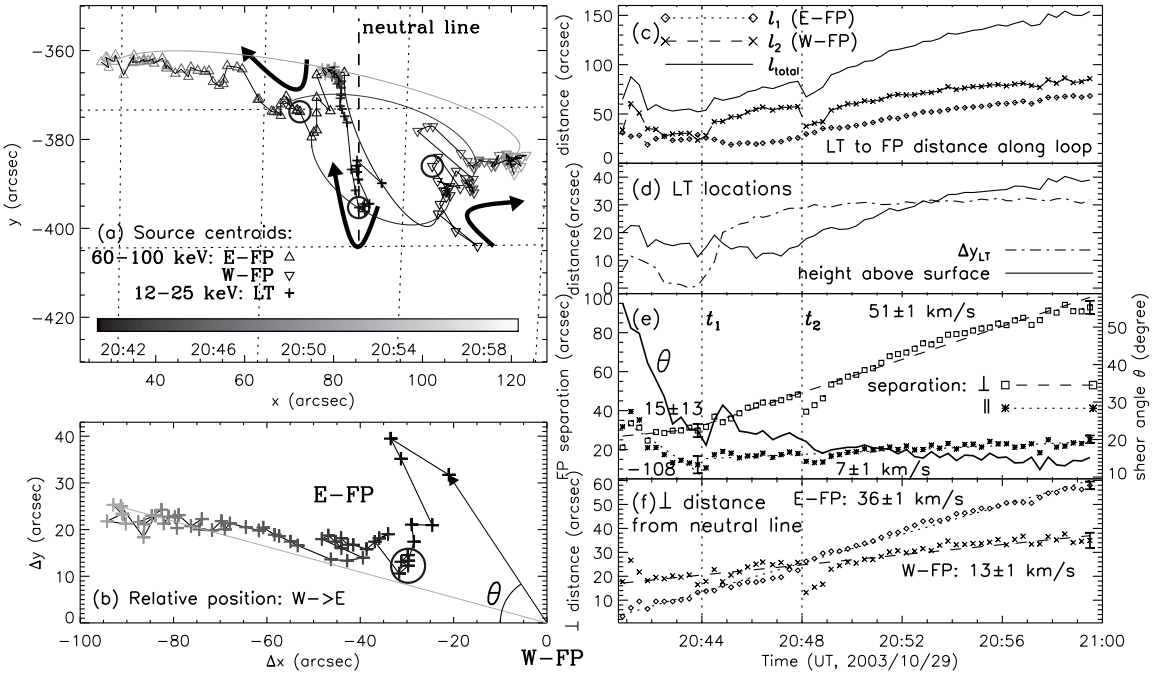

Figure 5.7: (*a*) Evolution of *RHESSI* centroids of the two FP sources at 60–100 keV (*triangles*) and of the LT source at 12–25 keV (*plus signs*), which are identical to those shown in Fig. 5.6*d*. Gray scales from dark to bright represent time at 20 s intervals from 20:40:40 to 20:59:40 UT. The vertical dashed line (∥ *y*-axis) is the general magnetic neutral line shown in Fig. 5.6*a*. We show semi-circular model loops at four times (labeled *a*, *d*, *f*, and *i* in Fig. 5.2) projected onto the sky plane, each of which connects three centroids (of two FPs & one LT) of the same time. The thick dark arrows indicate the general direction of motion for the LT and two FPs. (*b*) Relative centroid positions of E-FP with respect to W-FP which is selected as the origin. The start and end of the time evolution are marked by the black and light-gray arrows, respectively drawn from W-FP. θ is the shear angle between the normal (due west) to the neutral line and the line joining the two FP centroids. The circle here and those in (*a*) and the first vertical dotted line in (*e*) mark the transitional time t_1 from fast to slow unshearing motions of the FPs (see §5.3). (*c*) Distance (l_1 and l_2) from the LT centroid to the centroids of the two FPs along the semi-circular model loop as shown in (*a*), together with the length of the loop ($l_{\rm total} = l_1 + l_2$). The vertical dotted line labeled t_2 corresponds to the division between the two HXR peaks and the jump of the FP positions. (*d*) Relative displacement ($\Delta y_{\rm LT}$, *dot-dashed*) of the LT centroid parallel to the magnetic neutral line shown in (*a*) and estimated height of the LT centroid above the solar surface (*solid*). (*e*) Orthogonal components of the separation between W-FP and E-FP perpendicular (*squares*) and parallel (*asterisks*) to the neutral line. The straight lines are linear fits to the distances in the two phases, labeled with the corresponding velocities (in $\rm km\,s^{-1}$). The solid curve (*right scale*) is the shear angle θ defined in (*b*). (*f*) Perpendicular distances to the neutral line from E-FP (*diamonds*) and W-FP (*crosses*). Linear fits for the whole flare duration are shown as the straight lines. The error bar shown on the last data point of each line here and in (*e*) is the RMS deviation of the data from the corresponding fit [from Liu, W. et al. 2008a].

Similar unshearing motions were found in other flares in HXRs (Sakao, 1994; Masuda et al., 2001; Schmahl et al., 2006) and in EUV (Asai et al., 2003; Su et al., 2007). Note that the HXR flux (see Fig. 5.1) rapidly rises when the shear angle undergoes the fast decrease. An opposite process took place prior to the flare, that is, strong photospheric shearing flows observed near the neutral line (Yang et al., 2004, as mentioned earlier). This process increased the shear of field lines and built up magnetic stress and free energy in the system during the preflare phase (Metcalf et al., 2005).

It has been established for LT sources in limb flares that there is usually a decrease in altitude during the rising portion of the impulsive phase followed by a subsequent increase (e.g, Sui & Holman, 2003; Sui et al., 2004; Liu, W. et al., 2004a, 2008b). Holman et al. (2005) found 58 (66%) such events in a sample of 88 limb flares. For flares on the solar disk like the one under study, it is difficult to determine the LT height, but FP motions can be seen more clearly than those in limb flares. Our approach of determining a 3D semi-circle from the LT and FP centroids is an attempt to correct for projection effects and yields an estimate of the LT height as shown in Figure 5.7*d* (*solid line*).[6] As expected, the LT descent is evident especially before t_1=20:44 UT when the HXR flux is on the rise. It is associated with the southward motion of the LT along the neutral line before t_1 (Fig. 5.7*d*; *dot-dashed*). This suggests that the propagation of the reconnection site along the neutral line or the arcade in one direction and then the other temporally coincides with the decrease and then increaseof the LT altitude. The LT descent here is also associated in time with the decrease of the loop length (Fig. 5.7*c*, *solid line*) and the fast unshearing motion of the FPs (Fig. 5.7*e*, *solid line*), that is, with progressively shorter and less sheared loops. This association was previously proposed, based on a simple energy analysis, by Ji et al. (2007). They argued that an alternative interpretation for descending LTs that invokes the relaxation of cusp-shaped loops, however, cannot explain the approaching FPs which are expected otherwise not to move.

5.4 Temporal Correlations of Conjugate Footpoints

We now examine the temporal evolution of and correlations between various quantities of the two conjugate FPs, particularly spectral, spatial, and magnetic field parameters, which are summarized in Table 5.1.

5.4.1 Spectral Correlations

Figure 5.8*a* shows the history of the photon fluxes of E-FP (I_1, *diamonds*) and W-FP (I_2, *crosses*) at 50 keV obtained from the power-law fits in the 50–150 keV range mentioned in §5.2.2. We find that the two fluxes follow each other closely in their temporal trends and E-FP is always brighter than W-FP except for the first time interval. The correlation of the fluxes can also be seen in Figure 5.9*a* where one flux is plotted vs. the other. A linear regression is shown as the thick dashed line and given in Table 5.1. The correlation coefficients listed in Table 5.1 indicate a very high correlation in either a linear or a nonlinear sense. Such a correlation is expected for conjugate HXR FPs, since they are believed to be

[6]The slightly different temporal trends of the LT height and the loop length shown in Fig. 5.7*c* are due to the assumption that the semi-circle is not necessarily vertical to the solar surface.

Table 5.1: Correlation coefficients and linear regressions between various parameters of the conjugate footpoints for the full flare duration (20:40:40–20:59:40 UT).

Subscripts: 1: E-FP, 2: W-FP		r_p	No. of $\sigma(0.13)$	r_s	signif-icance	Linear regression (between quantities in first two columns)
I_1	I_2	0.98	8	0.97	10^{-35}	$I_2 = (-0.3 \pm 0.1) + (0.41 \pm 0.01) I_1$
γ_1	γ_2	0.90	7	0.89	10^{-20}	$\gamma_2 = (-0.5 \pm 0.3) + (1.17 \pm 0.07)\gamma_1$
B_1	B_2	0.39	3	0.40	10^{-3}	$B_2 = (-5.1 \pm 0.3) + (2.89 \pm 0.06) B_1$
B_1	$\log_{10} I_1$	0.50	4	0.49	10^{-4}	$I_1 = (0.014 \pm 0.002) \times 10^{(0.53 \pm 0.01) B_1}$
B_2	$\log_{10} I_2$	0.82	6	0.84	10^{-16}	$I_2 = (0.124 \pm 0.004) \times 10^{(0.150 \pm 0.001) B_2}$
$\bar{B}$	$\log_{10} \bar{I}$	0.77	6	0.84	10^{-16}	$\bar{I} = (0.140 \pm 0.007) \times 10^{(0.219 \pm 0.003) \bar{B}}$
v_1	v_2	0.63	5	0.29	10^{-2}	$v_2 = (-93 \pm 10) + (2.8 \pm 0.1) v_1$

r_p and No. of σ: Pearson's linear correlation coefficient and its multiple of 1σ uncertainty of $1/(57)^{1/2} = 0.13$, where 57 is the number of data points (time intervals), respectively;
r_s and significance: Spearman's rank correlation coefficient and significance level, respectively;
I (photons s^{-1} cm^{-2} keV^{-1}): HXR flux at 50 keV;
γ: spectral index between 50 and 150 keV (regression done only for 20:40:40–20:52:40 UT);
B (100 Gauss): magnetic field;
$\bar{B}$ (100 Gauss) and $\bar{I}$ (photons s^{-1} cm^{-2} keV^{-1}): B and I averaged between E-FP and W-FP;
v (km s^{-1}): FP velocity.

produced by similar populations of nonthermal electrons that escape the same acceleration region (believed to be at/near the LT source; Petrosian & Liu 2004; Liu, W. et al. 2008b) and travel down opposite legs of the same magnetic loop to reach the chromosphere.

We show the corresponding power-law indexes (γ) of the two FPs vs. time in Figure 5.8*d* and one index vs. the other in Figure 5.9*b*. Again we find that the two indexes are closely correlated, as can be seen from the large correlation coefficients (Table 5.1). The E-FP spectrum, however, is slightly harder than the W-FP spectrum, which it is persistent most of the time. The results from long integration intervals (2–3 minutes), which have better count statistics, exhibit the same pattern. We averaged the index values of the first six long intervals up to 20:52:40 UT, after which the uncertainties become large due to low count rates. This average gives $\langle\gamma_1\rangle = 3.63 \pm 0.06$ for E-FP and $\langle\gamma_2\rangle = 3.79 \pm 0.11$ for W-FP. Their difference of $\langle\gamma_2\rangle - \langle\gamma_1\rangle = 0.15 \pm 0.13$ is marginally significant at the 1σ level.

Let us compare the HXR fluxes and spectral indexes of the two FPs. As can be seen in Figures 5.8*a* and 5.8*d*, during HXR Peak 1 (before t_2=20:48 UT), the fluxes and indexes are anti-correlated, i.e., they follow the general "soft-hard-soft" (SHS) trend observed in many other flares (e.g., Grigis & Benz, 2004). However, during Peak 2 (after t_2), the indexes decrease through the HXR maximum and then vary only slightly (with relatively large uncertainties) around a constant level of 3.0. This trend can be characterized as "soft-hard-hard" (SHH). This flux-index relationship can also be seen in Figure 5.9*c* where the index averaged between the two FPs is plotted against the average flux. Note that the spectral index values during the late declining phase of the flare are even smaller than those at the maximum of the main HXR Peak 1. In this sense, the overall spectral variation can be characterized as "soft-hard-soft-harder". As we noted earlier, there were energetic protons detected in interplanetary space by *GOES* and *ACE* following the flare. These observations, when taken together, are consistent with the conclusion of the statistical study by Kiplinger

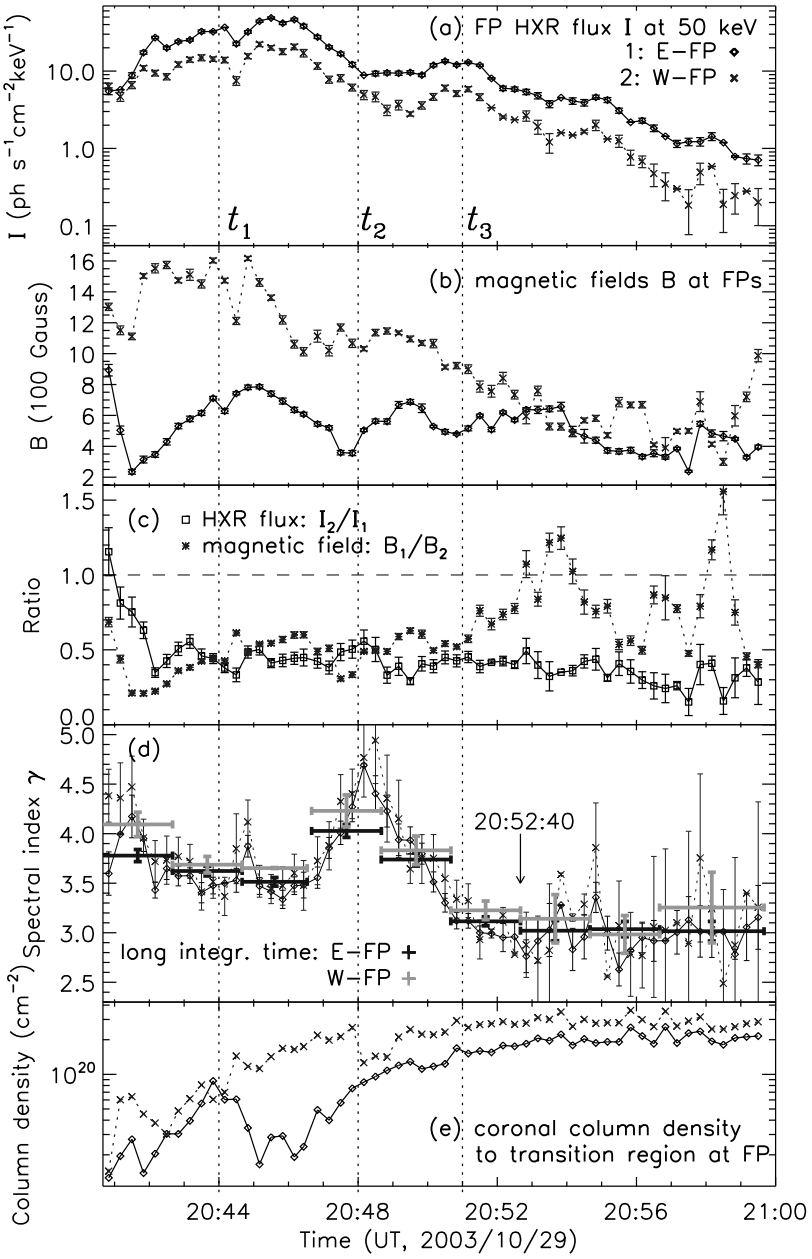

Figure 5.8: History of HXR and magnetic field parameters of the two footpoints. (*a*) HXR fluxes at 50 keV of E-FP (*diamonds*) and W-FP (*crosses*) obtained from power-law fits in the 50–150 keV range. The same symbol convention for E- and W-FP holds for the other panels. The vertical dotted lines correspond to the transitional times of t_1 and t_2 as shown in Fig. 5.1, and t_3, the maximum of HXR Peak 2. (*b*) *SOHO* MDI magnetic field strengths registered at the two FPs, with the $\pm\sigma$ uncertainties derived from 10 preflare magnetograms (see §5.4.3). (*c*) Ratios of the 50 keV fluxes (W-to-E) and magnetic fields (E-to-W) of the two FPs. (*d*) HXR spectral indexes of the two FPs from the same fits as in (*a*). The plus signs show results of long integration intervals (2–3 minutes) indicated by the wide horizontal error bars, which yield better count statistics. The arrow marks the end of the first six such intervals for averaging the index values (see §5.4.1). (*e*) Estimated coronal column densities from the edge of the LT source to the transition region at the two FPs [from Liu, W. et al. 2008a].

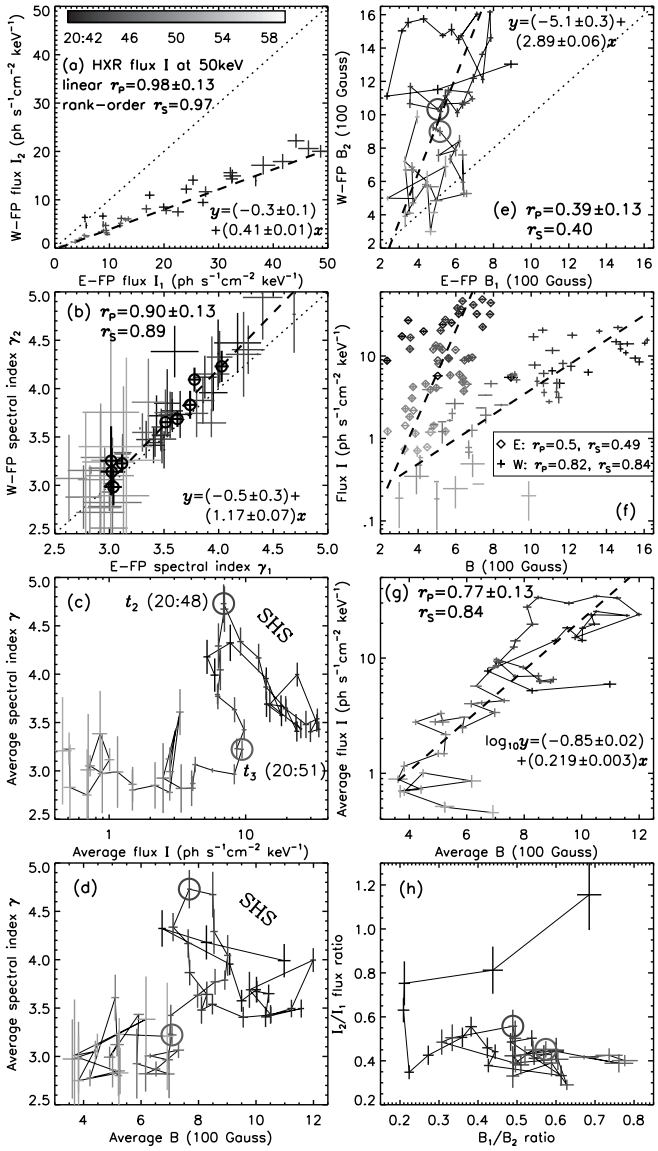

Figure 5.9: Various correlations between the HXR and magnetic field parameters of the two FPs. (*a*) HXR flux at 50 keV (Fig. 5.8*a*) of W-FP vs. E-FP with a linear regression fit (*dashed*). Pearson's linear and Spearman's rank-order correlation coefficients, r_p and r_s, are given in the legend. The color bar indicates the common time evolution for all panels of this figure. (*b*) Same as (*a*) but for the spectral indexes (γ) shown in Fig. 5.8*d*. The open circles represent the results obtained from longer integration intervals (2–3 minutes). The linear regression is done for the data points up to 20:52:40 UT. (*c*) and (*d*) Average (between the two FPs) spectral index $\bar{\gamma}$ vs. average flux $\bar{I}$ at 50 keV and vs. average magnetic field $\bar{B}$, respectively. The two open circles here and in (*e*) and (*h*) mark the times t_2 and t_3 shown in Fig. 5.8. Early in the flare, an usual "soft-hard-soft" (SHS) variation is present. (*e*) Same as (*a*) but for the magnetic field strengths of the two FPs as shown in Fig. 5.8*b*. (*f*) Logarithmic HXR flux at 50 keV vs. the corresponding magnetic field strength for E-FP (*diamonds*) and W-FP (*plus signs*). A general linear correlation is found for each FP, which translates to an exponential dependence of the HXR flux on the field strength. (*g*) Same as (*f*) but for the average values. (*h*) W-to-E HXR flux ratio vs. E-to-W magnetic field ratio of the two FPs as shown in Fig. 5.8*c*. A positive correlation is present only in the early stage of the flare [from Liu, W. et al. 2008a].

(1995) that this type of flare with progressive spectral hardening tends to be associated with SEP events (also see Saldanha et al., 2008). As we also noted, strong gamma-ray line emission was detected during this flare (Hurford et al., 2006), which indicates a significantly large population of accelerated protons at the Sun, but the relation to the SEPs at 1 AU is unclear.

5.4.2 Spatial Correlations

We now switch from the spectral characteristics of the two FPs to their spatial evolution. In §5.3 we focused on their relative motion, while here we examine their individual motions.

Figure 5.7*f* shows the perpendicular distance of each FP from the north-south neutral line (*dashed*, Fig. 5.7*a*) as a function of time. Linear fits of the full flare duration indicate mean velocities of $\langle v_\perp \rangle = 36 \pm 1$ and $13 \pm 1\,\mathrm{km\ s^{-1}}$ for E- and W-FP, respectively. These velocities are similar to those found by Xu et al. (2004) for white-light ribbons and by Krucker et al. (2005) for HXR FPs in this event. We also calculated the total velocities of the FP centroids i.e., $v = (v_\perp^2 + v_\parallel^2)^{1/2}$, where $v_\perp$ and $v_\parallel$ are the components perpendicular and parallel to the neutral line, respectively. The two resulting velocities have a linear temporal correlation at a 5σ level (see Table 5.1), which again provides evidence of the causal connection between the two conjugate FPs. However, the individual component, $v_\perp$ or $v_\parallel$, alone does not exhibit any noticeable correlation between the two FPs.

Figure 5.7*c* shows the distances from the LT centroid to the centroids of E-FP (l_1, *diamonds*) and W-FP (l_2, *crosses*) along the model semi-circular loop (see Fig. 5.7*a* and text in §5.3) as a function of time. Each curve follows the same general increase as the corresponding distance from the neutral line shown in Figure 5.7*f*.[7] We estimated the coronal column densities from the LT source to the transition region at the two FPs (see Appendix B.3 for details), $N_{\mathrm{tr},i} = 0.5 n_{\mathrm{LT}}(l_i - r)$, (where i=1, 2), using the distances l_1 and l_2 and the LT density n_{LT} and equivalent radius r obtained in §5.2.2 (Fig. 5.5). The results in Figure 5.8*e* show that there is a large relative difference from 20:44 to 20:48 UT during HXR Peak 1 but a smaller difference during Peak 2. Implications of these different column densities will be addressed in §5.5.2 and §5.5.3.

5.4.3 Magnetic Field Correlation

The magnetic field strengths of the two FPs were obtained from *SOHO* MDI magnetograms (e.g., see Fig. 5.6*a*) through the following steps: (1) We first selected a preflare[8] magnetogram at 08:30:35 UT and coaligned it with the *RHESSI* pointing and field of view (see Appendix B.1 for details). (2) For each time interval, the 90% brightness contour of each

[7] We note that the lines in Fig. 5.7*f* cross each other at ∼20:48 UT with that of E-FP increasing faster, while the lines in Fig. 5.7*c* increase at about the same rate with that of W-FP always being larger (apart from only one time interval). This is because the distances plotted in Fig. 5.7*f* are measured on the sky plane, while the distances in Fig. 5.7*c* are evaluated along the semi-circle in 3D space, which corrects for projection effects. Since the flare occurred in the western hemisphere, the distance of W-FP to the neutral line is a more significant underestimate of its true 3D distance to the LT than that of E-FP.

[8] Note that magnetograms during the flare cannot be used because measurements of magnetic fields in the flare kernels are not reliable (see Appendix B.1). However, photospheric magnetic fields usually show minimal changes or virtually no changes at all before and after a flare. This justifies our approach of using the preflare field to approximate the field during the flare.

RHESSI FP source was rotated back to the corresponding position at the time of the MDI map to account for the solar rotation. Then the MDI pixels enclosed in this contour were averaged to give a value of the magnetic field for this FP. (3) The above two steps were repeated for each of the ten MDI magnetograms recorded between 20:25 and 20:35 UT at a one minute cadence (excluding the one at 20:28 UT that are contaminated by artificial pixel spikes). The average of the ten independent measurements is used as the final result for the magnetic field (Fig. 5.8*b*) and the standard deviation gives the plotted uncertainty, which is on the order of a few percent, comparable to the nominal MDI noise of 20 G (Scherrer et al., 1995).

Figure 5.8*b* shows the history of the resulting magnetic field strengths. The field strength of W-FP generally decreases with time, while that of E-FP fluctuates about its mean value. Most of the time (especially before t_3=20:51 UT), the W-FP field (positive polarity) is stronger than the E-FP field (negative polarity), while their fractional difference generally decreases as time proceeds. The temporal variations of the two field strengths are only weakly correlated (again, particularly before t_3) at the 3σ level (see Table 5.1), as can also be seen in Figure 5.9*e*.

5.4.4 Inter-correlations Among Spectral, Spatial, and Magnetic Field Parameters

We are now ready to examine the relationship between the HXR fluxes and the magnetic fields of the two conjugate FPs. We plot the logarithmic HXR flux vs. the magnetic field strength for each FP in Figure 5.9*f*. As we can see here and noted before, E-FP (*diamonds*) has a larger flux and a weaker magnetic field, while W-FP (*plus signs*) has a smaller flux and a stronger magnetic field. In addition, the flux is correlated with the field strength for each FP (see Table 5.1 for the correlation coefficients and linear regressions). The logarithmic average flux ($\bar{I}$) and magnetic field ($\bar{B}$) of the two FPs are shown one vs. the other in Figure 5.9*g*. A linear relationship, as shown by the thick dashed line with a correlation coefficient of $r_p = 0.77\pm0.13$, is clearly present. In other words, $\bar{I}$ is exponentially (*nonlinearly*) correlated with $\bar{B}$, the expression of which is listed in Table 5.1. We also plot the average spectral index ($\bar{\gamma}$) vs. $\bar{B}$ in Figure 5.9*d*. Since $\bar{I}$ is correlated with $\bar{B}$, the "soft-hard-soft" type of relationship between $\bar{\gamma}$ and $\bar{I}$ translates to that between $\bar{\gamma}$ and $\bar{B}$. Namely, $\bar{\gamma}$ is anti-correlated with $\bar{B}$ during the early phase of the flare (before t_3=20:51 UT).

We now check the relationship of the spatial evolution and magnetic field variation of the two FPs. As noted in §5.4.2, E-FP moves faster than W-FP away from (perpendicular to) the magnetic neutral line. We also note that, (1) $B\langle v_\perp\rangle$ is proportional to the magnetic reconnection rate, and (2) E-FP (W-FP) is located in a weaker (stronger) magnetic field. This anti-correlation of the velocity and magnetic field strength means that, as expected, about the same amount of magnetic flux is annihilated from each side of the neutral line. However, the magnetic fluxes swept by the two FPs, $\int B\langle v_\perp\rangle dt$ integrated over the full flare duration, differ by 44% of their average value. This is not expected, but Fletcher & Hudson (2001) also reported such unbalanced magnetic fluxes for the 2000 July 14 flare. One explanation could be that the flare ribbons, which, when taken as a whole, may yield balanced fluxes, whereas the HXR FPs, which cover only parts of the ribbons, do not.

There are interesting relationships between the HXR FP positions and the magnetic

topology. The trajectory of E-FP is located in or next to a narrow channel of a strong negative magnetic field (see Fig. 5.6*a*), and its early portions are next to the three small sunspots just east of the neutral line (Fig. 5.6*c*). Meanwhile, W-FP runs through the umbra of a large sunspot where there is a strong positive magnetic field. Liu et al. (2007) found that these two HXR FPs were *adjacent* to two patches of positive current helicity that disappeared after the flare. It is also possible that the FPs were located at the *edges* of strong vertical currents, similar to the situation found by Canfield et al. (1993). In particularly, for E-FP alone, McTiernan et al. (2004) found that it moved along a morphological separatrix, based on a force-free extrapolation of the Mees vector magnetograms.

5.4.5 Implications of Various Correlations

The correlation (Fig. 5.9*g*) between the average HXR flux ($\bar{I}$) and the average magnetic field ($\bar{B}$) reveals important information about the magnetic reconnection and particle acceleration processes. Here we suggest two alternative interpretations that are consistent with the observations.

1. The *nonlinear* (exponential) nature of the $\bar{I}$-$\bar{B}$ correlation indicates that particle acceleration is very sensitive to the magnetic field strength. In the stochastic acceleration model of Petrosian & Liu (2004), this can be interpreted from the following aspects: (1) The level of turbulence is proportional to δB^2 (where δB is the magnetic field amplitude of plasma waves), which is proportional to the wave energy density and determines the number of the accelerated electrons. When the magnetic field strength B increases, δB is likely to increase as well and so does the flux of accelerated electrons. (2) The acceleration rate is proportional to $B(\delta B/B)^2$, which determines the spectral hardness of the electron distribution. When B increases, if $\delta B/B$ remains constant or even decreases but at a lower rate, the acceleration rate will increase and result in a harder electron spectrum. (3) In addition, the model predicts that the relative efficiency of acceleration of electrons, and thus their spectral hardness increase with decreasing values of the ratio of electron plasma frequency to gyrofrequency, $\alpha \equiv \omega_{pe}/\Omega_e \propto 1/B$. These theoretical arguments are qualitatively consistent with the observations that the magnetic field strength is correlated with the HXR flux and anti-correlated with the spectral index. Here we have assumed that the photospheric magnetic field strengths measured at the FPs are scaled with the field strength in the coronal reconnection region, measurements of which are difficult and unavailable.

2. Alternatively, noting that the velocities ($v_\perp$) of the two FPs perpendicular to the magnetic neutral line remain roughly constant during the flare (see Fig. 5.7*f*), the correlation between the average HXR flux and magnetic field strength simply translates into the correlation between the HXR production rate and the magnetic flux annihilation rate or reconnection rate, $Bv_\perp$. Furthermore, since $Bv_\perp$ is believed to be proportional to the electric field in the reconnection region (Forbes & Lin, 2000), it then follows that the particle acceleration rate correlates with the electric field. According to the DC electric field acceleration model (Holman, 1985; Benka & Holman, 1994), a larger electric field results in a larger high-energy cutoff ($E_{\max}$) for the electron spectrum. A higher value of $E_{\max}$ lead to a harder HXR spectrum below $E_{\max}$, if $E_{\max}$ is within one or two orders of magnitude at the observed photon energies (Holman, 2003). Therefore, the observed anti-correlation

between the magnetic field strength and spectral index may also be explained by the electric field acceleration mechanism, provided that $E_{\max}$ is not far above the energy range for fitting the photon spectrum. Note that Krucker et al. (2005) studied the motion of E-FP *alone* in this flare and found a rough temporal correlation between the HXR flux and reconnection rate, characterized by the product of Bv or B^2v, where v includes the velocity both perpendicular and parallel to the neutral line.

5.5 HXR Footpoint Asymmetries

As mentioned above and partly noted by Liu, W. et al. (2004b), Xu et al. (2004), and Krucker et al. (2005), the two conjugate FPs exhibit the following asymmetric characteristics: (1) the *brighter* E-FP is located in a *weaker*, negative magnetic field, while the *dimmer* W-FP is located in a *stronger*, positive field; (2) the two FPs have very similar spectral shapes with E-FP being slightly harder; (3) E-FP is located *closer* to the LT than W-FP; (4) E-FP moves *faster* away from the magnetic neutral line than W-F. These asymmetries are summarized in Table 5.2.

Table 5.2: Asymmetric characteristics of the conjugate footpoints (E-FP and W-FP): mean, median, and their E-to-W ratio of various quantities.

	Mean			Median		
	E	W	E/W	E	W	E/W
I	13.7	6.1	2.2	8.9	4.6	1.9
B	520	960	0.55	520	1010	0.51
γ	3.63	3.79	0.96	3.4	3.5	0.96
l	41	60	0.69	38	60	0.64
$N_{\rm tr}$	1.2	2.1	0.60	1.2	2.5	0.50
$v_\perp$	36	13	2.8	—	—	—

I (photons $\rm s^{-1}$ $\rm cm^{-2}$ $\rm keV^{-1}$): HXR flux at 50 keV;
B (Gauss): magnetic field strength;
γ: spectral index between 50 and 150 keV;
l (arcsecs): distance from the LT centroid to the FP centroid along the semi-circular loop;
$N_{\rm tr}$ ($10^{20}\,\rm cm^{-2}$): coronal column density from the edge of the LT source to the transition region at the FP.
$v_\perp$ ($\rm km\ s^{-1}$) : velocity perpendicular to the neutral line;
The mean spectral indexes are the averages of the results of the first six long integration intervals before 20:52:40 (see §5.4.1), while all the other values listed here are from the results of the 57 short intervals throughout the flare.

We explore in this section different possibilities that can cause such asymmetries, particularly the asymmetric HXR fluxes and spectra. Various physical processes can contribute and they fall into two categories according to their origins: (1) asymmetry during particle acceleration, and (2) asymmetry arising from particle transport. The second category includes effects of magnetic mirroring and column density, which will be examined in what follows together with other transport effects (§5.5.1–5.5.4). The first category was historically thought to be less likely and will be discussed later in §5.5.5. We use both the flux ratio $R_I \equiv I_2/I_1$ and the asymmetry (c.f., Aschwanden et al., 1999) defined by Alexander

& Metcalf (2002):

$$A \equiv (I_1 - I_2)/(I_1 + I_2) = (1 - R_I)/(1 + R_I), \tag{5.1}$$

to quantify the asymmetric HXR fluxes, with $A = \pm 1$ being 100% asymmetry and $A = 0$ being perfect symmetry.

5.5.1 Magnetic Mirroring

Asymmetric magnetic mirroring is commonly cited to explain asymmetric HXR fluxes observed at conjugate FPs. We examine to what extent mirroring alone can explain the observations of this flare. For simplicity, we make the following assumptions for our analysis below: (1) Disregard all non-adiabatic effects of particle transport, i.e., energy losses and pitch-angle diffusion due to Coulomb collisions. By this assumption, the magnetic moment of a particle is conserved and mirroring is the only effect that changes the pitch angle when the particle travels in the loop and outside the acceleration region. (2) Assume an isotropic pitch-angle distribution of the electrons at all energies upon release from the acceleration region. (3) Disregard details of bremsstrahlung, and assume that the nonthermal HXR flux is proportional to the precipitating electron flux at the FP.[9]

The loss-cone angle for magnetic mirroring is given as

$$\theta_i = \arcsin \sqrt{B_0/B_i} \tag{5.2}$$

where i=1 for E-FP and 2 for W-FP, B_0 is the magnetic field strength at the injection site in the corona where particles escape from the acceleration region, and B_i is the field strength at the ith FP in the chromosphere. By the isotropy assumption, the fractional flux of the forward moving electrons that will *directly* precipitate to the chromosphere (whose pitch angle is located inside the loss cone) can be evaluated by integrating over the solid angle (also see, Alexander & Metcalf, 2002):

$$F_i = \frac{1}{2\pi} \int d\Omega = \frac{1}{2\pi} \int_0^{2\pi} d\phi \int_0^{\theta_i} \sin\theta d\theta = 1 - \mu_i \,, \tag{5.3}$$

where the pitch-angle cosine is $\mu_i = \cos\theta_i = (1 - B_0/B_i)^{1/2}$. If there is strong mirroring, i.e., $B_0 \ll B_i$, we have $\mu_i \simeq 1 - B_0/(2B_i)$, and if there is no mirroring, i.e., $B_0 = B_i$, we have $\mu_i = 1$. By our assumptions (1) and (3) above, such a fraction should be independent of electron energy and is proportional to the HXR flux I_i at the corresponding FP. It then follows that

$$R_I \equiv \frac{I_2}{I_1} = \frac{F_2}{F_1} = \frac{1-\mu_2}{1-\mu_1} \simeq \begin{cases} \frac{B_1}{B_2} \equiv R_B^{-1}, & \text{if } B_0 \ll B_i,\ (i = 1,\ 2), \\ \frac{B_1}{2B_2} \equiv R_B^{-1}/2, & \text{if } B_0 = B_1,\ B_0 \ll B_2, \end{cases} \tag{5.4}$$

the second case of which corresponds to the possibility that mirroring occurs only at one FP, but the required condition $B_1 \ll B_2$ does not apply to this flare. In either case, the HXR flux ratio should be correlated with the inverse of the magnetic field ratio, R_B^{-1}. This result is consistent with that of the strong diffusion case obtained by Melrose & White (1981).

[9] This flux includes the precipitation of electrons previously reflected by mirroring back to the acceleration region at the LT where they may be scattered and/or re-accelerated, presumably by turbulence.

As shown in Table 5.2, the mean/median HXR flux of E-FP is about twice that of W-FP, while the mean/median magnetic field strength of E-FP is about a factor of two smaller. This is consistent with the mirroring effect in the average sense of the whole flare duration. We can further see if this relationship also holds at different times. Figure 5.8*c* shows the W-to-E ratio ($R_I = I_2/I_1$) of the HXR fluxes and the E-to-W ratio ($R_B^{-1} = B_1/B_2$) of the field strengths of the two FPs as a function of time. We find a temporal correlation between the two ratios during the first ∼3 minutes when both first decrease and then increase. In the middle stage (20:43–20:51 UT) of the flare, both ratios remain roughly constant with marginal fluctuations and similar mean values of $\langle R_I \rangle = 0.43$ and $\langle R_B^{-1} \rangle = 0.50$. After 20:51 UT, the magnetic field ratio increases significantly with large fluctuations and exceeds unity in 6 of the 57 time intervals, while the flux ratio remains at about the same level as before. The same temporal evolution can also be seen in Figure 5.9*h* where the flux ratio is plotted against the magnetic field ratio. The behavior of the two ratios before 20:51 UT is expected from magnetic mirroring, but their significant difference after 20:51 UT cannot be explained by mirroring alone.

5.5.2 Column Density

Another transport effect that can cause asymmetric HXR FPs is different coronal column densities experienced by electrons in traveling from the acceleration region to the transition region at the two FPs (Emslie et al. 2003; Liu, W. 2006). The effective column density is $N_{\rm tr,\,eff} = N_{\rm tr}/\langle\mu\rangle$, where $\langle\mu\rangle$ is the average pitch angle cosine, and $N_{\rm tr} = \int_0^{s_{\rm tr}} n(s)ds$ is the coronal column density to the transition region at distance $s = s_{\rm tr}$ along the magnetic field line with $n(s)$ being the ambient electron number density. A difference in $\langle\mu\rangle$, $s_{\rm tr}$, and/or $n(s)$ between the two legs of the flare loop can lead to different effective column densities. (1) Different pitch-angle distributions can be caused by asymmetric magnetic mirroring and/or asymmetric acceleration. (2) Different path lengths $s_{\rm tr}$ can be caused by a magnetic reconnection site located away from the middle of the loop (Falewicz & Siarkowski, 2007). (3) Different densities $n(s)$ can also occur because magnetic reconnection takes place between field lines that are previously not connected and their associated densities are not necessarily the same. It takes time (on the order of the sound travel time, $\gtrsim$ tens of seconds) for the newly reconnected loop to reach a density equilibrium, but the observed HXRs could be produced before then.

Column density asymmetry affects the FP asymmetry in two ways, since both energy losses and pitch-angle scattering due to Coulomb collisions take place at about the same rate that is proportional to the column density: (1) Column density asymmetry is related to energy losses, bremsstrahlung, and the way we calculate the FP photon flux in §5.2.2 (integrating HXR photons primarily produced below the transition region). Electrons with an initial energy of E are stopped after traveling through a column density $N_{\rm stop}(\,{\rm cm}^{-2})/\approx 10^{17}[E(\,{\rm keV})]^2$. If $N_{\rm stop}$ is smaller than or comparable to the column density to the transition region ($N_{\rm tr}$), in one half of the loop with a *larger* column density, there are *more* electrons stopped in the leg and thus less electrons reaching the transition region. This results in *more* HXRs produced in the leg and less HXRs beneath the transition region (counted as the FP flux), since bremsstrahlung is proportional to both column density and electron flux. (2) Different Coulomb scattering rates result from different column densities on the two sides

of the loop, which can cause different pitch-angle distributions, even if the particles are injected with symmetrical pitch angles from the acceleration region.

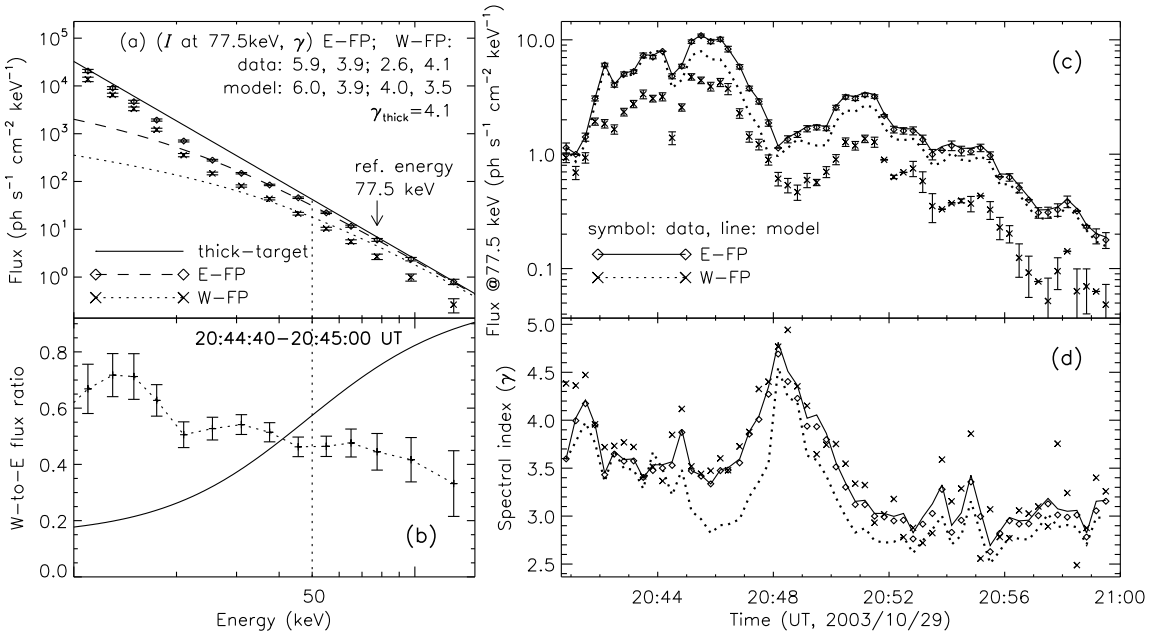

Figure 5.10: Effects of asymmetric coronal column densities. (*a*) Photon fluxes of E-FP (*diamonds*) and W-FP (*crosses*) vs. energy at 20:44:40–20:45:00 UT (same as Fig. 5.4*a*), superimposed with model fluxes (*lines*) evaluated below the transition region based on asymmetric coronal column densities using eq. (5.5). The solid line shows the power-law thick-target flux with an index of $\gamma_{\rm thick} = 4.1$. The legend shows the fluxes (I) at a reference energy of 77.5 keV (selected at the center of the middle energy bin above 50 keV) and the spectral indexes (γ) above 50 keV of the two FPs for both the data (from power-law fits to the 50–150 keV count rates) and model. (*b*) Ratio of the W-to-E FP fluxes shown in (*a*), with the plus signs and solid line from the data and model (given by eq. [B.5]), respectively. (*c*) Observed (*symbols*) and modeled (*lines*) fluxes of E- and W-FP at 77.5 keV vs. time (cf. Fig. 5.8*a* at 50 keV). (*d*) Same as (*c*) but for the spectral indexes above 50 keV. The data are the same as in Fig. 5.8*d* but plotted without error bars for clarity [from Liu, W. et al. 2008a].

Focusing on the energy dependence of FP HXR asymmetry, we present below an estimate of the column density effect *alone*, while assuming no magnetic mirroring and identical pitch-angle distributions (same $\langle\mu\rangle$) in the two loop legs. The relevant formulisms are derived in Appendix B.2. We assumed that identical power-law electron fluxes with a spectral index δ and the same pitch-angle distribution are injected into the two legs of the flare loop, which have the same ambient density but different path lengths $s_{\rm tr}$ to the FPs. Our goal is to examine if this scenario can yield photon fluxes and spectra consistent with observations for both FPs. For each of the 57 time intervals shown in Figure 5.8, we first used the E-FP column density N_{tr} (see §5.4.2 and Fig. 5.8*e*) from the edge of the LT source (assumed to be the acceleration region) to obtain its dimensionless form $\tau_{\rm tr} = N_{tr}/(5 \times 10^{22}\,{\rm cm}^{-2})$, which

ranges from 5×10^{-4} to 1×10^{-2}. We then substituted $\tau_{\rm tr}$ into

$$I_{\rm FP}(\tau_{\rm tr}, k) = A_0 k^{-(\delta-1)} \left(1 + \tau_{\rm tr} \frac{k+1}{0.37k^2}\right)^{1-\delta/2}, \tag{5.5}$$

rewritten from equation (B.4), where A_0 is the normalization for the thick-target flux and k is the photon energy in units of the rest electron energy 511 keV. With this equation, we fitted the E-FP spectrum above 50 keV in a least-squares sense by iteratively adjusting the free parameters A_0 and δ. Using the resulting A_0 and δ and W-FP's $\tau_{\rm tr}$, we then calculated the W-FP spectrum by equation (5.5) and the W-to-E flux ratio by equation (B.5).

Figure 5.10*a* shows an example of the spectra of the two FPs and their model predictions, together with the corresponding thick-target spectrum produced by the same power-law electron flux. We only trust the observed FP spectra > 50keV, as noted earlier, due to pulse pileup. As expected, the model FP fluxes are reduced from the thick-target flux, especially at low energies, because low-energy electrons are more susceptible to collisional energy loss and pitch-angle scattering. This results in a spectral flattening (hardening)[10] in the FP X-ray spectrum. Because of its larger column density, the W-FP's model spectrum exhibits more flux reduction at a given energy and a flattening to a higher energy. Above 50 keV the model spectrum of the brighter E-FP fits the data very well. However, that of the dimmer W-FP does not fit the data at all, since the model flux is much greater (e.g., at 77.5 keV $I = 4.0$ vs. 2.6 photons s^{-1} cm^{-2} keV^{-1}) and harder ($\gamma = 3.5$ vs. 4.1) than the observed flux, and even harder than the E-FP flux ($\gamma = 3.5$ vs. 3.9). This can be best seen in Figure 5.10*b* that shows the data (*plus signs*) and model (*solid line*) ratios of the W-to-E FP flux. The data ratio generally decreases with energy or stays roughly constant above 50keV within uncertainties, but the model ratio is an increasing function of energy. These trends generally hold throughout the flare as can be seen from the history of HXR fluxes and spectral indexes shown in Figures 5.10*c* and 5.10*d*.

In summary, the model predicts a much harder photon spectrum for the dimmer W-FP with the larger coronal column density, while according to the observations the dimmer W-FP is as hard as or slightly softer than the brighter E-FP (see Fig. 5.10*d*). Saint-Hilaire et al. (2008) reported similar results that the majority of the brighter FPs in their 172 pairs of FPs tend to have harder spectra. In addition, the differences between the model HXR fluxes of the two FPs are too small to explain the observations (Fig. 5.10*c*). One may attempt to increase the difference between the column densities in order to increase the flux difference and thus to merge this gap between the model and data, but the discrepancy of the spectral indexes would be worse since the W-FP spectrum would be relatively even harder. Therefore, we conclude that the column density effect alone cannot provide a self-consistent explanation for the asymmetric HXR FPs observed here.

Our conclusion is different from that drawn by Falewicz & Siarkowski (2007), who found in three flares that the HXR flux ratios of asymmetric FPs were consistent (within a factor of 2) with the predictions from asymmetric column densities. While the column density scenario may apply to those flares, we should note the following facts that can lead to different conclusions, because their observations set less stringent constraints than our

[10]This FP spectral flattening should not be confused with the flattening of the spatially integrated spectra found by Sui et al. (2007).

RHESSI observations: (1) The analyses of Falewicz & Siarkowski (2007) were limited to images made by *Yohkoh* HXT *Yohkoh* in the M1 (23–33 keV) and M2 (33–55 keV) bands, while our observations cover a higher and wider energy range from 50 to 150 keV. The column density effect is more pronounced in the M1 and M2 bands than at higher energies (see Fig. 5.10*a*). Moreover, M1 images could be contaminated by thermal emission that can mislead their prediction based on a nonthermal bremsstrahlung model. (2) They did not obtain the model spectra of the FPs and compare them with the observations, as we did with multiple energy bins. This was enabled by *RHESSI*'s ∼1 keV resolution in the energy range of 3 to a few hundred keV, as opposed to HXT's four broad energy bands in the 14–93 keV range.

5.5.3 Magnetic Mirroring and Column Density Combined

We have seen from the above discussions that each of the two transport effects *alone* can only explain to some extent the observed FP asymmetries: (1) Asymmetric magnetic mirroring is consistent with the asymmetric HXR fluxes in the average sense of the flare duration, but it has difficulties in accounting for the flux asymmetry later in the flare. (2) Asymmetric column densities in the two legs of the flare loop are qualitatively consistent with the asymmetric HXR fluxes, but their quantitative predictions of fluxes and spectral hardness contradict the observations. These two transport effects, in reality, operate at the *same time*, because electrons experience Coulomb collisions while being mirrored back and forth in the loop, and thus the collisionless (adiabatic) assumption that we adopted earlier for simplicity for magnetic mirroring needs to be dropped. In particular, since W-FP has stronger mirroring (than E-FP), the average pitch angle of electrons impinging there is larger, and thus the effective column density $N_{\rm tr,\,eff} = N_{\rm tr}/\langle\mu\rangle$ is greater than previously thought. This can enhance the column density asymmetry. In what follows, we attempt to provide an explanation for some aspects of the observations by combining the two effects.

From the above discussion and the observations presented earlier (see §5.4), we should pay attention to the distinction between the two HXR peaks: As shown in Figure 5.8*c*, during Peak 1 (before t_2=20:48 UT) the FP HXR flux asymmetry seems to be mainly controlled by magnetic mirroring, because of the temporal correlation between the HXR flux ratio and the inverted magnetic field ratio. During Peak 2 (after t_2) magnetic mirroring seemingly fails to control the asymmetry because the correlation gradually disappears, especially after the HXR maximum at t_3=20:51 UT. A viable explanation for the two-peak distinction is that (1) at early times, the density (Fig. 5.5*d*) and length (Fig. 5.7*c*) of the loop are small, resulting in small coronal column densities (Fig. 5.8*e*) from the acceleration site to the FPs. Energy losses and pitch-angle scattering due to Coulomb collisions are less important, and therefore the rates of electron precipitation to the FPs are mainly governed by mirroring. (2) Later in the flare, as the density and loop length have increased considerably, the column densities become larger and the collisional effects become more important than before in shaping the observed FP flux asymmetry. In addition, since magnetic mirroring depends on the gradient $d\ln B/dN$ (e.g., Leach & Petrosian, 1981), this effect becomes less important when the column density N increases faster than the relative change of magnetic field from the LT to the FP, which is possibly the case later in the flare. Therefore, at later times, the prediction of magnetic mirroring alone tends to deviate from the data, which might be

explained by the two transport effects combined. Unfortunately, we cannot offer a quantitative prediction about the outcome of the combination without detailed modeling, which is briefly discussed in §5.6 as future work.

There are several coincidences with the two-peak division which seem to have causal connections: (1) As noted in §5.4.1, the correlation between the HXR fluxes and spectral indexes (Figs. 5.8*a* and 5.8*d*) can be described as common "soft-hard-soft" during Peak 1 and as "soft-hard-hard" during Peak 2. The spectral hardening at later times may be associated with the increase of the column density in the loop (Fig. 5.8*e*), due to collision-caused hardening mentioned above (§5.5.2). (2) During Peak 1, the magnetic fields at the two FPs correlate with each other (Fig. 5.8*b*), while this correlation becomes progressively vague during Peak 2, especially after its maximum t_3=20:51 UT, possibly because of longer loops. (3) The transition (t_2=20:48 UT) between the two HXR peaks coincides with the sudden jump in the positions of both FPs (Figs. 5.7*a* and 5.7*f*), the dip in the loop length (Fig. 5.7*c*), and the valley in the magnetic field strengths (Fig. 5.8*b*). This points to the start of the new episode of energy release of Peak 2, presumably associated with a new series of loops that have physical conditions different from those in Peak 1. This transition may be related to the different behaviors of magnetic mirroring during the two peaks noted above.

5.5.4 Other Transport Effects and FP Asymmetries

Here we briefly discuss transport effects other than magnetic mirroring and column density that can contribute to the observed HXR flux and spectral asymmetries. Some of these effects compete with one another, which may explain why the spectral index difference is so small ($\langle\gamma_2\rangle - \langle\gamma_1\rangle = 0.15 \pm 0.13$).

1. **Non-uniform target ionization** along the path of high-energy electrons was ignored in the above analysis as we assumed fully ionized plasma in the background. However, in the 10^4–10^5 K chromosphere and transition region, the material is only partially ionized. The presence of neutral atoms reduces the rates of long-range collisional energy losses and pitch-angle scattering and thus increases the bremsstrahlung efficiency (Brown, 1973b; Leach & Petrosian, 1981; Kontar et al., 2002). For a power-law electron flux injected to a model of targets varying from fully ionized in the corona to neutral in the chromosphere, the high energy HXR flux can be elevated by a factor of 2.8 from that with fully ionized targets (Brown, 1973b). The photon spectral index has the usual relationship $\gamma = \delta - 1$ at low ($\lesssim$10–20 keV) and high ($\gtrsim$100–200 keV) energies, but in the intermediate energy range the index is smaller (flatter) by as much as $\sim$0.5. The energy E_* at the downward knee of the spectral hardness transition depends on the column density to the transition region, with $E_* \propto (N_{\rm tr})^{1/2}$ (Kontar et al., 2002). For the flare under study, electrons can penetrate deeper into the chromosphere and thus encounter more neutral atoms at the E-FP with weaker magnetic mirroring, while stronger mirroring at W-FP stops more electrons in the fully ionized corona. Equivalently, as we mentioned before, the effective column density to the transition region $N_{\rm tr,\,eff}$ and thus E_* are larger at W-FP because of larger average pitch angles. This results in a higher HXR flux and harder spectrum in the 50–150 keV range at E-FP than at W-FP, which qualitatively agrees with the observations.

2. **Relativistic beaming and photospheric albedo** associated with different pitch-angle distributions also play a role. At E-FP with weaker mirroring, the angular distribution of electrons are more concentrated to the forward direction down to the photosphere than at W-FP. The forward relativistic beaming effect of radiation is an increasing function of electron and thus photon energy. While the FPs are seen on the solar disk from above, we therefore expect to observe less high-energy photons emitted upward at E-FP (McTiernan & Petrosian, 1991), which would result in a softer spectrum there. In the meantime, since more photons are (beamed) emitted downward at E-FP, photospheric albedo or Compton back-scattering (Langer & Petrosian, 1977; Bai & Ramaty, 1978) is stronger there than at W-FP. Because the effect of albedo is basically moving photons from high to low energies, stronger albedo also leads to a softer spectrum at E-FP. Relativistic beaming and albedo are pronounced mainly at relativistic ($\gtrsim$MeV) and low ($\lesssim$40 keV) energies, respectively, but they may have residual effects in the 50–150 keV range. The spectral softening of these two effects competes with the hardening caused by other effects mentioned above (column densities and non-uniformly ionized targets), which may eventually lead to the observed similar spectral indexes of the two FPs.

3. **Return currents** are another possible origin of FP HXR asymmetry. The electric field associated with the return current decreases the energy of the downward-streaming electrons, with the major impact being on the lower-energy electrons (Zharkova & Gordovskyy, 2006). The result is a low-energy cutoff in the electron distribution, qualitatively similar to that produced by Coulomb collisions. Different precipitating electron beam fluxes in the two legs of the flare loop will induce different return current densities and associated electric field strengths, and thus result in different HXR fluxes and spectral shapes at the two FPs. However, asymmetric magnetic mirroring may or may not cause different electron beam fluxes, because the larger total number of precipitating electrons at the brighter E-FP with the weaker magnetic field may be canceled out by the larger cross-sectional area of that leg (due to conservation of the magnetic flux). Without an accurate measurement of the loop cross-sections, it is difficult to assess the effects of return currents on the FP HXR asymmetries in this flare.

5.5.5 Acceleration-induced Asymmetry

We address here the first category of explanations for FP HXR flux asymmetry that is related to intrinsic asymmetry or anisotropy arising from the particle acceleration process.

1. Acceleration-produced intrinsic anisotropy and its energy dependence are influenced by the following factors: (1) In the HXR producing energy range, ten to several hundred keV, the rate of scattering of electrons by *turbulence or plasma waves* increases with energy (see Fig. 11 in Petrosian & Liu, 2004). (2) On the other hand, as mentioned earlier, the pitch-angle scattering rate due to *Coulomb collisions* is a decreasing function of the electron energy. If we assume that the acceleration process produces some initial anisotropy (e.g., the pancake shaped pitch-angle distributions found by Minoshima et al., 2008) at all energies, a combination of these two effects will result in electrons at intermediate energies being better able to preserve their initial anisotropy, while higher and lower energy electrons are isotropized by waves and Coulomb collisions, respectively.

If we further neglect other asymmetry-causing effects, and if the initial anisotropy means

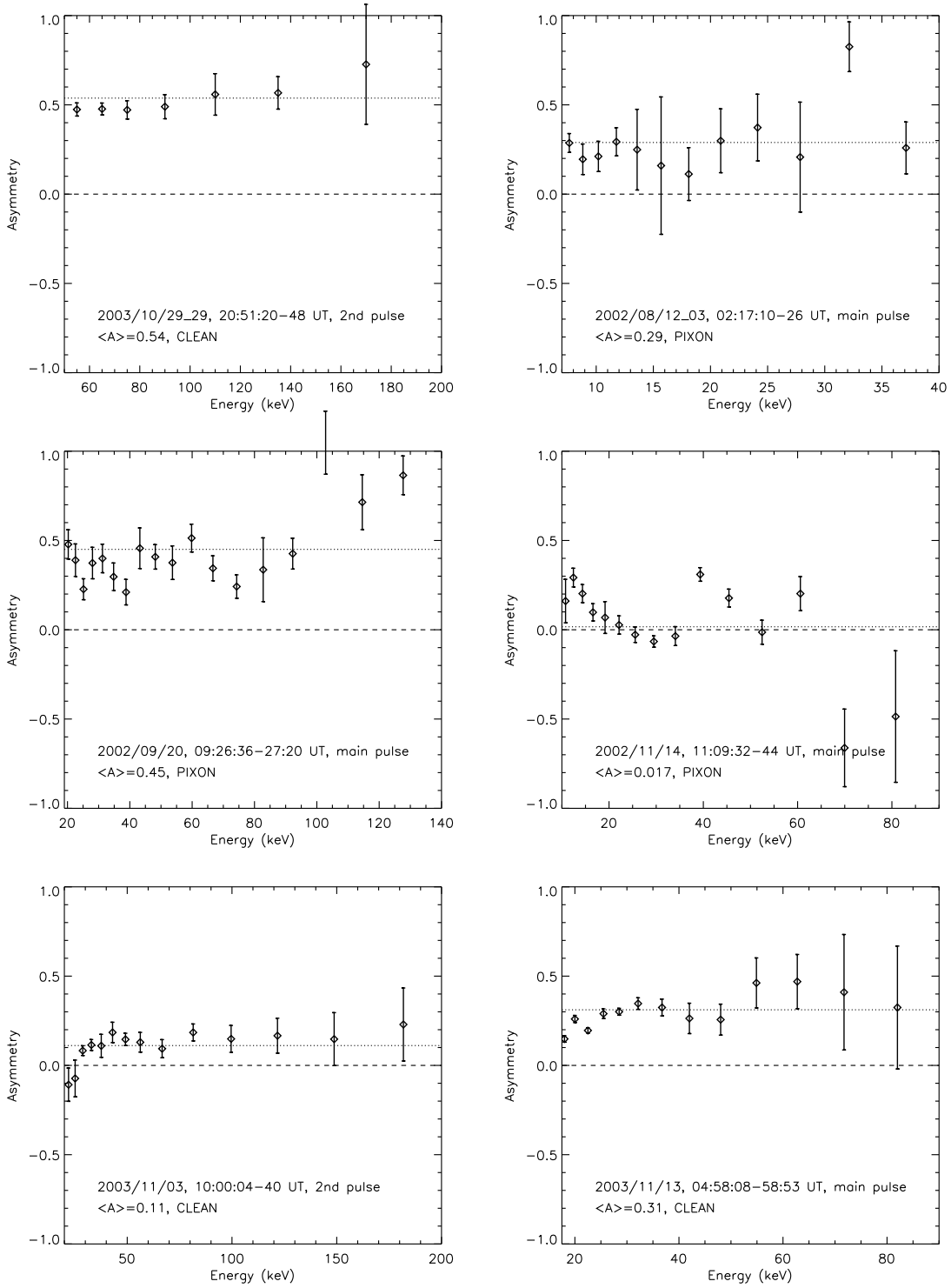

Figure 5.11: FP flux asymmetry vs. energy for the 2003-10-29 X10 flare (*top left*) and other events. The dotted line marks the mean value and the dashed line marks zero (perfect symmetry).

more electrons moving in *one* direction along the magnetic loop, the above outcome translates into a larger HXR flux asymmetry $|A|$ (see eq. [5.1]) at intermediate photon energies and a smaller asymmetry at higher and lower energies. This was found by Alexander & Metcalf (2002) in a flare whose maximum asymmetry $|A|_{\max}$ occurs in the energy range of 20–40 keV. McClements & Alexander (2005) attributed this to an asymmetric, energy-dependent injection in which more electrons are injected preferentially into one leg of the loop rather than into the other. Zharkova & Gordovskyy (2004) also found that in a reconnection current sheet the electric field can produce asymmetric electron and proton beams.

For the X10 flare under study here, however, it is difficult to check asymmetry in the low to intermediate energy range (below 50 keV) because of strong pileup effects as noted before. Above 50 keV, asymmetry either increases with energy (see the flux ratio in Fig. 5.4*b*) or remains constant, which is opposite to the decreasing asymmetry found by Alexander & Metcalf (2002) in this energy range. In addition, our initial analysis of several other flares of different *GOES* classes found no indication of a universal or general energy-dependent pattern of FP HXR flux asymmetry (see Fig. 5.11), which is consistent with that found by Aschwanden et al. (1999) from *Yohkoh* HXT *Yohkoh* data. Furthermore, in the stochastic acceleration model, it is difficult to realize in the turbulence region an asymmetric particle accelerator that can send significantly more particles to one side than to the other. Whether the scenario described above and proposed by McClements & Alexander (2005) is the rule or an exception remains an open question.

2. As one possible mechanism, *some* electrons might be accelerated locally by waves near/at the FPs, as suggested by Liu, W. et al. (2006) based on *RHESSI* observations and by Fletcher & Hudson (2008) based on theoretical arguments. On the one hand, this scenario could contribute to FP asymmetries in various ways; on the other hand, it has difficulties such as in accelerating particles in the dense chromosphere and in explaining the observed time-of-flight energy dependencies (Aschwanden et al., 1995).

5.6 Summary and Discussion

We have presented imaging and spectral analysis of the *RHESSI* observations of the 2003 October 29 X10 flare showing two conjugate HXR footpoints (FPs), which are well-defined during the bulk of the flare duration. One FP lies to the east (E-FP) and the other to the west (W-FP) of the north-south magnetic neutral line. This flare provides a unique opportunity to study in great detail the spatial, temporal, and spectral properties of the FPs and their associated magnetic fields. The impulsive phase was relatively long (∼20 minutes), HXR fluxes were detected by *RHESSI* at energies up to hundreds of keV, and it was located close to disk center, resulting in minimum projection effects and excellent magnetic field measurements from *SOHO* MDI. Our main findings regarding the unshearing motions, various correlations, and asymmetric characteristics of the two FPs are as follows.

1. **Two-phase unshearing motions** are present in the flare: In Phase I the two identified FPs become closer to each other as they rapidly move almost parallel to the magnetic neutral line. In Phase II the FPs move away from each other more slowly, mainly perpendicular to the neutral line (Fig. 5.7*a*). In other words, the shear angle θ between the normal to the neutral line and the line connecting the two FPs exhibits a fast and then slow decrease from 56° to 12° (Fig. 5.7*e*). This indicates that the newly reconnected magnetic

field lines are progressively less sheared (closer to a potential field), which is consistent with the results of Ji et al. (2008). In addition, the transition between the two phases of the FP motions coincides with the direction reversal of the apparent motion of the loop-top (LT) source along the neutral line (Fig. 5.7*d*, *dot-dashed*), and the minima of the estimated loop length (Fig. 5.7*c*, *solid line*) and LT height (Fig. 5.7*d*, *solid line*). This suggests that the *initial decrease* of the LT altitude observed in many other *RHESSI* flares (e.g., Sui & Holman, 2003; Sui et al., 2004; Liu, W. et al., 2004a, 2008b) may be associated with progressively shorter loops during the *fast unshearing* motion phase when the reconnection site propagates along the arcade. The subsequent increase of the LT altitude could be due to reconnection occurring in progressively longer and higher loops.

2. There are **correlations** among the temporal evolutions of various quantities (Table 5.1). Some of them exhibit distinct differences between the two HXR peaks (transition at 20:48 UT): (*a*) The HXR fluxes (Figs. 5.8*a* and 5.9*a*) and spectral indexes (Figs. 5.8*c* and 5.9*b*) of the two FPs are strongly correlated. This is strong evidence that the two HXR sources are from conjugate FPs at the two ends of the same magnetic loop. (*b*) The HXR flux and spectral index of each FP show a commonly observed "soft-hard-soft" evolution (Figs. 5.8*a*, 5.8*d*, and 5.9*c*) during HXR Peak 1, while during Peak 2 the spectrum becomes harder and stays hard even as the HXR flux decays. This event falls into the statistical category (Kiplinger, 1995) of the association of progressive flare spectral hardening with SEPs. (*c*) The magnetic field strengths at the two FPs also exhibit some temporal correlation (Figs. 5.8*b* and 5.9*e*) particularly during Peak 1. This is further evidence that the selected FPs are conjugate. (*d*) The FP HXR flux exponentially correlates with the magnetic field strength (Figs. 5.9*f* and 5.9*g*). There is also an anti-correlation between the average spectral index and magnetic field strength during Peak 1 (Fig. 5.9*d*). These correlations suggest that stronger magnetic fields, and/or larger reconnection rates or larger electric fields in the reconnection region are responsible for producing larger fluxes and harder spectra for the accelerated electrons and thus the resulting HXRs. This is in qualitative agreement with the predictions of the stochastic acceleration model (Petrosian & Liu, 2004) and the DC electric field acceleration model (Holman, 1985). In particular, the exponential nature of the correlation means that particle acceleration is very sensitive to the magnetic field strength, which is consistent with the prediction of the stochastic acceleration model that electrons are preferentially accelerated in strongly magnetized plasma.

3. Various **asymmetries** are observed between the conjugate FPs (Table 5.2): (*a*) On average, the eastern footpoint (E-FP) HXR flux is 2.2 times higher than that of the western footpoint (W-FP; Fig. 5.8*a*), while its magnetic field strength is 1.8 times weaker (520 G vs. 960 G; Fig. 5.8*b*). This is consistent with asymmetric magnetic mirroring that predicts a smaller HXR flux at the FP with the stronger magnetic field (§5.5.1). (*b*) Both FPs move away from the magnetic neutral line at roughly constant velocities, but the brighter E-FP moves 2.8 times faster in the weaker magnetic field than does the dimmer W-FP in the stronger field ($\langle v \rangle = 36 \pm 1$ vs $13 \pm 1\,\mathrm{km\,s^{-1}}$; Fig. 5.7*f*). This means that roughly equal amounts of magnetic fluxes from both polarities are being annihilated during reconnection. (*c*) The average estimated coronal column density from the edge of the LT source (assumed to be the acceleration region) to the transition region at E-FP is 1.7 times smaller than that of W-FP (1.2×10^{20} vs. $2.1 \times 10^{20}\,\mathrm{cm^{-2}}$; Fig. 5.8*e*). This qualitatively agrees with the HXR flux asymmetry, because a larger coronal column density results in

more HXRs produced in the loop legs and thus less HXRs emitted from the FP below the transition region, especially at low energies (Fig. 5.10; §5.5.2). (*d*) The photon spectra above 50 keV of the two FPs are almost parallel to each other (Fig. 5.4*a*), with the brighter E-FP being consistently slightly harder than the dimmer W-FP (Fig. 5.8*d*). Their mean index values $\langle\gamma_1\rangle = 3.63 \pm 0.06$ and $\langle\gamma_2\rangle = 3.79 \pm 0.11$ have a marginal difference of $\langle\gamma_2\rangle - \langle\gamma_1\rangle = 0.15 \pm 0.13$. In other words, the W-to-E ratio of the photon fluxes is a constant or a slightly decreasing function of energy. This contradicts the column density effect which would produce a much harder spectrum at the dimmer W-FP (Fig. 5.10). (*e*) As expected from asymmetric magnetic mirroring, there is a temporal correlation between the W-to-E HXR flux ratio and the E-to-W magnetic field ratio. However, this correlation only holds during HXR Peak 1 but gradually breaks down during Peak 2 (Figs. 5.8*c* and 5.9*h*). We suggest that a combination of the asymmetric magnetic mirroring and column density effects could explain this variation (§5.5.3). This is because as the column densities in the loop increase with time (Fig. 5.8*e*), collisions become more important, making the HXR flux ratio deviate from the prediction of mirroring alone. The increased column densities, possibly together with magnetic trapping, may also contribute to the observed spectral hardening later during the flare mentioned above. (*f*) Other *transport* effects including non-uniform target ionization, relativistic beaming, and photospheric albedo in the presence of different pitch-angle distributions caused by asymmetric mirroring, and/or return current losses, may also play a role in determining the relative HXR fluxes and spectral shapes of the conjugate FPs (§5.5.4). It is unclear whether there is observational evidence of asymmetry produced in the particle *acceleration* process (§5.5.5).

In our analysis we have treated the magnetic mirroring and column density effects separately in order to make the problem analytically tractable, yet without loss of the essential physics. However, in reality, the two effects are coupled and they should be studied together self-consistently to obtain a quantitative model prediction. This is done with the Fokker-Planck particle transport model of Leach & Petrosian (1981) in a converging magnetic field geometry. Results from such an analysis will be published in the future. In addition to numerical modeling, we have started a statistical study of *RHESSI* flares showing double FP sources that are close to disk center and thus have less projection effects. We hope to conduct future joint observations with *RHESSI*, *Hinode*, and the *Solar Dynamic Observatory* (*SDO*) to obtain more advanced measurements of the magnetic fields at FPs. These future investigations will help improve our understanding of the underlying physics of asymmetric HXR FPs.

Chapter 6

RHESSI Observation of Chromospheric Evaporation: The 2003-11-13 M1.7 Flare[1]

6.1 Introduction

Chromospheric evaporation was first suggested by Neupert (1968) to explain the origin of the hot, dense, soft X-ray–emitting plasma confined in the coronal loops during solar flares. The basic scenario is as follows. Magnetic reconnection leads to heating of the plasma and acceleration of particles high in the corona. The released energy is transported downward along the newly reconnected closed flaring loop by nonthermal particles and/or thermal conduction, heating the chromospheric material rapidly (at a rate faster than the radiative and conductive cooling rates) up to a temperature of $\sim 10^7$ K. The resulting overpressure drives a mass flow upward along the loop at a speed of a few hundred km s^{-1}, which fills the flaring loop with a hot plasma, giving rise to the gradual evolution of soft X-ray (SXR) emission. This process should also result in a derivative of the SXR light curve in its rising portion that closely matches the hard X-ray (HXR) light curve, which is called the Neupert effect and is observed in some (but not all) flares (Neupert, 1968; Hudson, 1991; Dennis & Zarro, 1993; Dennis et al., 2003; Veronig et al., 2005).

Hydrodynamic (HD) simulations of chromospheric evaporation have been carried out with an assumed energy transport mechanism (e.g., electron "beam" or conductive heating, Fisher et al., 1985c; Mariska et al., 1989; Gan et al., 1995; Yokoyama & Shibata, 2001; Allred et al., 2005) leading to various predictions on the UV-SXR spectral lines produced by the evaporated plasma, as well as the density and temperature profiles along the flaring loop. Most of the observational tests of these predictions rely on the blueshifted components of SXR emission lines produced by the up-flowing plasma, first reported by Doschek et al. (1980) and Feldman et al. (1980), who used spectra obtained from the *P78-1* spacecraft. Similar observations were subsequently obtained from X-ray spectrometers on the *Solar Maximum Mission* (*SMM*; Antonucci et al., 1982, 1984), the *Hinotori* spacecraft (Watanabe, 1990), the *Yohkoh* spacecraft (Wuelser et al., 1994), and the *Solar and Heliospheric*

[1]Most of the material in this chapter was published in Liu, W., Liu, Jiang, & Petrosian (2006).

Observatory (*SOHO*; Brosius, 2003; Brosius & Phillips, 2004). Wuelser et al. (1994), on the other hand, observed co-spatial SXR blueshifts (upflows) and Hα redshifts (downflows), as expected from HD simulations (Fisher et al., 1985a). A summary of relevant observations from *SMM* can be found in Antonucci et al. (1999).

All the aforementioned observations, however, were indirect evidence in the sense that the evaporation process was not imaged directly. On the basis of HD simulations, Peres & Reale (1993) derived the expected X-ray brightness profile across the evaporation front and suggested that the *Yohkoh* Soft X-Ray Telescope (SXT) or X-ray imagers with equivalent or better spatial and temporal resolution should be able to detect the front. Indeed, Silva et al. (1997) found that the HXR and SXR sources of the 1994 June 30 flare moved toward the loop top (LT) during the impulsive phase. Since the flare was located near the center of the solar disk, they identified such motions as the horizontal counterpart of the line-of-sight motion revealed by the blueshifted emission lines observed simultaneously by the *Yohkoh* Bragg Crystal Spectrometer (BCS).

RHESSI, with its superior spatial, temporal, and spectral resolution (Lin et al., 2002), provides us with opportunities to study the chromospheric evaporation process in unprecedented detail. We report in this chapter our analyses of the spatial and spectral evolution of a simple flare on 2003 November 13 with excellent *RHESSI* coverage. Because the flare occurred near the solar limb, it presented minimum projection effects and a well-defined loop geometry that allows direct imaging of the HXR brightness profile along the loop. The observations and data analyses are presented in §6.2, followed by a derivation of the evolution of the density profile along the flaring loop in §6.3. We summarize the major findings of this chapter and draw conclusions in §6.4.

6.2 Observations and Data Analyses

The flare under study is a *Geostationary Operational Environmental Satellite* (*GOES*) M1.7-class flare that occurred on 2003 November 13 in AR 0501 after it appeared on the east limb. This event followed a period of extremely high solar activities in late October and early November when a series of X-class flares, including the record-setting X28 flare of 2003 November 4, took place (Xu et al., 2004; Liu, W. et al., 2004a; Metcalf et al., 2005; Veronig et al., 2006). *RHESSI* had excellent coverage of this flare. Figure 6.1 shows the *RHESSI* and *GOES-10* light curves. The *GOES* 8-1 Å (1.6-12.4 keV) and 4.0-0.5 Å (3.1-24.8 keV) fluxes rise gradually and peak at 05:00:51 and 05:00:15 UT, respectively. The *RHESSI* high-energy (> 25 keV) count rates, on the other hand, exhibit two pulses peaking at 04:58:46 and 05:00:34 UT, the first one of which is stronger. The steps in the *RHESSI* light curves are due to the attenuator (shutter) movements (Lin et al., 2002). Before 04:57:57 UT and after 05:08:59 UT, there were no attenuators in, and between the two times the thin attenuator was in, except for a short period near 05:05 UT when the attenuator briefly moved out. Note that pulse pileup (Smith et al., 2002) has insignificant effects on this flare (see Appendix A.4.1 for details).

Figure 6.2 shows the evolution of the flare at different energies, which may be divided into three phases. (1) Before 04:57:57 UT is the rising phase, when the emission mainly comes from a flaring loop to the south. (2) Between 04:57:57 and 05:08:59 UT is the impulsive phase, during which another loop to the north dominates the emission. This loop appears to

share its southern footpoint (FP) with the loop to the south, which is barely visible because of its faintness as compared with the northern loop and *RHESSI*s limited dynamic range of ∼10:1. (3) After 05:08:59 UT is the decay phase, when the shutters are out and two off-limb sources (identified as the LTs of the two loops) dominate. The relatively higher altitudescompared with earlier LT positions are consequences of the preceding magnetic reconnection, as seen in several other *RHESSI* flares (Liu, W. et al., 2004a; Sui et al., 2004).Clearly the southern loop, which extends to a relatively higher altitude, evolves more slowly and is less energetic than the northern one. We focus on the evolution of the northern loop during the first HXR pulse (04:58-05:00 UT) in this chapter.

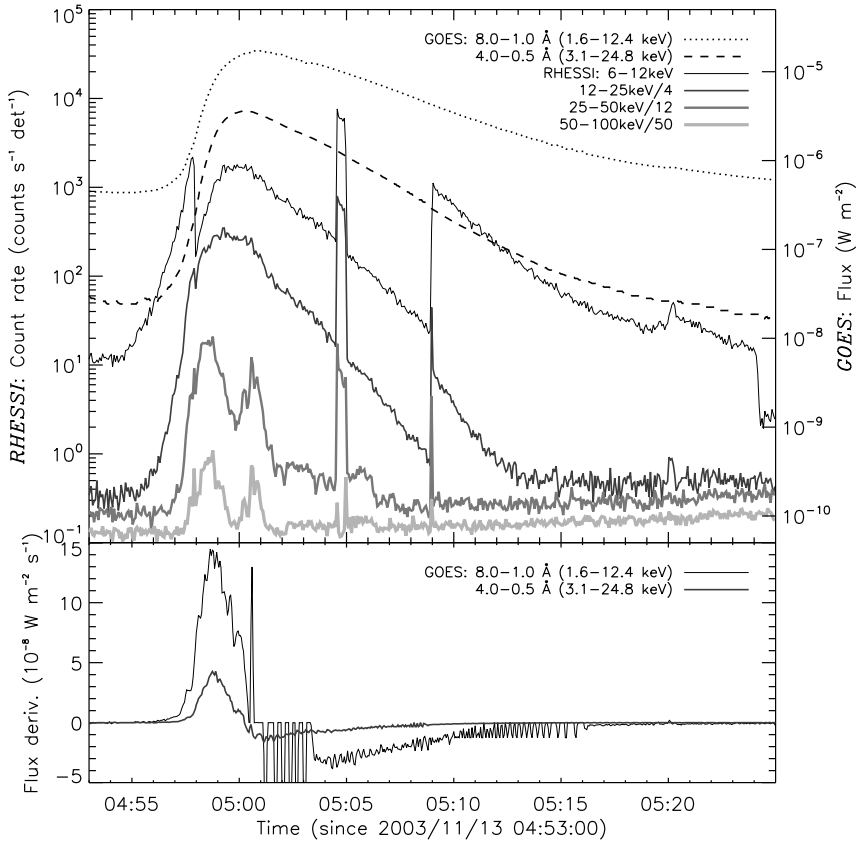

Figure 6.1: *Top*: *RHESSI* and *GOES-10* light curves. The *RHESSI* count rates are averaged over every 4 s, with scaling factors of 1, 1/4, 1/12, and 1/50 for the energy bands 6-12, 12-25, 25-50, and 50-100 keV, respectively. The sharp steps in the *RHESSI* light curves are due to attenuator state changes, and the sudden drop of the 6-12 keV count rate near 05:24 UT results from the spacecraft eclipse. The *GOES* fluxes in the bandpass of 8-1 Å (1.6-12.4 keV) and 4.0-0.5 Å (3.1-24.8 keV) are in a cadence of 3 s. *Bottom*: Time derivative of the *GOES* fluxes. Note that the periodic spikes of the low-energy channel after 05:00:24 UT are calibration artifacts [from Liu, W. et al. 2006].

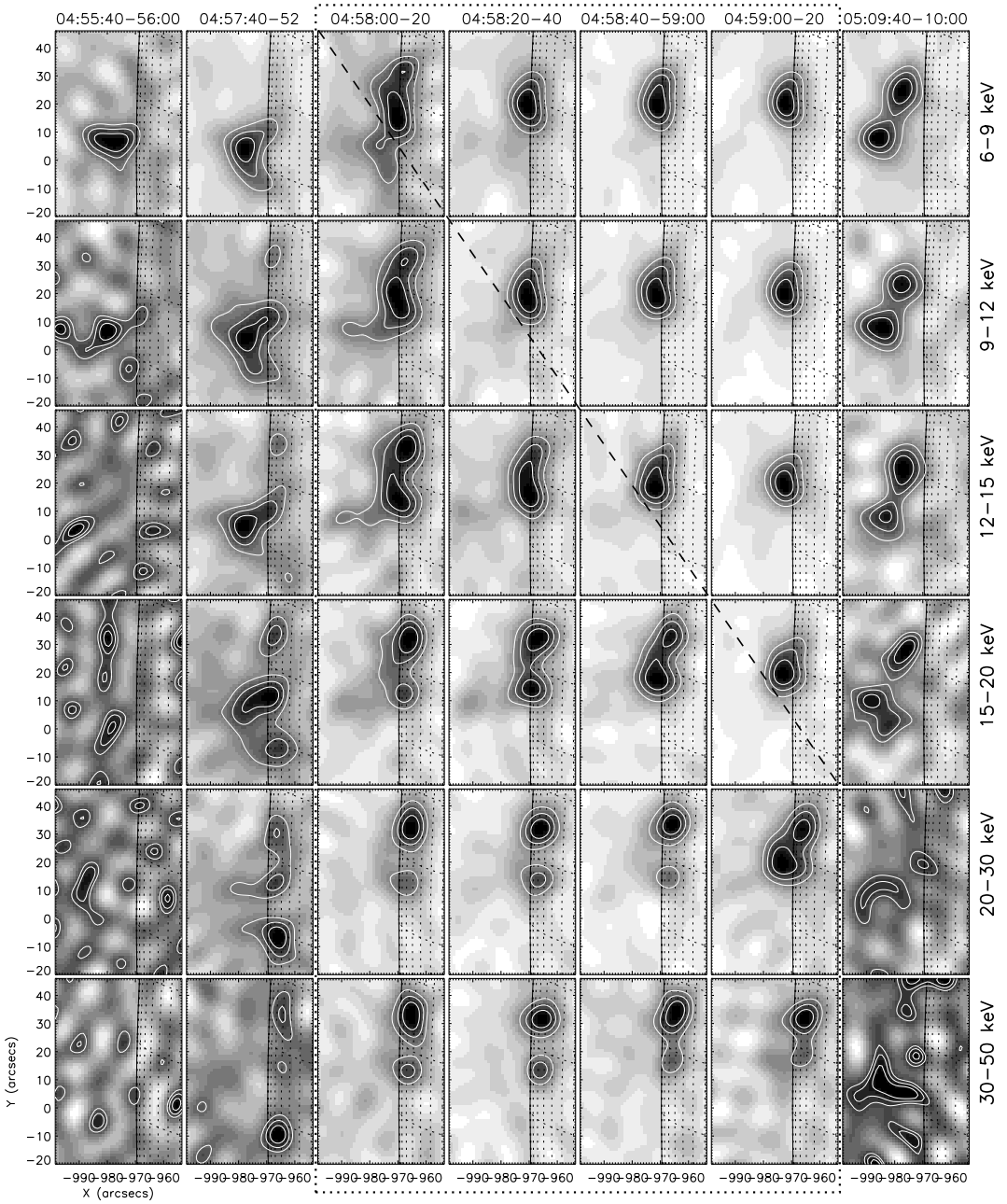

Figure 6.2: Mosaic of CLEAN images at different energies (*rows*) and times (*columns*). Contour levels are set at 40%, 60%, and 80% of the maximum brightness of each image. The front segments of detectors 3-6 and 8 were used for reconstructing these images and the others presented in this chapter, yielding a spatial resolution of $\sim 9.5''$. We selected the integration intervals to avoid the times when the attenuator state changed. The large dotted box encloses the images during the first pulse of the impulsive phase, and within this time interval the dashed diagonal line separates the frames showing double sources or an extended source from those with a compact single LT source [from Liu, W. et al. 2006].

6.2.1 Source Structure and Evolution

We now examine the images in greater detail. The top left panel of Figure 6.3 shows *RHESSI* CLEAN (Hurford et al., 2002) images of the northern loop at 9-12, 12-18, and 28-43 keV for 04:58:22-04:58:26 UT. (Although the 4 s integration time is rather short, the image quality is reliable, with a well-defined source structure.) At 9-12 keV the LT dominates and the emission extends towards the two FPs, which dominate the emission at 28-43 keV and above, with the northern FP (N-FP) much brighter than the southern one (S-FP). One of the most interesting features of the source structure is that emission from the legs of the loop dominates at the intermediate energy (12-18 keV). Similar structures are also observed for several other time intervals during the first HXR pulse (see discussions below). We find that emission from the legs is a transient phenomenon at intermediate energies, because when we integrate over a long period and/or a broad energy band, the LT and/or FP sources become dominant. To our knowledge, no images like this have been reported before. We attribute this in part to the relatively short integration time and to *RHESSI*'s high energy resolution.

For comparison with observations at other wavelengths, the same images at 9-12 and 28-43 keV (*solid contours*) are shown with the *SOHO* EUV Imaging Telescope (EIT), the Michelson Doppler Imager (MDI) magnetogram, and the MDI white-light maps in the other panels of Figure 6.3, where the dashed contours depict the southern loop at 6-9 keV for 04:57:40-04:57:52 UT. The EIT image at 04:59:01 UT (*top right*) shows emission at 195 Å that is co-spatial with the SXR emission from the northern loop. The brightest 195 Å emission, an indicator of the highest differential emission measure (and thus the highest density) at $\sim 1.3 \times 10^6$ K, appears to be close to the N-FP, which is also the strongest FP in HXRs.[2] The bottom left panel of Figure 6.3 displays the X-ray emission along with the post-flare (05:57 UT) MDI magnetogram. This clearly shows that the northern loop straddles a polarity reversal, with the brighter N-FP associated with a stronger magnetic field.[3] The southern loop (*dashed contours*) is associated with an even weaker magnetic field. Here we show the MDI magnetogram recorded 1 hr after the flare's impulsive phase, because during a flare there are many uncertainties in the magnetic field measurement. The bottom right panel of Figure 6.3 shows the MDI continuum map at 12:47 UT (about 8 hr after the flare), suggesting that the flare occurred above the lower sunspot region (*dark area*). Note that during this interval the sunspot has moved westward about 4° in heliographic longitude. We do not plot the MDI white-light map at the time of the flare because then the sunspot was nearly on the limb and was barely visible.

Next we consider the evolution of the northern loop. We note that, as shown in the four columns for 04:58:00-04:59:20 UT (boxed by the dotted line) in Figure 6.2, the FPs

[2]EIT 195 Å passband images have a relatively narrow temperature response range, with a characteristic temperature of 1.3×10^6 K (see Dere et al., 2000, Fig. 12), and emission intensity would be lower for both higher and lower temperatures.

[3]Note that since this flare occurred near the solar limb, the line-of-sight magnetogram measures mainly the horizontal (parallel to the solar surface) component of the magnetic field. The vertical component is more relevant here because flaring loops are usually perpendicular to the surface. However, it would be reasonable to assume that the vertical component scales with the horizontal one, and the polarity reversal line in the latitudinal direction is essentially not subject to the line-of-sight projection effect, as seems very likely here.

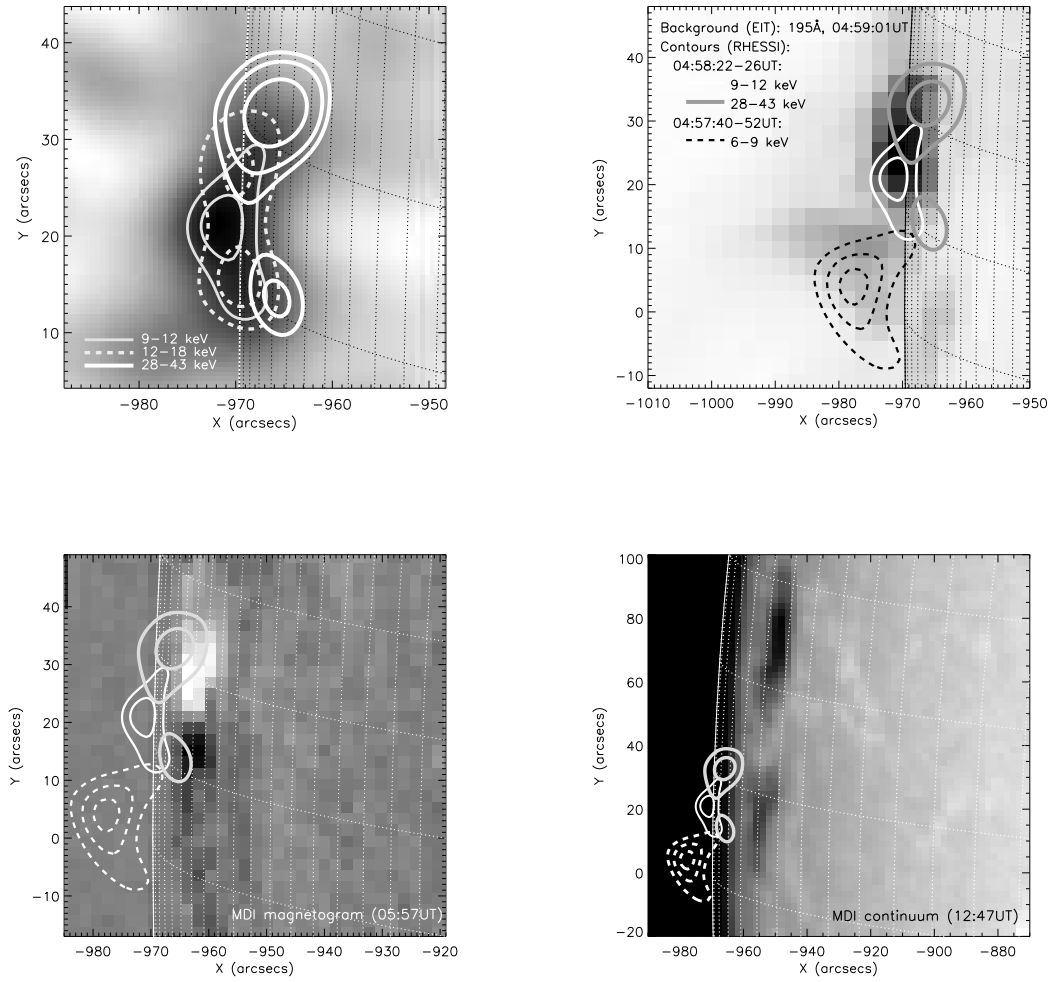

Figure 6.3: *Top left*: *RHESSI* images for 04:58:22-04:58:26 UT during the first HXR pulse. The background is the image at 9-12 keV. The contour levels are at 75 and 90% for 9-12 keV, 70% and 90% for 12-18 keV, and 50%, 60%, and 80% for 28-43 keV. *Top right*: EIT 195 Å image at 04:59:01 UT, showing co-spatial EUV emission in the northern HXR loop. The solid contours are the same as in the top left panel at 9-12 and 28-43 keV, except that the contour levels are 50% and 80% for the latter. A 6-9 keV *RHESSI* image (same as the second panel in the first row of Fig. 6.2) for 04:57:40-04:57:52 UT is plotted as dashed contours (at 50%, 70%, 90% levels) that depict the southern loop. The same set of contours is plotted in the two bottom panels as well. *Bottom left*: MDI magnetogram at 05:57 UT. The line-of-sight magnetic field in the map ranges from -351 G (*black*; away from the observer) to 455 G (*white*), with the FPs near the strong magnetic field regions. *Bottom right*: MDI continuum map at 12:47 UT, showing the sunspots. The heliographic grid spacing is 2° [from Liu, W. et al. 2006].

initially appear at all energies but later on dominate only in the high-energy bands, while the LT is first evident at low energies and becomes more and more prominent at relatively higher energies, as indicated by the dashed diagonal line. The emission from the LT also extends towards the legs at intermediate energies, and in a given energy band the emission concentrates more and more at the LT with time. These are expected to be common features of flares with a single loop because of chromospheric evaporation, which can increase the plasma density in the loop, making the LT dominant at progressively higher energies. However, because the 20 s integration time is relatively long, these images do not uncover the details of the evaporation process. To remedy this, we have carried out three different but complementary analyses of the images with higher time or energy resolution.

Temporal Morphological Evolution at Different Energies

To study the source morphology change over short time intervals, we model the loop geometry and study the evolution of the HXR brightness profile along the loop. We first

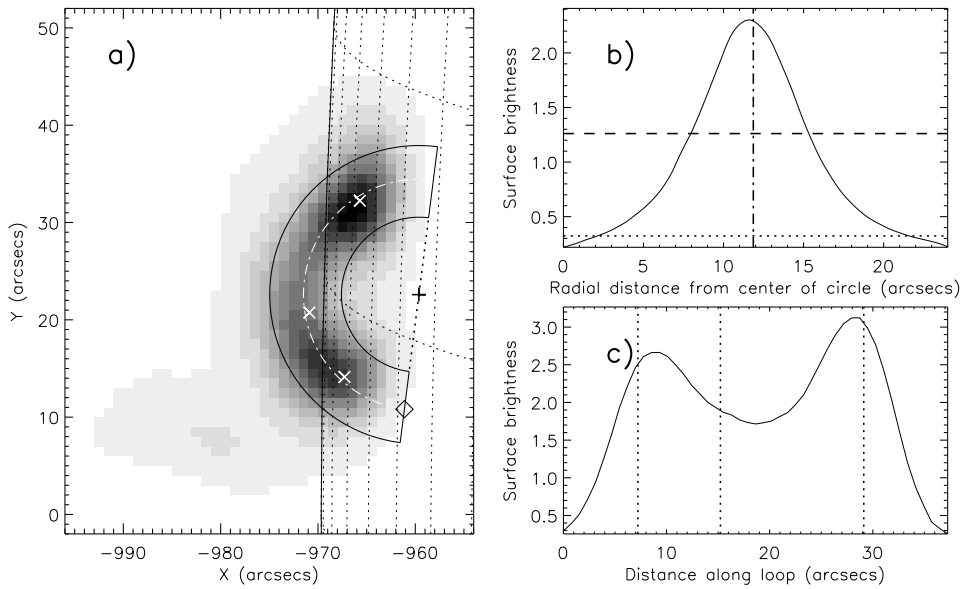

Figure 6.4: (*a*) Synthesized image obtained by superimposing 30 8 s images between 04:58:08 and 04:58:56 UT for 5 energy bands: 9–12, 12–15, 15–20, 20–30, and 30–50 keV. The three crosses mark one LT and two FP emission centroids of the corresponding sources in the 04:58:12-04:58:53 UT images at 6-9 and 50-100 keV, respectively. The solid lines represent the semi-circular model loop with the center of the circles marked by the plus sign. The white dot-dashed line indicates the central arc (see below) of this loop, and the diamond indicates the start point of the distance in (*c*). (*b*) Radial brightness profile averaged along the loop, obtained from the image shown in (*a*). The distance is measured from the center of the circles. The horizontal dashed line marks the 50% level of the maximum, and the crossings of this line with the profile define the radii of the two solid semi-circles in (*a*). The 5% level is represented by the horizontal dotted line. The vertical dot-dashed line denotes the radial position of the central arc of the loop. (*c*) Same as (*b*), but for the surface brightness along the loop's central arc, averaged perpendicular to the loop. The three vertical dotted lines mark the corresponding positions of the crosses in (*a*) [from Liu, W. et al. 2006].

made CLEAN images in two energy bands of 6-9[4] and 50-100 keV over the time interval of 04:58:12-04:58:53 UT which covers the plateau portion of the first HXR pulse. From these two images we obtained the centroids (indicated by the white crosses in Fig. 6.4*a*) of the sources identified as the LT (6-9 keV) and the two FPs (50-100 keV), respectively. Assuming a semi-circular loop that connects the three centroids, we located the center of the circle, which is marked by the plus sign in Figure 6.4*a*. The gray scale in Figure 6.4*a* was obtained by superposition[5] of 30 images (six 8 s intervals from 04:58:08 to 04:58:56 UT in five energy bands: 9-12, 12-15, 15-20, 20-30, and 30-50 keV) reconstructed with the PIXON algorithm (Metcalf et al., 1996; Hurford et al., 2002). Figures 6.4*b* and 6.4*c*, respectively, show the intensity profiles perpendicular to and along the loop (averaged over the respective orthogonal directions). The inner and outer circles (at $r = 8\farcs0$ and $15\farcs3$) in Figure 6.4*a* show the positions of the 50% values of the maximum intensity in Figure 6.4*b*. However, to infer the intensity profile along the loop, we use radially integrated flux down to the 5% level. This enables us to include as much source flux as possible (with little contamination from the southern loop). We define the mean of the radii at the 5% level as the radius of the central arc of the loop (indicated by the white dot-dashed line in Fig. 6.4*a*).

With the above procedure, one can study the evolution of the brightness profile along the loop at different energies. Figure 6.5 shows the results obtained from PIXON images with an integration time of one spacecraft spin period ($\sim$4 s) from 04:58:01 to 04:59:49 UT for three energy bands (20-30, 15-20, and 12-15 keV). Using a simple algorithm, we determine the local maxima whose slopes on both sides exceed some threshold value and mark them with filled circles. We compare each profile with its counterpart obtained from the CLEAN image (with the same imaging parameters) and use the rms of their difference to estimate the uncertainty as indicated by the error bar near the right-hand end of the corresponding profile. For each panel, the rms difference of all the profiles, as a measure of the overall uncertainty, is shown by the error bar in the upper right corner. This uncertainty is about 10% for the three energy bands; as expected, it increases slightly at higher energies, which have lower counts.

Figure 6.5*a* displays the profile at 20-30 keV, which, as expected (see Fig. 6.2), shows emission from the two FPs with fairly constant positions until the very last stage, when the LT emission becomes dominant.[6] At this stage, the S-FP becomes undetectable and the

[4]Since the thin attenuator was in at that time, counts below 10 keV are likely dominated by photons whose real energy is about 10 keV higher than the detected energy. This is due to strong absorption of lower energy (< 10 keV) photons by the attenuator and escape of the germanium K-shell fluorescence photons that are produced by photoelectric absorption of higher energy (10-20 keV) photons in the germanium detector (see Smith et al., 2002, §5.2). However, for the flare under study, the 6-9 keV image most likely reveals the real LT morphology, because there are ample thermal photons at lower energies originating from the LT source and photons at slightly higher energies seem to come from the same location.

[5]Because we are interested in determining the average loop geometry during the first pulse when the low-energy X-ray flux has changed dramatically, using this approach to map the loop will ensure a relatively uniform brightness profile along the whole loop by assigning equal weights to images at different energies. On the other hand, if one simply integrates over the entire time range of 04:58:08-04:58:56 UT and the energy band of 9-50 keV, the source morphology will be dominated by the LT source that emits most of the photons at a later time and at relatively lower energies, which may not properly depict the loop geometry during the HXR pulse.

[6]As noted earlier, pulse pileup in the 20-40 keV range becomes relatively important at this late stage, meaning that a fraction of the 20-30 keV photons seen in the image are piled-up photons from lower energies.

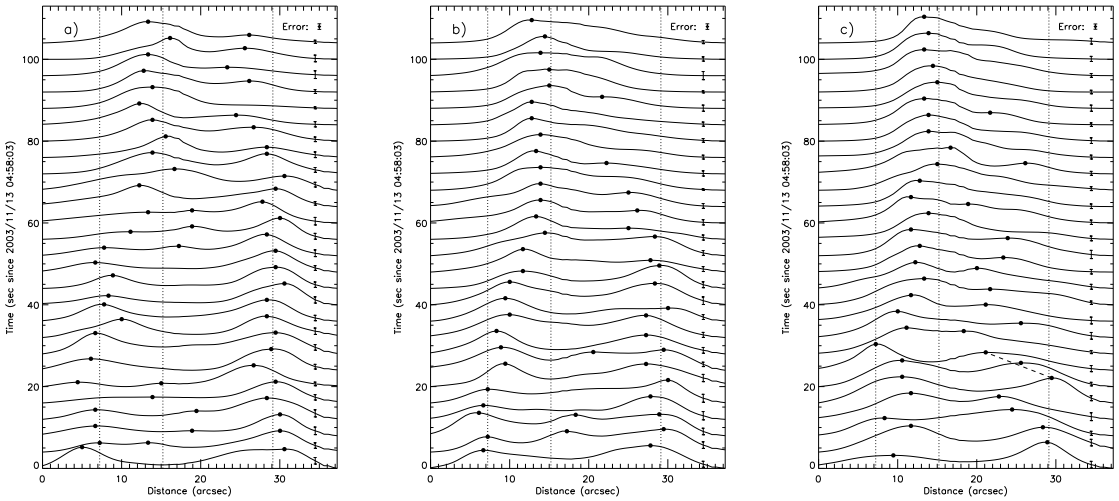

Figure 6.5: (*a*) Evolution of the 20-30 keV brightness profile along the loop in a cadence of 4 s starting at 04:58:03 UT. Each profile is normalized to its own maximum and has an integration time of 1 spacecraft spin period (∼4 s) whose central time is used to label the vertical axis. The filled circles mark the local maxima, and the three vertical lines are the same as those in Fig. 6.4*c*. The error bar on each curve indicates an estimated uncertainty of the profile, and the stand-alone error bar in the upper right corner represents the overall uncertainty (13%) of all the profiles. (*b*, *c*) Same as (*a*) but for 15-20 and 12-15 keV, with an overall uncertainty of 12% and 10%, respectively. With the dashed straight line in (*c*), we estimate the speed of the emission maximum at $\sim 10^3$ km s^{-1}. Note the slightly different scales among the three panels for the profiles and their error bars [from Liu, W. et al. 2006].

N-FP has moved very close to the LT. At lower energies (15-20 keV; Fig. 6.5*b*) the maxima tend to drift toward the LT gradually and eventually merge into a single LT source. At even lower energies (12-15 keV; Fig. 6.5*c*) this trend becomes even more pronounced and the drift starts earlier, except that here the shift is not monotonic and there seems to be a lot of fluctuation. We also repeated the same analysis at a higher cadence (every 1 s, $\sim$ 4 s integration interval) with both the PIXON and CLEAN algorithms. The evolution of the resulting profiles (although oversampled and thus not independent for neighboring profiles) appears to be in line with that shown here at a 4 s cadence obtained with PIXON. The general trends of these results indicate that high-energy HXR-producing electrons lose their energy and emit bremsstrahlung photons higher and higher up in the loop as the flare progresses. This can come about simply by a gradual increase of the density in the loop, presumably due to evaporation of chromospheric plasma. From the general drift of the maxima we obtain a timescale (∼tens of seconds) and a velocity of a few hundred km s^{-1}, consistent with the sound speed or the speed of slow magnetosonic waves. As stated above, at low energies we see some deviations from the general trend, some of which do not appear to be random fluctuations. If so, and if we take one of the evident shorter timescale trends, that shown by the dashed line in Figure 6.5*c*, we obtain a large velocity[7]

[7]Among the highest observed upflow velocities in chromospheric evaporation are $\sim 10^3$ (Antonucci et al., 1990) and ∼800 km s^{-1} (Doschek et al., 1994), obtained from blueshifted Fe XXV spectra.

of $756\,\mathrm{km\,s^{-1}}$ that is comparable to the Alfvén or fast magnetosonic wave speed. This may indicate that another outcome of energy deposition by nonthermal particles is the excitation of such modes, which then propagate from the FPs to the LT and might be responsible for the circularly polarized zebra pattern observed in the radio band (Chernov et al., 2005). This, however, is highly speculative, because the spatial resolution ($\sim 7''$) is not sufficiently high for us to trust the shorter timescale variation. The longer timescale general trend, however, is a fairly robust result.

Energy-dependent Structure at Separate Times

Instead of examining the source structure with high time resolution, we can investigate it with higher energy resolution at longer integration intervals as a tradeoff for good count statistics and image quality. To this end, we have made PIXON images during three consecutive 24 s intervals starting from 04:58:00 in 20 energy bins within the 6-100 keV range. Figure 6.6 shows a sample of these images at 04:58:24-04:58:48 UT.

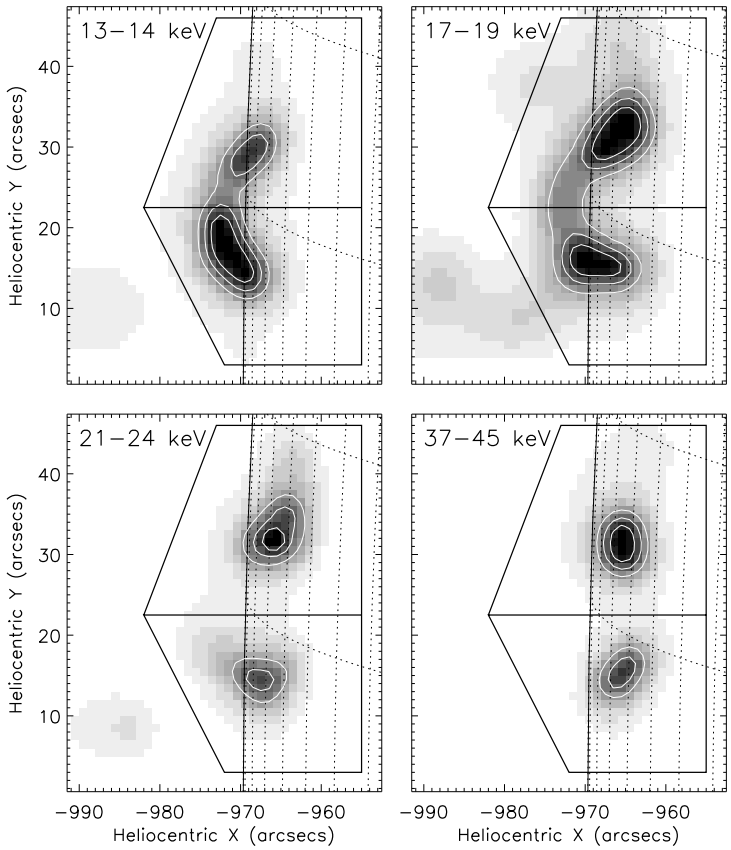

Figure 6.6: PIXON images at 04:58:24-04:58:48 UT in four energy bands. The overlaid polygons were used to divide the loop into halves to obtain the emission centroids [from Liu, W. et al. 2006].

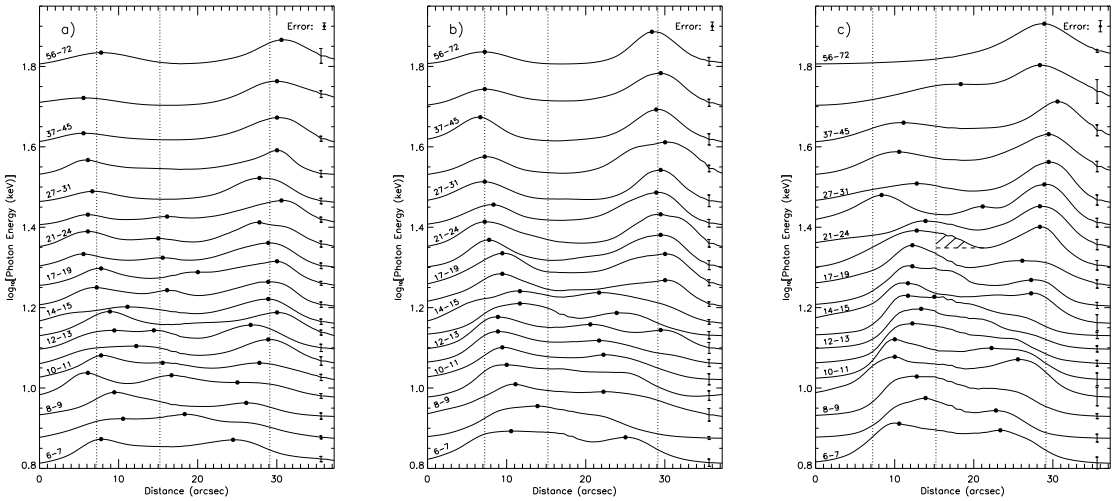

Figure 6.7: (*a*) Brightness profiles (obtained in the same way as in Fig. 6.5) at different energies for the time interval of 04:58:00-04:58:24 UT. The vertical axis indicates the average photon energy (in logarithmic scale) of the energy band for the profile. Representative energy bands (in units of keV) are labeled above the corresponding profiles. The vertical dotted lines are the same as in Figs. 6.4 and 6.5. (*b*, *c*) Same as (*a*) but for 04:58:24-04:58:48 and 04:58:48-04:59:12 UT, respectively. The error bars show the uncertainties of the corresponding profiles. The overall uncertainties, as indicated by the stand-alone error bar in the upper right corner of each panel (note different scales, similar to Fig. 6.5), are 14%, 13%, and 14%, respectively. The hatched region in (*c*) represents the LT emission (19-21 keV) removed for the derivation of the density distribution in Fig. 6.14 (see text) [from Liu, W. et al. 2006].

Figures 6.7*a*-6.7*c* show the X-ray emission profile along the loop at different energies for the three intervals.[8] As in Figures 6.5*a*-6.5*c*, the high-energy emission is dominated by the FPs, but there is a decrease of the separation of the FPs with decreasing energies and with time. Again, at later stages the LT dominates and the profile becomes a single hump. The general trend again suggests an increase of the gas density in the loop. At lower energies (< 15 keV), the profile is more complicated, presumably due to many physical processes (in addition to chromospheric evaporation), such as thermal conduction and transport of high-energy particles, thermal and nonthermal bremsstrahlung, wave excitation and propagation, wave-particle coupling, and even particle acceleration, which may be involved. We believe that a unified treatment of acceleration and HD processes with physical conditions close to the flare is required for interpretation of these results to uncover the details.

To quantify this aspect of the source structure evolution, we divided the loop into two halves, as shown by the polygons in Figure 6.6, and calculated their emission centroids. The resulting centroids at the three times, together with the central arc of the model loop, are plotted in Figure 6.8. As can be seen, for each time interval the centroids are distributed along the loop, with those at higher energies being further away from the LT, and the entire pattern shifts toward the LT with time. Figure 6.9 shows the centroid positions of the northern half of the loop (where the source motions are more evident) along and

[8]Note that pileup effects, as discussed earlier, are insignificant during this period of time (see Fig. A.1).

perpendicular to the loop during the three intervals. This again shows that the higher energy emission is farther away from the LT and that the centroids shifted towards the LT with time, but similarly there are some complicated patterns at low and intermediate energies. All these are consistent with the general picture proposed above for the chromospheric evaporation process.

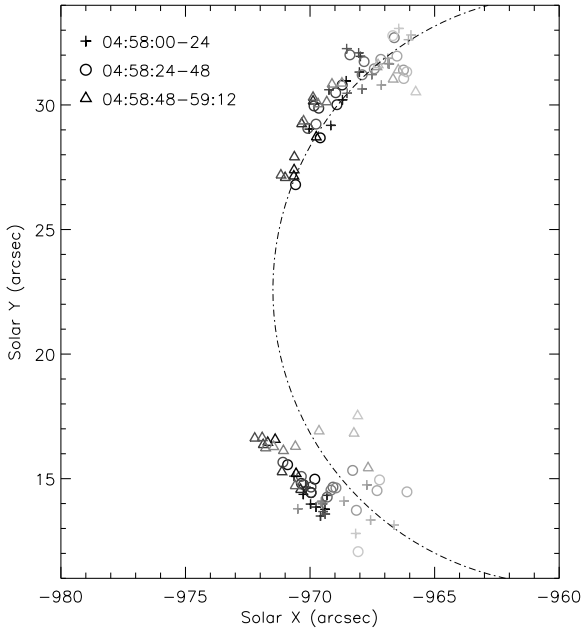

Figure 6.8: Centroids of the northern and southern halves of the loop at different energies for the three 24 s time intervals (same as those in Figs. 6.7*a*-6.7*c*). Energy increases from dark to light gray symbols. The dot-dashed line marks the central arc of the model loop (same as in Fig. 6.4*a*) [from Liu, W. et al. 2006].

Evolution of Overall Source Compactness

To further quantify the source motions, we obtained the brightness-weighted standard deviation or the second moment of the profiles. In general, the moment measures the compactness of the overall emission but does not yield the sizes of individual sources whose measurement is still challenging for *RHESSI* (Schmahl & Hurford, 2002). Hence, our attention should be paid to the general trend of the moment rather than to its absolute values, which may be subject to large uncertainties and thus may be less meaningful. The moments of the profiles resulting from CLEAN images (in three energy bands over 8 s intervals) are plotted in Figure 6.10*b*. There is a general decrease of the moment, with the decline starting earlier at lower energies. Such a decrease is expected if the two FPs move closer to each other. However, caution is required here because a decrease of this quantity could also come about by other causes, say, by an increasing dominance of the brightest source. We therefore checked the original images and the corresponding profiles when interpreting our results. To estimate the uncertainty of the moment, for each energy band we repeated the

calculation with different integration time (6.10*c*). The resulting moments remain essentially unchanged, and, as expected, the fluctuations of the moment decrease with increasing integration time. We also plot in 6.10*c* the moment (*solid curve*) obtained from PIXON images with an integration time interval of two spin periods ($\sim$ 8 s), which basically agrees with its CLEAN counterpart in the general trend. The gradual[9] decrease of the moment is consistent with the motion of the centroids of sources up the legs of the loop, which can take place by a continuous increase of the gas density in the loop due to evaporation.

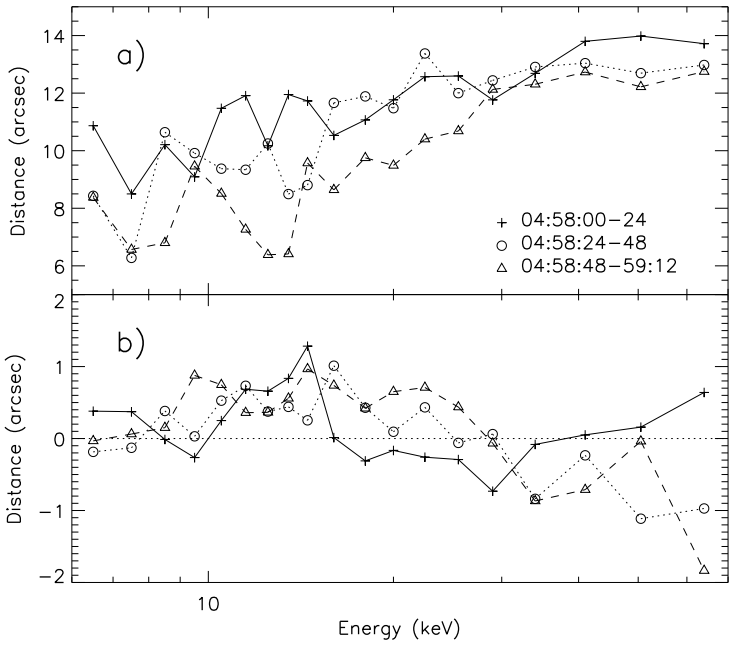

Figure 6.9: Positions of the northern centroids projected along (*a*) and perpendicular to (*b*; note the different scales) the central arc (the line in Fig. 6.8) of the loop. The distance in (*a*) is calculated from the average LT position, as shown in Fig. 6.4*a* [from Liu, W. et al. 2006].

6.2.2 Spectral Analysis

Spectral analysis can be used to study the evaporation process as well. With an isothermal plus power-law model, we fitted the spatially integrated *RHESSI* spectra down to 6 keV (Smith et al., 2002) for every 8 s interval during the impulsive phase. The emission measure (EM) and temperature of the isothermal component (*asterisks*) are plotted in Figures 6.10*d* and 6.10*e*, respectively. The EM rises almost monotonically with time from 0.6 to 14.2 $\times 10^{49}$ cm^{-3}. This translates into an increase of the plasma density [$n = (\mathrm{EM}/V)^{1/2}$] by a factor of $\sim$5 if we assume a constant volume V. The temperature remains almost constant with a trend of slight decrease with time. The EM and temperature derived from the *GOES* data (*plus signs*) are also shown for comparison. In general, the *GOES* results are smoother and the temperature increases monotonically but remains below that of the *RHESSI* data,

[9]On the other hand, the jumps (if real) of the moment may suggest a transient phenomenon.

consistent with previous results (Holman et al., 2003). This is expected because *RHESSI* is more sensitive to higher temperatures than *GOES*. However, surprisingly, the *GOES* emission measure is also lower than that of *RHESSI*, as opposed to what is the case more generally (see Holman et al., 2003). It is not clear whether or not this is due to a problem related to the *RHESSI* calibration at low energies. Nevertheless, the continuous increase of the EM at comparable rates does suggest a gradual increase of the plasma density.

The best-fit parameters of the power-law component with a low-energy cutoff are plotted in Figure 6.10*f*. The power-law index γ (*plus signs*) is anti-correlated with the high-energy light curves (see Fig. 6.10*a*) and shows a soft-hard-soft behavior. It starts at 4.43 at 04:58:02 UT, drops to 3.82 at the impulsive peak (04:58:26 UT), and rises to 7.12 at 04:59:46 UT. The high indexes (> 5) may be an indicator of high-temperature thermal rather than nonthermal emission. Thus, in what follows we limit our analysis to times up to 04:59:20 UT. The low-energy cutoff (*asterisks*) of the power law is about 15 keV and is near the intersection of the isothermal (exponential) and power-law components.

6.2.3 The Neupert Effect

The Neupert effect is commonly quoted as a manifestation of chromospheric evaporation (Dennis & Zarro, 1993), and a simple energy argument (e.g., Li et al., 1993) is often used to account for the relationship between SXR and HXR fluxes (F_{SXR} and F_{HXR}). In the thick-target flare model, the nonthermal F_{HXR} represents the *instantaneous* energy deposition rate ($\dot{\mathcal{E}}_e$) by the electron beam precipitating to the chromosphere, but the thermal F_{SXR} is proportional to the *cumulative* energy deposited; that is, the time integral of $\dot{\mathcal{E}}_e$. It naturally follows that the temporal derivative of the SXR flux, $\dot{F}_{SXR}$, should be related to F_{HXR}.

The simplest test of the Neupert effect is usually carried out by plotting $\dot{F}_{SXR}$ and F_{HXR} in some energy band. There are many reasons why a simple linear relationship would not be the case here. The first and most important is that $\dot{\mathcal{E}}_e$ is related to F_{HXR} through the bremsstrahlung yield function Y ($F_{HXR} = \dot{\mathcal{E}}_e Y$), which is not a constant and depends on the spectrum of the electrons or HXRs (see, e.g., Petrosian 1973). Here the most crucial factor is the low-energy cutoff (E_1) of the nonthermal electrons, but the spectral index also plays some role. The total yield of all the bremsstrahlung photons produced by a power-law spectrum of electrons with energies above E_1 (in units of 511 keV) is

$$Y_{total} = \frac{16}{3}\left(\frac{\alpha}{4\pi \ln \Lambda}\right) E_1 \left(\frac{\delta - 2}{\delta - 3}\right), \tag{6.1}$$

and the yield of the photons whose energies are greater than E_1 is

$$Y_{E_1} = \frac{16}{3}\left(\frac{\alpha}{4\pi \ln \Lambda}\right) E_1 \left(\frac{2}{\delta - 1}\right)^2 \left(\frac{1}{\delta - 3}\right), \tag{6.2}$$

where $\alpha = 1/137$, $\ln \Lambda = 20$ is the Coulomb logarithm, and δ is the spectral index of the power-law electron flux. We plot in Figure 6.11 Y_{E_1} as a function of δ for $E_1 = 20$ keV. As shown in Figure 6.10*f*, both the low-energy cutoff and the spectral index of the nonthermal emission vary during the pulse, indicating variations in the electron spectrum and thus breaking the linearity of the SXR-HXR relationship. Other factors that can also produce

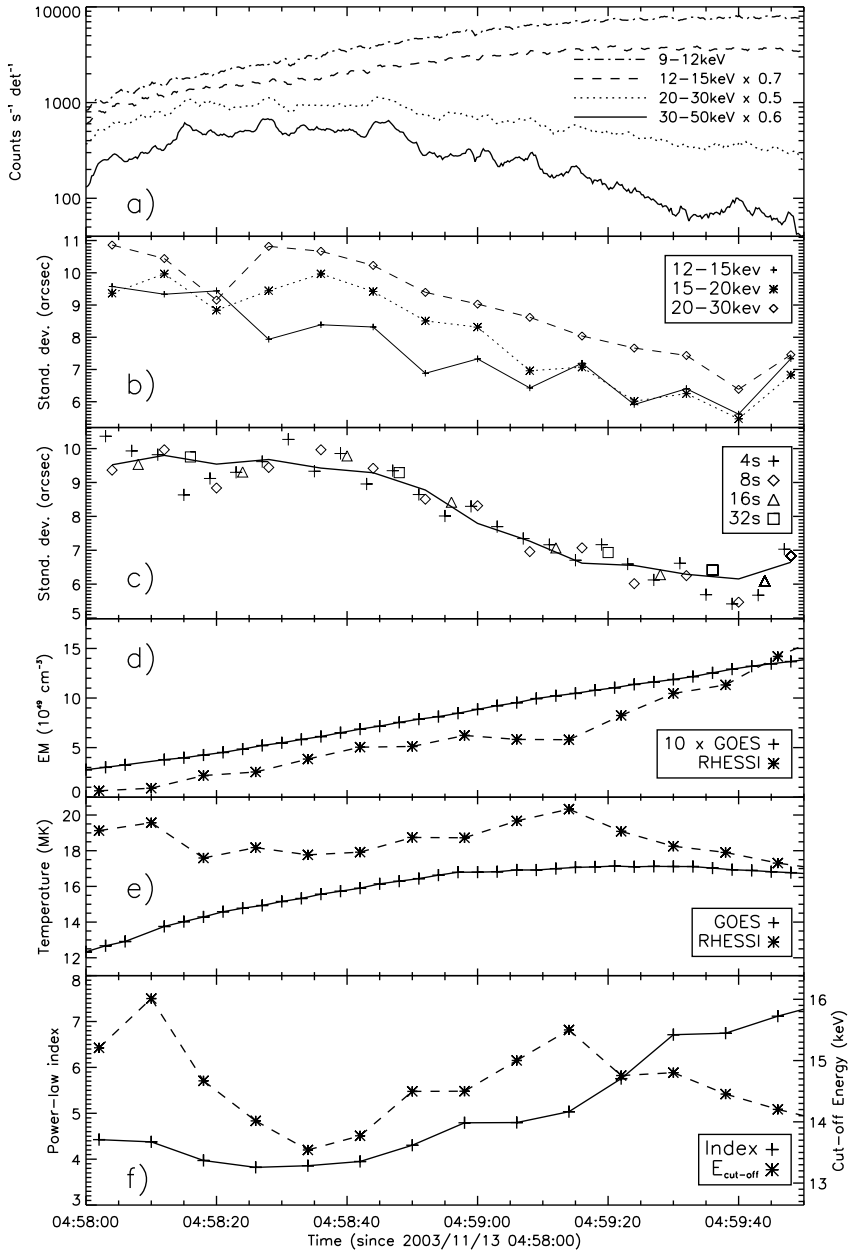

Figure 6.10: (*a*) *RHESSI* light curves (demodulated to remove artificial periodicity caused by the spacecraft spin). (*b*) Evolution of the standard deviation of the brightness profiles along the loop in three different energy bands obtained from CLEAN images. (*c*) Same as (*b*) but in the 15-20 keV band and with different integration time intervals indicated in the legend. The solid curve denotes the result from the PIXON images with an ~ 8 s integration time interval. (*d*, *e*) Evolution of the emission measure (in units of 10^{49} cm^{-3}) and temperature (in units of MK), respectively, of the thermal component of the spatially integrated *RHESSI* spectrum obtained from fits to a thermal plus power-law model and from thermal fits to the *GOES* spectrum. The *GOES* emission measure is scaled by a factor of 10. (*f*) Evolution of the power-law index and the low-energy cutoff of the *RHESSI* power-law component [from Liu, W. et al. 2006].

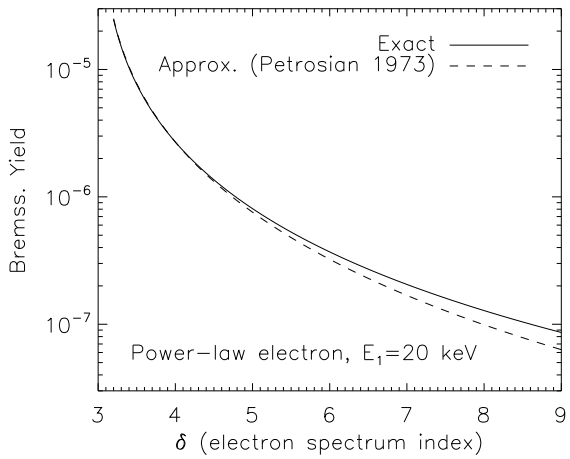

Figure 6.11: Bremsstrahlung yield in the thick-target model for a power-law electron spectrum with a low-energy cutoff of $E_1 = 20$ keV. The dashed line corresponds to the approximate result from eq. (6.2) here or eq. (30) in Petrosian (1973). The solid line comes from more accurate results from numerical integration of eq. (29) in Petrosian (1973).

further deviations are energy deposition by protons (and other ions), by conduction, and possible ways of dissipation of energy other than simply heating and evaporating the chromospheric plasma by nonthermal electrons. A detailed treatment of the problem requires solutions of the combined transport and HD equations, which is beyond the scope of this chapter. Veronig et al. (2005), who included some of these effects in an approximate way, found that the expected relationship was mostly not present in several *RHESSI* flares. Finally, one must include the fact that the chromospheric response of SXR emission will be delayed by tens of seconds, depending on the sound travel time (and its variation) and other factors.

The flare under study has shown no indication of gamma-ray line emission, which means that the contribution of protons most probably is small. In the currently most favorable model, in which the electrons are accelerated stochastically by turbulence (see, e.g., Petrosian & Liu, 2004) The turbulence can suppress heat conduction during the impulsive phase and possibly also during the decay phase (Jiang et al., 2006). Because there do not appear to be large changes in the shape of the loop during the impulsive phase, other energy dissipation processes, such as cooling by expansion, may also be negligible. Assuming these to be the case, we have performed the Neupert effect test in two ways, the first of which is the common practice of examining the relation between $\dot{F}_{SXR}$ and F_{HXR}. We then examine the relation between $\dot{\mathcal{E}}_e$ and $\dot{F}_{SXR}$ by taking into account the variation of the bremsstrahlung yield.

Correlation of $\dot{F}_{SXR}$ and F_{HXR}

The temporal derivatives of the fluxes of the two *GOES* channels are shown in the bottom panel of Figure 6.1. As is evident, during the rising portion of the *GOES* fluxes the

derivatives of both channels indeed match the first pulse of the *RHESSI* HXR light curves (> 25 keV), but not during the second weaker pulse (where the 1-8 Å derivative shows some instrumental artifacts). This may be due to the fact that the Neupert effect of the second pulse is overwhelmed by the cooling of the hot plasma produced during the first stronger pulse. Nevertheless, the SXR light curves (of both *GOES* and *RHESSI*) exhibit a slightly slower decay rate than that expected from the first pulse alone. This most likely is the signature of the energy input by the second pulse, which slows down the decay of the first pulse.

We note in passing that the SXR light curves start rising several minutes prior to the onset of the HXR impulsive phase. This is an indication of preheating of the plasma before production of a significant number of suprathermal electrons. The 6-12 keV curve rises faster than the *GOES* curves at lower photon energies, which is consistent with the picture that the primary energy release by reconnection occurs high in the corona, where the relatively hotter plasma is heated before significant acceleration of electrons (as suggested in Petrosian & Liu, 2004), and before transport of energy (by accelerated electrons or conduction) down the flare loop to lower atmospheres where cooler plasmas are heated subsequently and produce the *GOES* flux. On the other hand, the increase of the SXR flux at the beginning is dominated by the southern loop, which shows little evidence of chromospheric evaporation. The phenomenon therefore may be a unique feature of this flare.

To quantify the SXR-HXR relationship, we cross-correlated the *RHESSI* 30-50 keV photon energy flux (F_{30-50}; Fig. 6.12*a*) and the derivative of the *GOES* low-energy channel flux ($\dot{F}_{SXR}$; Fig. 6.12*c*) in the SXR rising phase (04:58:00-04:59:51 UT). The resulting Spearman rank correlation coefficient (see Fig. 6.12*f*), an indicator of an either linear or nonlinear correlation, shows a single hump with a maximum value of 0.91 (corresponding to a significance of $\sim 10^{-13}$) at a time lag of 12 s. This suggests a delay of $\dot{F}_{SXR}$ relative to F_{30-50}, which is expected given the finite hydrodynamic response time (on the order of the sound travel time of $\sim$20 s for a loop size of $\sim 10^9$ cm and $T \sim 10^7$ K) required for redistribution of the deposited energy. Such a delay is evident in the numerical simulations of Li et al. (1993), who also found that the density enhancement contributes more to the total SXR emissivity than the temperature increase for longer duration ($\geq$ 30 s) HXR bursts during the decay phase. In Figure 6.12*d*, we plot the two quantities with the *GOES* derivative shifted backward by 12 s to compensate the lag of their correlation. A linear regression (*dotted line*) gives $F_{30-50} = (1.95 \pm 0.15)\dot{F}_{SXR} - (3.68 \pm 0.48)$ with an adjusted coefficient of determination (the so-called R-squared) of $R^2_{adj} = 0.81$, which is close to 1, suggesting a good linear correlation.

Correlation of $\dot{F}_{SXR}$ and $\dot{\mathcal{E}}_e$

We also carried out the same analysis for the electron energy power $\dot{\mathcal{E}}_e$, assuming a thick-target model of power-law electrons with a low-energy cutoff of $E_1 = 25$ keV. We first obtained the energy flux of all the photons with energies greater than E_1, F_{E_1}, from the 30-50 keV photon energy flux F_{30-50}:

$$F_{E_1} = \int_{E_1}^{\infty} J(E) E dE = F_{30-50} \frac{E_1^{-\gamma+2}}{30^{-\gamma+2} - 50^{-\gamma+2}}, \tag{6.3}$$

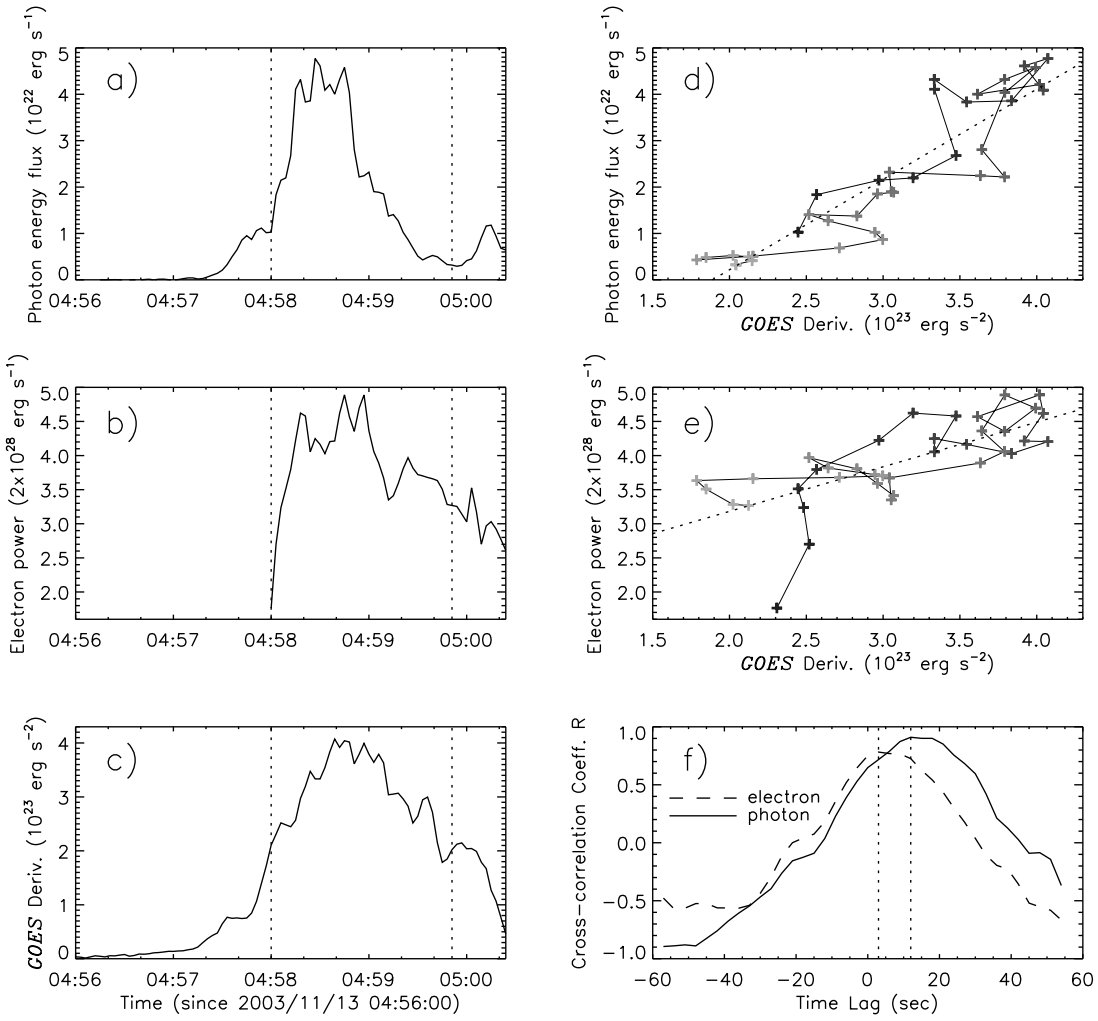

Figure 6.12: (*a*) Photon energy flux at 30-50 keV (F_{30-50}) at the Sun inferred from the *RHESSI* observation at 1 AU, assuming isotropic emission. The two vertical dotted lines outline the time interval (04:58:00-04:59:51 UT) used for the cross-correlation analysis (see below). (*b*) Power ($\dot{\mathcal{E}}_e$) of the power-law electrons with a low-energy cutoff of 25 keV inferred from the photon energy flux assuming a thick-target model. (*c*) Same as (*a*) but for the derivative ($\dot{F}_{SXR}$) of the *GOES* low-energy channel (1-8 Å) flux. (*d*) HXR energy flux F_{30-50} vs. SXR derivative $\dot{F}_{SXR}$ (shifted back in time by 12 s to account for its delay, as revealed by the cross-correlation analysis; see *f*) within the interval of 04:58:00-04:59:51 UT. The gray scale of the plus signs (connected by the solid lines) from dark to light indicates the time sequence. The dotted line is the best linear fit to the data. (*e*) Same as (*d*) but for $\dot{\mathcal{E}}_e$ and $\dot{F}_{SXR}$, which is shifted back by 3 s in time. (*f*) Spearman rank correlation coefficient R of the photon energy flux (electron power) and $\dot{F}_{SXR}$ plotted as a function of time lag of the latter relative to the former. The dotted lines mark the peak values of $R = 0.91$ and 0.78 at a lag of 12 and 3 s, respectively [from Liu, W. et al. 2006].

where $J(E) \propto E^{-\gamma}$ is the photon flux distribution at the Sun (in units of photons keV^{-1} s^{-1}), which is obtained from spectrum fitting (see §6.2.2) and is assumed to extend to infinity in energy space. We then calculated the power of the electrons by

$$\dot{\mathcal{E}}_e = F_{E_1}/Y_{E_1}, \tag{6.4}$$

where the bremsstrahlung yield Y_{E_1} is given by equation (6.2).[10] The resulting value of $\dot{\mathcal{E}}_e$ is plotted versus time and versus the *GOES* derivative in Figures 6.12*b* and 6.12*e*, respectively. The dotted line in Figure 6.12*e* shows a linear fit ($R^2_{adj} = 0.49$) to the data: $\dot{\mathcal{E}}_e = (0.65 \pm 0.11)\dot{F}_{SXR} + (1.88 \pm 0.34)$. The corresponding Spearman rank correlation coefficient has a peak value of 0.78 (significance of $\sim 10^{-8}$) at a time lag of 3 s (Fig. 6.12*f*). As evident, $\dot{\mathcal{E}}_e$ yields no better correlation with $\dot{F}_{SXR}$ than F_{30-50} does, which is similar to the conclusion reached by Veronig et al. (2005). During the HXR decay phase (after 04:59:20 UT), the spectrum becomes softer ($\gamma > 5$) and $\dot{\mathcal{E}}_e$ decreases much slower than F_{30-50}, since the bremsstrahlung yield (eq. [6.2]) decreases with the spectral index. As noted above, for these high spectral indexes, the emission might be thermal rather than nonthermal. The inferred electron power is thus highly uncertain for these times.

As stated earlier, the total energy of the nonthermal electrons is very sensitive to the low-energy cutoff E_1, which is generally not well determined (cf. Sui et al., 2005). We thus set E_1 as a free parameter and repeat the above calculation for different values of E_1 (ranging from 15 to 28 keV). We find that, as expected, the temporal $\dot{\mathcal{E}}_e$-$\dot{F}_{SXR}$ relationship highly depends on the value of E_1. For a small value of E_1 ($\lesssim$ 20 keV), $\dot{\mathcal{E}}_e$ keeps rising until ~04:59:50 UT (near the bottom of the F_{30-50} light curve), which makes the $\dot{\mathcal{E}}_e$-$\dot{F}_{SXR}$ correlation completely disappear. On the other hand, for a large value of E_1 (> 20 keV), the correlation is generally good during the impulsive pulse (through 04:59:10 UT), and the larger the value of E_1, the better the correlation. This is because the conversion factor $E_1^{-\gamma+2}/(30^{-\gamma+2} - 50^{-\gamma+2})$ in equation (6.3) is an increasing (decreasing) function of the photon spectral index γ if value of E_1 is sufficiently small (large). For a small value of E_1, for example, the photon energy flux F_{E_1} may have a somewhat large value in the valley of the F_{30-50} light curve when γ is high. In addition, during this time interval the bremsstrahlung yield Y_{E_1} becomes small, since δ is large (see eq. [6.2]), and consequently this may result in a very large value of $\dot{\mathcal{E}}_e$ by equation (6.4).

As to the magnitude of the energy flux of nonthermal electrons, Fisher et al. (1985c) in their HD simulations found that the dynamics of the flare loop plasma is very sensitive to its value. For a low-energy flux ($\leq 10^{10}$ ergs cm^{-2} s^{-1}), the upflow velocity of the evaporating plasma is approximately tens of km s^{-1}; for a high-energy flux ($\geq 3 \times 10^{10}$ ergs cm^{-2} s^{-1}), a maximum upflow velocity of approximately hundreds of km s^{-1} can be produced. For the flare under study, we estimate the area of the cross-section of the loop to be $A_{loop} \lesssim 1.6 \times 10^{18}$ cm^2, where the upper limit corresponds to the loop width determined by the 5% level in Figure 6.4*b*. We read the maximum electron power of $\dot{\mathcal{E}}_{e,max} = 9.8 \times 10^{28}$ ergs s^{-1} from Figure 6.12*b*, which is then divided by $2A_{loop}$ (assuming a filling factor of unity) to yield the corresponding electron energy flux: $f_{e,max} \gtrsim 3.1 \times 10^{10}$ ergs cm^{-2} s^{-1}.

[10] We used more accurate results from numerical integration of eq. (29) in Petrosian (1973), rather than the approximate eq. (6.2) here. However, one can still use eq. (6.2) with a simple correction factor of $0.0728(\delta - 4) + 1$ in the range $4 \leq \delta \leq 9$ to achieve an accuracy of $\lesssim 1\%$.

The source velocity estimated in §6.2.1 on the order of a few hundred km s^{-1} is consistent with that predicted by Fisher et al. (1985c). For comparison, we note that Milligan et al. (2006) also obtained an energy flux of $\geq 4 \times 10^{10}$ ergs cm^{-2} s^{-1} from *RHESSI* data for an M2.2 flare during which an upflow velocity of ∼230 km s^{-1} was inferred from simultaneous co-spatial *SOHO* Coronal Diagnostic Spectrometer (CDS) Doppler observations.

In summary, the *GOES* SXR flux derivative $\dot{F}_{SXR}$ exhibits a Neupert-type linear correlation with the *RHESSI* HXR flux F_{30-50} during the first HXR pulse. However, unexpectedly, the correlation between the electron power $\dot{\mathcal{E}}_e$ and $\dot{F}_{SXR}$ is not well established on the basis of the simple analysis presented here, which suggests that a full HD treatment is needed to investigate the chromospheric evaporation phenomenon (see discussions in §6.4).

6.3 Loop Density Derivation

For the 1994 June 20 disk flare, Silva et al. (1997) interpreted the moving SXR sources as thermal emission from the hot ($\sim 30 - 50$ MK) plasma evaporated from the chromosphere on the basis of the good agreement of the emission measure of the blueshifted component and that of the SXR from the FPs. For the limb flare under study here, Doppler shift measurements are not available. Meanwhile, a purely thermal scenario would have difficulties in explaining the systematic shift of the centroids towards the FPs with increasing energies up to ∼70 keV, as shown in Figure 6.9. A nonthermal scenario appears more appropriate. That is, the apparent HXR FP structure and motions can result from a decrease in the stopping distance of the nonthermal electrons with decreasing energy and/or increasing ambient plasma density caused by the chromospheric evaporation (as noted earlier in §6.2.1). One can therefore derive the density distribution along the loop from the corresponding X-ray emission distributions (e.g., Fig. 6.7) without any preassumed density model (cf. Aschwanden et al., 2002).This approach is described as follows.

For a power-law X-ray spectrum produced by an injected power-law electron spectrum, Leach (1984) obtained a simple empirical relation (also see Petrosian & Donaghy, 1999, §2) for the X-ray intensity $I(\tau, k)$ per unit photon energy k (in units of 511 keV) and column depth τ [in units of $1/[4\pi r_0^2 \ln\Lambda] = 5 \times 10^{22}$ cm^{-2} for $r_0 = 2.8 \times 10^{-13}$ cm and $\ln\Lambda = 20$]:

$$I(\tau, k) = A \left(\frac{\delta}{2} - 1\right) \left(\frac{k+1}{k^{2+\gamma}}\right) \left(1 + \tau \frac{k+1}{k^2}\right)^{-\delta/2}, \tag{6.5}$$

where γ and δ (which is equal to $\gamma + 0.7$) are the photon and electron spectral indexes, respectively, A is a constant normalization factor, and $d\tau = nds$, where s is the distance measured from the injection site. This equation quantifies the dependence of the emission profile (or source morphology) on the electron spectral index and column depth. In general, when δ decreases (spectrum hardening), the intensity at a given photon energy rises (drops) at large (small) values of τ and thus the emission centroid shifts to larger values of τ. This is expected because for a harder spectrum, there are relatively more high-energy electrons that can penetrate to larger column depths and produce relatively more bremsstrahlung photons there. The opposite will happen when the spectrum becomes softer. During the impulsive peak, which shows a soft-hard-soft behavior (see §6.2.2), one would expect that the emission centroids would shift first away from and then back toward the LT (if the

density in the loop stays constant). If we know the spectral index, the emission profile can therefore yield critical information about the density variation in both space and time.

To compare the above empirical relation with observations, we first integrate $I(\tau, k)$ over an energy range $[k_1, k_2]$,

$$J(\tau; k_1, k_2) = \int_{k_1}^{k_2} A \left(\frac{\delta}{2} - 1\right) \left(\frac{k+1}{k^{2+\gamma}}\right) \left(1 + \tau \frac{k+1}{k^2}\right)^{-\delta/2} dk, \tag{6.6}$$

and then integrate $J(\tau; k_1, k_2)$ over τ to obtain the cumulative emission,

$$F(\tau; k_1, k_2) = \int_0^{\tau} J(\tau; k_1, k_2) d\tau = \frac{1-\gamma}{k_2^{1-\gamma} - k_1^{1-\gamma}} \int_{k_1}^{k_2} \left[1 - \left(1 + \tau \frac{k+1}{k^2}\right)^{1-\delta/2}\right] k^{-\gamma} dk, \tag{6.7}$$

where we have chosen

$$A = \left(\int_{k_1}^{k_2} k^{-\gamma} dk\right)^{-1} = \frac{1-\gamma}{k_2^{1-\gamma} - k_1^{1-\gamma}}, \tag{6.8}$$

so that $F(\tau = \infty; k_1, k_2) = 1$. Comparison of $F(\tau; k_1, k_2)$ with the observed emission profiles gives the column depth $\tau(s)$, whose derivative with respect to s then gives the density profile along the loop.

Specifically for this flare, we assume that the nonthermal electrons are injected at the LT indicated by the middle vertical dotted line in Figure 6.7 and denote the profile to the right-hand side of this line (i.e., along the northern half of the loop) as $J_{obs}(s; k_1, k_2)$, where $[k_1, k_2]$ is the energy band of the profile. The observed cumulative emission is then given by

$$F_{obs}(s; k_1, k_2) = \frac{\int_0^s J_{obs}(s; k_1, k_2) ds}{\int_0^{s_{max}} J_{obs}(s; k_1, k_2) ds}, \tag{6.9}$$

where s_{max} (corresponding to $\tau = \infty$) is the maximum distance considered and $F_{obs}(s; k_1, k_2)$ has been properly normalized. Then $\tau = \tau(s; k_1, k_2)$ can be obtained by inverting

$$F(\tau; k_1, k_2) = F_{obs}(s; k_1, k_2), \tag{6.10}$$

where the integration over k in equation (6.7) can be calculated numerically.

It should noted, however, that not all the profiles in Figure 6.7 are suitable for this calculation, because low-energy emission is dominated by a thermal component, especially in the LT region and at later times. We thus restrict ourselves to the energy ranges of 12-72, 13-72, and 17-72 keV, respectively, for the three 24 s intervals. The lower bound is the energy above which the power-law component dominates over the thermal component, determined from fits to the spatially integrated spectrum for each interval, as shown in Figure 6.13. Within these energy ranges, separate leg or FP sources rather than a single LT source can be identified in the corresponding image, which is morphologically consistent with the nonthermal nature of emission assumed here. To further minimize the contamination of the thermal emission in our analysis, we have excluded the LT portion of the emission profile in excess of the lowest local minimum (if it exists) between the LT and leg (or FP) sources. An example of this exclusion is illustrated by the hatched region in Figure 6.7*c* for

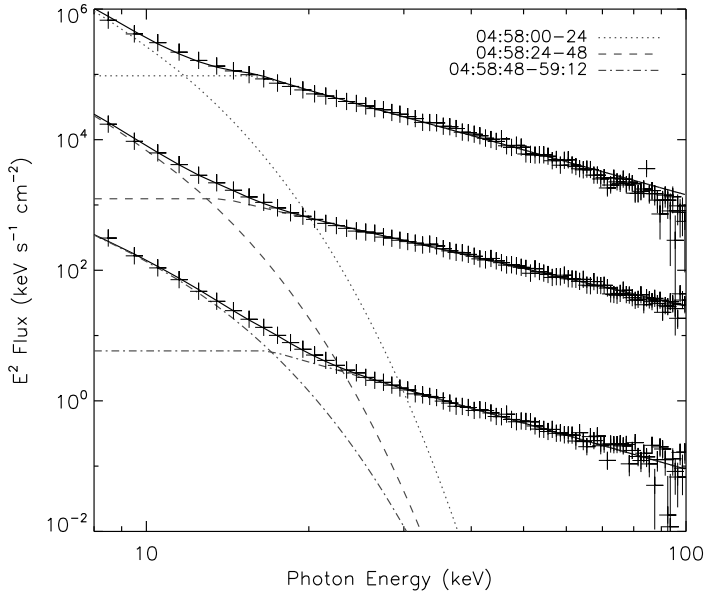

Figure 6.13: Spatially integrated spectra (νF_ν) for the three 24 s time intervals, as indicated in the legend. From the top to the bottom, the second and third spectra are shifted downward by 2 and 4 decades, respectively. The broken lines indicate the thermal and power-law components of the fits to the data, and the solid lines are the sum of the two components. The thermal and power-law components intersect at about 12, 13, and 17 keV, respectively for the three intervals, above which the power-law component dominates [from Liu, W. et al. 2006].

the 19-21 keV profile. This was done by simply replacing the profile values between the LT and the local minimum positions with the value at the minimum.

We calculated $\tau(s; k_1, k_2)$ for every emission profile within the energy ranges mentioned above for the three intervals in Figure 6.7, with photon indexes of $\gamma = 4.46$, 3.97, and 4.23, respectively. From the geometric mean of the column depths obtained at different energies, $\bar{\tau}$, we derived the density profile $n(s) = \mathrm{d}\bar{\tau}(s)/\mathrm{d}s$ for each time interval. The results are shown in Figure 6.14, where we bear in mind that attention should be paid to the overall trend rather than the details of the density profile and its variation, because the profile here only spans about 3 times the resolution ($\sim 7''$) and thus is smoothed, making neighboring points not independent. As can be seen, between the first and second intervals, the density increases dramatically in the lower part of the loop, while the density near the LT remains essentially unchanged. The density enhancement then shifts to the LT from the second to the third interval. This indicates a mass flow from the chromosphere to the LT. The density in the whole loop is about doubled over the three intervals, which is roughly consistent with the density change inferred from the emission measure[11] (see Fig. 6.10*d*). These results are again compatible with the chromospheric evaporation picture discussed in §6.2.1.

[11] From 04:58:12 through 04:59:00 UT, the *RHESSI* (*GOES*) emission measure rises by a factor of 5.3 (2.3), which translates to an increase of the density by a factor of 2.3 (1.5), assuming a constant volume.

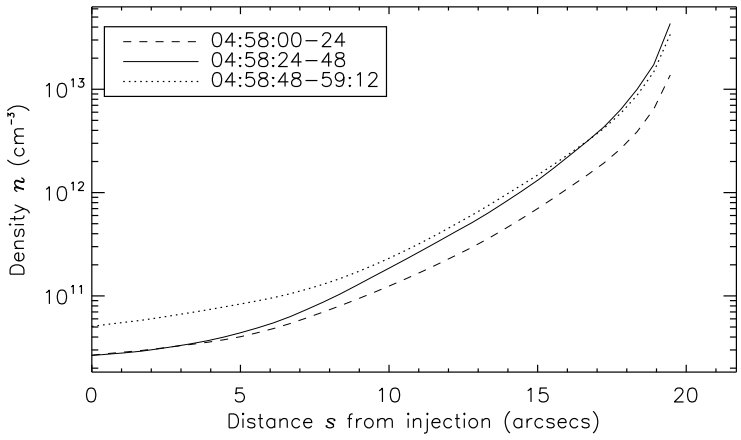

Figure 6.14: Averaged density profiles along the loop inferred from the HXR brightness profiles during the three time intervals [from Liu, W. et al. 2006].

6.4 Summary and Discussion

We have presented in this chapter a study of *RHESSI* images and spectra of the 2003 November 13 M1.7 flare. *RHESSI*'s superior capabilities reveal great details of the HXR source morphology at different energies and its evolution during the impulsive phase. The main findings are as follows.

1. The energy-dependent source morphology in general shows a gradual shift of emission from the LT to the FPs with increasing energies. Over some short integration intervals, emission from the loop legs may dominate at intermediate energies.

2. The emission centroids move toward the LT along the loop during the rising and plateau portions of the impulsive phase. This motion starts at low energies and proceeds to high energies. We estimate the mean velocity of the motion to be hundreds of km s^{-1}, which agrees with the prediction of the hydrodynamic simulations by Fisher et al. (1985c). There are also shorter time scale variations that imply much higher velocities ($\sim 10^3$ km s^{-1}) but we are not certain if they are real because of instrumental limitations.

3. Fits to the spatially integrated *RHESSI* spectra with a thermal plus power-law model reveal a continuous increase of the emission measure (EM) while the temperature does not change significantly. The *GOES* data show a similar trend of the EM but a gradual increase of the temperature.

4. The time derivative of the *GOES* SXR flux is correlated with the *RHESSI* HXR flux, with a peak correlation coefficient of 0.91 at a delay of 12 s, in agreement with the general trend expected from the Neupert effect. However, the correlation between the electron power and the *GOES* derivative is no better than the SXR-HXR correlation.

5. From the observed brightness profiles, we derive the spatial and temporal variation of the plasma density in the loop, assuming a nonthermal thick-target bremsstrahlung model. We find a continuous increase of the density, starting at the FPs and legs and then reaching to the LT. All these results fit into a picture of continuous chromospheric evaporation caused by the deposition of energy of electrons accelerated during the impulsive phase.

Several of the new features of this event (such as the leg emission at intermediate energies) may be common to many solar flares. Expanding the sample of flares of this kind will be very helpful in understanding the underlying physical processes. The new findings reside near the limit of *RHESSI*'s current temporal, spatial, and spectral resolution. As advanced imaging spectroscopy capabilities are being developed and spatial resolution is being improved in the *RHESSI* software (Hurford et al., 2002), it will be critical to obtain the spatially resolved photon spectrum along the loop. This will yield incisive clues to the nature of the moving X-ray sources and relevant energy transport mechanisms and will be useful to check the reality of the short-timescale variations.

There are several important questions that need to be further addressed in future observational and theoretical investigations: (1) What is the nature of the moving X-ray sources? Could they be characterized as thermal emission from the evaporated hot plasma or as nonthermal emission from the precipitating electrons, or a mixture of both? Could they be related to magnetohydrodynamic (MHD) waves or evaporation fronts? (2) What are the roles of different heating agents of the chromosphere; that is, electron beams, thermal conduction, and/or direct heating by turbulence or plasma waves during the impulsive phase?

We have pointed out some of the many physical processes that come into play in answering such questions. Here we describe possible directions for future theoretical studies. We have shown that a more physical test of the Neupert effect between the electron power and the SXR flux derivative does not reveal a better correlation than the usual HXR versus SXR derivative correlation. Although the observed source velocity agrees with those of HD simulations, there are some features that current simulations have not addressed. To answer these questions requires an updated numerical calculation in which one combines the model of particle acceleration and transport with the HD simulation of the atmospheric response to energy deposition to form a unified picture of solar flares. For example, one can use the output electron spectrum from the stochastic particle acceleration model (Hamilton & Petrosian, 1992; Miller et al., 1997; Park et al., 1997; Petrosian & Liu, 2004) as the input to the transport and HD codes rather than simply assuming a power-law electron spectrum, as in previous HD simulations. Such a study can shed light on the relative importance of particle beams and thermal conduction in evaporating chromospheric plasma and the roles that MHD waves may play in heating the flaring plasma; in particular, addressing our tentative observation of the fast source motion, which suggests possible presence of MHD waves in the flare loop. A better understanding of their propagation, damping, and excitation mechanisms is necessary for uncovering the energy release process during flares. In the following two chapters, we will present our combined Fokker-Planck and HD simulations along this line of research.

Chapter 7

Modeling Impulsive Phase Solar Flares: a Combined Hydrodynamic and Fokker-Planck Approach

7.1 Introduction

Particle acceleration & transport and the dynamical response of the atmosphere are two of various important processes of energization and dynamics involved in solar flares. As mentioned earlier in Chapter 1, these two processes are in fact coupled and must be studied together in a self-consistent way. Due to the forbidding complexity of the subject, however, people tend to decouple the processes and study one at a time while assuming some simple forms for the others. The past efforts, according to their focus, can be divided into two categories: particle acceleration and/or transport and atmospheric response.

For the former, one of the main streams of study solves the Fokker-Planck equation and and keeps track of the particle distribution function (while there have been researchers who took the approach of Monte Carlo simulation). For example, by assuming a static atmosphere model, particle transport (including Coulomb collision and magnetic mirroring) was studied by Leach & Petrosian (1981) and was extended to the relativistic regime (including synchrotron loss and pitch-angle scattering) by McTiernan & Petrosian (1990). Other similar studies were performed by MacKinnon & Craig (1991), McClements (1992), Syniavskii & Zharkova (1994), Zharkova et al. (1995). Particle acceleration by turbulence, for instance, was investigated by Hamilton & Petrosian (1992), Miller et al. (1996), Park et al. (1997), Petrosian & Liu (2004) in more recent years.

For the atmospheric response, although the solar atmosphere is magnetized and thus a full magnetohydrodynamic (MHD) description is desired, a majority of efforts were put into numerical hydrodynamic (HD) simulations assuming a fixed magnetic configuration. Because in a low β (magnetic field dominated) environment as in the solar corona, the plasma cannot move across the magnetic field line readily, it is reasonable to assume the material flow follows the magnetic field, which justifies 1D (distance along the magnetic field line) HD models. These models usually assume a simple spectrum of the accelerated particles which are injected at the apex of the loop and the energy deposited by the particles

at different distances along the loop is calculated in a simplified way. This energy deposition, which drives fluid dynamics, is the input to the HD code. Such studies include Nagai & Emslie (1984), Fisher et al. (1985a,b,c), Mariska et al. (1989), Gan & Fang (1990), and recent works by Abbett & Hawley (1999), and Allred et al. (2005).

From a theoretical point of view, a combined treatment of particle acceleration and transport and the atmospheric response has become progressively desired and doable, based on advances in both directions over two decades and particularly in recent years. Miller has made progress (Miller & Mariska, 2005) in coupling his stochastic particle acceleration code (Miller et al., 1996) with the Naval Research Laboratory (NRL) Solar Flux Tube Model hydrodynamic code (Mariska, Li, & Emslie 1989, hereafter MEL89). Winter & Martens (2006) combine their Monte Carlo simulation of test particle dynamics and a similar HD code. They inject a power-law electron beam at the apex of the loop and tracked the particle transport and the atmospheric response processes.

From an observational point of view, new observations, particularly X-ray images and spectra obtained by the recent *RHESSI* satellite and the previous *Yohkoh* satellite, have posed new challenges and questions to theories. For example, we (Liu, W. et al., 2006) reported an event of chromospheric evaporation imaged by *RHESSI* for the first time. As shown in Chapter 6, during this event, HXR sources at intermediate energies (12-15 keV) were observed to appear at the leg of the flaring loop, in contrast to the commonly observed LT and FP sources at low and high energies, respectively. Such sources shifted from the FPs to the LT as time progressed, and exhibited very high speeds ($\sim 10^3$ km s^{-1}) during several short time intervals. Surprisingly, our Neupert (1968) effect test revealed that the electron energy power, a more physically relevant quantity, did not yield a better correlation with the *GOES* SXR flux derivative than the more conventional HXR flux. To fully understand these observations and address the apparent discrepancies, again, requires a coupled treatment of the particle acceleration and transport and the atmospheric response processes.

An accurate treatment of this problem requires a detailed evaluation of the heating rate by nonthermal electrons, which is a key input to flare HD simulations. Previous works in this regard suffer from two major shortcomings. (1) The first is that the calculation of the energy deposition is based on approximate analytical solutions (e.g., Brown, 1973a; Emslie, 1978). This can be remedied by a combined particle and HD simulation, with the inclusion of a full Fokker-Planck treatment of the electron transport. (2) The other drawback is the simple, non-realistic, form of the injected electron spectrum used, which was usually assumed to be some form of power-law distribution that makes the solution analytically tractable. Fisher et al. (1985c), for example, assumed a power-law spectrum with an index of $\delta = 4$ and a sharp low-energy cutoff at $E_1 = 20$ keV (i.e., no electrons below E_1). MEL89 introduced a "soft" cutoff, below which the spectrum is a power-law with a positive index of 2. Recently, Allred et al. (2005)[1] used a comparably more realistic broken power-law electron spectrum derived from *RHESSI* observations (Holman et al., 2003). As we will show later, the heating rate is sensitive to the electron spectrum and thus use of inaccurate spectrum would make the HD result deviate from reality significantly. On the basis of the SA model, Petrosian & Liu (2004) have provided a more realistic electron spectrum that has a continuous form from a background thermal distribution at low energies to a nonthermal

[1]They also improved the heating rate calculation by adopting the technique of Hawley & Fisher (1994) to include the variation of hydrogen ionization state and by calculating radiative transfer and XEUV heating.

distribution at high energies. We use such an spectrum in the work described below. We will see that the low-energy electrons play an important role in heating (via collision and conduction) and in affecting the subsequent hydrodynamical process.

In this chapter, we present a review of the Fokker-Planck modeling and show it can be combined with a HD simulation of the atmospheric response during the impulsive phase (§7.2). The former component uses the unified code of particle acceleration, transport, and bremsstrahlung radiation (Petrosian et al., 2001). The latter uses the NRL Solar Flux Tube Model code (MEL89). We obtained the spatial distribution and temporal evolution of the resulting HXRs and SXRs, and check them against available *RHESSI* observations (e.g., Liu, W. et al., 2006; Sui et al. 2006). Results from some model calculations are presented in §7.3. We summarize the major findings of this chapter and draw conclusions in §7.4.

7.2 Simulation Models

7.2.1 Stochastic Acceleration Model

Here we briefly summarize the acceleration model used in this study, which was adopted from Petrosian & Liu (2004, hereafter PL04). We focus on acceleration by waves that propagate parallel to the background magnetic field.

The Fokker-Planck Equation

Let us rewrite the Fokker-Planck (F-P) equation that governs electron acceleration (eq. [1.1])

$$\frac{\partial f_{\rm ac}}{\partial t} = \frac{\partial}{\partial E}\left[D(E)\frac{\partial f_{\rm ac}}{\partial E}\right] + \frac{\partial}{\partial E}\{[A(E) - \dot{E}_L]f_{\rm ac}\} - \frac{f_{\rm ac}}{T_{\rm esc}(E)} + Q(E)\,. \tag{7.1}$$

where $f_{\rm ac} \equiv f_{\rm ac}(t, E)$ is the electron distribution function (in units of electrons $\rm cm^{-3}\,keV^{-1}$, integrated over all pitch angles; the subscript "ac" denotes acceleration region, cf. the $f(E, s, \mu)$ in the transport code), $E = \gamma - 1$ (γ being the Lorentz factor) is the electron kinetic energy in units of $m_e c^2$ (m_e is the electron mass), $D(E)$ and $A(E)$ are the energy diffusion and systematic acceleration coefficients, $T_{\rm esc}$ is the particle escape time, $Q(E)$ is the total injection flux of particles into the acceleration region that acts as source term in the equation.

$$\dot{E}_L = \dot{E}_{\rm Coul} + \dot{E}_{\rm synch} \tag{7.2}$$

is the absolute value of the net systematic energy loss rate, which is a combination of Coulomb loss (assuming a cold background plasma)

$$\dot{E}_{\rm Coul} = 4\pi r_0^2 \ln\Lambda c n_e/\beta\,, \tag{7.3}$$

and synchrotron loss

$$\dot{E}_{\rm synch} = 4 r_0^2 B^2 \beta^2 \gamma^2 / 9 m_e c\,, \tag{7.4}$$

where $\beta = v/c$, n_e is the electron number density, $r_0 = e^2/m_e c^2 = 2.8 \times 10^{-13}\,\rm cm$ is classical electron radius, $\ln\Lambda = 20$ (good for coronal conditions, Leach 1984) is the Coulomb logarithm, and B is the background magnetic field. Note equation (7.4) is valid only for

isotropic pitch-angle distribution, which is assumed to be the case in the acceleration region because of strong scattering of particles by turbulence.

In order to solve the F-P equation and keep tracking the evolution of the distribution function $f_{\rm ac}(t,E)$, one needs to know all the terms in the equation. Since the form of the energy loss rates are well known and the injection flux $Q(E)$ (say, thermal or Maxwellian distribution) is to be assumed by specific models, the central task left is to determine the diffusion coefficient $D(E)$, the direct acceleration rate $A(E)$, and the escape time $T_{\rm esc}$, which we describe as follows.

Dispersion Relation and Resonance Condition

In general, plasma waves can be described by their dispersion relations, and when particles are accelerated by turbulence, the wave-particle interaction is determined by the resonance condition.

We assume a fully ionized H and ^{4}He plasma with the relative abundance of electron/proton/α-particle = 1/0.84/0.08. The **dispersion relation** for parallel propagating waves in such a plasma is:

$$\frac{k^2}{\omega^2}=1-\frac{\alpha^2}{\omega}\left[\frac{1}{\omega-1}+\frac{(1-2Y_{\rm He})\delta}{\omega+\delta}+\frac{Y_{\rm He}\delta}{\omega+\delta/2}\right], \tag{7.5}$$

where ω *is the wave frequency in units of the nonrelativistic electron gyrofrequency* $\Omega_e=(eB_0)/(m_ec)$ (e is the electron charge and B_0 the large-scale magnetic field), k *is the wavenumber in units of* Ω_e/c, $Y_{\rm He}=0.08$ is the ^{4}He abundance, the *plasma parameter* α and the electron-to-proton mass ratio δ are given by

$$\alpha=\omega_{pe}/\Omega_e=3.2(n_e/10^{10}{\rm cm}^{-3})^{1/2}(B_0/100\,{\rm G})^{-1}\quad\text{and}\quad\delta=m_e/m_p\,, \tag{7.6}$$

where $\omega_{pi}=(4\pi n_e e^2/m_e)^{1/2}$ is the electron plasma frequency and m_p is the proton mass. From this dispersion relation, we have five distinct wave modes (branches): electromagnetic wave branch (EM), electron-cyclotron branch (EC), modified proton-cyclotron branch (PC'), ^{4}He-cyclotron branch (HeC), and a second electromagnetic wave branch (EM') (see PL04, Fig. 11, for details).

Via the **resonance wave-particle interaction**, energy can be transferred from particles to waves and vice versa (Dung & Petrosian, 1994). For a particle with a velocity βc and a pitch-angle cosine μ the resonance condition can be written as

$$\omega-k_{||}\beta\mu=\frac{n\omega_i}{\gamma}\,, \tag{7.7}$$

where n is the harmonic number of the gyrofrequency (not particle number density), $k_{||}$ is the parallel component of the wave vector, $\omega_i=q_im_e/em_i$ is the particle gyrofrequency in units of Ω_e. In our case of electron acceleration by parallel waves, $k_{||}=k$, $n=-1$, $\omega_e=-1$ (while $\omega_p=m_e/m_p=\delta$ for protons), and the resonance condition reduces to

$$\omega-k\beta\mu=\frac{1}{\gamma}\,. \tag{7.8}$$

It appears as a straight line in the k–ω plot, with the $v=\beta\mu$ being the slope and $1/\gamma$ being

the intercept. For an electron with a given velocity and pitch angle, in order to determine how it is accelerated by waves, one must first need to determine with which wave branch(es) (see PL04, Fig. 11) and at what frequency (or wave number) this straight line intersect. That is, one needs to find the roots k_j and their corresponding ω_j ($j = 1, ..., N$) of the combined nonlinear equations (7.5) and (7.8), which is done numerically in the SA code. Because of the complexity of the dispersion relation and the large dynamic range of the wavenumber, it is not a trivial task to accurately find the roots. For different particles, say, electrons and protons, their roots are located on different branches, and thus they are accelerated at different rates (see PL04, e.g., Fig. 12 for a comparison).

Turbulence Spectrum and Fokker-Planck Coefficients

To determine how much energy a particle can gain from its interaction with waves, one also needs to know the **energy spectrum of the turbulence**. Following PL04, we assume a turbulence spectrum of a broken power-law with three indexes q, $q_{\rm l}$ and $q_{\rm h}$ and two critical wavenumbers $k_{\rm min}$ and $k_{\rm max}$,

$$\mathcal{E}(k) = (q-1)\mathcal{E}_0/k_{\rm min} \begin{cases} (k/k_{\rm min})^{q_{\rm l}}, & \text{for } k < k_{\rm min}; \\ (k/k_{\rm min})^{-q}, & \text{for } k_{\rm min} < k < k_{\rm max}; \\ (k_{\rm max}/k_{\rm min})^{-q}(k/k_{\rm max})^{-q_{\rm h}}, & \text{for } k > k_{\rm max}, \end{cases} \tag{7.9}$$

where we choose $q_{\rm l} = 2 (> 0)$, $q = 1.7$ is the Kolmogorov value, and $q_{\rm h} = 4$ is a typical index for waves subject to strong damping (Vestuto et al., 2003). The cutoff at high wavenumber $k_{\rm max}$ is assumed to be caused by, say, thermal damping. Following Liu et al. (2006c), we define

$$\bar{\mathcal{E}}_0 \equiv (q-1)\mathcal{E}_0 k_{\rm min}^{q-1} \tag{7.10}$$

and a characteristic interaction rate τ_p^{-1} (or its inverse, the characteristic timescale, PL04) that is an indicator of the turbulence intensity

$$\tau_p^{-1} = \frac{\pi}{2}\Omega_{\rm e}\left(\frac{\mathcal{E}_0}{B_0^2/8\pi}\right)(q-1)k_{\rm min}^{q-1} = \frac{\pi}{2}\Omega_{\rm e}\left(\frac{\bar{\mathcal{E}}_0}{B_0^2/8\pi}\right). \tag{7.11}$$

Once the resonance interactions are found and the turbulence spectrum is given, one can proceed to evaluate the **Fokker-Planck coefficients**:

$$D_{ab} = \frac{(\mu^{-2}-1)}{\tau_p\gamma^2}\sum_{j=1}^{N}\chi(k_j) \begin{cases} \mu\mu(1-x_j)^2, & \text{for } ab = \mu\mu; \\ \mu p x_j(1-x_j), & \text{for } ab = \mu p \text{ or } p\mu; \\ p^2 x_j^2, & \text{for } ab = pp, \end{cases} \tag{7.12}$$

where

$$\chi(k_j) = \frac{\mathcal{E}(k_j)/\bar{\mathcal{E}}_0}{|\beta\mu - \beta_g(k_j)|} \quad \text{and} \quad x_j = \mu\omega_j/\beta k_j\,, \tag{7.13}$$

p is the particle momentum, $\beta_g = d\omega/dk$ is the wave group velocity, and the summation over j is for all the possible resonance interactions (the roots found above). Note the F-P coefficients are symmetric, $D_{p\mu} = D_{\mu p}$.

Fokker-Planck Equation Coefficients and Timescales

Finally, we are ready to derive the coefficients in the Fokker-Planck equation. Let us first define two ratios of the F-P coefficients:

$$R_1(\mu,p)=\frac{D_{pp}}{p^2D_{\mu\mu}}\,,\quad R_2(\mu,p)=\frac{D_{p\mu}}{pD_{\mu\mu}}\,. \tag{7.14}$$

We also define the pitch-angle averaged acceleration and scattering times (PL04, cf., Liu, S., Petrosian, & Mason 2006):

$$\tau_{\rm ac} = \frac{p^2}{\bar{D}_{pp}}=\frac{2p^2}{\int_{-1}^{1}d\mu(D_{pp}-D_{p\mu}^2/D_{\mu\mu})}=\frac{2}{\int_{-1}^{1}d\mu D_{\mu\mu}(R_1-R_2^2)}\,, \tag{7.15}$$

$$\tau_{\rm sc} = \frac{1}{2}\int_{-1}^{1}d\mu\frac{(1-\mu^2)^2}{D_{\mu\mu}}\ll L/v\,,\quad \bar{D}_{pp}\equiv\frac{1}{2}\int_{-1}^{1}d\mu(D_{pp}-D_{p\mu}^2/D_{\mu\mu})\,, \tag{7.16}$$

where the factor $2=\int_{-1}^{1}d\mu$ and L is the size of the acceleration region. Note that we assume isotropic pitch-angle distribution here and the R_2^2 term in equation 7.15 should be dropped if isotropy is not satisfied (e.g., Liu, S., Petrosian, & Mason 2006). Accordingly, the diffusion coefficient[2] (Petrosian, 2001) and the direct acceleration rate[3] can be written as

$$D(E) = \beta^2\bar{D}_{pp}=\frac{\beta^2}{2}\int_{-1}^{1}d\mu(D_{pp}-D_{p\mu}^2/D_{\mu\mu}) \tag{7.17}$$

$$= \frac{\beta^2p^2}{\tau_{\rm ac}}=\frac{\beta^2p^2}{2}\int_{-1}^{1}d\mu D_{\mu\mu}(R_1-R_2^2)\,, \tag{7.18}$$

$$A(E) = \frac{1}{\beta\gamma^2}\frac{d\beta\gamma^2D(E)}{dE}-\frac{d}{dE}D(E)=\frac{D(E)}{E}\frac{2-\gamma^{-2}}{1+\gamma^{-1}}\,. \tag{7.19}$$

We also obtain the escape time that combines nonrelativistic and extreme relativistic cases

$$T_{\rm esc}=\frac{L}{\sqrt{2}v}\left(1+\frac{\sqrt{2}L}{v\tau_{\rm sc}}\right), \tag{7.20}$$

and define the direct acceleration time, $\tau_a=E/A(E)$.

Now that all the coefficients, including $D(E)$, $A(E)$, and $T_{\rm esc}$ in the F-P equation have been evaluated, the equation can be solved numerically by the Chang-Cooper method (Park & Petrosian, 1996). In this particular study, we assume a steady state solution (the acceleration code is capable of solving the time-dependent F-P equation though), because the transport code is of steady state and we need a self-consistent treatment throughout. Once

[2]There is a typo in eq. (12) of PL04, where E^2 should be replaced with β^2p^2, but the calculation there was actually correct.

[3]Subtracting the $dD(E)/dE$ term results from the different ways of writing the F-P equation, see eq. (7.1) here and eq. (10) of PL04.

the electron spectrum, $f_{\rm ac}(E)$, in the acceleration region is obtained, we evaluate the *escaping electron flux*

$$F_{\rm esc}(E) = \frac{f_{\rm ac}(E)}{T_{\rm esc}(E)} L\,, \tag{7.21}$$

which is then passed to the transport code as an injection. We can define the ratio between the escape flux and the LT flux ($v f_{\rm ac}$):

$$R_{\rm esc} = \frac{F_{\rm esc}}{v f_{\rm ac}} = \frac{L}{v T_{\rm esc}} = \sqrt{2}\left(1 + \frac{\sqrt{2}L}{v\tau_{\rm sc}}\right)^{-1}. \tag{7.22}$$

The equivalent *thick-target electron flux* (Petrosian & Donaghy 1999; PL04) is calculated by:

$$F_{\rm thick}(E) = \frac{\beta c}{\dot{E}_L}\int_E^\infty \frac{f_{\rm ac}(E')}{T_{\rm esc}(E')} dE'. \tag{7.23}$$

7.2.2 Particle Transport and Radiation Model

The next step is to run the **transport code** that follows the electron distribution as the electrons stream down the newly reconnected magnetic field line and travel through different layers of the atmosphere. In order to run the transport code, we need the knowledge of two things. The first is the energy and pitch-angle distribution of the injected particles, which is given above as the escaping electron flux (assumed isotropic in the forward direction) by the acceleration code. The second is the background density and abundance distribution along the loop. Here we assume a fully ionized, pure hydrogen plasma,[4] whose distribution is taken from the result of the HD code (see below).

The transport code solves the fully relativistic, steady-state, F-P equation (see eq. (1) in McTiernan & Petrosian, 1990), which includes Coulomb energy loss (no energy diffusion)[5] and pitch-angle diffusion, synchrotron energy loss and pitch-angle diffusion, as well as magnetic field convergence. Following McTiernan (1989), we neglect the return current (Syniavskii & Zharkova, 1994; Zharkova et al., 1995), which is a good approximation if the electron flux is sufficiently small; we hope to include this effect in the future to achieve a more self-consistent treatment. The variable[6] to be solved is the electron flux spectrum $F(E, s, \mu)$ as a function of energy E, distance s from the injection point (at the boundary

[4] Although this assumption is not self-consistent with the abundance assumed in the acceleration code, it simplifies the calculation of the Coulomb logarithm (assume $\ln\Lambda = 20$) which is needed for evaluating the Coulomb loss. This assumption will only affect the normalization in the resulting electron flux as well as the photon emission very slightly. Again, this makes room for future improvement.

[5] We again assume a cold background plasma here, which is a good approximation for solar flares, particularly because accelerated particles lose most of their energy in the cold chromosphere. However, in principle, particles could gain energy as well by colliding with background particles when their velocities are smaller than those of the background ones, and thus Coulomb diffusion in energy should be included in the future (see more discussion in Chapter 10).

[6] The code actually solves for $F(E, s, \mu)/\beta^2 = cf(E, s, \mu)A(s)/(\beta A_0) \equiv c\Phi A(s)/A_0$, where Φ is the same as that defined in (McTiernan & Petrosian, 1990).

of the acceleration region), and pitch-angle cosine μ. It is evaluated as

$$F(E,s,\mu) = \frac{1}{A_0}\int c\beta f(E,s,\mu)dA(s) = c\beta f(E,s,\mu)\frac{A(s)}{A_0} \tag{7.24}$$

where $f(E,s,\mu)$ is the density distribution function in units of electrons $\mathrm{cm}^{-3}\,\mathrm{keV}^{-1}\mathrm{sr}^{-1}$ (cf. $f_{\rm ac}(E)$ in the acceleration code which is integrated over all pitch angles), and we integrate the differential electron flux $c\beta f(E,s,\mu)$ over the cross-sectional area $A(s)$ of the loop and then divide it by a constant equivalent area A_0. Thus $F(E,s,\mu)$ (a real physical flux) has units of electrons $\mathrm{s}^{-1}\,\mathrm{cm}^{-2}\,\mathrm{keV}^{-1}\mathrm{sr}^{-1}$ (in the code, $\mathrm{keV}^{-1}\mathrm{sr}^{-1}$ is replaced with per $m_e c^2$ per unit pitch-angle cosine). The (angle integrated) injection from the acceleration code serves as the boundary condition at $s = 0$, namely,

$$F(E,s,\mu)|_{s=0} = F_{\rm esc}(E)/2\,, \tag{7.25}$$

where the factor $2 = \int_{-1}^{1} d\mu = \cos 0 - \cos\pi$ is the range of the pitch-angle cosine. During the steady state calculation, we also set a symmetric boundary condition at the injection site, where particles running away from the domain is reflected back to the loop with identical energy but opposite pitch-angle cosine.

Once we know the electron distribution at all the depths, we calculate the thin-target nonthermal **bremsstrahlung radiation** intensity, $I(\epsilon,s)$, as a function of photon energy ϵ and distance s. $I(\epsilon,s)$, emitted by a unit length along the loop, is integrated over the loop cross-sectional area $A(s)$ and has units of photons $\mathrm{s}^{-1}\,\mathrm{cm}^{-1}\,\mathrm{keV}^{-1}$,

$$I(\epsilon,s) = A_0\int_{\epsilon}^{\infty} dE\left[n_p(s)\frac{d\sigma}{d\epsilon}\int_{-1}^{1} d\mu F(E,s,\mu)\right]\,, \tag{7.26}$$

where $n_p(s)$ is the proton number density[7] ($n_p = n_e$ in our case) and $d\sigma/d\epsilon$ is the angle-averaged[8] differential bremsstrahlung cross-section given by Koch & Motz (1959). The looptop (LT) emission is evaluated as

$$I_{\rm LT}(\epsilon) = A_0\int_{\epsilon}^{\infty} dE\left[n_p(0)\frac{d\sigma}{d\epsilon}\right] c\beta f_{\rm ac}(E)\,, \tag{7.27}$$

where $n_p(0) = n_p(s)|_{s=0} = n_{p,\rm ac}$ is the proton density and $c\beta f_{\rm ac}(E)$ is the angle-integrated electron flux, both in the acceleration region. The equivalent footpoint (FP) photon spectrum is calculated by averaging the intensity below the transition region, located at distance of $s = s_{tr}$

$$I_{\rm FP}(\epsilon) = \frac{1}{s_{max} - s_{tr}}\int_{s_{tr}}^{s_{max}} I(\epsilon,s)ds\,. \tag{7.28}$$

Both $I_{\rm LT}(\epsilon)$ and $I_{\rm FP}(\epsilon)$ can be compared with HXR observations, say, obtained by the *Yohkoh* and *RHESSI* satellites. If the coronal density is negligibly tenuous and if the

[7] In general, n_p should include H^+ as well as protons in He^{++} and other ions.

[8] Angle-dependent radiation will be included in the future (see Chapter 10)

chromospheric density is sufficiently high, $(s_{max} - s_{tr})I_{\rm FP}(\epsilon)$ would approach the thick-target spectrum

$$I_{\rm thick}(\epsilon) = \int_0^\infty I(\epsilon, N) dN \,, \tag{7.29}$$

where $dN = n_p ds$ is the column depth.

7.2.3 NRL Hydrodynamic Model

The NRL Solar Flux Tube Model (MEL89) assumes a two-fluid plasma composed of electrons and ions that can only move along the magnetic field in a flux tube, due to the line-tying condition in a low-β environment. The user-specified geometry (e.g., vertical or semi-circular) of the tube is characterized by $A(s)$, the cross-sectional area of the tube as a function of distance s, and $g(s)$, the component of the gravitational acceleration in the direction of the magnetic field. The model solves the one-dimensional equations of mass, momentum, and energy conservation,

$$\frac{\partial \rho}{\partial t} + \frac{1}{A(s)} \frac{\partial}{\partial s}[A(s)\rho v] = 0, \tag{7.30}$$

$$\frac{\partial}{\partial t}(\rho v) + \frac{1}{A(s)} \frac{\partial}{\partial s}[\rho v^2 A(s)] = \rho g - \frac{\partial P}{\partial s}, \tag{7.31}$$

$$\frac{\partial U}{\partial t} + \frac{1}{A(s)} \left\{ \frac{\partial}{\partial s} A(s) \left[(E + P)v - \kappa_e \frac{\partial T_e}{\partial s} - \kappa_i \frac{\partial T_i}{\partial s} \right] \right\} = \rho v g - L_{\rm rad} + S, \tag{7.32}$$

$$\frac{\partial}{\partial t} \left(\frac{P_e}{\gamma - 1} \right) + \frac{1}{A(s)} \left[\frac{\partial}{\partial s} A(s) \left(\frac{\gamma v P_e}{\gamma - 1} - \kappa_e \frac{\partial T_e}{\partial s} \right) \right] = -L_{\rm rad} + S + \gamma_{\rm eq}(T_i - T_e), \tag{7.33}$$

where ρ is the mass density, v is the fluid velocity, and $P = P_e + P_i$ is the total pressure, a combination of the electron pressure P_e and the ion pressure P_i, which are given by the equations of state

$$P_e = n_e k_{\rm B} T_e \quad \text{and} \quad P_i = n_i k_{\rm B} T_i \,, \tag{7.34}$$

where $k_{\rm B}$ is the Boltzmann constant, n_e and T_e (n_i and T_i) are the electron (ion) number density and temperature, respectively. Here, the combined kinetic and thermal energy is given by

$$U = \frac{1}{2}\rho v^2 + \frac{P}{\gamma - 1} \,, \tag{7.35}$$

where $\gamma = 5/3$ is the ratio of specific heats; κ_e and κ_i are the electron and ion thermal conductivities, respectively,

$$\kappa_e = 1.1 \times 10^{-6} T_e^{5/2} \,, \quad \kappa_i = \kappa_e / 25 \,; \tag{7.36}$$

$L_{\rm rad} = n_e n_p \Phi(T_e)$ is the radiative energy loss rate (MEL89), where n_p is the hydrogen number density and $\Phi(T_e)$ is the optically-thin radiative loss function; S is the heating rate,

$$S = S_0 + S_e \,, \tag{7.37}$$

where S_0 is the background heating, set to be $8.31 \times 10^{-3}\,\mathrm{ergs\,s^{-1}\,cm^{-3}}$ (MEL89), presumably caused by coronal heating in the quiet sun active region, and S_e is heating by nonthermal electrons, which will be provided by the Fokker-Planck transport model in this study. $\gamma_{\rm eq} = 1.4 \times 10^{-17} n_e^2 T_e^{-3/2}$ is the rate coefficient for electron-ion temperature equilibration; in this particular study, we assume $T_e = T_i$ and thus the $\gamma_{\rm eq}(T_i - T_e)$ term vanishes. We also assume that the plasma consists of fully ionized hydrogen. The electron and ion number densities, n_e and n_i, are then related to the mass density by

$$n_e = \frac{\rho Z}{\mu m_p (1+Z)} \quad \text{and} \quad n_i = n_e/Z\,, \tag{7.38}$$

where $Z = 1.0$ is the mean ionic charge and $\mu = 0.5$ (in units of proton masses m_p) is the mean mass[9] per particle.

The hydrodynamic equations are solved by a finite difference scheme. The code uses time-step splitting, in which the hydrodynamic calculation takes place first, using the Flux Corrected Transport (FCT) method, and then the implicit part of the code takes care of thermal conduction and radiation. Note that there is no physical or artificial viscosity in this model, but the FCT achieves similar effects to stabilize the calculation as artificial viscosity usually does and make conservative physical quantities actually conserved in the meantime. Because of lacking of viscosity, hydrodynamic waves, once excited, can exist for a long duration with little or no damping, as we will see in Chapter 9. A reflective (or symmetric) boundary condition is imposed at both the top (loop apex) and bottom (deep into the chromosphere) boundaries. Details of the numerical scheme and the model parameters can be found in Mariska et al. (1982) and MEL89.

7.2.4 Combining the Particle and Hydrodynamic Codes

We now describe how we combine the flare particle code and the NRL HD code. Since the two codes are independent and mature on their own rights, there is no need to rewrite a whole new code that includes functionality of both. Rather, one would like to have a wrapper that can coordinate between the two codes and have them communicate while running independently on each side. By doing so, one can keep each code essentially intact and self-contained. Fortunately this is possible because the communication between the two codes could be as simple as passing back and forth a 1D array. As we noted above, in order to determine the electron distribution at each depth, the transport code needs the background density profile that can be provided by the HD code. On the other hand, the HD code needs to know how much energy[10] is deposited by the accelerated electrons as a function of distance, which can be obtained from the particle transport calculation. Then this energy deposition rate (or electron heating rate) will work as a driver for the hydrodynamics, which will change the density distribution, which, in turn, will be fed back to the particle code. We detail below how to implement this approach.

[9] In the original model of MEL89, the plasma consists of fully ionized hydrogen and helium with the helium assumed to be 6.3% of the hydrogen by number density, corresponding to $Z = 1.059$ and $\mu = 0.5724$. This minor difference would only affect the mass normalization here slightly.

[10] We neglect the momentum exchange between accelerated electrons and the background particle, which is a valid approximation because of electron's small mass. See Chapter 10 for a discussion on future work.

Electron Heating Rate and Thermal Conduction

As we noted in §7.1, the **heating rate** is critical in HD simulations, but was not calculated properly in previous works. Here we improve on this by calculating the electron energy loss directly from the electron distribution obtained from the transport calculation, with two equivalent approaches.

The electron heating rate S_e (in units of $\mathrm{ergs\,s^{-1}\,cm^{-3}}$), as defined in the HD equations (see eq. [7.37]), is equal to the energy deposition rate in a unit volume by fast electrons. It can be evaluate from the energy loss rate $\dot{E}_{\rm Coul}$ (due to Coulomb collisions) as

$$S_e(s) = \int_{E_{\rm min}}^{E_{\rm max}} dE \int_{-1}^{1} f(E,s,\mu)\dot{E}_{\rm Coul} d\mu\,, \tag{7.39}$$

where $[E_{\rm min}, E_{\rm max}]$ is the range of the energy bins used, $\dot{E}_{\rm Coul}$ is given by equation (7.3), the electron distribution function $f(E,s,\mu)$ can be obtained from the corresponding electron flux $F(E,s,\mu)$ via equation (7.24).

Alternatively, one can calculate the (net downward) energy flux carried by the electrons

$$F_{\rm erg}(s) = \frac{A_0}{A(s)} \int_{E_{\rm min}}^{E_{\rm max}} dE \left[\int_0^1 \mu E F(E,s,\mu) d\mu - \int_{-1}^{0} \mu E F(E,s,\mu) d\mu \right], \tag{7.40}$$

and differentiate it to obtain the net energy gain in a unit volume

$$S_e(s) = dF_{\rm erg}(s)/ds\,, \tag{7.41}$$

where $\mu E F(E,s,\mu)$ is the energy flux projected (by the factor μ) along the loop the factor $A_0/A(s)$ accounts for the variation of the cross-sectional area. This approach is, in practice, equivalent to the above one (eq. [7.39]), because, in the deka keV to hundreds of keV energy range, the combination of synchrotron loss and bremsstrahlung HXRs only constitutes a negligible fraction ($\lesssim 10^{-4}$) of the total energy loss due to Coulomb collisions. We took the second approach in our simulation, and let the transport code calculate the heating rate and pass it to the HD code.

As to **thermal conduction**, we use the usual Spitzer conductivity without suppression, unlike what we do for the decay phase (see Chapter 9). This is because, during the impulsive phase, in addition to direct turbulence heating (believed to be present in the turbulence or acceleration region), there is significant acceleration taking place. The energized particles can escape and carry energy away from the acceleration region, which serves as a energy "conduction" channel. In contrast, during the decay phase, acceleration already subsides, and heating and suppression of conduction due to turbulence is the main energization agent. In addition, strong turbulence during the impulsive phase might act differently from weak turbulence in the decay phase. These arguments, however, are speculative and more in-depth investigation is required in the future.

Code Communication Timescale

Ideally, the flare particle code and the hydrodynamic code should work interactively and communicate at every time step during the time advance. Unfortunately, although we have a

time-dependent acceleration code, the transport code is of steady state and it would require extensive programming to upgrade it to a time-dependent version. However, fortunately, under certain assumptions, the required programming work can be significantly simplified and reasonably good accuracy can be achieved.

Our approach is to have the two codes communicate at certain intervals. Each communication consists of two parts. The first part is that the HD code passes the density profile to the flare particle code. Then the flare code runs a full *steady state* calculation from acceleration of particles, to the particle transport and bremsstrahlung radiation. Then it comes the second part of the communication, in which the flare code passes the electron heating rate (energy deposition) to the HD code. The HD code then runs its own time-dependent calculation until the next communication. Then two questions arise: (1) what is the optimum timescale for the two code to communicate; (2) what heating rate function should be provided to the HD code between adjacent communications. We address these below.

(1) The **communication timescale** should not be shorter than that on which a steady state particle transport calculation is valid. The timescale in the electron transport process can be expressed in terms of the lifetime τ_e of electrons. It is determined by the energy loss (mainly due to Coulomb collisions for nonrelativistic electrons) time in a given magnetic loop geometry and the atmospheric condition. For a low-energy electron, the Coulomb loss time is relatively short, but it would take relatively longer time for the electron to reach the dense transition region where it can lose most of its energy. The opposite is true for a high-energy electron. A combination of these factors results in the lifetime $\tau_e(E)$, which depends on the electron energy E and the atmospheric structure. For example, Petrosian (1973, see eq. (9) and Fig. 1 there) assumed a gravitationally stratified atmosphere with a scale height of $H = kT/mg$, and obtained $\tau_e(E)$ as a function of E for nonrelativistic electrons. $\tau_e(E)$ has a maximum (at some critical energy $E_{\rm cr}$) which is (eq. (11) in Petrosian, 1973)

$$\tau_{e,\,\max}(H, n_e) \approx 0.07\,\sec \left(\frac{H}{10^8\,\rm cm}\right) \left(\frac{n_e H}{10^{18}\,\rm cm^{-2}}\right)^{-1/4}, \tag{7.42}$$

where n_e is the electron number density at the injection site. For timescales greater than $\tau_{e,\,\max}$, it is reasonable to assume a steady state solution for the F-P transport equation. To be conservative, if we take the coronal temperature to be $T = 10^6$ K and the density at the acceleration region to be $n_e = 10^{10}\,\rm cm^{-3}$, we obtain $\tau_{e,\,\max} = 1.5$ s at $E_{\rm cr} = 65$ keV. On the other hand, if one assumes a constant coronal density of $n_e = 10^{10}\,\rm cm^{-3}$ and an exponential rise of density (with a scale height of $H = 603\,$km, given $T \approx 10^4\,$K in the chromosphere) starting at the transition region, then the required time is

$$t_e = l/v + \tau_{e,\max}(H, n_e) \lesssim 0.1\,\sec \left(\frac{l}{10^9\,\rm cm}\right) \left(\frac{E}{25\,\rm keV}\right)^{-1/2} + 0.05\,\sec\,, \tag{7.43}$$

where l is the length of the coronal portion of the loop, the electron velocity v is evaluated with the non-relativistic approximation, and $\tau_{e,\max}(H, n_e) = 0.05\,$s (at $E_{\rm cr} = 6.5$ keV) is obtained from equation (7.42). For a loop of $l = 10^4\,$km and an electron of $E = 25\,$keV, such a timescale is $t_e \lesssim 0.15\,$s. We therefore take a conservative $\Delta t = 2\,$s as the time interval for the two codes to communicate.

(2) Since the $\Delta t = 2\,\mathrm{s}$ interval is much shorter than the HD response time[11], **between adjacent communications**, we assume that the energy deposition by nonthermal electrons as a function of column depth $S_e(N)$ (in units of $\mathrm{ergs\,s^{-1}\,cm^2}$, where $\mathrm{cm^2}$ means per unit column depth) is constant in time. This is true (i) if we neglect energy losses (synchrotron and bremsstrahlung) other than Coulomb loss, which is valid for X-ray producing electrons (energy range from tens of keV to hundreds of keV); and (ii) if the loop cross-sectional area $A(s)$ is a constant, i.e., a uniform loop. We have made the code meet these two conditions. Then the spatial distribution of the heating rate $S_e(s,t)$ varies with time only according to the redistribution of density and the variation of column depth as a function of distance,

$$S_e(s,t) = S_e(N) n_e(s,t)\,. \tag{7.44}$$

This means that at each time t, for a given distance s, we first identify its corresponding column depth $N(s,t) = \int_0^s n_e(s,t)ds$, then use this $N(s,t)$ to evaluate the heating rate $S_e(N)$, and finally multiply $S_e(N)$ with the local density to convert the units from $\mathrm{ergs\,s^{-1}\,cm^2}$ to $\mathrm{ergs\,s^{-1}\,cm^{-1}}$ (because $S_e(s)ds = S_e(N)dN$ and $dN = n_e ds$).

Summary of Communication: Task Flow Chart

Figure 7.1: Task flow chart for Particle & HD code communication

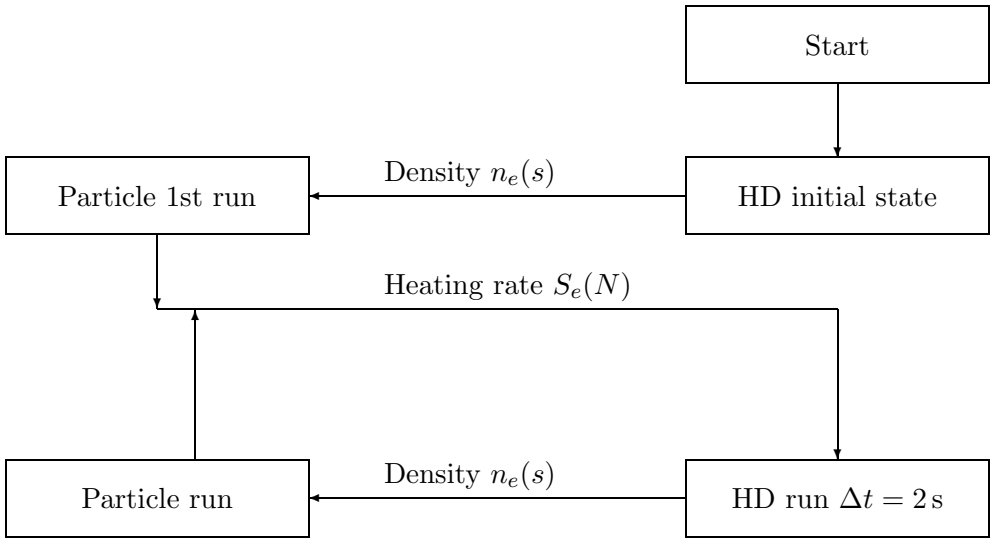

[11] This can be characterized by the sound travel time, which is about 60 s in a coronal loop of 10^4 km long with a temperature of $T = 10^6$ K (sound speed $c_s = 166\,\mathrm{km\,s^{-1}}$).

Let us now summarize the communication between the two codes with the following task flow chart. At the beginning of the simulation, the HD code passes its initial density distribution to the particle code. Based on this density profile, the particle code runs its first steady state calculation and returns the heating rate $S_e(N)$ as a function of column depth N to the HD code. Now the HD code takes this heating rate and converts it to a function of distance, $S_e(s)$, at each time step using the current density profile. While doing so, the HD code advances a time interval of $\Delta t = 2\,\mathrm{s}$, and then passes the updated density distribution back to the particle code again. This finishes a full cycle of calculation and next cycle starts over from the particle calculation again.

7.3 Simulation Result

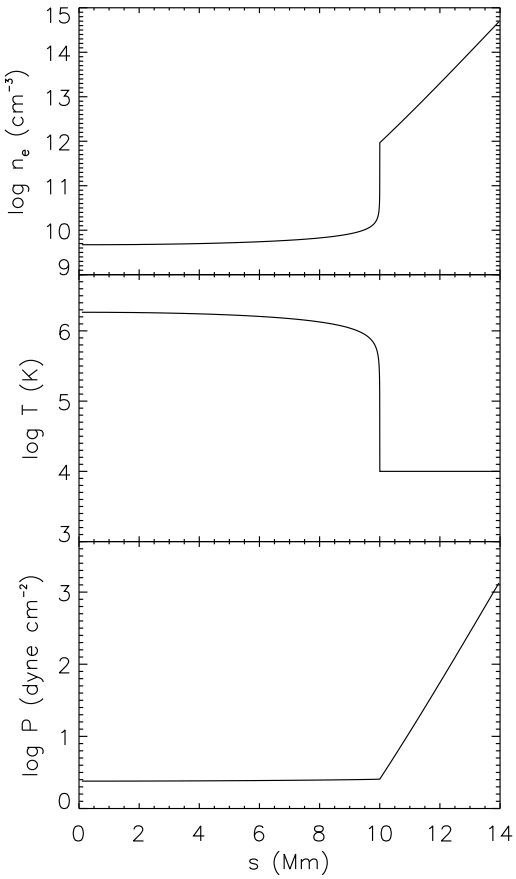

Figure 7.2: Initial state of the flare loop for the HD simulation. Distance starts from the LT where particles escape from the acceleration region.

Figure 7.2 shows the initial hydrostatic state of the plasma in one half of the loop (assumed to be symmetric), which displays the electron number density, temperature, and gas pressure vs. distance. We have a hot coronal region with $T \gtrsim 10^6\,\mathrm{K}$ and a transition

region (TR) at around $s = 10\,\mathrm{Mm}$ where T quickly drops to the chromospheric value of $10^4\,\mathrm{K}$. The density, on the contrary, increases with distance from the tenuous ($< 10^{10}\,\mathrm{cm}^{-3}$) coronal portion, experiences a sharp jump at the TR, and reaches close to $10^{15}\,\mathrm{cm}^{-3}$ at the bottom ($\sim 4\,\mathrm{Mm}$ below the TR) of the simulation domain.

From the same initial state, we have run five cases using different heating model parameters (which are summarized in Table 7.1). For each case, we use the identical loop geometry as MEL89 (see Chapter 9). We take a linear ramp in time for the normalization of the electron heating, with a rise of 30 s followed by a decline of another 30 s. After the first 60 s of impulsive phase calculation, we continue the simulation well into the decay phase until $t = 90\,\mathrm{s}$. We describe each of the simulation cases in the rest of this section, focusing on the evolution of the hydrodynamics and the energy and spatial distribution of the accelerated electrons and bremsstrahlung photons. We defer our investigation on the energy budget and the Neupert effect test of these case to next chapter.

7.3.1 Case R: Reference Calculation

It is instructive to run the first case with the original model of MEL89 and use it as a reference for comparing new results from our model. We use almost identical parameters as the "Reference Calculation" case in MEL89: spectrum index $\delta = 6$ and "knee" energy $E_1 = 15\,\mathrm{keV}$. The only two differences are: (1) here the "peak beam flux",[12] i.e., parameter F in equation (9) of MEL89, is $2.67 \times 10^{10}\,\mathrm{ergs\,cm^{-2}\,s^{-1}}$, while they used $5 \times 10^{10}\,\mathrm{ergs\,cm^{-2}\,s^{-1}}$; (2) we assume a fully ionized hydrogen plasma while they included helium which constitutes 6.3% of hydrogen number density.

The evolution of the flaring plasma is shown in Figure 7.3. We plot electron number density n_e, temperature T, gas pressure P, upward velocity v, energy deposition rate S_e, radiative loss rate L_{rad}, and heat conduction flux F_{cond} at selected times during the first 60 s of simulation. The plasma exhibits the same general evolution as that in Figure 1 of MEL89, which we briefly account as follows. As is evident, electron beam heating (S_e), which acts as the driver of the simulation, is concentrated in the upper chromosphere just below the transition region and heating in the corona is negligible early in the simulation. Heat conduction also carries energy that is deposited in the corona by nonthermal electrons down to the upper chromosphere, but this energy flux is overwhelmed by direct beam heating, particularly on the early stage of the flare. This localized beam heating, although counteracted by radiative loss that appears to be co-spatial, quickly heats chromospheric plasma, produces overpressure, and drives mass upflow. A downflow (with a velocity down to $-115\,\mathrm{km\,s^{-1}}$) in a narrow region of the chromosphere is also present to counterbalance the upward moment. Such a downflow is usually observed in blueshifted SXR or EUV line spectrum. The downward momentum produced by electron heating could be partly responsible for photospheric seismic waves observed during major flares (Kosovichev & Zharkova, 1998; Kosovichev, 2006).

At $t = 10\,\mathrm{s}$, the upflow velocity exceeds $100\,\mathrm{km\,s^{-1}}$ and a discontinuity or an evaporation front[13] has already developed near the transition region (see the n_e panel). It travels upward

[12] cf., the actual energy deposition flux in Table 7.1.

[13] The discontinuity is not necessarily a shock if the Rankine-Hugoniot (RH) relations are not satisfied. We have not checked the RH relations since we are not concerned with such detailed gas dynamics here.

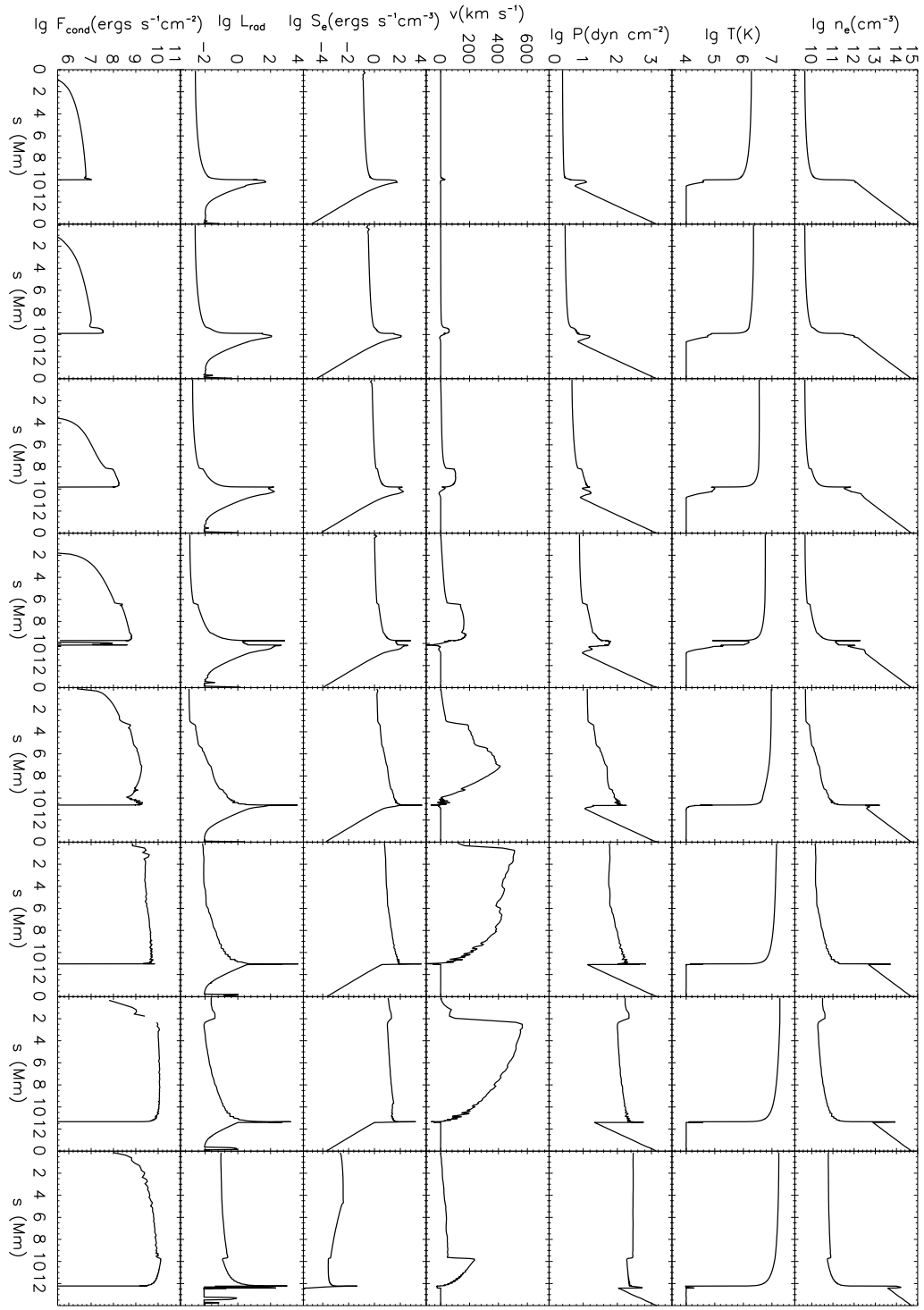

Figure 7.3: Evolution of electron density, temperature, pressure, upward velocity, energy deposition rate S_e, radiative loss rate $L_{\rm rad}$ (in same units as S_e), and heat conduction flux $F_{\rm cond}$ for Case R.

and reaches the loop apex at $\sim 29\,\mathrm{s}$. It is then reflected back and material piles up there due to the reflective boundary condition imposed. This reflection can be understood as plasma flow from the other end of the loop in a symmetric loop geometry where there is no acceleration region present in the middle of the loop; or it can be assumed to be due to the encountering of the plasma with the acceleration region boundary where the upflow is stuck by strong turbulence, if we assume a geometry with an acceleration region sitting near the LT. The upflow reaches its maximum velocity of $565\,\mathrm{km\,s^{-1}}$ at $\sim 35\,\mathrm{s}$, which is delayed by 5 s from the maximum energy deposition at $t = 30\,\mathrm{s}$. The strength of evaporation subsides afterwards, but the coronal density continues to rise through the end of the simulation.

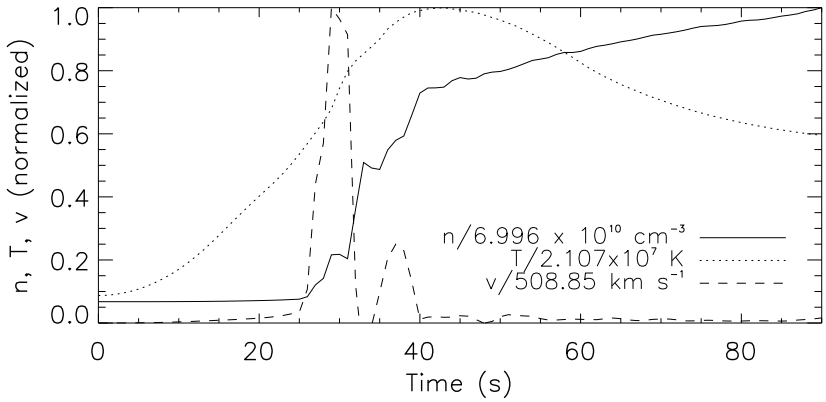

Figure 7.4: History of various quantities (electron number density, temperature, and upward velocity) at 1 Mm from the LT for Case R. Each variable is normalized to its maximum, as shown in the legend. The density curve have two sharp jumps, one followed by the other. The first jump is due to the arrival of the evaporation front from *below*, and the second one comes about because of the reflection of the front at the loop apex (coming from *above*).

We can also inspect the plasma evolution by following the temporal variation of a physical quantity at a position fixed in space. Figure 7.4 shows the history of electron number density, temperature, and velocity at $s = 1\,\mathrm{Mm}$ (in the corona) from the loop apex. As can be seen, the density and velocity stay almost constant until $\sim 25\,\mathrm{s}$ when the evaporation front arrives and produces a sudden jump. The second jump in density results from the evaporation front reflection. In contrast, the temperature varies much smoother. It attains its maximum of $2.11 \times 10^7\,\mathrm{K}$ at $t = 44\,\mathrm{s}$ and decreases monotonically since then because conductive cooling overtakes beam heating at this position in the loop.

7.3.2 Case A: Fiducial Run with SA Model

We used the same parameters for acceleration as in PL04 (see their Fig. 12), i.e., $\tau_p^{-1} = 70\,\mathrm{s^{-1}}$, $n_e = 1.5 \times 10^{10}\,\mathrm{cm^{-3}}$, $B = 400\,\mathrm{G}$, $k_BT = 1.53\,\mathrm{keV}$, and the acceleration region size $L = 5 \times 10^8\,\mathrm{cm}$. The peak rate of particle injection was set at $Q_0 = 5.73 \times 10^{11}$electrons $\mathrm{s^{-1}\,cm^{-3}}$ to provide a peak energy deposition flux of $2.56 \times 10^{10}\,\mathrm{ergs\ s^{-1}\,cm^{-2}}$ similar to that of Case R. We chose 200 energy bins uniformly spaced in the logarithmic space that covers the range of $[10^{-3}, 10^3] \times 511$ keV. There are 24 pitch-angle bins set in the

transport code, with 12 uniform bins symmetrically spanning each half of the $[0, \pi]$ range ($0 \leq \theta < \pi/2$ and $\pi/2 < \theta \leq \pi$; note $\theta \neq \pi/2$). We modulate the injection rate $Q(t, E)$ linearly in time, with a 30 s rise followed by a 30 s decay.

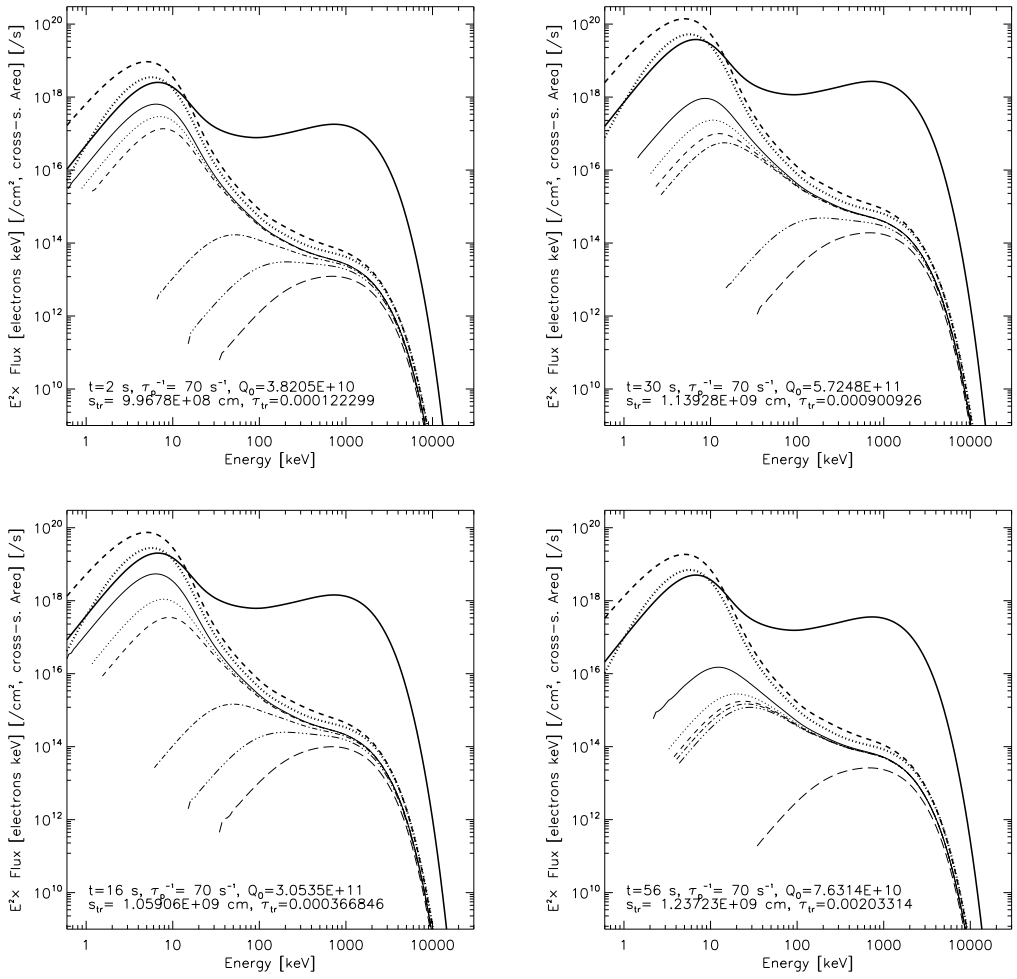

Figure 7.5: Evolution of $E^2F(E)$ spectra for Case A, where $F(E)$ is the angle-integrated electron flux. The thick dashed, dotted, and solid lines indicate the LT, escaping, and equivalent thick-target electron flux, respectively. The thin lines (from top to bottom: *solid*, *dotted*, *dashed*, *dot-dashed*, *triple-dot–dashed*, and *long-dashed*) are for the spectrum at distances of $s = 4$, 8, 10, 11, 12, and 13 Mm from the injection site at the LT, respectively. The legend includes the current values of τ_p^{-1}, the particle injection rate Q_0 (in units of electrons $\mathrm{s}^{-1}\,\mathrm{cm}^{-3}$), and the distance ($s_{\mathrm{tr}}$) and column depth ($\tau_{\mathrm{tr}}$, in units of $5 \times 10^{22}\,\mathrm{cm}^{-2}$) from the LT to the transition region.

The $E^2F(E)$ electron flux spectrum [where $F(E) = f(E)\beta c$ is the angle-integrated electron flux] at the LT (*thick dashed line*) is shown in Figure 7.5. It contains a quasi-thermal portion at low energies and a nonthermal tail at high energies, with a smooth transition in between (PL04). It does not invoke any artificial low-energy cutoff or energy break. This particular spectrum shape is consistent with observed HXR spectra that can

often be fitted with an isothermal plus power-law model. Since the acceleration parameters (e.g., τ_p^{-1}) are set constant in time, this spectrum does not change in shape, but does vary in normalization. The thick dotted line indicates the electron flux escaping from the acceleration region, which is the input to the transport code and acts as a driver to the electron-beam heated HD evolution. We describe the plasma evolution below and defer a discussion of the corresponding particle transport and radiation effects afterwards.

HD Evolution

Figure 7.6 shows the evolution of the plasma in the loop. As we can see, the general evolution is similar to that of Case R, though much faster. The evaporation front reaches the loop apex at $t = 22\,\mathrm{s}$ (instead of 29 s in Case R), the maximum upflow velocity of $627\,\mathrm{km\,s^{-1}}$ is attained at $t = 22\,\mathrm{s}$ (instead of $565\,\mathrm{km\,s^{-1}}$ at $t = 22\,\mathrm{s}$ in Case R), and the maximum coronal temperature is 2.61 K (2.11 K in Case R).

These differences are a consequence of the spatial distribution of the energy deposition S_e, which first decreases (while it increases in Case R) with distance from the LT and then increases and peaks just below the transition region. In addition, the peak of the S_e curve in the chromosphere is relatively narrower than that in Case R, which means a comparably smaller fraction of energy is directly deposited in the chromosphere. This is because the electron spectrum here (Fig. 7.5) has a smooth continuous distribution including the high-energy nonthermal regime and the low-energy quasi-thermal regime. There is a significant portion of the total energy content that resides in low-energy electrons. These electrons give up most of their energy to the coronal portion of the loop, resulting in significant coronal heating. The coronal temperature thus increases rapidly and produces a relatively sharp temperature gradient and large heat conduction flux (see panels at $t = 2\,\mathrm{s}$ and $t = 5\,\mathrm{s}$). We note that the peak of the conduction flux, which is close to the LT at the beginning ($t = 2\,\mathrm{s}$), shifts downward and reaches the transition region at $t = 9\,\mathrm{s}$ when the upflow velocity rises sharply and exceeds $100\,\mathrm{km\,s^{-1}}$. In this sense, the evaporation is driven more by conduction than by direct heating. As evaporation develops and the coronal density increases, the coronal fraction of the energy deposition increases as well and dominates over the chromospheric portion on the late stage.

In contrast, the spectrum adopted in MEL89 is a power-law ($\delta = 6$) with a low-energy cutoff at $E_1 = 15\,\mathrm{keV}$ below which the electron spectrum has a positive index of 2. This spectrum has its peak at 15 keV and electrons of this energy are stopped in the chromosphere where they lose most of their energy, where the radiative loss (which acts like a sink in the energy transfer) is most efficient. This means that a significant part of energy deposited by beaming electrons is quickly radiated away (also see Fig. 8.2 and text there) in situ in the upper chromosphere and a smaller fraction of energy is available to evaporate chromospheric material than in Case A. Note that the conductively driven scenario in Case A has energy input into the transition region and produces evaporation, which occurs slightly above the radiatively-efficient layer in the upper chromosphere. This makes conductively-driven evaporation more efficient and results in higher upflow velocity and higher coronal temperature and density, as can also be seen in Figure 7.19.

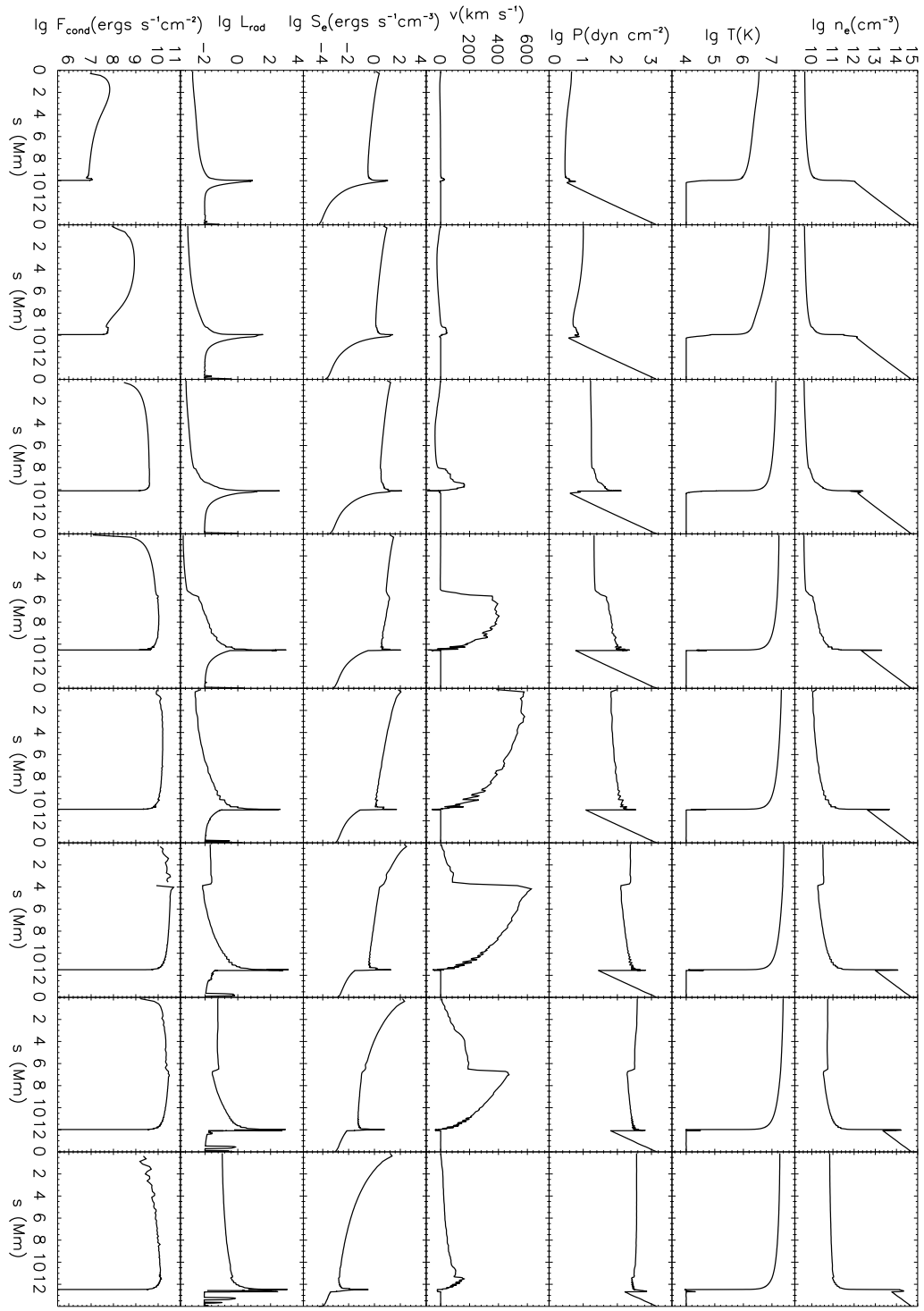

Figure 7.6: HD evolution of various quantities for Case A, similar to Fig. 7.3.

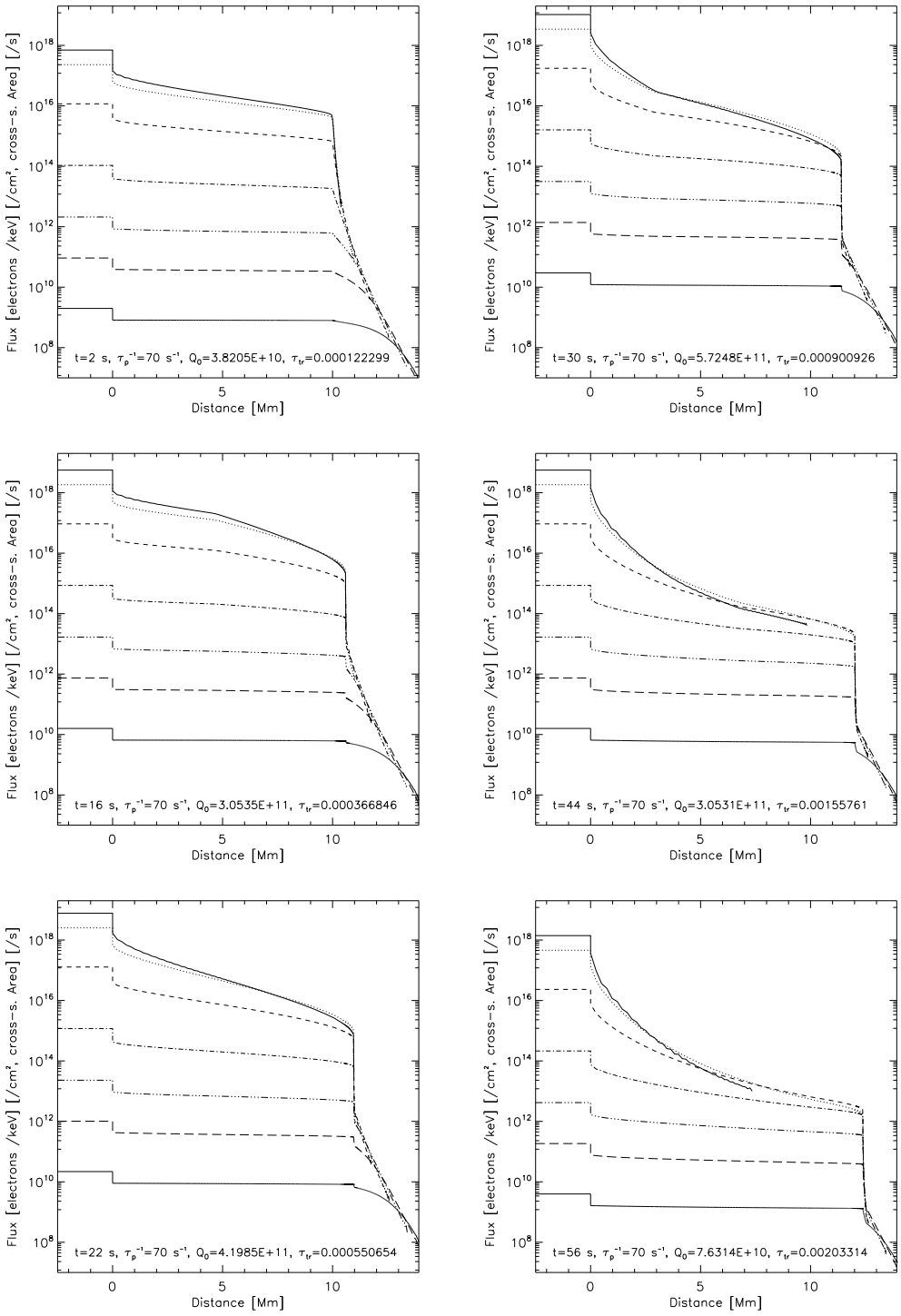

Figure 7.7: Evolution of electron flux vs. depth at different energies for Case A. From top to bottom, the curves correspond to electron energies of 3.1, 6.1, 12.3, 24.5, 48.8, 97.4, and 294.1 keV, respectively. The steps in the region of negative distance denote the average electron flux ($f_{\rm ac}(E)\beta c$) in the acceleration region, one half of whose length is shown here.

Evolution of Electron Distribution

Figure 7.5 shows the evolution of **electron flux spectrum** at different locations in the loop. The thick solid line represents the equivalent thick-target electron flux (see eq. [7.23]). As expected, it appears to be much harder than the LT flux in the 10–1000 keV range. The broken gray-scale lines (from top to bottom) are for spectra at $s = 4$, 8, 10, 11, 12, and 13 Mm from the LT injection site. Early into the flare ($t = 2\,\mathrm{s}$), the transition region is located at $s = 9.97\,\mathrm{Mm}$ and its column depth $\tau = 1.22 \times 10^{-4}$ (in units of $5 \times 10^{22}\,\mathrm{cm}^{-2}$). At this time, the top two gray-scale lines (solid and dotted) indicate spectra in the corona, which are very similar to the escape flux because of small column depths from the injection site. The other four gray-scale lines are spectra below the transition region, which, as expected, become harder with an increasing deficit of low-energy electrons as column depth increases. This is because only high-energy electrons can penetrate deep into the chromosphere.

In this simulation case, because the LT spectrum shape does not change with time (so does the escape flux and thick-target flux), the spectrum at a particular column depth should also remain constant in shape and only vary in normalization. However, as time progresses, evaporation takes place and the height of the transition region drops, while the coronal density increases. This causes variations with time of the column depth (and the electron spectrum) at each position in space. This is just what we see here. At $t = 56\,\mathrm{s}$, for example, the transition region shifts down to $s = 12.4\,\mathrm{Mm}$ at a column depth of $\tau = 2.02 \times 10^{-3}$. In the lower-right panel of Figure 7.5, only one chromospheric spectrum is left, and the other (coronal) spectra are very alike because they are exposed in the corona and their column depths are very close.

We can also check the electron **flux distribution vs. distance** at different energies, which is shown in Figure 7.7. We also display the flux in the acceleration region (LT) for comparison as the region of negative distance. In general, the electron flux decreases with distance from the injection site. The slope of these curves is steeper for low energy electrons than that for high-energy electrons because low-energy electrons lose energy faster (due to the $1/\beta$ dependence of Coulomb loss rate). The flux drops much steeper in the chromosphere (than in the corona) because of its high density and thus large column depth per unit distance. This produces a break in the curve around the transition region and wherever a sharp density change occurs. At $t = 16\,\mathrm{s}$, for example, a break near $s = 5\,\mathrm{Mm}$ is obvious for electron energies of 3.1 and 6.1 keV. This is actually where the evaporation front is located. At $t = 22\,\mathrm{s}$, because the evaporation front already reaches the apex of the loop and the density in the whole loop has increased significantly, the electron flux distribution is much steeper than before in the whole coronal portion. Similar evaporation signatures are present throughout the duration of the flare (see the right column of Fig. 7.7).

Evolution of Bremsstrahlung Radiation

Figure 7.8 shows the bremsstrahlung **photon spectra** at different depths that are produced by the accelerated electrons discussed above (see the corresponding Fig. 7.5). Likewise, the LT photon spectrum (*thick dashed*) also shows a thermal-like component in the low-energy range. It hardens in the intermediate energy range and softens again to the high-energy end. The FP spectrum (*thick solid*) is much harder (than the LT spectrum), and in the range from tens of keV to a few hundred keV, it mimics the commonly observed power-law

FP spectrum. As distance increases, the spectrum (*thin lines*) becomes harder because the electron spectrum has the same trend of variation.

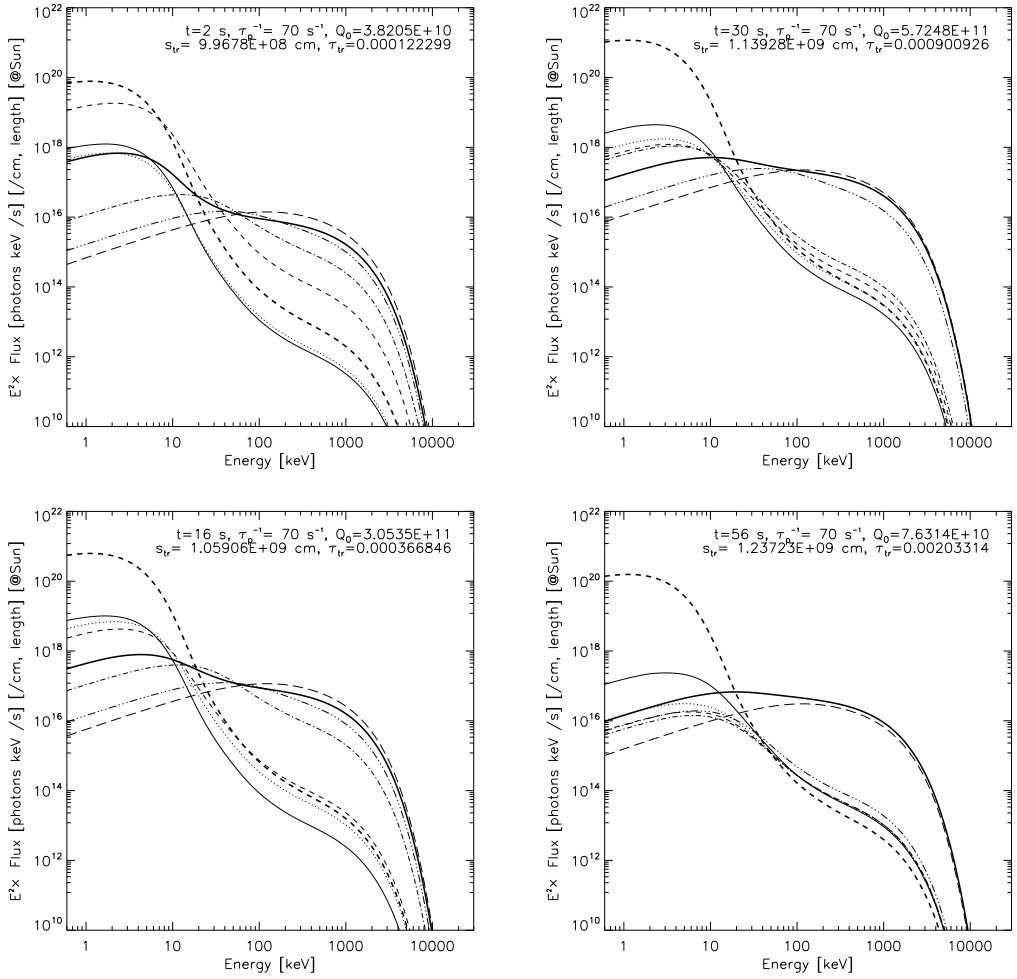

Figure 7.8: Evolution of νF_ν photon spectra at different locations for Case A. The spectrum is of photons emitted by a unit length of the loop, integrated over the loop cross-sectional area. The thick dashed line indicates the LT spectrum, and the thick solid line is the averaged spectrum below the transition region, which is analogous to observed FP spectra. The thin lines, same as those in Fig. 7.5, are for distances s = 4, 8, 10, 11, 12, and 13 Mm from the LT.

Note that, at $t = 2s$, the two coronal spectra (*thin solid* and *dotted*, close to the LT spectrum in shape) are lower than the first chromospheric spectrum (*thin dashed*) at all energies. This is because early in the course of the flare, the coronal density is low and thus the bremsstrahlung production there is at a low level too. As evaporation develops and the coronal density increases, the photon spectrum in the upper-corona portion ($s \leq 8\,\mathrm{Mm}$) of the loop becomes harder because the electron spectrum there hardens. At the same time, as more and more volume of the loop turns into the corona (since the transition region drops), some locations previously buried in the chromosphere are now exposed in the corona. These

locations have lower (than before) column depth and thus softer electron spectrum, which produces softer photons spectrum as well. This can be seen from the evolution of the three spectra at s= 10, 11, and 12 Mm in Fig. 7.8. At $t = 56$ s, all the thin-lined spectra (except the long-dashed line) are from coronal locations and they appear alike in both shape and normalization simply because the density differences among these locations are now much smaller than before.

The **spatial distribution** of the photon emission at different energies (same as in Fig. 7.7) is plotted in Figure 7.9. On the early stage of the flare evolution, low-energy emission comes primarily from the LT, while high energy emission is concentrated below the transition region. Because the bremsstrahlung radiation is proportional to the product of the electron spectrum and the local proton density, the photon emission profile can reveal more details of the density distribution than the electron flux profile (Fig. 7.7). As is evident, the emission profile follows the density features (including the evaporation front and the density spike at the transition region, see Fig. 7.6) very well. As the flare develops and evaporation continues, more and more emission comes from the coronal portion of the loop. At low energies, the emission drops with distance much steeper than before in the corona due to the dramatic density increase there. At intermediate energies, we find a temporal transition from FP-dominated emission to LT-dominated emission. At very high energies, such a change is not present because even the high density corona is still more or less transparent for high energy electrons. However, the retreat of the transition region down to chromospheric heights is visible in all the emission profiles.

We should bear in mind that all the emission features described here are not necessarily observable given the current technology and spatial resolution of the active space missions. However, it is worth trying to make a comparison with observations. As shown in Chapter 6, in the 2003 November 13 flare, we identified an XR emission feature that shifts from the FP toward the LT with time. In this simulation case, we also find the bremsstrahlung XR emission tracks the evaporation front. At low energies, e.g., $E = 3$ keV, there is a local brightness enhancement at the evaporation front due to the sharp jump of density and thus increased bremsstrahlung productivity. Such a local brightness blob can exceeds the FP intensity (spatially integrated and averaged) and is comparable to the LT intensity. In principle, this blob could be imaged by *RHESSI* and could be responsible for the observed moving source. Note that at high energies, although the evaporation front is also visible in the HXR emission profile, its intensity is dwarfed by the FP emission and thus is not observable due to limited dynamic ranges of the instruments (e.g., 10 for *RHESSI*). On the other hand, thermal emission from the heated and evaporated plasma could also contribute to low energy X-rays, and such contributions could be comparable at certain energies. Of course, as photon energy increases, the thermal emission drops quickly due to its exponential decay with energy; and thus thermal contribution at high energies are negligible compared with nonthermal emission. At what photon energy thermal and nonthermal emissions are comparable? Answers to this question depends on the electron spectrum, as well as the density and temperature distribution of the thermal plasma. It would be interesting to check the relative importance of thermal vs. nonthermal emission and their spatial distribution, with different model parameters. Unfortunately, such a study would be beyond the scope of the current investigation.

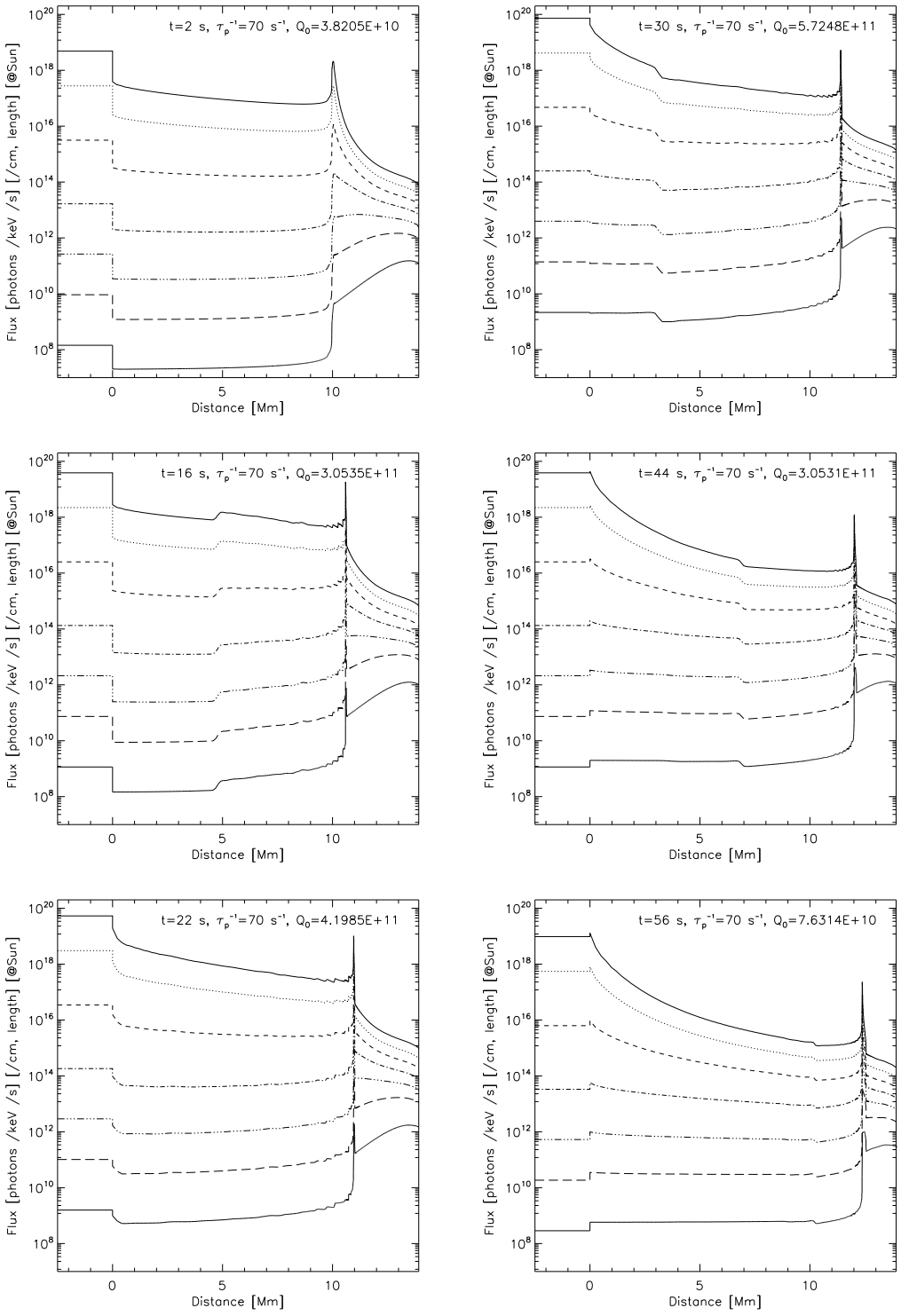

Figure 7.9: Evolution of photon emission vs. depth at different photon energies of Case A. As in Fig. 7.7, the energies are 3.1, 6.1, 12.3, 24.5, 48.8, 97.4, and 294.1 keV.

7.3.3 Case B: Variable Electron Spectrum

This is the second simulation case using the combine particle and HD code. In addition to the time modulation of the spectrum normalization, we vary the acceleration rate τ_p^{-1} linearly with time, in the same triangular pattern. This means that the electron spectrum experiences a *soft-hard-soft* variation, as is commonly observed in solar flares (Grigis & Benz, 2004), and can be seen here.

Figure 7.10 shows the evolution of the **electron spectra** at different depths. Clearly, at the beginning ($t = 0\,\mathrm{s}$) when there is very little acceleration ($\tau_p^{-1} = 2.33\,\mathrm{s}^{-1}$), the spectra at all the depths look similar to the injected thermal distribution (not shown) which has a sharp exponential cutoff. Note that some electron spectra at large depths are too small to appear in the plot due to the extreme softness of the spectrum and the resulting sharp decrease of electron flux with distance. As time proceeds and the acceleration rate increases, the spectrum becomes harder and harder, particularly in the energy range of $[10, 10^3]$ keV. At $t = 30\,\mathrm{s}$, the thick-target flux exhibits a hump with a positive slope. Meanwhile, the quasi-thermal component at the low-energy end is present all the time. After the peak time of 30 s, spectrum softening takes place and the spectrum shape returns to that of the quasi-thermal one in the end. The corresponding photon spectra (Fig. 7.11) show the same trend of soft-hard-soft variation. Other spectrum (of both electrons and photons) variations (such as those due to chromospheric evaporation) are similar to those of Case A.

Figure 7.12 shows the evolution of the electron flux (*left*) and photon intensity (*right*) **vs. distance** at different energies, which is similar to that of Figures 7.7 and 7.9, respectively. One of the main differences is that electron spectrum here is soft on the early and late stages, and consequently the plot spans a wide range on the vertical scale.

Another spectrum feature that makes Case B different from Case A is the **escaping electron flux**. As we can see from Figure 7.10, on the early and late stages of the flare when the acceleration rate is low, the escape flux (*thick dotted*) and the LT flux (*thick dashed*) are almost identical above $\sim 10\,\mathrm{keV}$; below such an energy, their difference increases with decreasing energy. Around the acceleration rate peak time (similar in Case A), such an critical energy shifts to $> 10^3$ keV. This is because the escape flux is inversely proportional (eq. [7.21]) to the escape timescale, $T_{\rm esc}$, which depends on the scattering timescale $\tau_{\rm sc}$ through equation (7.20). From equations (7.22), (7.16), and (7.12), we see the escape-to-LT electron flux ratio $R_{\rm esc}$[14] is a decreasing function of the acceleration rate τ_p^{-1}. When τ_p^{-1} is low and the scattering timescale $\tau_{\rm sc}$ is large, at a given energy, $R_{\rm esc}$ would be relatively large. Because of this, there are relatively more electrons that escape the acceleration region and deposit their energy into the loop in Case B than in Case A, since here τ_p^{-1} has a triangular time profile with its peak value equal to that of Case A (which is constant in time there). We find the mean energy deposition flux here is $9.8 \times 10^{10}\,\mathrm{ergs\,s^{-1}\,cm^{-2}}$, while in Case A it is $8.3 \times 10^{10}\,\mathrm{ergs\,s^{-1}\,cm^{-2}}$ (also see Table 7.1). Since this case has a larger energy input rate, we would expect stronger chromospheric evaporation here, which we discuss below.

Let us now check the corresponding **HD evolution**, which is shown in Figure 7.13 At the very beginning, because very little acceleration takes place and the spectrum is very soft, the energy deposition curve drops sharply (cf., Case A) with depth into the chromosphere.

[14]The functional (vs. E) form of $R_{\rm esc}(E)$ would depends on that of $T_{\rm esc}(E)$ or $\tau_{\rm sc}(E)$. See Figs. 11 and 12 in PL04.

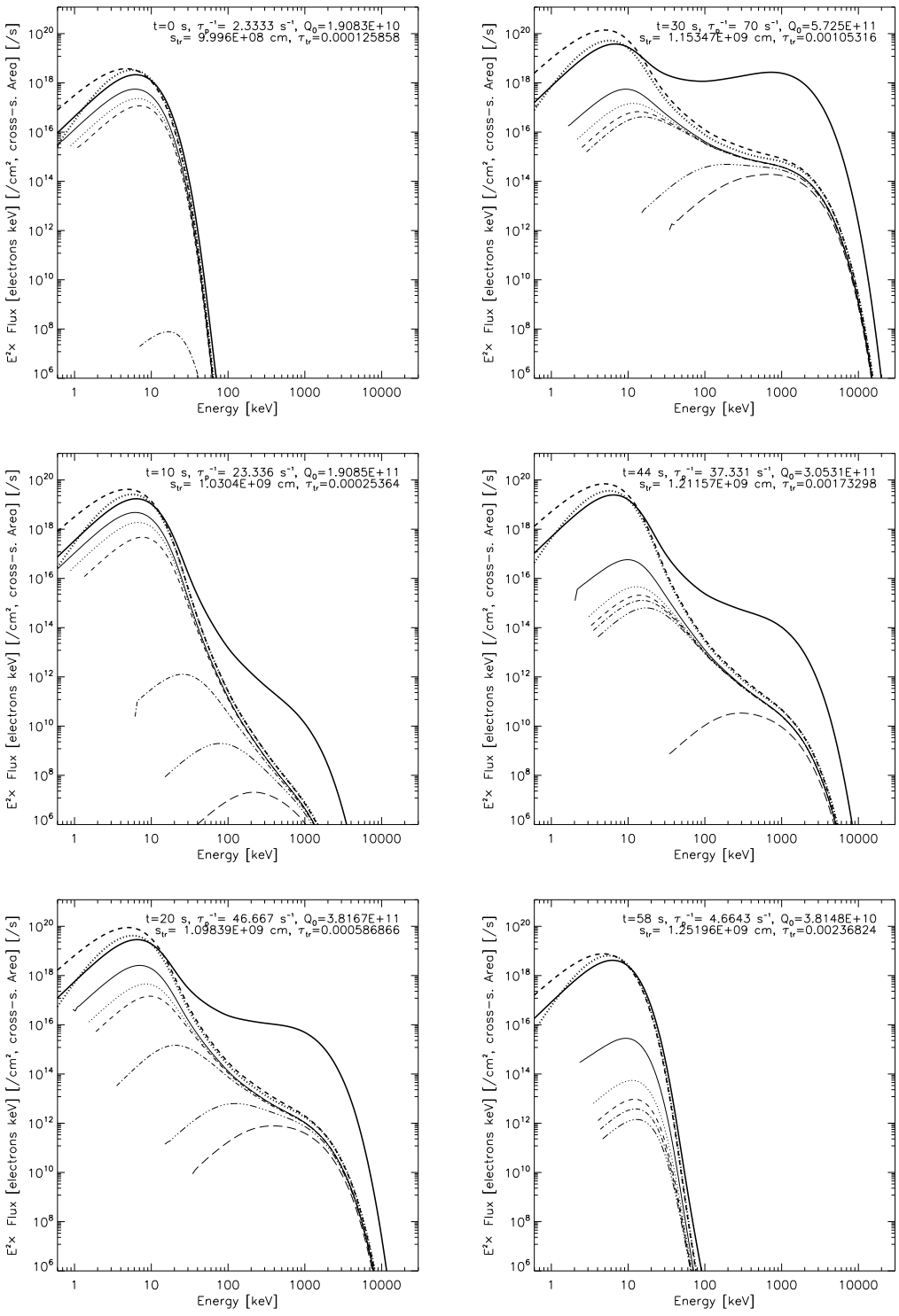

Figure 7.10: Same as Fig. 7.5 (electron spectra at different depths), but for Case B. Note that at $t = 0\,\mathrm{s}$, some spectra at large depths ($s > 10\,\mathrm{Mm}$) are too small to be shown.

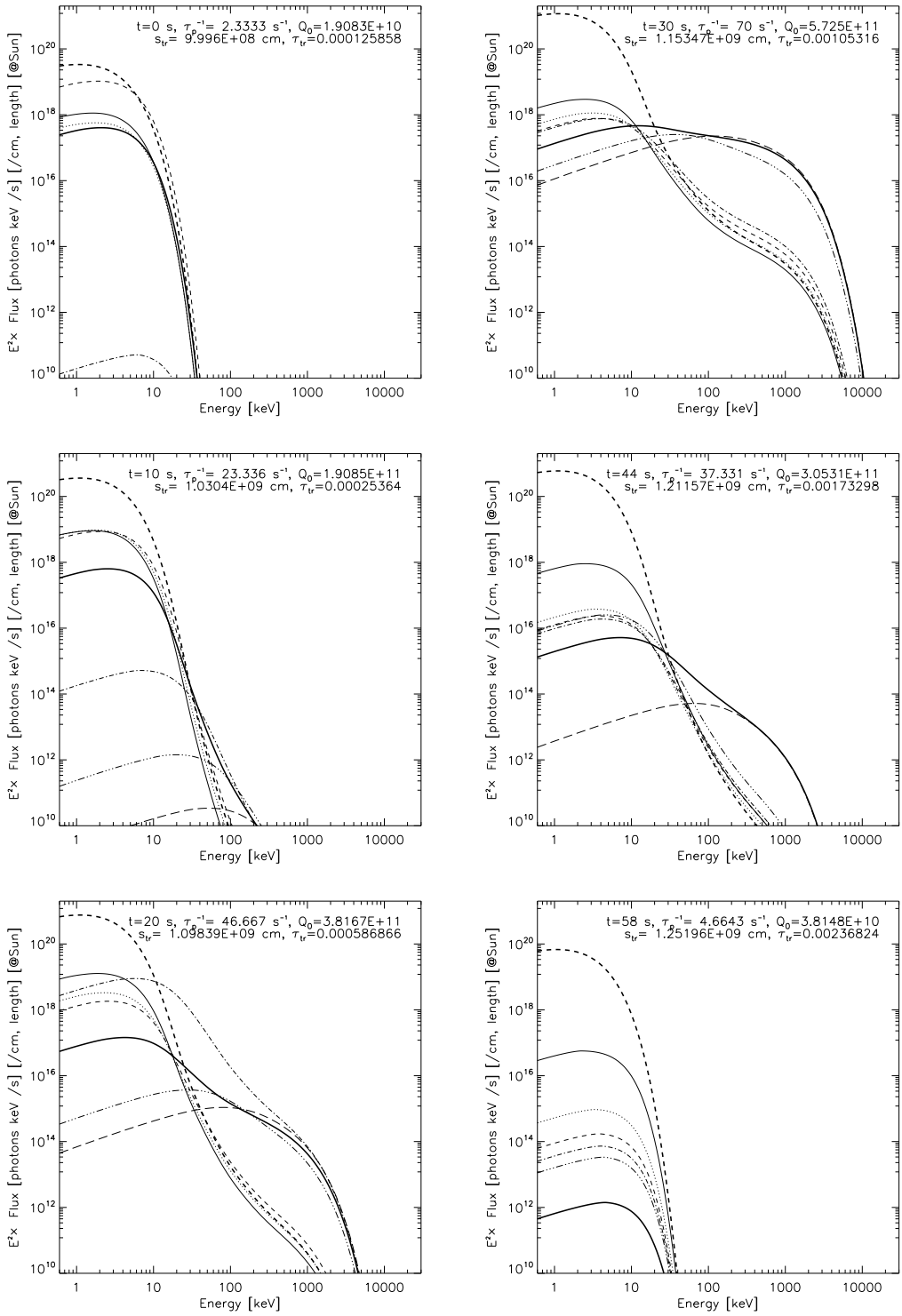

Figure 7.11: Same as Fig. 7.8 (evolution of photon spectra at different depths), but for Case B.

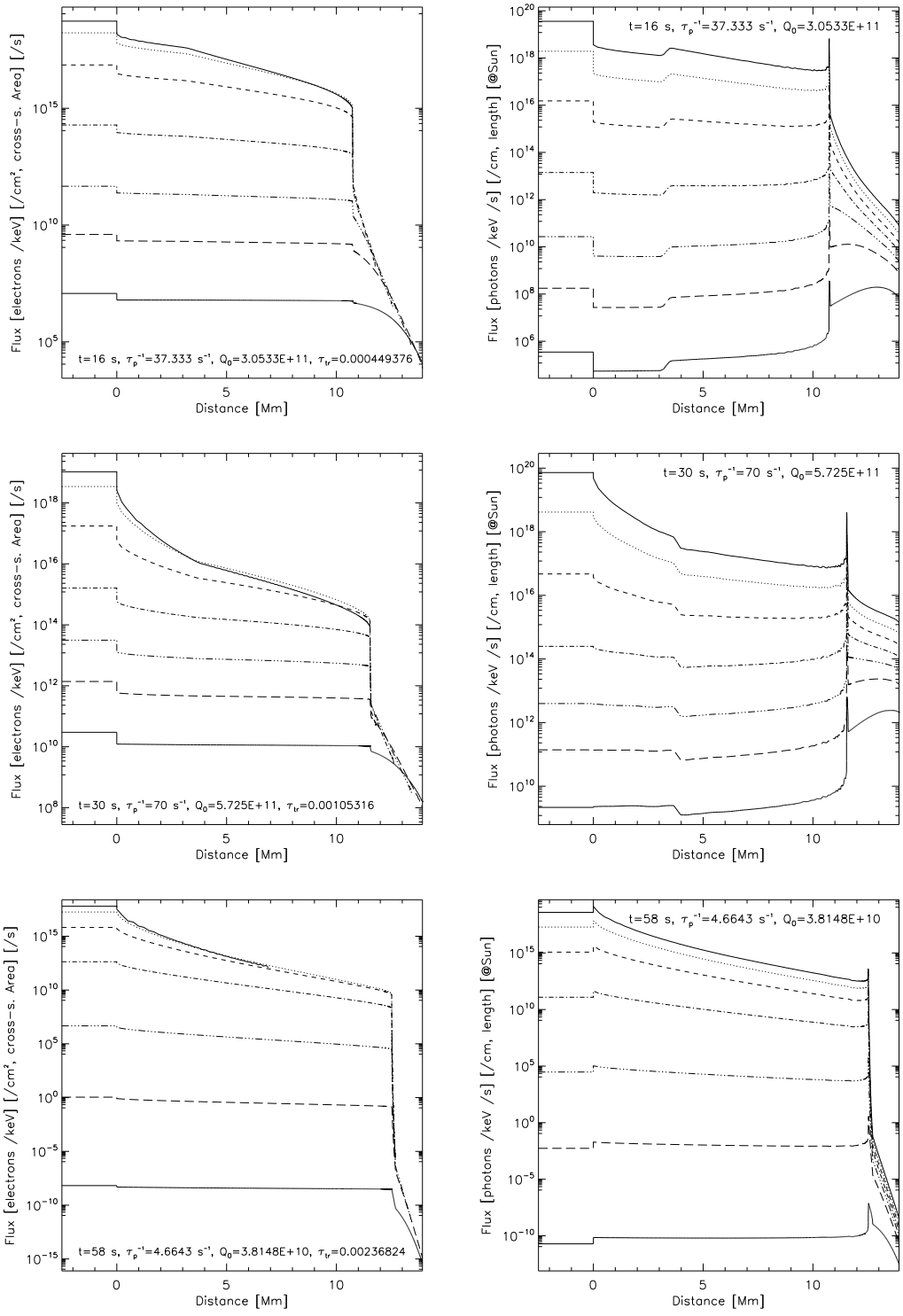

Figure 7.12: Evolution of electron (*left*) and photon (*right*) fluxes vs. distance at different energies (same as Figs. 7.7 & 7.9) for Case B. Time goes from top to bottom (note different vertical scales).

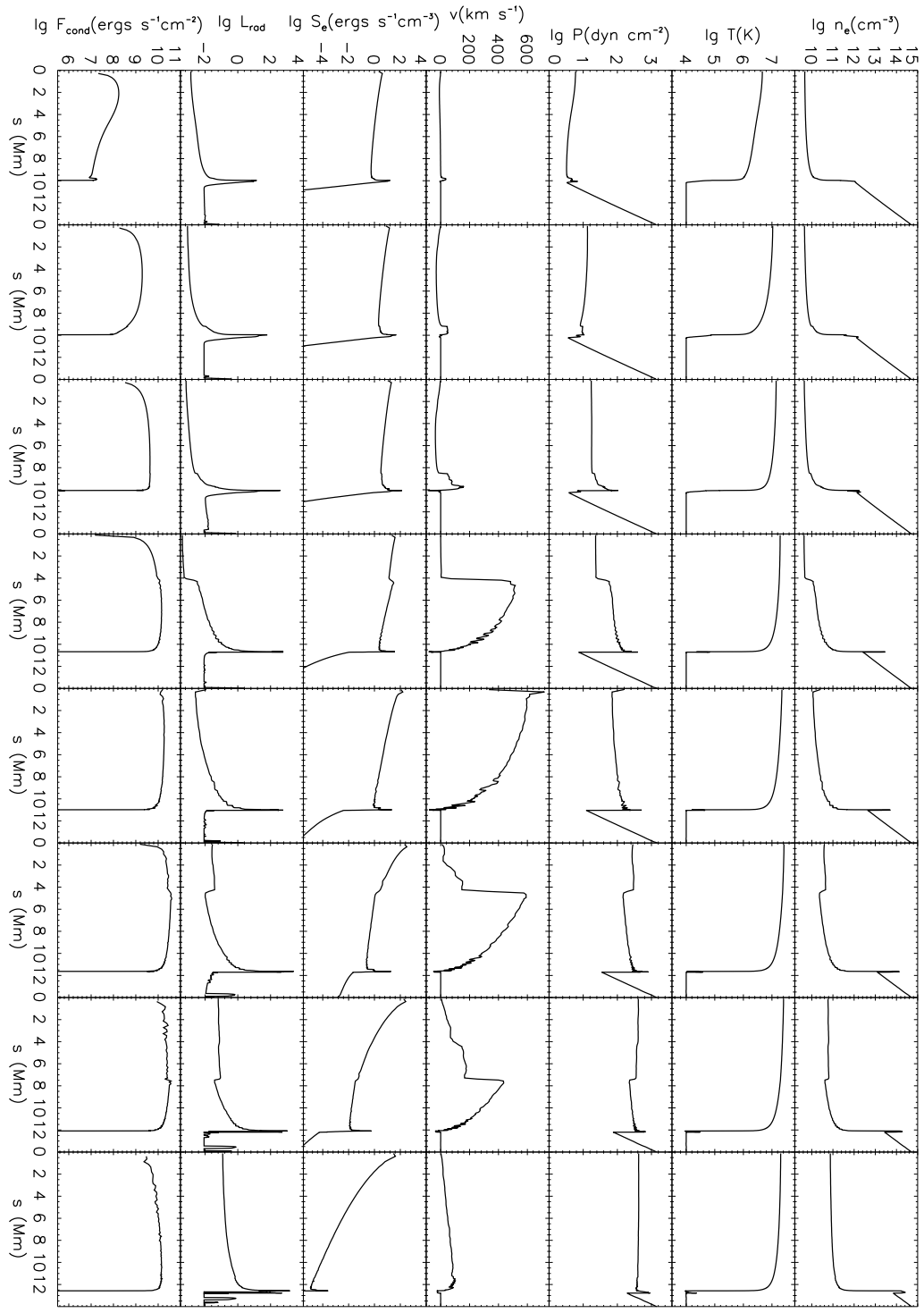

Figure 7.13: HD evolution of various quantities for Case B.

As noted earlier, low-energy electrons are more efficient at heating the corona and we would expect that the softer spectrum, on top of the larger escaping electron flux discussed above, will generally result in stronger coronal heating. This is just the case in this run, which shows a faster evolution and more dramatic evaporation than Case A. At $t = 7\,\mathrm{s}$ (vs. 9 s in Case A), the peak conduction has already reached the transition region and upflow velocity has become greater than $100\,\mathrm{km\,s^{-1}}$. At $t = 20\,\mathrm{s}$ (cf., 22 s in Case A) the evaporation front is reflected at the loop apex and at the same time the upflow attains its maximum velocity of $718\,\mathrm{km\,s^{-1}}$ (cf., $627\,\mathrm{km\,s^{-1}}$ at $t = 32\,\mathrm{s}$ in Case A). This case has also the highest values of maximum downflow velocity, maximum coronal temperature and density out of the five cases under study (see Table 7.1).

7.3.4 Case C: Harder Electron Spectrum

In this case, we set $\tau_p^{-1} = 100\,\mathrm{s^{-1}}$, which means higher rate of acceleration, and we would expect harder electron spectrum than Case A ($\tau_p^{-1} = 70\,\mathrm{s^{-1}}$). This is true as can be seen from the electron and photon spectra shown in Figure 7.14. Compared with Case A, the electron (*left*) flux also decreases with distance slightly slower and the photon (*right*) distribution shows relatively more emission coming from below the transition region than in the corona (see Fig. 7.15). The normalization of HXR emission[15] is also much higher than that of Case A, again, because the harder electron spectrum here has a higher bremsstrahlung yield (see, e.g., Fig. 6.11).

Another effect of the larger acceleration rate is the relatively smaller flux of escaping electrons that enters the loop. Although there are more electrons in the high-energy portion of the spectrum (thus more energy content there), most of the energy is still contained in the low-energy electrons because of the steepness of the spectrum). Therefore, the addition of energy due to more accelerated high-energy particles is relatively small, and it loses to its competing factor, i.e., the smaller escape flux, which produces a smaller overall energy flux input to the loop than Case A.

We note from Figure 7.16 that the energy deposition rate decreases slower with distance in the corona and beyond the transition region, particularly in the late phase of the flare, than that in Case A. This is due to the harder spectrum we have here, which produces slightly less coronal heating and more chromospheric heating. In addition, the relatively smaller escaping electron flux here results in less energy flux. For the same reasons discussed above, as opposed to Case B, we would also expect slightly weaker evaporation and slower evolution of the plasma, which is the case (see Table 7.1 and Figs. 7.19 and 7.16). For example, the maximum coronal temperature and density are $2.48 \times 10^7\,\mathrm{K}$ and $7.84 \times 10^{10}\,\mathrm{cm^{-3}}$, respectively, which is on the order of 10% lower than those in Case A. MEL89 reached a qualitatively similar conclusion by using a harder ($\delta = 4$, vs. 6) power-law spectrum.

7.3.5 Case D: Smaller Normalization

In the last case, we used smaller normalization of $Q_0 = 5.73 \times 10^{10}\mathrm{particles\,s^{-1}\,cm^{-3}}$, which is about one order of magnitude smaller than the fiducial Case (A). This change is

[15]The spatially integrated HXR light curve and its normalization can be seen in Fig. 8.11 of next chapter too.

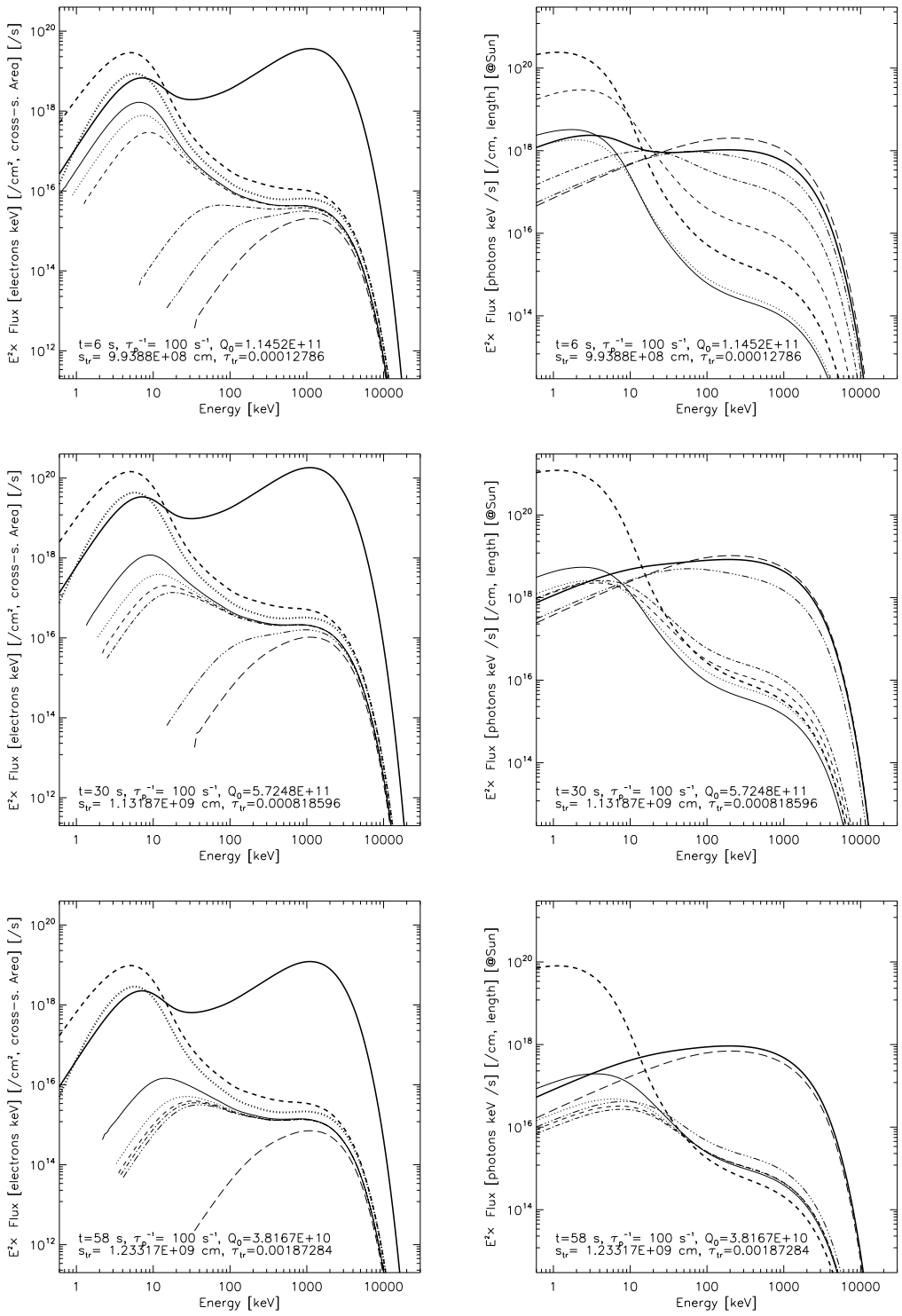

Figure 7.14: Evolution of electron (*left*) and photon (*right*) spectra at different depths for Case C. Time goes from top to bottom (similar to Figs. 7.5 and 7.8).

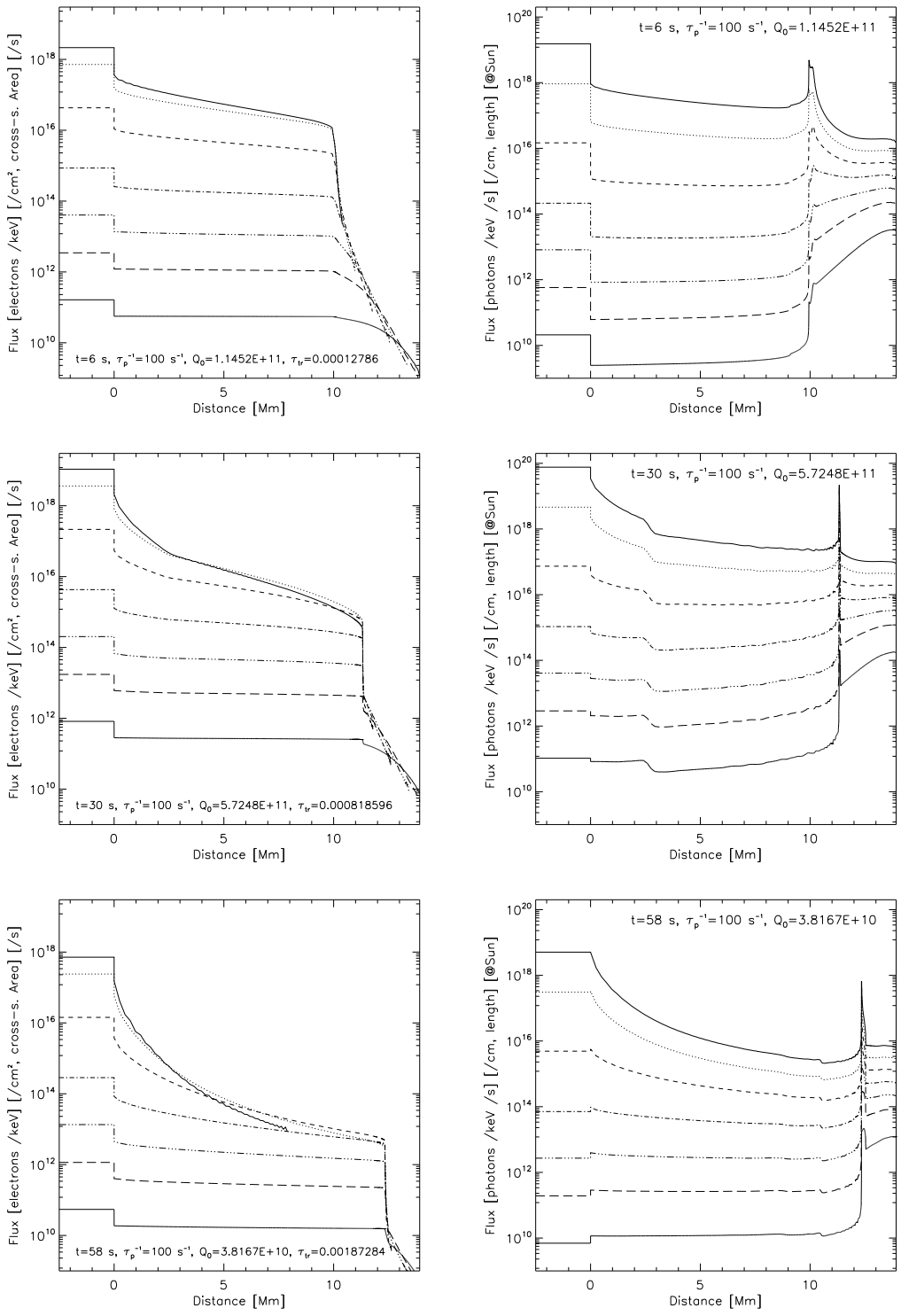

Figure 7.15: Evolution of electron (*left*) and photon (*right*) fluxes at different energies for Case C (similar to Figs. 7.7 and 7.9).

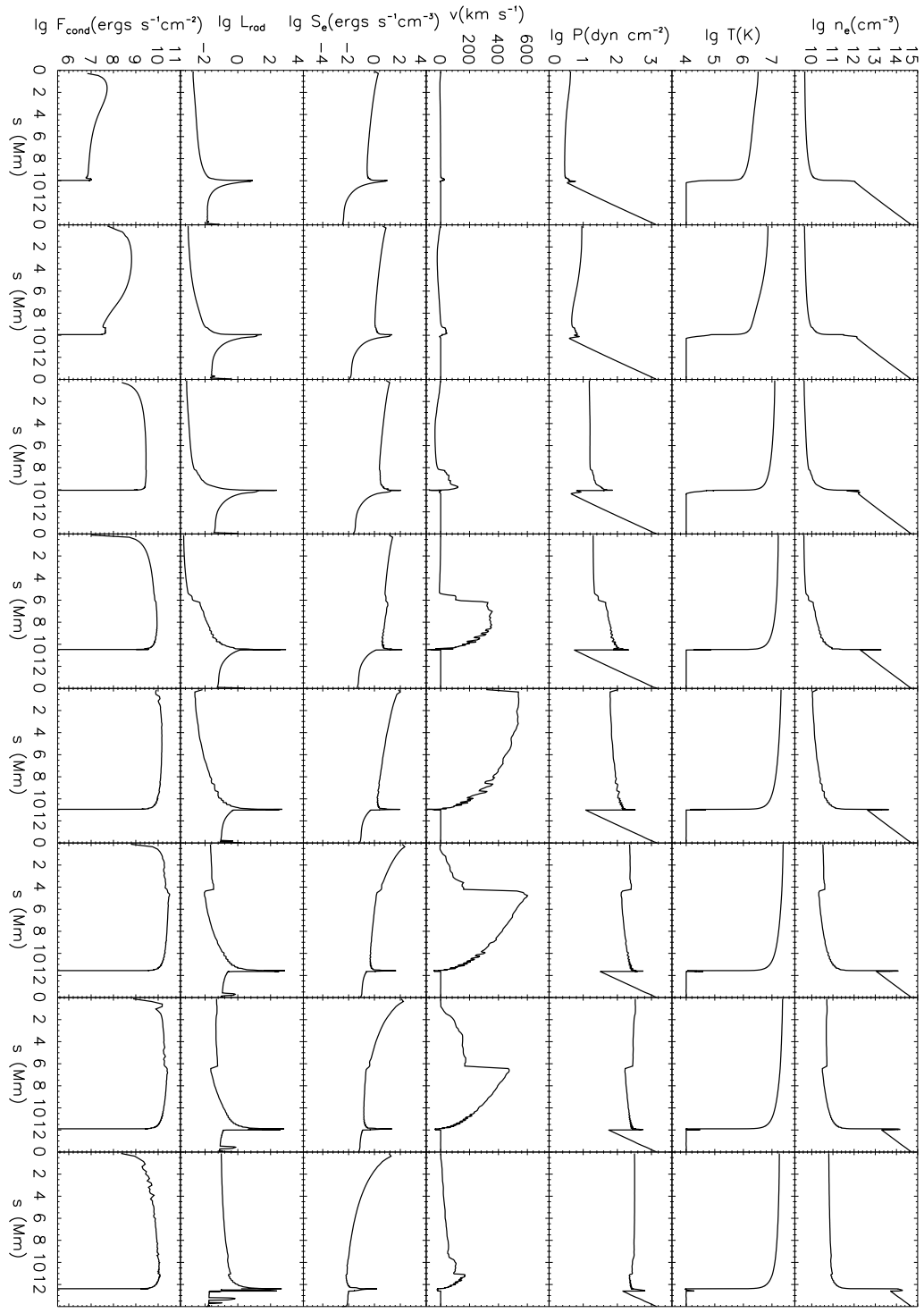

Figure 7.16: HD evolution of various quantities for Case C.

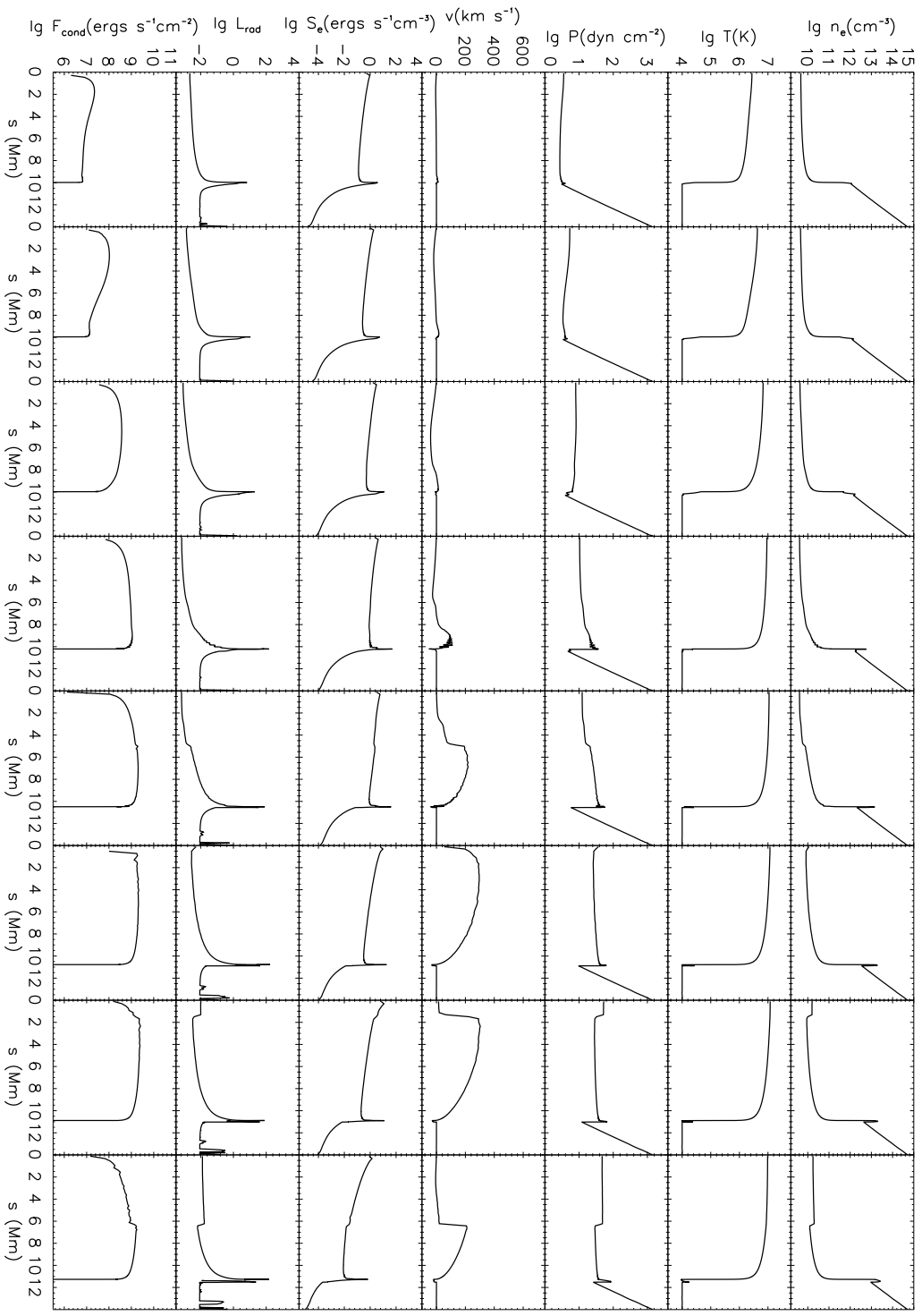

Figure 7.17: HD evolution of various quantities for Case D.

similar to those adopted in earlier HD simulations (see, e.g., Fisher et al., 1985c). The electron and photon spectra and spatial distribution are shown in Figure 7.18, which, as expected, all show similar shape as in Case A, but with a smaller normalization. As to the hydrodynamics, we would accordingly expect much weaker evaporation and slower and less dramatic HD evolution, as can be seen from Figure 7.17.

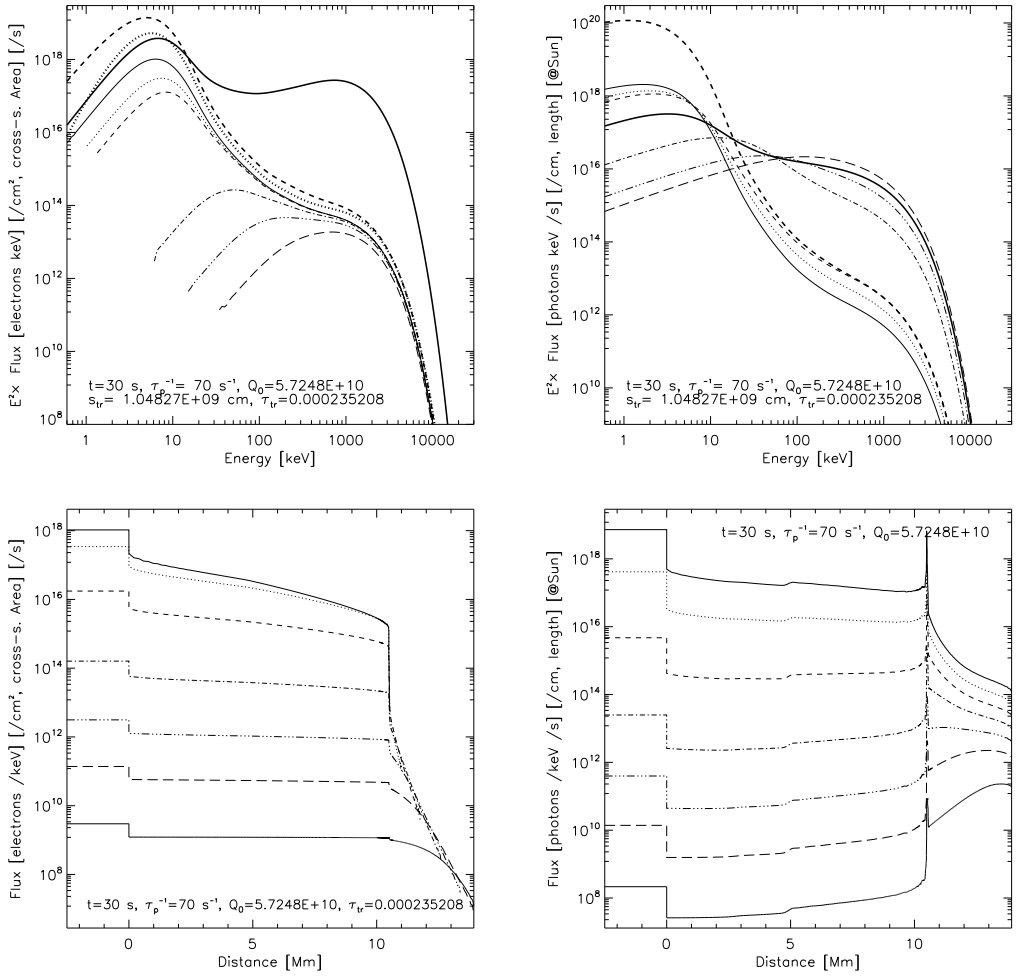

Figure 7.18: Electron & photon spectrum and flux spatial distributions for Case D at the peak injection time.

We note that, in this simulation case, we have a very low peak energy deposition flux of $2.58 \times 10^9\,\mathrm{ergs\,cm^{-2}\,s^{-1}}$, while the maximum upflow velocity is at a moderate value of $303\,\mathrm{km\,s^{-1}}$. Fisher et al. (1985c), however, reported that the evaporation velocity is sensitive to the energy flux carried by nonthermal electrons, and they found an energy flux $F < 3 \times 10^{10}\,\mathrm{ergs\,cm^{-2}\,s^{-1}}$ results in a gentle evaporation ($v < 100\,\mathrm{km\,s^{-1}}$). This difference is because Fisher et al. (1985c) considered a power-law electron spectrum with a sharp low-energy cutoff of 20 keV (cf., 15 keV of MEL89), while our model has a continuous electron distribution extending from the thermal background at low energies to the nonthermal tail

at high energies. For the same reason noted above, low-energy electrons are more efficient in evaporating the chromospheric plasma via conduction. Consequently, although Case D has a low energy flux, it can produce a moderately high evaporation velocity, because a significant portion of this energy flux resides in low-energy particles. In addition, Fisher et al. (1985c) used an index of $\delta = 4$ for the power-law electron spectrum, which is somewhat hard and thus less effective in evaporating chromospheric material than a softer electron population. We also note that Milligan et al. (2006), in supporting the result of Fisher et al. (1985c) from their joint EUV Doppler and HXR observations, also used a power-law electron spectrum with a cutoff energy.

7.3.6 Comparing The Cases: A Summary

Table 7.1: Summary of simulation cases.

Cases	τ_p^{-1} (s^{-1})	Q_0	$F_{\max}$	$\bar{F}$	$v_{\max}$ ($\mathrm{km\,s}^{-1}$)	$t_{v_{\max}}$ (s)	$v_{\min}$ ($\mathrm{km\,s}^{-1}$)	$t_{v>100}$ (s)	t_{apex} (s)	$T_{\max}$ (10^7 K)	$n_{\max}$ ($10^{10}\,\mathrm{cm}^{-3}$)
R	$\delta = 6$ $E_1 = 15\,\mathrm{keV}$	—	2.54	8.58	565	35	-115	10	29	2.11	6.96
A	70, const	57.3	2.56	8.30	627	32	-113	9	22	2.61	8.82
B	peak=70	57.3	2.54	9.80	718	20	-194	7	20	2.65	9.84
C	100, const	57.3	2.21	7.20	601	35	-153	9	23	2.48	7.84
D	70, const	5.73	0.258	0.853	303	43	-90.3	22	39	1.20	1.93

NOTE — τ_p^{-1} is set as a constant except for Case B in which τ_p^{-1} varies linearly with time and its peak value is 70; Q_0 (in $10^{10}\,\mathrm{s}^{-1}\,\mathrm{cm}^{-3}$): peak value of injected number of electrons; $F_{\max}$ (in $10^{10}\,\mathrm{ergs\,s}^{-1}\,\mathrm{cm}^{-2}$) and $\bar{F}$ (in $10^{9}\,\mathrm{ergs\,s}^{-1}\,\mathrm{cm}^{-2}$): peak and mean energy deposition flux integrated over the whole loop; $v_{\max}$ and $t_{v_{\max}}$: maximum upflow velocity and time at which it is reached; $v_{\min}$: maximum downflow velocity, appearing in the upper chromosphere; $t_{v>100}$ and t_{apex}: time at which the upflow velocity exceeds $100\,\mathrm{km\,s}^{-1}$ (usually when the conduction front reaches the transition region) and the density jump (evaporation front) reaches the apex of the loop, respectively; $T_{\max}$ and $n_{\max}$: maximum coronal temperature and density.

We now summarize the comparison among the five cases, particularly of their HD response. The key parameters are listed in Table 7.1. The first two parameters that we care about are the maximum and mean electron energy deposition fluxes ($F_{\max}$ and $\bar{F}$), because they determine, to some extent, the consequent HD evolution. As we can see, in terms of these two parameters, Cases R and A–C are very close, while Case D stands alone as a dwarf (also in terms of all the other parameters). Let us now take a close look at the group of Cases R and A–C, using Case A as the fiducial point.

Case R has a similar value of $F_{\max}$ as Case A (and even a slightly higher $\bar{F}$). However, its HD evolution is less dramatic. Its maximum upflow velocity of $v_{\max} = 565\,\mathrm{km\,s}^{-1}$ is much lower than the $627\,\mathrm{km\,s}^{-1}$ value of Case A; it takes longer (at $t = 29\,\mathrm{s}$) for the evaporation front to reach the loop apex, as opposed to the 22 s of Case A; the maximum coronal temperature of $T_{\max} = 2.11 \times 10^7\,\mathrm{K}$ and maximum coronal density of $n_{\max} = 6.96 \times 10^{10}\,\mathrm{cm}^{-3}$ are lower (by tens of percent) than those of Case A. By these criteria, Case R is also the extreme case of weak evaporation among the whole group of Cases R and A–C. Such a difference, as we elaborated earlier, mainly comes from the different electron spectrum, a power-law with a low-energy cutoff, that Case R assumes, while all the other cases take a continuous spectrum that extends to the low-energy quasi-thermal component. Another contribution to the different HD evolution is that Case R uses the approximate analytical solutions for the heating rate (e.g., Emslie, 1978), while we performed more

rigorous Fokker-Planck calculation for the other cases.

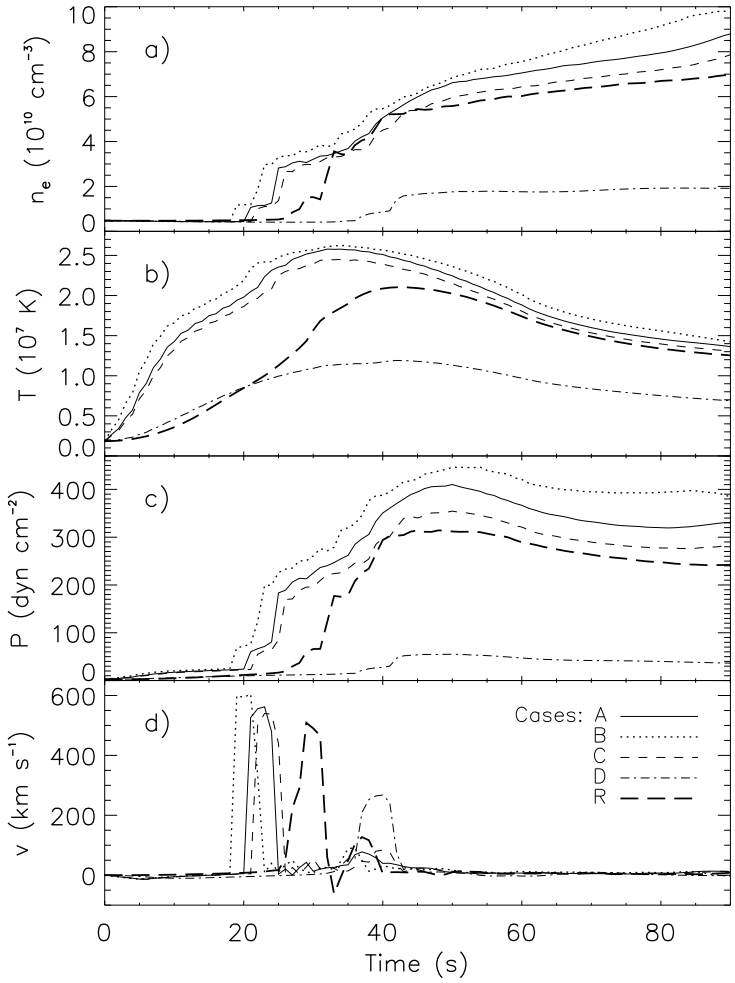

Figure 7.19: Comparison of history of various quantities (electron number density, temperature, gas pressure, and upward velocity) at 1 Mm from the LT for the five cases. Note that each of the density and pressure curve general includes two sharp jumps, which are caused by the arrival of the evaporation front, similar to that shown in Fig. 7.4.

Case B, in contrast, is another extreme in the group of Cases R and A–C. It has a very similar maximum energy flux, compared with Case A, but it has a mean energy flux about 18% higher (also the highest in the group), because Case B has a softer (except at the peak energy input time $t = 30\,\mathrm{s}$) electron spectrum and thus a higher escaping electron flux than Case A. Consequently, this case has the strongest evaporation, with a maximum upflow velocity of $718\,\mathrm{km\,s^{-1}}$, coronal $T_{\max} = 2.65 \times 10^7\,\mathrm{K}$ and $n_{\max} = 9.84 \times 10^{10}\,\mathrm{cm^{-3}}$, all being the highest in the group. This is also because the softer electron spectrum here has relatively more low-energy electrons, who contribute more to heating the corona than heating the chromosphere. This generally results in a higher coronal temperature and more

dramatic chromospheric evaporation, for the reason discussed earlier.

Case C, on the other hand, has a harder electron spectrum ($\tau_p^{-1} = 100\,\mathrm{s}^{-1}$) and somewhat smaller energy input rates ($F_{\max}$ and $\bar{F}$ are smaller than those of Case A by $\sim 13\%$). The harder electron spectrum generally results in more direct chromospheric heating than coronal heating, and it is less efficient in evaporating plasmas due to the competing radiative loss (see earlier discussions). Consequently, the resulting coronal $T_{\max} = 2.48 \times 10^7\,\mathrm{K}$ is 5% lower and $n_{\max} = 7.84 \times 10^{10}\,\mathrm{cm}^{-3}$ is 11% lower, and the maximum upflow velocity of $v_{\max} = 601\,\mathrm{km\,s}^{-1}$ is 4% smaller than that of Case A. We also note Case R has a somewhat larger downflow velocity ($v_{\min} = -153\,\mathrm{km\,s}^{-1}$) than Case A ($v_{\min} = -113\,\mathrm{km\,s}^{-1}$), which is due to more in situ direct chromospheric heating by its harder electron spectrum.

We can appreciate some of the above differences among the simulation cases from a different angle. Figure 7.19 shows the history of the electron number density n_e, temperature T, gas pressure P, and upward velocity v at $s = 1\,\mathrm{Mm}$ (in the corona) from the loop apex for all the five cases. As can be seen, Case D (*dot-dashed*) is an outlier and the curves of other cases (the group of Cases R and A–C) more or less cluster together. Among this group, Case R (*long-dashed*) is much smaller in the values and its response is significantly delayed compared with the other three. Its temperature, in particular, increases more slowly and the maximum value is much less than Cases A–C, whose differences in temperature are much smaller. This indicates much weaker coronal heating in Case R, as mentioned before.

7.4 Summary and Discussion

We have performed a combined simulation of nonthermal particles using the unified *$\mathcal{F}$lare* code (of particle acceleration, transport, and radiation) and of the hydrodynamic response of the atmosphere using the NRL HD code. We summarize our results as follows.

1. We have demonstrated that a combined simulation of particles and HD response is possible and have engineered the two codes to work together. This accomplishment marks a significant advance in computational high-energy solar physics in general and provides a powerful simulation tool to improve our understanding of solar flares in particular.

2. We have shown that using the more realistic electron spectrum from the SA model affects the spatial distribution of energy deposition and thus influences the HD evolution. The quasi-thermal component in the electron spectrum produces more coronal heating than previous models, which have a low-energy cutoff (e.g., $E_1 = 15\,\mathrm{keV}$) in the power-law distribution and thus have more direct chromospheric heating. Because of the cospatial radiative loss in the upper chromosphere, direct chromospheric heating results in a significant portion of the energy being radiated away and less energy left available to evaporate the plasma. In this sense, our new model generally drives chromospheric evaporation more efficiently.

3. The change of the acceleration rate (τ_p^{-1}) affects the accelerated electron spectrum, as well as the escaping electron spectrum, and thus modifies the consequent HD evolution. In general, a higher acceleration rate produces a harder electron spectrum but smaller escaping electron flux, because stronger turbulence scatters particles more

and traps them longer in the acceleration region. These two factors add together to produce less coronal heating (although relatively more chromospheric heating). Therefore, for the same reason mentioned above, this results in a comparably weaker chromospheric evaporation for a harder electron spectrum.

4. For the reasons noted above, the overall energy input rate is only one indicator, to some extent, of the agent for HD energetics. A smaller energy deposition flux (e.g., the $\bar{F}$ value, Case A vs. Case R) does not necessarily yield a slower HD evolution or a weaker chromospheric evaporation. Therefore, detailed energy deposition by electrons, particularly its spatial distribution affects the resulting HD response.

5. Variation in the electron spectrum influences the HD response and bremsstrahlung emission in different ways. A harder electron spectrum can produce HXRs more effectively due to its higher bremsstrahlung yield, but does not necessarily produce more heating (e.g., Case C). Therefore, HXRs alone should not be used as an indicator of the electron energy input rate or subsequent plasma heating. This will be addressed in detail regarding the Neupert effect in next chapter.

This simulation experiment has just been started. However, it opens a door to a vast area of applications to many other research areas where particle acceleration and transport and plasma flows are present, such as stellar flares and flares near the black holes and on the accretion disks. For example, We (Liu, W. & Airapetian, 2008) have proposed to apply this technique to simulate auroral processes on Jupiter-like planets around red giants. There is plenty of room for future improvement in both numerics and physics, which will be discussed in the Chapter 10.

Chapter 8

Testing the Neupert Effect With the Combined Fokker-Planck and Hydrodynamic Codes

8.1 Energy Budget and the Neupert Effect

As shown in Chapter 6 (also Liu, W. et al., 2006), a simple test of the Neupert effect does not yield a better correlation between the SXR derivative and the electron power than that between the former and the HXR flux. This is not expected to be the case, but it is not surprising either because of nonlinearity involved in the energy redistribution and radiation processes. To further understand this question, one needs to check the energy budget and calculate HXR and SXR radiation properly. Veronig et al. (2005) investigated the Neupert effect using *RHESSI* observations and reached similar conclusion as we did. However, they calculated the various energy contents in an approximate way. The combined HD and particle calculation we have done here can help shed light on this question more quantitatively.

In general, the total energy $U(t)$ in the plasma consists of thermal energy $U_{\rm th}(t)$, kinetic energy $U_k(t)$, and gravitational energy $U_g(t)$.

$$U(t) = U_{\rm th}(t) + U_k(t) + U_g(t), \tag{8.1}$$

which can be readily calculated (integrating over the loop volume) from the distribution of density ρ (or n_e and n_i), temperature T, velocity v. For example,

$$U_{\rm th} = \int \frac{P}{\gamma - 1} dV = \int 3 n_e k T dV, \tag{8.2}$$

for $\gamma = 5/3$, and $n_e = n_i$. We set the reference level (zero height) of the gravitational potential at the bottom boundary (about 4 Mm below the transition region) and this gives the the value of U_g about 1/3 of the total energy in the initial state ($t = 0$). We find in all of our simulations that the temporal variation rate of the gravitational energy only constitutes about 1% of that of the total energy and thus is unimportant in the energy budget (and

not shown in our discussion below). The time derivative of these energies,

$$\dot{U}(t) = \dot{U}_{\rm th}(t) + \dot{U}_k(t) + \dot{U}_g(t), \tag{8.3}$$

gives the net energy gain of the system and should be balanced by the energy input (by electrons) rate $\dot{\mathcal{E}}_e$ and the energy loss rate L, namely,

$$\dot{U} = \dot{\mathcal{E}}_e - L\,. \tag{8.4}$$

The total energy loss rate generally has two components, radiative loss ($L_{\rm rad}$) and conductive loss ($L_{\rm cond}$) from the loop volume. In this particular study, the conduction flux vanishes at both the top and bottom boundaries, where we set the symmetric boundary condition and fix the temperature at $T = 10^4\,{\rm K}$, respectively, both giving rise to $\nabla T = 0$. Therefore, the only energy loss channel is through radiation (UV and optical),

$$L = L_{\rm rad} + L_{\rm cond}\,;\;\; L_{\rm cond} = 0 \implies L = L_{\rm rad}\,. \tag{8.5}$$

Thermal bremsstrahlung radiation at photon energy ϵ produced by a single temperature (i.e., Maxwellian distribution) plasma can be calculated via (Cox 2000, p. 184; Tandberg-Hanssen & Emslie 1988 p. 114):

$$I_{\rm SXR} = D({\rm EM})\frac{\exp(-\epsilon/kT)}{\epsilon\sqrt{T}}g(\epsilon/kT), \tag{8.6}$$

in which

$$D = (8/\pi m_e k)^{1/2}\,\kappa_{BH} Z^2 = 5.7\times10^{-12} Z^2 (\,{\rm cm^3\,s^{-1}\,K^{1/2}}),$$

where Z is the mean ionic charge which equals unity in our model and $\kappa_{BH} = (8\alpha/3) r_0^2 m_e c^2 = 7.9\times10^{-25}\,{\rm cm^2\,keV}$ is the constant in the Bethe-Heitler bremsstrahlung cross-section ($\alpha = 1/137$), ${\rm EM} = \int n_e n_i dV = \int n_e^2 dV$ is the emission measure (assuming $n_e = n_i$), $g(\epsilon/kT) = (kT/\epsilon)^{2/5}$ is the Gaunt factor (valid for temperature range $T > 7\times10^5\,{\rm K}$, Li et al. 1993). Substituting these quantities into equation (8.6), we have

$$I_{\rm SXR} = \frac{5.7\times10^{-12}}{\epsilon\sqrt{T}}\exp\left(-\frac{\epsilon}{kT}\right)\left(\frac{kT}{\epsilon}\right)^{2/5}\int n_e^2 dV \quad ({\rm photons\,s^{-1}\,keV^{-1}}), \tag{8.7}$$

where ϵ is in keV, T in K, and n_e in ${\rm cm^{-3}}$. In contrast to $U_{\rm th}$, $I_{\rm SXR}$ depends on n_e and T nonlinearly. In addition, $I_{\rm SXR}$ is not a monotonic function of T (see Fig. 8.1). Differentiating equation (8.7) gives the temperature where the maximum of $I_{\rm SXR}$ is located,

$$\frac{\partial I_{\rm SXR}}{\partial T} = \frac{I_{\rm SXR}}{T}\left(\frac{\epsilon}{kT} - \frac{1}{10}\right) \implies T_{\rm max} = 10\epsilon/k, \tag{8.8}$$

below (above) which $I_{\rm SXR}$ increases (decreases) monotonically with T. In other words, when a plasma is overheated and its temperature exceeds $10\epsilon/k$, its thermal radiation will decrease with increasing temperature[1]. This introduces more nonlinearity into the

[1]However, the total bremsstrahlung radiation increases as $\sqrt{T}$.

dependence of $I_{\rm SXR}$ on T. In the low temperature range, $T < T_{\rm max}$, however, a positive correlation (not necessarily linear though) between the thermal bremsstrahlung radiation $I_{\rm SXR}$ and the thermal energy $U_{\rm th}$ is expected. Or equivalently, their time derivatives, $\dot{I}_{\rm SXR}$ and $\dot{U}_{\rm th}$, would also exhibit a similar correlation.

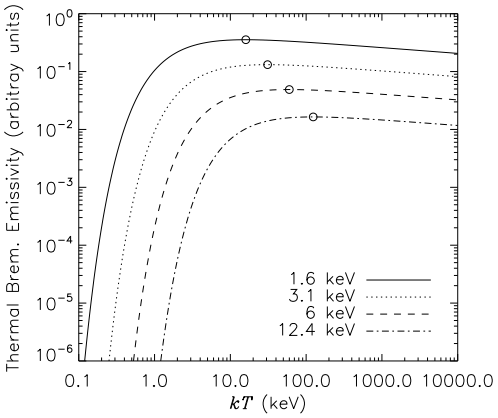

Figure 8.1: Thermal bremsstrahlung emissivity as a function of plasma temperature at different photon energies: $\epsilon = 1.6$, 3.1, 6, 12.4 keV. The open circles mark the maxima of these curves at the corresponding temperature of $T_{\rm max} = 10\epsilon/k$.

The *GOES* low channel (1–8 Å , 1.6–12.4 keV) flux is usually used as the SXR emission in Neupert effect studies. As long as $kT < 16\,{\rm keV}$ (which is usually the case for solar flares) the condition of $kT < 10\epsilon$ is satisfied in the entire 1–8 Å channel, so that $I_{\rm SXR}$ is an increasing function of T and we expect a positive $\dot{I}_{\rm SXR}$–$\dot{U}_{\rm th}$ correlation. To check if such an correlation is present in our five simulation cases we calculate, as shown in the following subsections, the thermal bremsstrahlung emission at $\epsilon = 1.6\,{\rm keV}$ [2] and $\epsilon = 6\,{\rm keV}$, which are at the low energy end and near the middle of the 1–8 Å channel, respectively.

8.2 Case R: Reference Calculation

8.2.1 History of Energy Budget

Let us check the **energy budget history** of Case R, which is shown in Figure 8.2. The total energy, thermal energy, and kinetic energy integrated over the whole loop are plotted in panel *a*; their time derivatives together with the electron energy deposition power $\dot{\mathcal{E}}_e$ and radiative loss rate $L_{\rm rad}$ are shown in panel *b*. As is evident, early on ($t \lesssim 15\,{\rm s}$) most of the energy deposited by electrons is quickly radiated away. This is because the coronal density is low at this time and the electron energy deposition is concentrated in the upper

[2]Note that continuum emission dominates over line emission in the *GOES* 1–8 Å channel (Culhane & Acton, 1970) and thus thermal free-free emission at a photon energy of 1.6 keV would be a good protocol for the *GOES* 1–8 Å flux. We take the low energy end (1.6 keV) because of the exponential decay (with photon energy) of thermal free-free emission. However, if one attempts to make a direct comparison with *GOES* observations, line emission must be calculated, say, using the current Chianti code, and then be added to the continuum and integrated over the entire 1–8 Å range, which is beyond the scope of this study.

chromosphere where radiative loss is the highest (see Fig. 7.3). As a result, only a small fraction of electron energy is available to heat the plasma and produces a slow increase of the total energy (Fig. 8.2*b*). However, as the flare evolves and chromospheric evaporation takes place, the coronal density increases and more electron energy is deposited above the transition region. This part of energy in turn heats and evaporates plasma more efficiently than in the upper chromosphere. Therefore, the radiative loss rate gradually drops and its competitor, electron energy deposition, takes over the control of the energy budget. This effect is present in Figure 8.2*b* as the rapid rise of the total energy change rate at about $t = 20\,\mathrm{s}$.

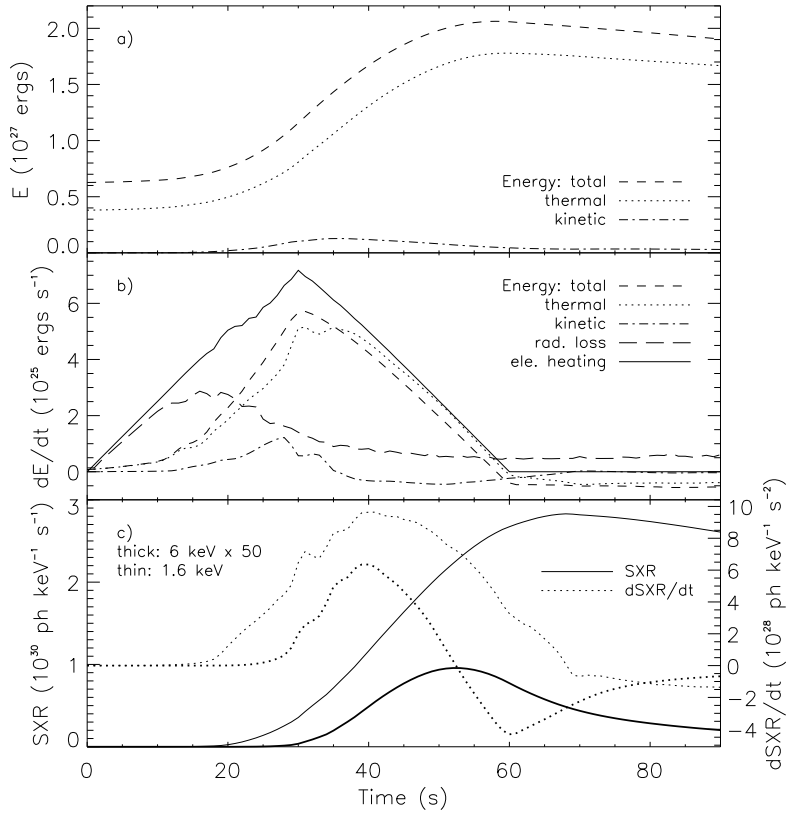

Figure 8.2: History of energy budget and X-ray emission for Case R. (*a*) Spatially integrated total energy (U), thermal energy ($U_{\rm th}$), and kinetic energy (U_k) of the whole loop. (*b*) Time derivative ($\dot{U}$, $\dot{U}_{\rm th}$, and $\dot{U}_k$) of the above three energies (same line styles), together with the total electron energy deposition power ($\dot{\mathcal{E}}_e$, *solid*) and the radiative loss power (L_{rad}, *long dashed*). (*c*) SXR fluxes ($I_{\rm SXR}$, *solid*) at photon energy of 1.6 (*thin*) and 6 keV (*thick*) and their time derivatives ($\dot{I}_{\rm SXR}$, *dotted*). The 6 keV light curve is rescaled up by a factor of 50.

The energy partition between the thermal and kinetic energy also evolves with time. Early in the flare, because evaporation is still in its infancy, the kinetic energy of the system is very small, and the total energy change is dominated by the variation of the thermal energy (Figs. 8.2*a* and 8.2*b*). For example, at $t = 10\,\mathrm{s}$, the kinetic energy is only $8.35 \times 10^{23}\,\mathrm{ergs}$ changing at a rate of $1.91 \times 10^{23}\,\mathrm{ergs\,s^{-1}}$, compared with the values of the

thermal energy: $U_{\rm th} = 3.99 \times 10^{26}$ ergs and $\dot{U}_{\rm th} = 3.50 \times 10^{24}\,{\rm ergs\,s^{-1}}$. As evaporation grows, the kinetic energy rises gradually, which makes the thermal energy deviates from the total energy curve at about $t = 15\,{\rm s}$. The kinetic energy change rate reaches its maximum at $t = 28\,{\rm s}$ just before the evaporation front arrives at the loop apex. Afterwards, $\dot{U}_k$ decreases quickly because of the reflection of the evaporation front and part of the kinetic energy is converted into the thermal energy due to local gas compression at the apex, which leads to the rapid rise of the $\dot{U}_{\rm th}$ curve (Fig. 8.2*b*), although there is no sudden change in the electron energy deposition at this time. This means that, on top of the electron beam heating, gas dynamics can also change energy partition and thus can modulate the thermal energy which would be manifested in the change of the SXR flux (see below). (This would produce further deviation from the Neupert effect.)

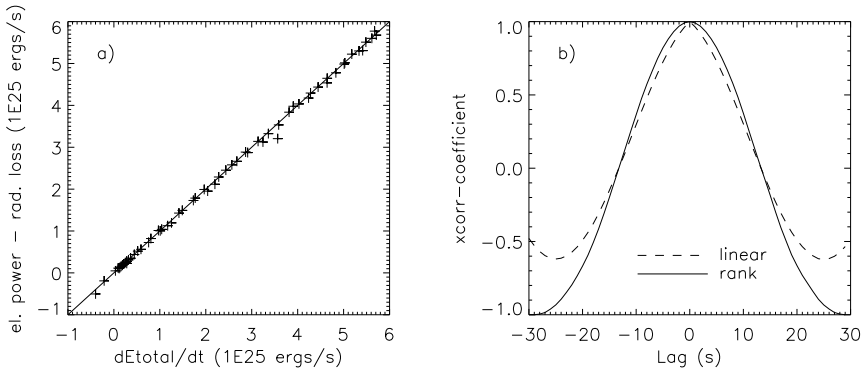

Figure 8.3: Consistency test of eq. (8.4) for Case R. (*a*) The electron energy deposition power minus the radiative loss ($\dot{\mathcal{E}}_e - L_{rad}$) vs. the total energy change rate ($\dot{U}$). The diagonal line corresponds to a perfect agreement. (*b*) Pearson linear (dashed) and Spearman rank (solid) cross-correlation coefficients of the two quantities shown in (*a*), plotted as a function of the time lag. The two coefficients have their maxima of 0.99950 and 0.99956, respectively, at the zero lag.

It is necessary to see if **energy gain and loss** is actually balanced as a consistency check of the code. In Figure 8.3*a* we plot the net energy input ($\dot{\mathcal{E}}_e - L_{\rm rad}$) vs. the total energy change rate ($\dot{U}$). Clearly, the two quantities are almost in perfect agreement. We also cross-correlate the two and the Pearson linear (*dashed*) and Spearman rank[3] (*solid*) cross-correlation coefficients (Fig. 8.3*b*) have a peak value of 0.99950 and 0.99956, respectively, indicating a very high correlation. Therefore we are assured that energy is conserved and equation (8.4) is indeed satisfied in our simulations. We note that this correlation is actually the "real" Neupert effect on the basis of an exact energy budget argument and we will use it as a reference point in this study.

8.2.2 Neupert Effect Test

Let us now check if the Neupert effect is present. We plot in Figure 8.2*c* the spatially integrated thermal SXR photon flux $I_{\rm SXR}$ (*solid*, photons ${\rm keV^{-1}\,s^{-1}}$, at the Sun) at two energies, 1.6 keV (*thin*) and 6 keV (*thin*, scaled by a factor of 50). We find the lower energy

[3]The Spearman rank correlation coefficient is an indicator of an either linear or nonlinear correlation.

SXR light curve rises earlier and faster, and decays later and slower, than the higher energy one. The shape of the 1.6 keV curve resembles that of the thermal energy (8.2*a*) because of their close relationship due to their dependence on n_e and T as noted above. It also mimics commonly observed *GOES* light curves (see, e.g., Fig. 6.1 in Chapter 6). The 6 keV light curve, however, appears comparably short in duration. This is because the 6 keV thermal emission is more sensitive to higher temperature plasmas (peak temperature response at 60 keV) and the temperature dependence of the thermal bremsstrahlung emissivity is very sharp in its rise portion (see Fig. 8.1). Therefore, early in the flare, when high temperature emission measure is small, there is very little 6 keV thermal emission; similarly in the decay phase, the 6 keV emission decreases quickly when the plasma cools off.

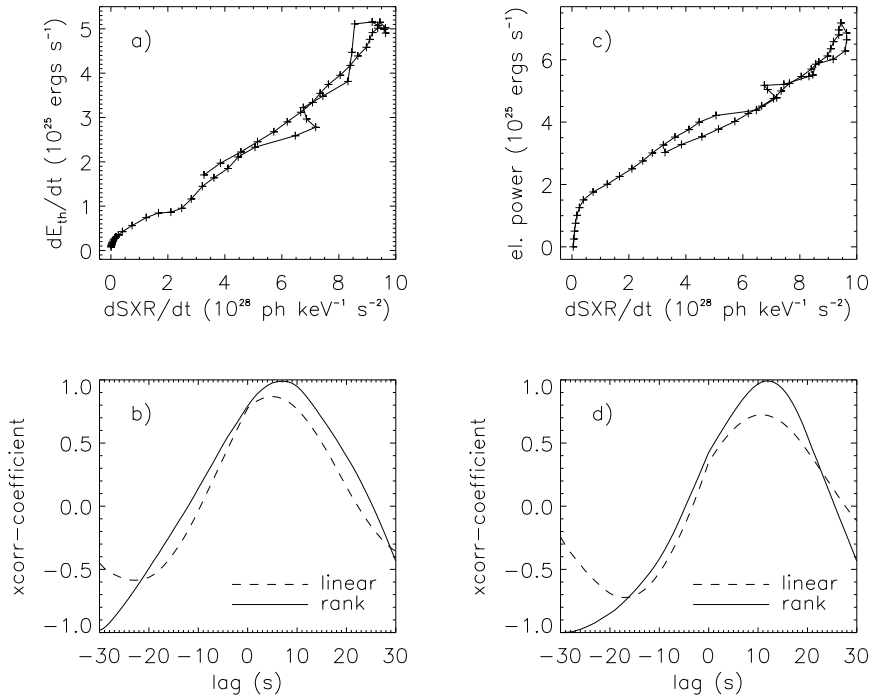

Figure 8.4: Neupert effect test for Case R. (*a*) Thermal energy change rate $\dot{U}_{\rm th}$ vs. SXR derivative $\dot{I}_{\rm SXR}$ (at photon energy of $\epsilon = 1.6\,{\rm keV}$) during the first 60 s of the flare. The solid line that connects the symbols indicates the time evolution, starting near the lower-left corner at $t = 0\,{\rm s}$. $\dot{I}_{\rm SXR}$ has been shifted back in time by 7 s to compensate its delay, as indicated by the cross-correlation analysis (see below and text). (*b*) Pearson linear (dashed) and Spearman rank (solid) cross-correlation coefficients of the two quantities shown in (*a*), plotted as a function of the time lag (> 0 means delay) of $\dot{I}_{\rm SXR}$ relative to $\dot{U}_{\rm th}$. The rank correlation coefficient reaches its maximum value of 0.989 at a lag of 7 s. (*c*) and (*d*) same as (*a*) and (*b*), respectively, but for the correlation between $\dot{\mathcal{E}}_e$ (electron energy deposition power) and $\dot{I}_{\rm SXR}$ (shifted back by 12 s).

To get more detailed timing information, we took the time derivatives of the two SXR fluxes, following the common practice for Neupert effect studies. The result is shown as the dotted lines (*thin*: 1.6 keV, *thick*: 6 keV) in Figure 8.2*c*. By visual comparison with the electron energy deposition power ($\dot{\mathcal{E}}_e$) and the thermal energy change rate ($\dot{U}_{\rm th}$) in

Figure 8.2*b*, we find that these curves resemble each other in one way or another. They all roughly show a triangular shape. Particularly, the $\dot{I}_{\rm SXR}$ curves even follow $\dot{U}_{\rm th}$ in some detail. For example, $\dot{I}_{\rm SXR}$ at both energies exhibits a rapid rise at about $t = 29\,{\rm s}$ when an abrupt increase in $\dot{U}_{\rm th}$ occurs (due to gas dynamics, see above). However, such a detailed change is not present in the $\dot{\mathcal{E}}_e$ curve, which is equivalent to the HXR flux here[4]. Therefore, if one attempts to look for the Neupert effect by comparing the SXR derivative and the HXR flux (as people usually do), such a subtle correlation could be missing in HXRs. In this sense, a more physical Neupert effect would be the relationship between the thermal energy change rate and the SXR derivative.

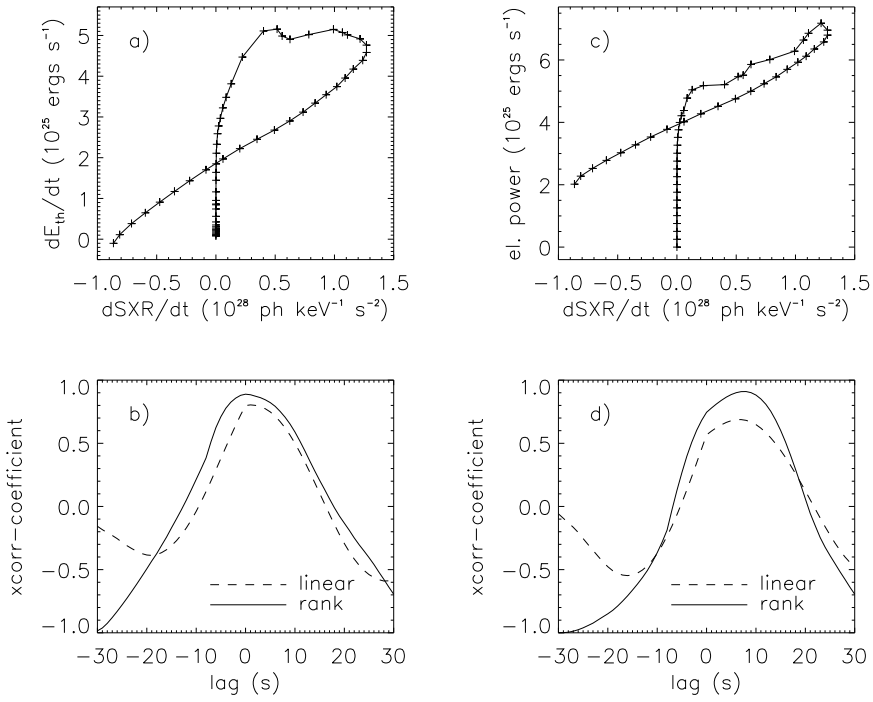

Figure 8.5: Same as Fig. 8.4 (Case R), but for photon energy $\epsilon = 6\,{\rm keV}$. $\dot{I}_{\rm SXR}$ in (*c*) is shifted back by 8 s to compensate its delay.

We have carried out statistical analysis and checked the correlations between these various variables more quantitatively. We first cross-correlated the SXR derivative $\dot{I}_{\rm SXR}$ at 1.6 keV with the thermal energy change rate $\dot{U}_{\rm th}$ and with the electron energy deposition power $\dot{\mathcal{E}}_e$, the correlation coefficients of which are shown in Figures 8.4*b* and 8.4*d*, respectively. For $\dot{I}_{\rm SXR}$ and $\dot{U}_{\rm th}$, the linear correlation coefficient has a peak value of 0.868 at a lag of 5 s, and the rank correlation peaks (max = 0.989) at a lag of 7 s, both indicating a significant correlation and a delay of $\dot{I}_{\rm SXR}$ relative to $\dot{U}_{\rm th}$. Such a delay is also visible in

[4]For Case R only, the HXR flux could not be readily calculated without running the transport and radiation code for the assumed power-law electron spectrum. Here, we use $\dot{\mathcal{E}}_e$ as a protocol for the HXR flux since they are proportional to each other (because the electron spectrum remains constant in time and the bremsstrahlung yield is thus a constant as well).

Figures 8.3*b* and 8.3*c*, say, by comparing the rise portion and the peak position of the corresponding curves. Since their physical relationship is nonlinear *per se* as discussed above, we believe the rank correlation can describe the connection between $\dot{I}_{\rm SXR}$ and $\dot{U}_{\rm th}$ more generally than the linear correlation, although the two correlations give us different perspectives when looking at the same phenomenon. We thus use the delay indicated by the rank correlation to shift $\dot{I}_{\rm SXR}$ back in time and plot $\dot{U}_{\rm th}$ vs. $\dot{I}_{\rm SXR}$ in Figure 8.4*a*. We find these two quantities indeed have a strong correlation since their data points in the scatter plot very much distribute along a straight line. In contrast, for $\dot{I}_{\rm SXR}$ and $\dot{\mathcal{E}}_e$, the linear (rank) correlation coefficients reaches its maximum of 0.724 (0.993) at a lag of 11 s (12 s). This indicates a weaker linear correlation (although a slightly stronger rank correlation), compared with the correlation for $\dot{I}_{\rm SXR}$ and $\dot{U}_{\rm th}$. It also reveals a longer delay, which could be ascribed to the fact that the rise portion of $\dot{U}_{\rm th}$ itself actually delays relative to the energy deposition rate, $\dot{\mathcal{E}}_e$, (Fig. 8.3*b*) because of the strong radiative loss at early times as noted before.

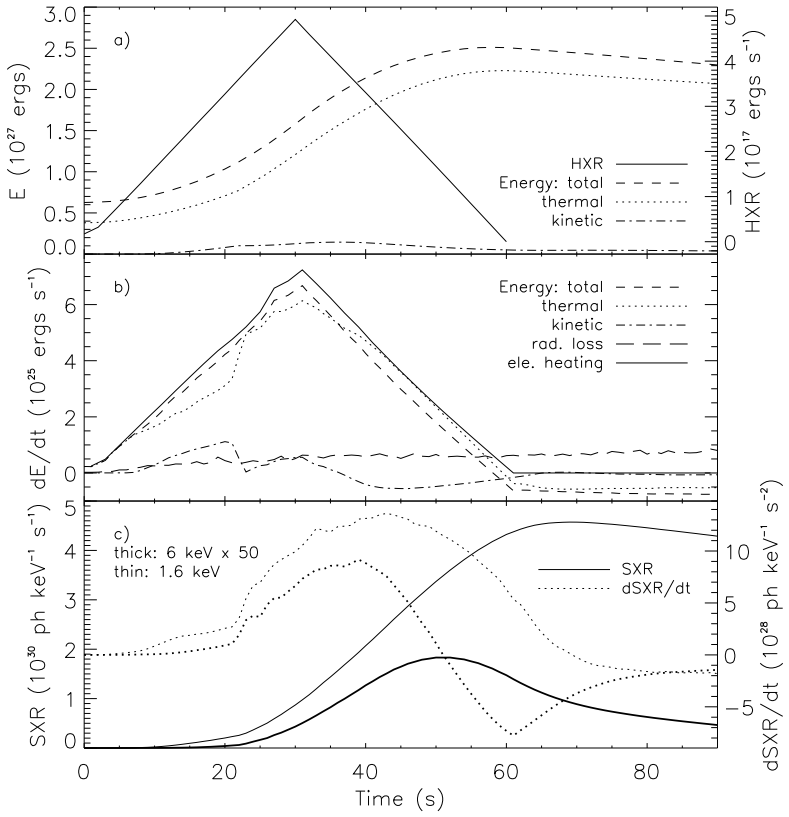

Figure 8.6: Same as Fig. 8.2, but for Case A, with the HXR power of all $\geq$20 keV photons in (*a*).

We also repeated the above analysis for SXR emission at photon energy of 6 keV for comparison. The result is shown in Figure 8.5. In general, we find a weaker correlation and a shorter delay (see Table 8.1). The shorter delay (despite its actual delay in the rise portion) is due to the rapid decrease of the 6 keV light curve during its decay, which mimics

the same trend in the $\dot{\mathcal{E}}_e$ and $\dot{U}_{\rm th}$ curves (Fig. 8.2). However, it is noted that the 1.6 and 6 keV derivatives both peak at about the same time, $t = 40\,$s. As we will show below, this is a particular feature of this Case. It is interesting to see that the curves in Figures 8.5*a* and 8.5*c* both show a crossed loop-like shape, reminiscence of that in Figure 6.12*e*.

8.3 Cases A-D: Combined HD & Particle Calculation

For comparison, we did the same analysis as above for the other four cases, which we describe as follows. The only new quantity is the HXR ($E > 20\,$keV) flux calculated from our radiation code, which we will use here in place of the electron energy deposition power for cross-correlating with the SXR derivative.

8.3.1 Case A: Fiducial Run with SA Model

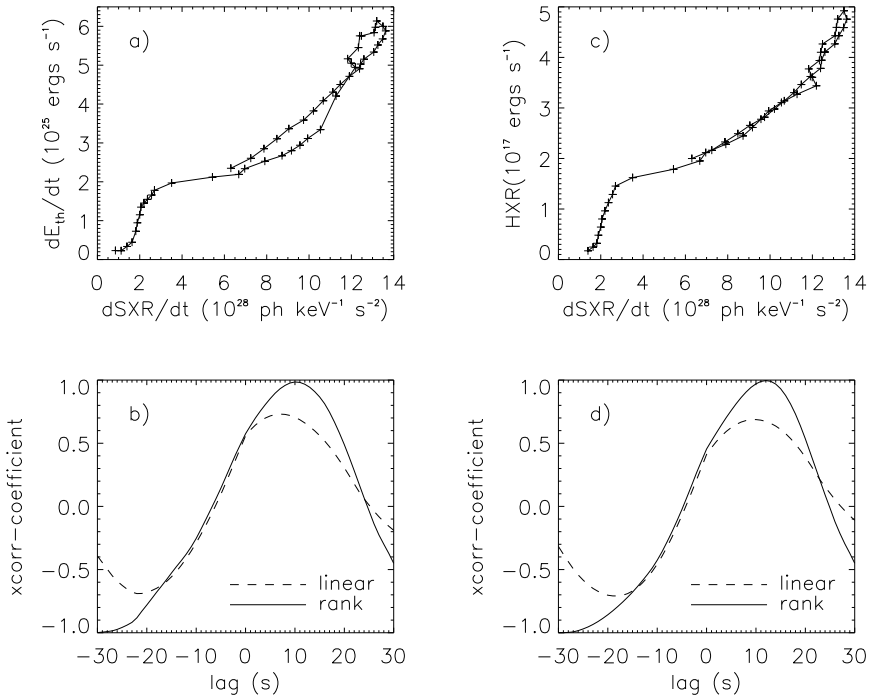

Figure 8.7: Same as Fig. 8.4 but for Case A and the ≥20 keV HXR emission power ($I_{\rm HXR}$) (rather than the electron energy deposition power). SXR derivatives in (*a*) and (*c*) are shifted back in time by 10 and 12 s, respectively, according to their delays indicated by the peak of the Pearson rank correlation coefficient shown in (*b*) and (*d*).

For Case A, the energy budget history is shown in Figure 8.6. We find that the overall evolution of the energies is similar to that of Case R (Fig. 8.6). However, we do see three major differences, the first of which is relatively small importance of the radiative loss here, particularly during the rise phase of the flare. This is because, as we discussed

earlier, the electron spectrum contains a quasi-thermal component at low energies and this produces relatively more energy deposition in the corona than in the upper chromosphere where radiative loss is most efficient. As a result, less energy is available for radiative loss and more energy is left to evaporate the chromospheric plasma. The second difference is that the 6 keV light curve starts its rise earlier than in Case R, because the preferential coronal heating here (vs. more chromospheric heating in Case R) produces relatively higher emission measure at high temperatures from which the 6 keV emission is more productive. The 6 keV light curve also peaks earlier than the 1.6 keV one by about 5 s, as opposed to their concurrence in Case R. For the same reason, we have stronger chromospheric evaporation, and thus higher coronal temperature and density here, resulting in a higher SXR flux with a maximum of 4.57 (vs. 2.83 in Case R) $\times 10^{30}$photons keV^{-1} s^{-1} at 1.6 keV. The third major difference is that Case A has a faster evolution and the evaporation front reaches the loop apex earlier at $t = 22$ s (vs 29 s in Case R). The associated compressional heating produces a sudden jump at this time in the thermal energy change rate, as well as in the two SXR derivative curves.

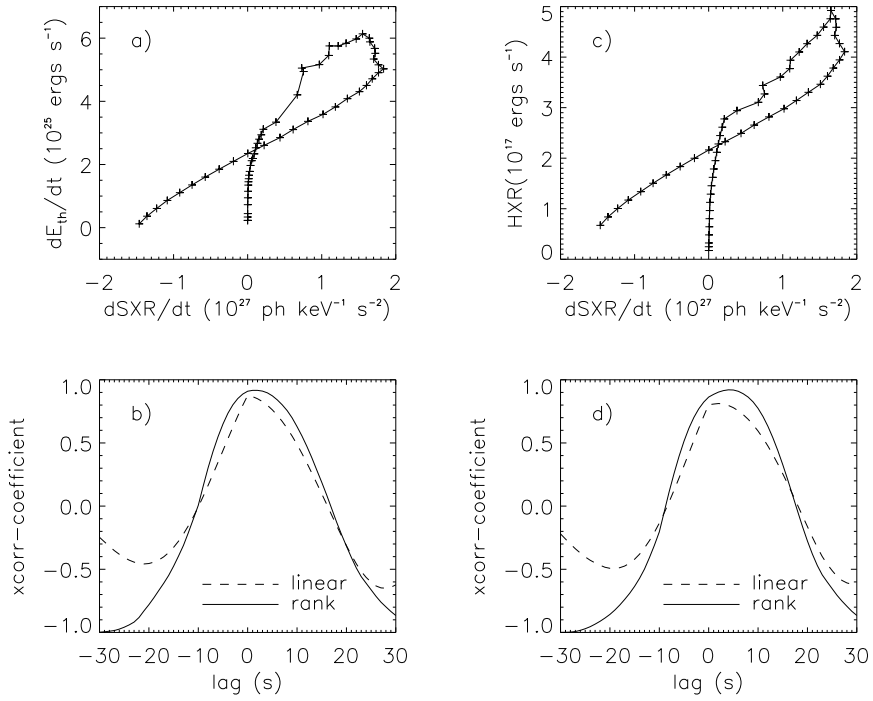

Figure 8.8: Same as Figure 8.7 for Case A but at a photon energy of 6 keV.

We also cross-correlated the SXR derivative with the thermal energy change rate $\dot{U}_{\rm th}$ and the HXR energy flux $I_{\rm HXR}$. The resulting correlation coefficients for the 1.6 keV photon energy are shown in Figure 8.7 We find a weaker linear correlation[5] for both $\dot{U}_{\rm th}$ and

[5]This may have to do with stronger evaporation and more dramatic evolution in this Case, and thus more nonlinear phenomena are invoked.

$I_{\rm HXR}$ with $\dot{I}_{\rm SXR}$, compared with that in Case R (Fig. 8.4), and the peak linear correlation coefficients are 0.731 and 0.687, respectively.

The Pearson rank correlation, however, are very close to that of Case R, and the correlation coefficient for $I_{\rm HXR}$ is even higher (see Fig. 8.7*c* and Table 8.1). This is not surprising, since a linear correlation between these quantities are actually not expected, as we discussed earlier, and their nonlinear correlation seems more likely. In contrast, the correlations for 6 keV photon energy (Fig. 8.8, cf. Fig. 8.5) are somewhat better than those of Case R (see Table 8.1). This might be due to the stronger coronal heating here that favors higher photon energy thermal emission. The shorter (than that in Case R) delay of the 6 keV derivative relative to the HXR flux, which was mentioned above, is also evident from the lag corresponding to the peak (linear or rank) correlation coefficient.

8.3.2 Case B: Variable Electron Spectrum

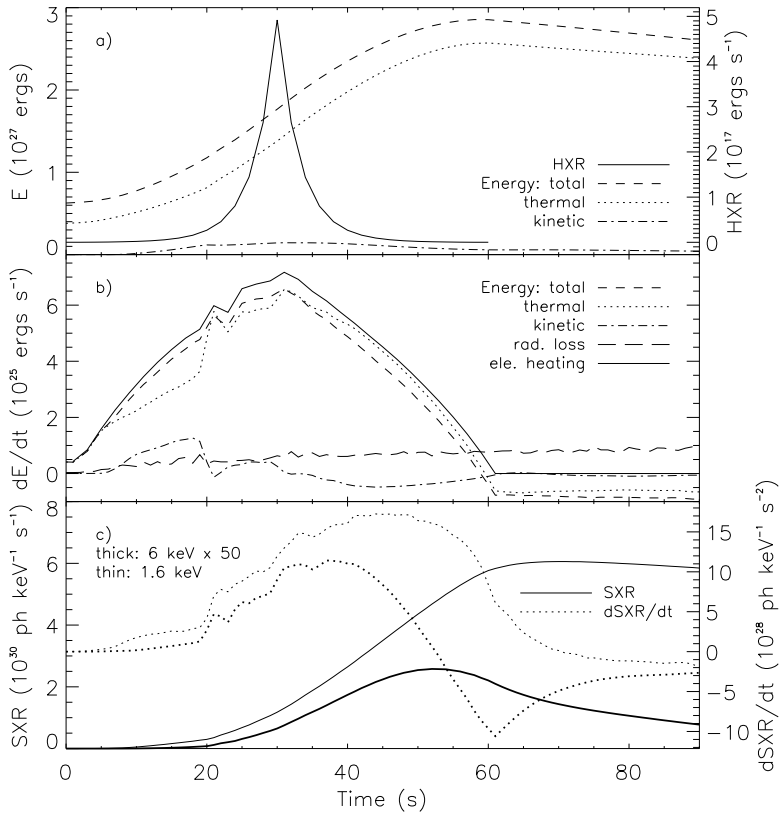

Figure 8.9: Same as Fig. 8.6, but for Case B.

Case B has a particular electron spectrum that experiences a soft-hard-soft variation. The energy budget history is shown in Figure 8.9. Compared with Case A, one of the main differences is the shape of the energy deposition rate, which appears to be warped and slightly higher than the linear one in Case A. This results in somewhat higher heating

rate and faster evaporation (see Table 7.1). Another difference is the shape of the HXR light curve which differs quite a bit from the triangular one in Case A. This is due to the soft-hard-soft variation of the electron spectrum, which modulates the bremsstrahlung yield and thus HXR flux on top of the triangular normalization variation. We also show the cross-correlation result for the 1.6 keV SXR in Figure 8.10. As can be seen, the linear correlation is somewhat weaker than that of Case A, especially for the HXR flux (see Fig. 8.10*c*; note logarithm scale). However, the rank correlation coefficients are similar to that of Case A.

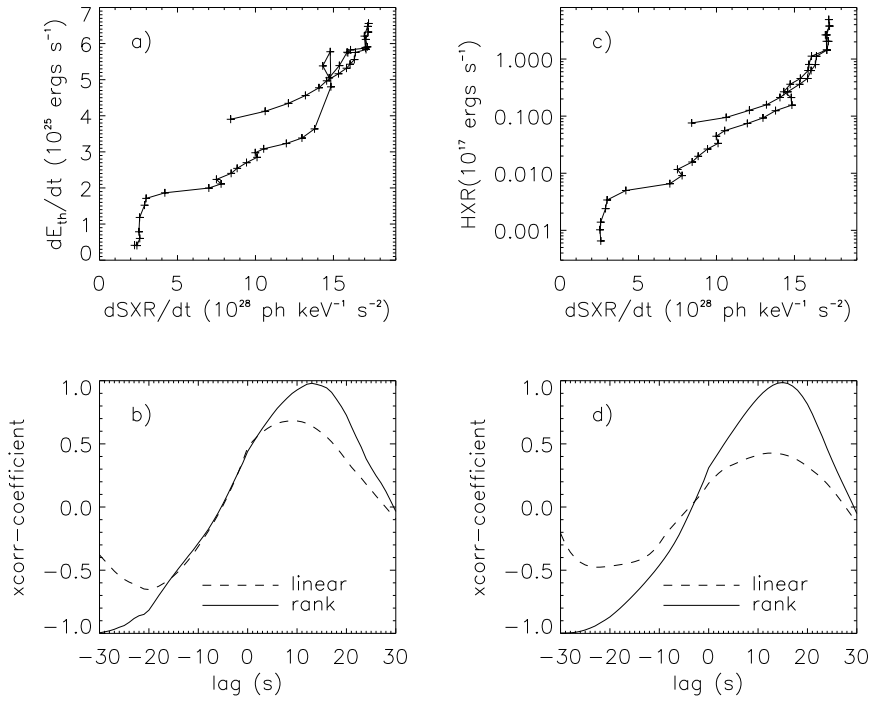

Figure 8.10: Same as Fig. 8.7 but for Case B (at 1.6 keV). SXR derivatives in (*a*) and (*c*) are shifted back by 13 and 15 s, respectively, to account for their delays indicated in (*b*) and (*d*).

8.3.3 Case C: Harder Electron Spectrum

Case C has a harder electron spectrum compared with Case A because of its relatively shorter acceleration timescale ($\tau_p = 100\,\mathrm{s}^{-1}$ vs. $70\,\mathrm{s}^{-1}$). The history of the energy budget (Fig. 8.11) and the cross-correlations (Fig. 8.12) are similar to those of Case A, although its electron spectrum is much harder than that in Case A. The main difference is in the normalization of the HXR flux (see Fig. 8.11*a*) which is about 28 times higher than that of Case A, simply because of harder electron spectrum results in a higher bremsstrahlung yield (see Fig. 6.11) and thus higher HXR emission.

8.3.4 Case D: Smaller Normalization

Case D has an energy input rate 10 times smaller than that of Case A and thus the flare

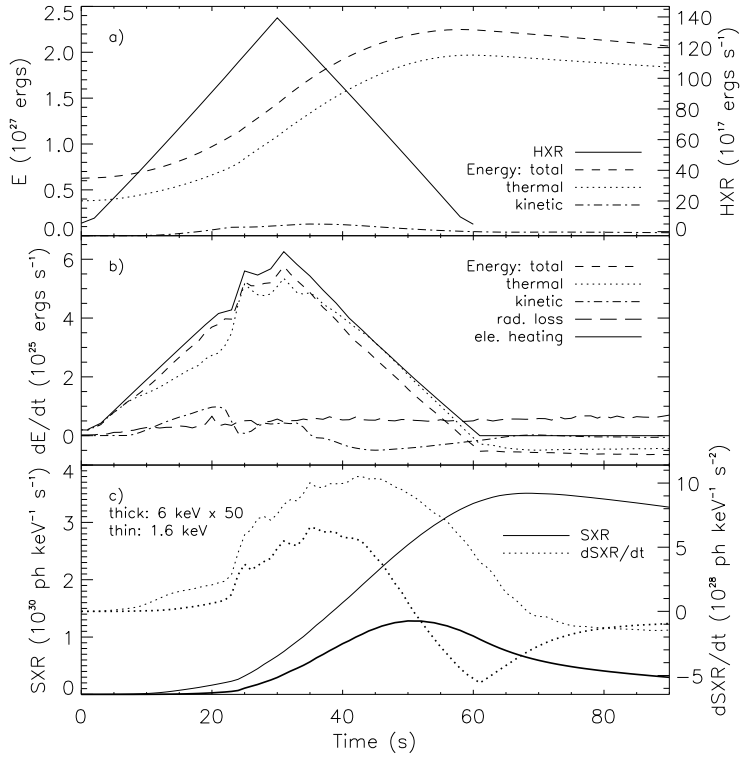

Figure 8.11: Same as Fig. 8.6, but for Case C.

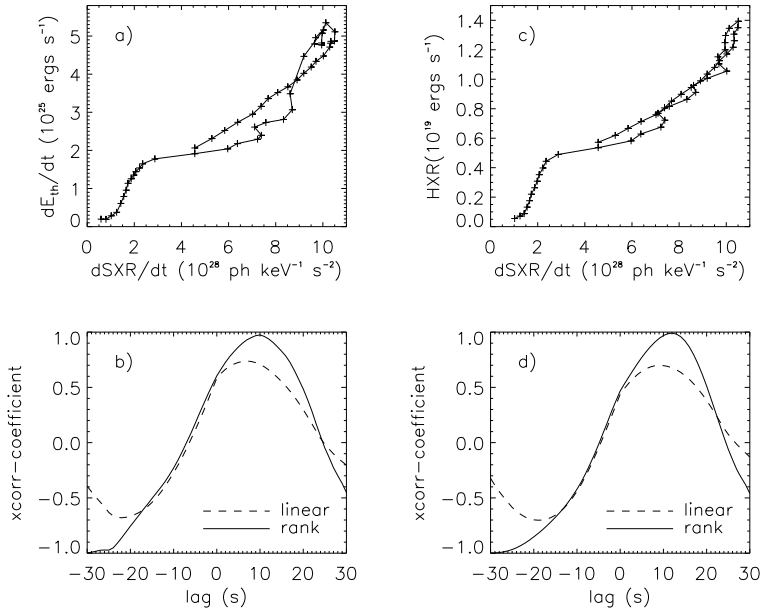

Figure 8.12: Same as Fig. 8.7 but for Case C (at 1.6 keV). SXR derivatives in (*a*) and (*c*) are shifted back by 10 and 12 s, respectively, to make up for their delays.

is weaker by an order of magnitude, as can be seen from the various quantities shown in Figure 8.13. The overall energy evolution appears similar to Cases A-C, except that the evaporation front arrives at the loop apex late ($t = 39\,\mathrm{s}$, well into the decline phase). At this time, the kinetic energy change rate ($\dot{U}_k$) shows the largest continuous drop (with a range of $\Delta\dot{U}_k/\dot{U}_{\max} = 0.33$, normalized by the peak energy input rate $\dot{U}_{\max}$, cf., e.g., 0.16 for Case A) among all the five cases, partly because this drop coincides with the

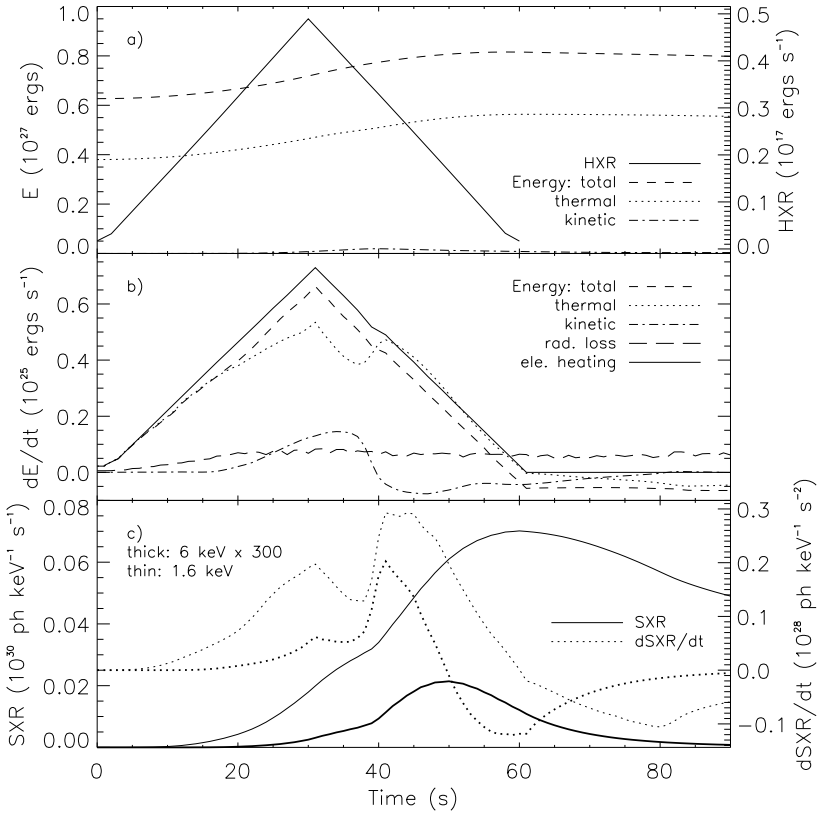

Figure 8.13: Same as Fig. 8.6, but for Case D. Note that the 6 keV SXR light curve in (c) is rescaled by a factor of 300 (cf. 50 in the other four cases) due to the softness of the thermal spectrum in this case of weak evaporation.

decrease of the energy input rate and that of the other cases takes place during the rise phase. In exchange of the decrease in $\dot{U}_k$, the thermal energy change rate still attains a net gain, despite the decrease of the total energy change rate. This rise produces a dramatic increase in SXR flux derivatives at both the 1.6 and 6 keV, which even dwarfs the first peak produced at the time of the maximum total energy input rate. The relative height of the two peaks on the $\dot{U}_{\mathrm{th}}$ curve (Fig. 8.13), however, does the opposite, although the timing of the two peaks agrees with that of the SXR derivative pulses. We attribute this, again, to the nonlinearity of the contribution of density and temperature to thermal bremsstrahlung emission, and particularly to the sensitive dependence on temperature, i.e., the sharp rise

at low temperatures below the maximum of the emissivity curve (see Fig. 8.1). The cross-correlation result is shown in Figure 8.14. Clearly, we find a correlation much weaker the other cases for both the thermal energy change rate and the HXR flux, which can also be seen from the coefficients tallied in Table 8.1.

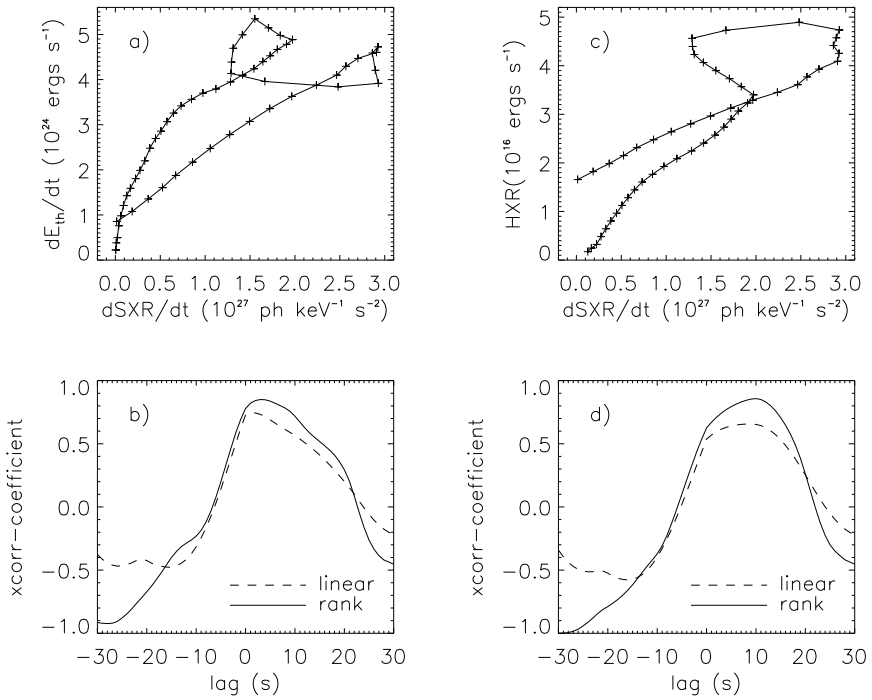

Figure 8.14: Same as Fig. 8.7 but for Case D (at 1.6 keV). SXR derivatives in (*a*) and (*c*) are shifted back by 3 and 10 s, respectively.

8.4 Summary and Discussion

We have performed a test of the Neupert effect for five simulation cases described in Chapter 7, using our SA model and the NRL HD flux tube model. We followed the temporal evolution of various energies (thermal, kinetic, and total), the electron energy deposition power, and the radiative loss, together with thermal and nonthermal bremsstrahlung radiation, spatially integrated over the whole flare volume. We then checked the temporal and statistical correlation between the SXR derivative ($\dot{I}_{\rm SXR}$) and the HXR flux ($I_{\rm HXR}$), and between $\dot{I}_{\rm SXR}$ and the thermal energy change rate ($\dot{U}_{\rm th}$). The statistical correlation analysis for all the five cases is summarized in table 8.1 and we itemize our results as follows.

1. We find that a correlation exists between $\dot{I}_{\rm SXR}$ and $\dot{U}_{\rm th}$, as well as between $\dot{I}_{\rm SXR}$ and $I_{\rm HXR}$. The latter correlation is in agreement with the empirical Neupert effect observed in some (but not all) flares.

Table 8.1: Neupert effect test of simulation cases (ϵ = 1.6, 6 keV).

ϵ	Case	Pearson Linear Correlation				Spearman Rank Correlation			
(keV)		$U_{\rm th}$: coef,	lag (s);	$I_{\rm HXR}$: coef,	lag	$U_{\rm th}$: coef,	lag;	$I_{\rm HXR}$: coef,	lag
1.6	R	0.868	5	0.724	11	0.989	7	0.993	12
	A	0.731	7	0.687	10	0.985	10	0.996	12
	B	0.683	9	0.427	13	0.980	13	0.985	15
	C	0.738	7	0.699	9	0.975	10	0.991	12
	D	0.744	2	0.656	9	0.850	3	0.857	10
6	R	0.804	1	0.688	7	0.889	0	0.909	8
	A	0.876	0	0.812	2	0.916	1	0.920	4
	B	0.890	0	0.624	7	0.923	2	0.933	5
	C	0.875	0	0.815	2	0.907	1	0.910	3
	D	0.696	0	0.589	3	0.854	0	0.833	5

NOTE — For case R, the electron energy deposition rate is used as a protocol for the HXR flux (not available) to calculate the correlation with the SXR derivative.

2. The resulting Spearman rank (linear or nonlinear) correlation coefficients are generally greater than the Pearson (linear) correlation coefficients. When the linear correlation breaks down, the nonlinear correlation still holds (see, e.g., Case B). This is expected since the correlation is essentially nonlinear due to the nonlinearity involved in the radiation (thermal and nonthermal bremsstrahlung) processes.

3. $I_{\rm HXR}$ and $\dot{U}_{\rm th}$ both yield comparable nonlinear correlations with $\dot{I}_{\rm SXR}$, while $\dot{U}_{\rm th}$ is relatively better correlated with $\dot{I}_{\rm SXR}$ linearly.

4. For the rank correlation, the 6 keV SXR has a smaller coefficient in each case than the 1.6 keV one. For the linear correlation, on the other hand, three (Cases A, B, & C) out of the five cases have a stronger correlation in the 1.6 keV category.

5. For the five cases, the cross-correlation analysis indicates that the 1.6 keV SXR derivative is delayed relative to the thermal energy change and the HXR flux. The delay from $I_{\rm HXR}$ is longer than that from $\dot{U}_{\rm th}$ by several seconds, this is because $\dot{U}_{\rm th}$ itself actually lags from $I_{\rm HXR}$ due to the interplay of the energy input and radiative loss, as well as the variation of energy (between thermal and kinetic) partition.

6. The 6 keV SXR exhibits a similar pattern as the 1.6 keV one, but it yields a relatively shorter delay in each category. This is because the 6 keV thermal emission is sensitive to higher temperature plasmas and thus it decays faster as the loop cools, while the 1.6 keV emission lasts longer and then decays more slowly after the impulsive phase.

7. In terms of timing of more subtle features (e.g., spikes in the curves), $\dot{U}_{\rm th}$ generally matches $\dot{I}_{\rm SXR}$, while $I_{\rm HXR}$ does not.

8. In a smaller flare (Case D), all the correlations are much weaker compared with the other flares. This is because a relatively larger fraction of the total energy variation comes from the kinetic energy in this case.

From these findings, we can conclude that, in terms of timing (concurrence and shorter delay) and both linear and nonlinear correlations, the SXR flux is better correlated with

the thermal energy than with the commonly used HXR flux. Many processes, such as gas dynamics, can change the thermal energy in various ways, and signatures of such changes can appear in the SXR radiation, but not in HXRs. This is because thermal SXRs are more directly related to the thermal energy as they are both a function of plasma temperature and density. However, it should be noted that their correlation is not necessarily linear. The reason is that the thermal energy is linearly proportional to n_e and T, while the thermal bremsstrahlung emissivity is a nonlinear function of n_e and T (see eq. [8.7]).

There seems to be a bias for the Neupert effect in the solar physics community that a simple energy argument supports the empirical Neupert effect and a common practice of studying this is to plot the time history of the HXR flux together with the SXR derivative. We point out that a simple linear correlation between $\dot{I}_{\rm SXR}$ and $I_{\rm HXR}$ is not expected, even for purely nonthermal electron heated flare models. As we already noted in Chapter 6, there are several reasons why linearity could break down here. (1) $\dot{I}_{\rm SXR}$ is not proportional to the electron energy input power, but rather closely related (not proportional either) to the thermal energy change rate $\dot{U}_{\rm th}$. (2) The HXR flux is proportional to the electron energy deposition power with a factor of the bremsstrahlung yield, which is not a constant in time but varies with the electron spectrum in a nonlinear way. The energy deposition power also depends on the electron spectrum, but in a different way. (3) The total energy gain is a result of electron energy input power minus radiative loss rate and most of the radiative loss resides in UV and optical (not SXR) wavelengths. (4) The total energy gain is redistributed (partitioned) to different energy forms, i.e., thermal, kinetic, and gravitational energies. Clearly, through this long chain of energy transform, a linear correlation between the SXR derivative and the HXR flux is not expected to be the case. The existence of the Neupert effect in a particular flare supports the purely electron-heating model, but not vice versa. Further deviation from such a correlation will occur when other processes, such as direct heating by turbulence (rather than electrons) is present.

Chapter 9

Hydrodynamic Simulations of the Decay Phase: Testing Suppression of Conduction

9.1 Introduction

Suppression of thermal conduction by turbulence plays important roles in many astrophysical and space plasma environments. Chandran & Cowley (1998), for example, found entangled magnetic fields in a turbulent intracluster plasma can reduce the Spitzer (1962) conductivity by a factor of 10^2–10^3.

For solar flares, Jiang et al. (2006) reported spatial confinement and lower than expected energy decay rate of the X-ray loop-top (LT) source during the flare decay phase observed by *RHESSI* . This observation was interpreted as suppressed thermal conduction and/or simultaneous heating, which were assumed to be produced by turbulence or plasma waves at the LT. The same turbulence, with different strength and other properties, could also be responsible for acceleration of particles during the impulsive phase.

Jiang et al. (2006) assumed that the plasma in the flaring loop is in a hydrostatic state, which works well as a zeroth order approximation and made their semi-analytical work tractable. Antiochos & Sturrock (1978), however, from their simplified analytical derivation, found the bulk flow of the plasma could suppress thermal conduction as well, but they did not include radiative loss in their model. Plasma flows (or convection), in general, can carry energy from one place to another, in a way that works in parallel with thermal conduction.

It is thus necessary to improve on previous works by Jiang et al. (2006) and Antiochos & Sturrock (1978) by including the hydrodynamic response of the plasma, its feedback to the conduction, and a full calculation of radiative loss. This will help shed light on energy transport and the evolution of the flaring plasma. We will also extend the domain considered in Jiang et al. (2006) to beneath the transition region, such that we can include all the energy flow channels, i.e., radiative loss in the chromosphere and possible conduction flux through there. Such a work is reported in this chapter. The numerical model and simulation result are presented in §9.2 and §9.3, respectively. We summarize the main findings in §9.4.

9.2 Simulation Model of Suppression of Conduction and Plasma Heating

We use the NRL flux-tube model by Mariska et al. (1989), as described in Chapter 7. The only difference here is that we used the abundance in the original code, i.e., helium being 6.3% of the hydrogen number density, rather than a simply pure hydrogen plasma. Accordingly, the mean ionic charge is taken as $Z = 1.059$ and the mean mass per particle is $\mu = 0.5724$ in units of proton masses m_p. We have adopted the suppression of conduction and additional heating due to turbulence from Jiang et al. (2006), with necessary modifications due to the absence of the isobaric condition, which we describe as follows.

The electron, ion (as in Chapter 7), and combined Spitzer conductivities are

$$\kappa_e = 1.1\times10^{-6}T_e^{5/2}, \qquad \kappa_i = \kappa_e/25, \tag{9.1}$$

$$\kappa = \kappa_e+\kappa_i = \kappa_S T^{5/2} \ (\text{where } \kappa_S = 1.14\times10^{-6}\,\text{ergs}\,\text{cm}^{-1}\,\text{s}^{-1}\,\text{K}^{-7/2}), \tag{9.2}$$

in which we assume $T_e = T_i = T$. The corresponding conductive heat flux is

$$\mathcal{F}_{\rm Spit} = \kappa\nabla T = \kappa_S T^{5/2}\nabla T\,. \tag{9.3}$$

Following Jiang et al. (2006), in presence of suppression of thermal conduction, the conductive flux should be modified as (Spicer, 1979):

$$\mathcal{F}_{\rm cond} = \frac{1}{1+\tau_{\rm sc}^{-1}/\tau_{\rm Coul}^{-1}}\mathcal{F}_{\rm Spit} = \left(\frac{\kappa_S T^{5/2}}{1+\tau_{\rm sc}^{-1}/\tau_{\rm Coul}^{-1}}\right)\nabla T\ , \tag{9.4}$$

where

$$\tau_{\rm Coul}^{-1} \simeq 150\left(\frac{T}{10^7\,\text{K}}\right)^{-3/2}\left(\frac{n_e}{10^{11}\,\text{cm}^{-3}}\right)\quad \text{s}^{-1} \tag{9.5}$$

is the mean Coulomb collision rate of the thermal electrons carrying the heat flux, and the mean wave scattering rate is assumed to be a Gaussian (width w) function of distance ($l = s_{\rm max} - s$) from the loop apex,

$$\tau_{\rm sc}^{-1} = 150\mathcal{S}_0\exp[-(l/w)^2]\quad \text{s}^{-1}\,, \tag{9.6}$$

such that the ratio of the wave scattering to Coulomb collision rate is

$$\tau_{\rm sc}^{-1}/\tau_{\rm Coul}^{-1} = S(s)\left(\frac{T}{10^7\,\text{K}}\right)^{3/2}\left(\frac{n}{10^{11}\,\text{cm}^{-3}}\right)^{-1}\,, \tag{9.7}$$

where $\mathcal{S}(l) = \mathcal{S}_0\exp[-(l/w)^2]$ and the dimensionless $\mathcal{S}_0$ represents the strength of suppression (and of turbulence). Note that here we dropped the isobaric assumption taken by Jiang et al. (2006), which is not necessarily satisfied in a dynamic flare loop. Consequently equation (9.7) here is slightly different from that given by Jiang et al.

For a given turbulence condition, the inverse of the corresponding particle acceleration

(or heating) timescale is (Jiang et al., 2006)

$$\tau_{\rm ac}^{-1} \simeq \xi(v_{\rm A}/v_{\rm th})^2\tau_{\rm sc}^{-1} = \xi\left(\frac{B^2 m_e}{12\pi k_B\rho T}\right)\tau_{\rm sc}^{-1}\,, \tag{9.8}$$

where $v_{\rm A} = B/(4\pi\rho)^{1/2}$ is the Alfvén velocity (B the magnetic field), $v_{\rm th} = (3k_{\rm B}T/m_e)^{1/2}$ is the thermal velocity of the electrons (m_e the electron mass), and the coefficient ξ depends on the wave spectrum and wave-particle coupling (Schlickeiser, 1989). Accordingly, the energy change (heating) rate can be written as

$$\dot{\mathcal{E}}_h = U_{\rm th}\tau_{\rm ac}^{-1} = U_{\rm th}\xi\left(\frac{B^2 m_e}{12\pi k_B\rho T}\right)\tau_{\rm sc}^{-1} \tag{9.9}$$

$$= \frac{25}{2\pi}\left(\frac{m_e}{\mu m_p}\right)\frac{\mathcal{S}_\prime}{\gamma-1}\exp[-(l/w)^2](\xi B^2)\,, \tag{9.10}$$

where we have substituted equations (9.6) and (9.8), and used $U_{\rm th} = P/(\gamma-1)$ for the thermal energy density, and $P = P_e + P_i = (n_e + n_i)k_BT = \rho k_BT/\mu m_p$ for the pressure. We use this $\dot{\mathcal{E}}_h$ for the heating rate S_e in equation (7.37) in the HD calculation and use ξB^2 as a parameter to adjust the relative importance of heating (vs. suppression of conduction, see discussions in §3 of Jiang et al., 2006).

9.3 Numerical Results

We have performed a simulation of four cases with model parameters summarized in Table 9.1. For each case, we used the data saved at $t = 64\,$s from a previous impulsive phase simulation as the initial state, from which we continue the calculation. A uniform background heating of $8.31\times10^{-3}\,{\rm ergs\,s^{-1}\,cm^{-3}}$ (same as that used in Chapter 7, which translates to a total energy input rate of $2.35\times10^{22}\,{\rm ergs\,s^{-1}}$)[1] was applied. On top of that, for Cases B and C, we alternatively applied additional heating ($\dot{\mathcal{E}}_h$, or S_e) and suppression of conduction, respectively; for Case D, we used both additional heating and suppression, while we used none of them for Case A.

Table 9.1: Summary of simulation cases.

Cases	model	ξB^2	$\mathcal{S}_0$	mean energy decay ($10^{24}\,{\rm ergs\,s^{-1}}$)	n_e ($10^{10}\,{\rm cm^{-3}}$)	T ($10^6\,{\rm K}$)
A	none	–	–	8.07	6.16	1.48
B	heating only	10	20	6.66	7.78	6.54
C	suppression	0	20	7.24	4.68	7.20
D	heating & suppression	10	20	6.01	4.11	15.9

Note — The mean energy decay rate is calculated for the time interval of $[0, 500\,{\rm s}]$. n_e and T are the values at the loop apex at $t = 500$ s.

[1] As we will see later, this amount of energy input is negligible compared with the other energy contents.

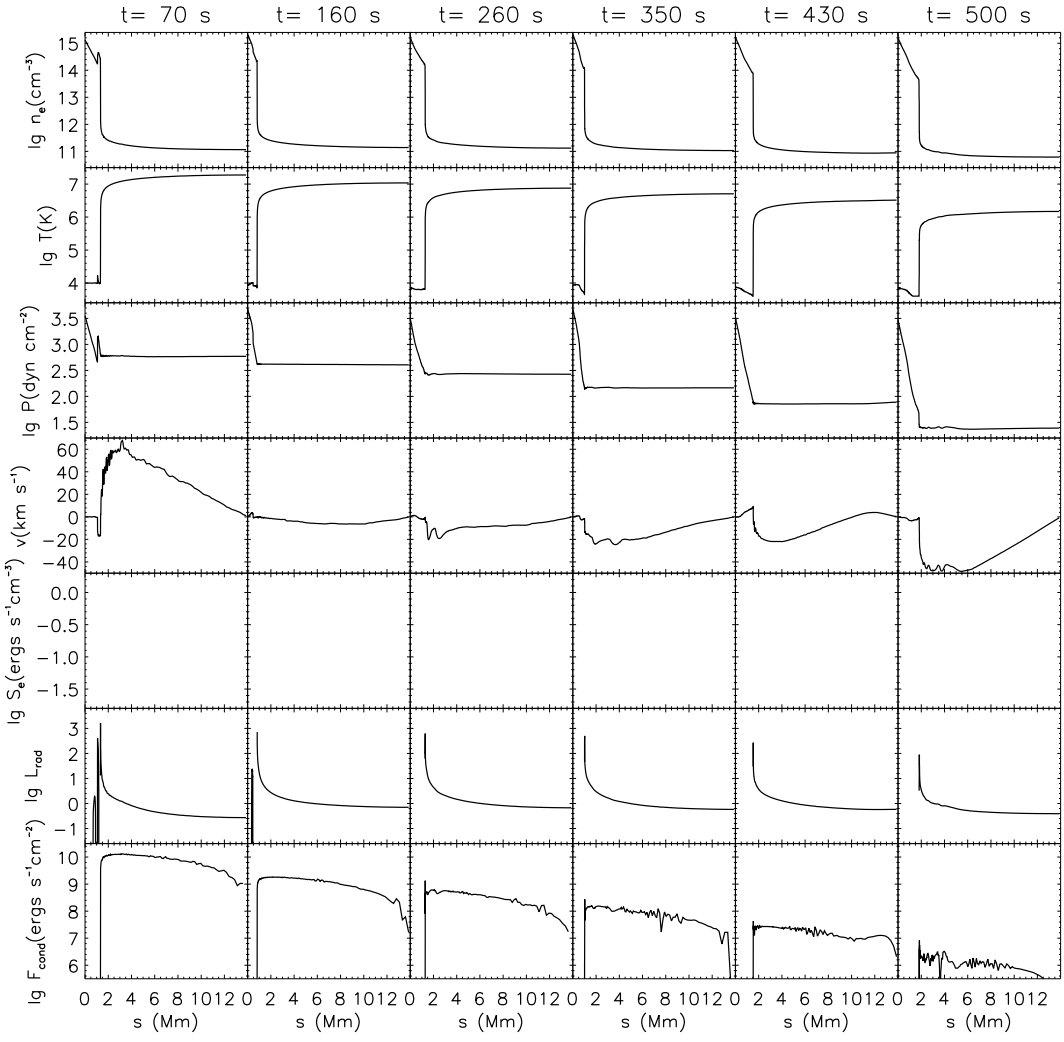

Figure 9.1: HD evolution of various quantities for Case A: electron number density, temperature, gas pressure, upward velocity, heating rate S_e, radiative loss rate $L_{\rm rad}$ (in same units as S_e), and heat conduction flux $F_{\rm cond}$, as a function of distance from the bottom (FP) of the loop. Note that $S_e = 0$ in this Case and the corresponding panels are left blank intentionally for a better comparison with the other cases.

9.3.1 Case A: No Heating or Suppression of Conduction

Figure 9.1 shows the evolution of various HD variable as a function of distance along the loop (from the bottom, cf., Fig. 7.3). The system starts with a hot, relatively dense corona, heated by electrons during the preceding impulsive phase. We find the density and temperature in the coronal portion of the loop decreases with time. This occurs because of cooling in the form that heat conduction (*bottom*, not suppressed here) carries energy to the transition region and the upper chromosphere where radiative loss function (second to the *bottom*) peaks, and then energy is radiated away there. Note that direct radiative loss in the upper corona is negligibly small compared with conductive cooling (also see, e.g., Jiang et al., 2006). As a result of cooling and reduced pressure gradient (not sufficient to support material against gravity) in the corona, the plasma simply condenses and falls back to the chromosphere. This can be seen from the velocity curve, which shows generally increasing negative (downward) values. We also note that early in the decay phase (e.g., $t = 70\,\mathrm{s}$), however, chromospheric evaporation (upflow) still takes place because of residual conductive heating from the hot corona.

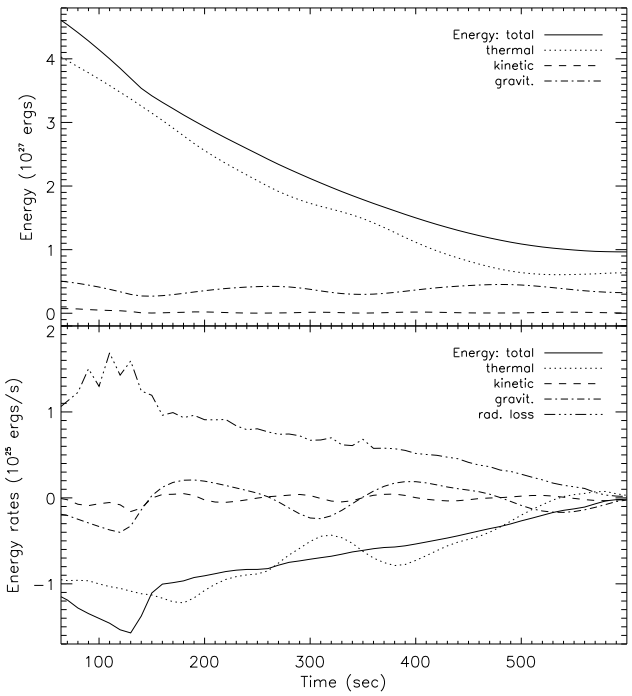

Figure 9.2: Energy evolution for Case A. *top*: Total, thermal, kinetic, and gravitational energy, integrated over the volume of the loop, as a function of time. *bottom*: Time derivative of the above energy contents, together with the radiative loss rate.

The evolution of the energy contents, which are spatially integrated over the loop volume, is shown in Figure 9.2 (*top*). The total energy monotonically decreases with time. The thermal energy (*dotted*) follows the same trend and clearly dominates over the gravitational (*dot-dashed*) and kinetic (*dashed*) energy, which stay at about the same level. The *bottom*

panel shows the time derivatives of these energy contents, together with the radiative loss rate. We find the absolute value of the total energy change rate decreases with time, which is correlated with the radiative loss (this simply means energy conservation, see §8.2.1).

We note that there are some fluctuations in the gravitational and kinetic (smaller *absolute* amplitudes) energy, which are more pronounced in the *bottom* panel of Figure 9.2. The absolute value of the thermal energy change rate (< 0) also show, on top of its general decreasing trend, some modulations that seem to be anti-correlated with those of the gravitational and kinetic energy. We interpret this as conversion of energy among different forms in the plasma (also see Chapter 8).

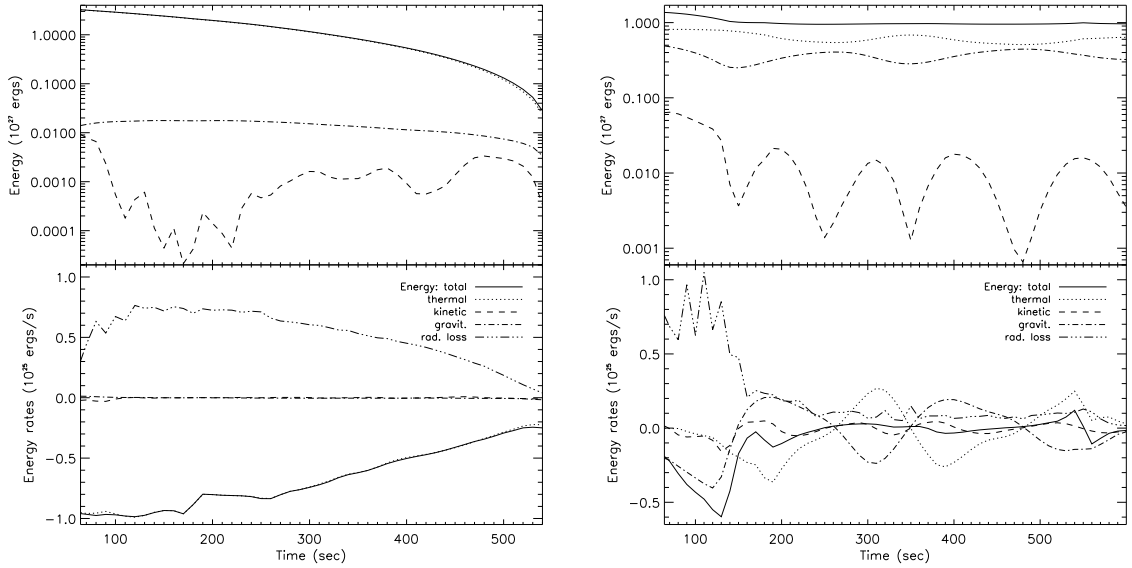

Figure 9.3: Same as Fig. 9.2, but for the corona (*left*) and chromosphere (*right*) only.

To see this point clearly and identify the source of the fluctuations, we plot the same energy budget history for the corona (*left*) and for the chromosphere (*right*) separately in Figure 9.3 in which we used the position where $T = 1 \times 10^7$ K as the boundary between the two regions. For the corona portion (Fig. 9.3), the thermal energy and the total energy curves almost overlap each other, and they simply show a featureless monotonic decay; so does the gravitational energy. Only the kinetic energy exhibits some fluctuations, but without a simple pattern. For the chromosphere (Fig. 9.3, *right*, note logarithmic scale), in contrast, the total energy initially decrease slightly and then stays almost constant and the fraction of the thermal energy is smaller than that in the corona. The fluctuations and the anti-correlation of the gravitational and thermal energy are evident. This results from the **chromospheric oscillation** (Mariska et al., 1982), which can be seen from the top panel of Figure 9.1, where the height of the transition region rises and drops back and forth. (This can be more clearly seen in a movie, not shown). The alternative rarefaction and compression of the chromospheric material performs energy conversion between the two forms: thermal and gravitational energy. We note that the kinetic energy (Fig. 9.3, *upper right*) shows larger *relative* amplitudes and, particularly, a $\sim$2 times higher frequency than

the gravitational energy. The kinetic energy reaches its minimum when the gravitational energy reaches its maximum or minimum. This is because the chromosphere oscillates like a loaded[2] spring in the vertical direction and each cycle in the gravitational energy variation includes *two* cycles of acceleration and deceleration, resulting two cycles in the kinetic energy curve.

9.3.2 Case B: Heating Only

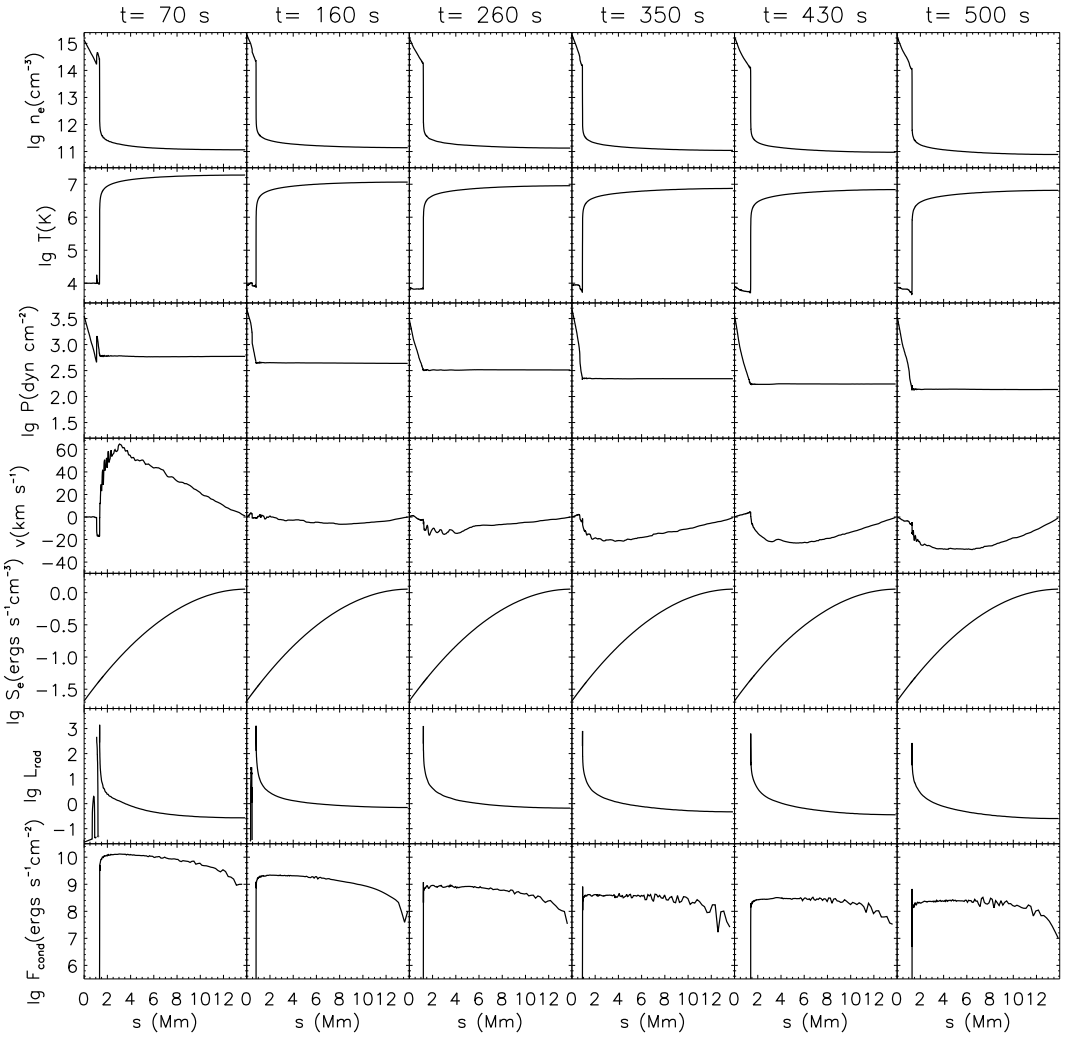

Figure 9.4: Same as Fig. 9.1, but for Case B.

In this Case, we applied additional heating in the corona. The spatial distribution of

[2]Most of the loading is provided by cooling and condensation in the overlying layers in this simulation (Mariska et al., 1982), simply because material falls back from the corona and thus pushes chromosphere downward.

the heating is of a Gaussian shape which peaks at the loop apex (see Fig. 9.4, row 5). The evolution of the HD variable is shown in Figure 9.4, which is very similar to Figure 9.1 for Case A, except that here the coronal density, temperature, and pressure decay slightly more slowly due to heating. Note that the temperature still distributes more or less uniformly in the corona despite more heating at the LT. The downflow (due to condensation) velocity is lower than that in Case A too. The conduction flux stays higher because of higher temperature here. The history of the energy budget (not shown) is also very similar to that of Case A (Fig. 9.2).

9.3.3 Case C: Suppression of Conduction Only

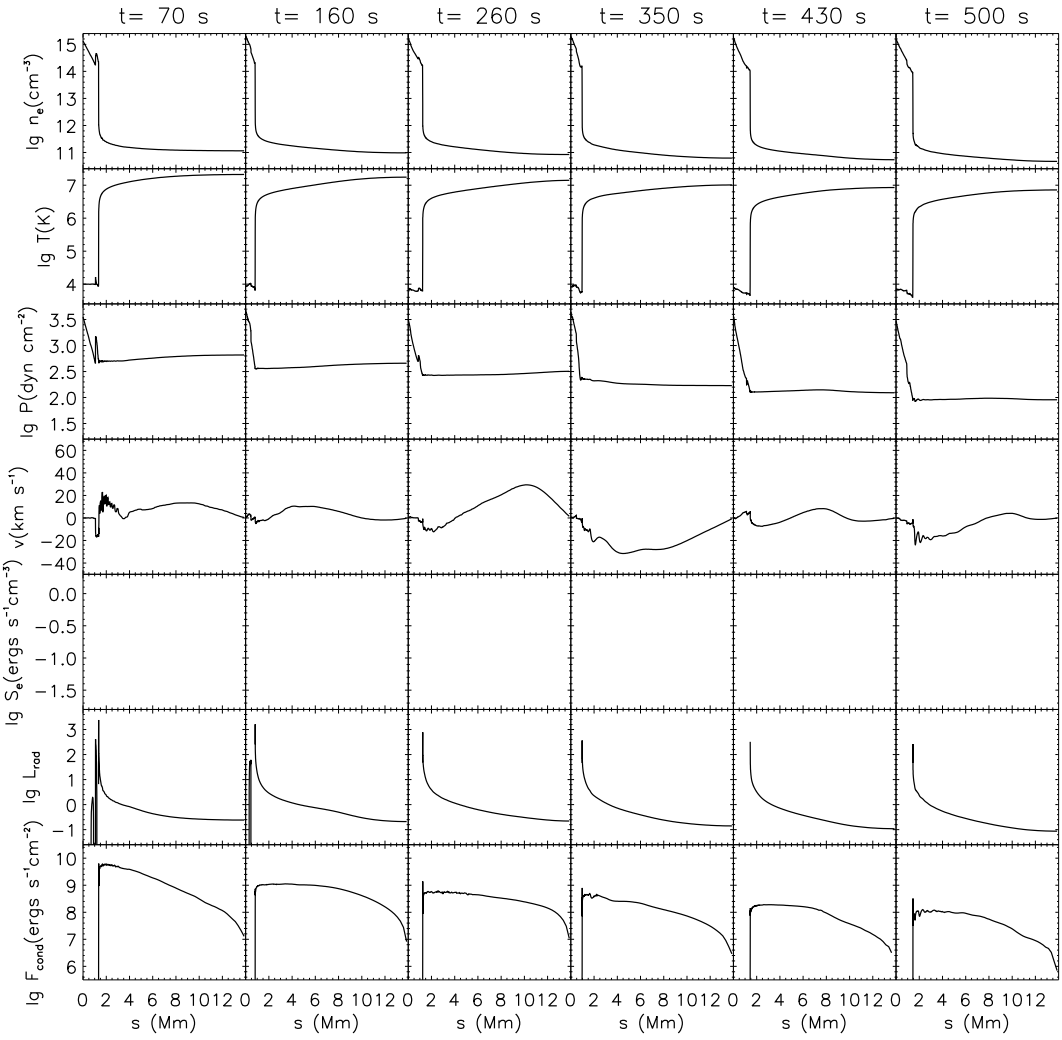

Figure 9.5: Same as Fig. 9.1, but for Case C.

Here instead of applying additional heating, we suppress the conduction with a Gaussian

profile. Compared with Case A, the heat conduction flux (Fig. 9.5) varies more dramatically from the LT to the FP. At $t = 70\,\mathrm{s}$, for example, F_{cond} increases by nearly three orders of magnitude from the loop apex to near the transition region, as opposed to the variation of about one order of magnitude in Case A. As a result, the temperature slope in the corona is larger here (because there is more suppression in the LT than near the FP). The overall temperature decay, as expected, is delayed, compared with Case A. The energy budget is very similar to that of Case D (see below, Fig. 9.7) and thus is not shown here. A new feature caused by suppression of conduction here is the traveling waves (see the velocity in Fig. 9.5) in the corona, for which we defer our discussion to next section.

9.3.4 Case D: Heating and Suppression of Conduction

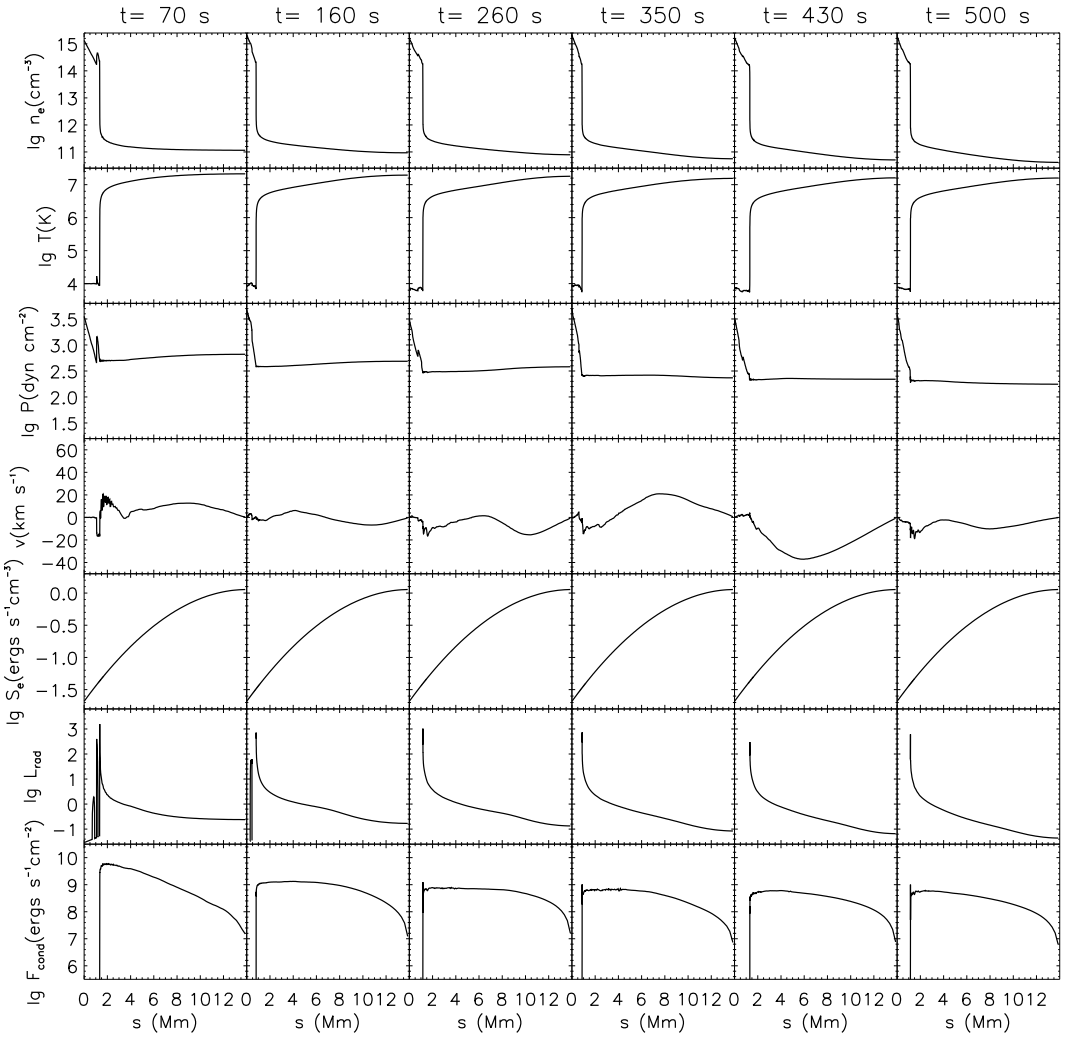

Figure 9.6: Same as Fig. 9.1, but for Case D.

Now we combine heating and suppression of conduction used above together in Case D. As can be seen in Figure 9.6, the overall evolution is similar to that of Case C, except even more delayed decay here. The energy history is plotted in Figure 9.7 (*left*). The constant heating rate is shown as the *long dashed* line, which in addition to the suppression of conduction, counteracts the energy decay.

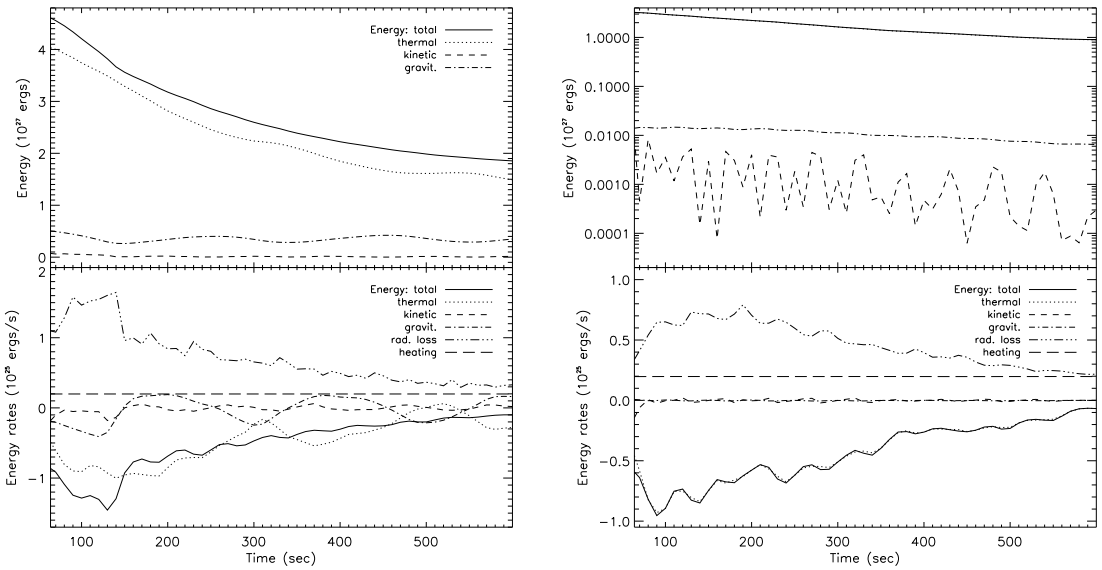

Figure 9.7: Same as Fig. 9.3, but for the whole loop (*left*) and the corona portion (*right*) of Case D, with the additional quantity, heating rate, plotted as the *long-dashed* line in the bottom panels.

Another difference here, compared with Figure 9.2 for Case A, is the short-period fluctuations in the thermal energy change rate (*dotted*, *bottom* panel). Such fluctuations are superimposed on the existing long-period ($\sim$ 200 s) fluctuations caused by the chromospheric oscillation. Again, we plot the energy contents in the corona and the chromosphere separately, and we find the chromosphere (not shown) has a similar energy evolution as in Case A. However, the corona behaves quite differently, as can be seen in Figure 9.7 (*right*). The above mentioned short-period fluctuations are present in the velocity (*dashed*, *top right*), the thermal (and total) energy change rate, as well as the radiative loss (*bottom right*). These fluctuations are caused by the traveling waves, which results in alternative compression (heating) and rarefaction (cooling) of the plasma. Such waves can also be seen in the velocity curves in Figure 9.6. The same effects are present in Case C, but not in Case B. We suggest the imposed suppression of conduction is responsible for the growth of such waves,[3] for which the strong disturbance to the fluid during the turbulent impulsive phase could be the seeds.

We also note that the lifetime of the traveling waves here may be exaggerated, because there is no viscosity included in this model. Such an approximation is good for the impulsive phase since the contribution of viscosity to the momentum and energy equations are

[3]Note there are similar coronal waves in Cases A and B, but they are of much smaller amplitudes and do not produce noticeable effects as in Cases C and D.

overwhelmed by the other more dramatic agents (e.g., electron heating). However, during the slow (on timescales of 10 times longer than that of the impulsive phase) evolution of the decay phase, viscosity may play a role, particularly in damping the waves.

9.3.5 Comparing Cases A-D

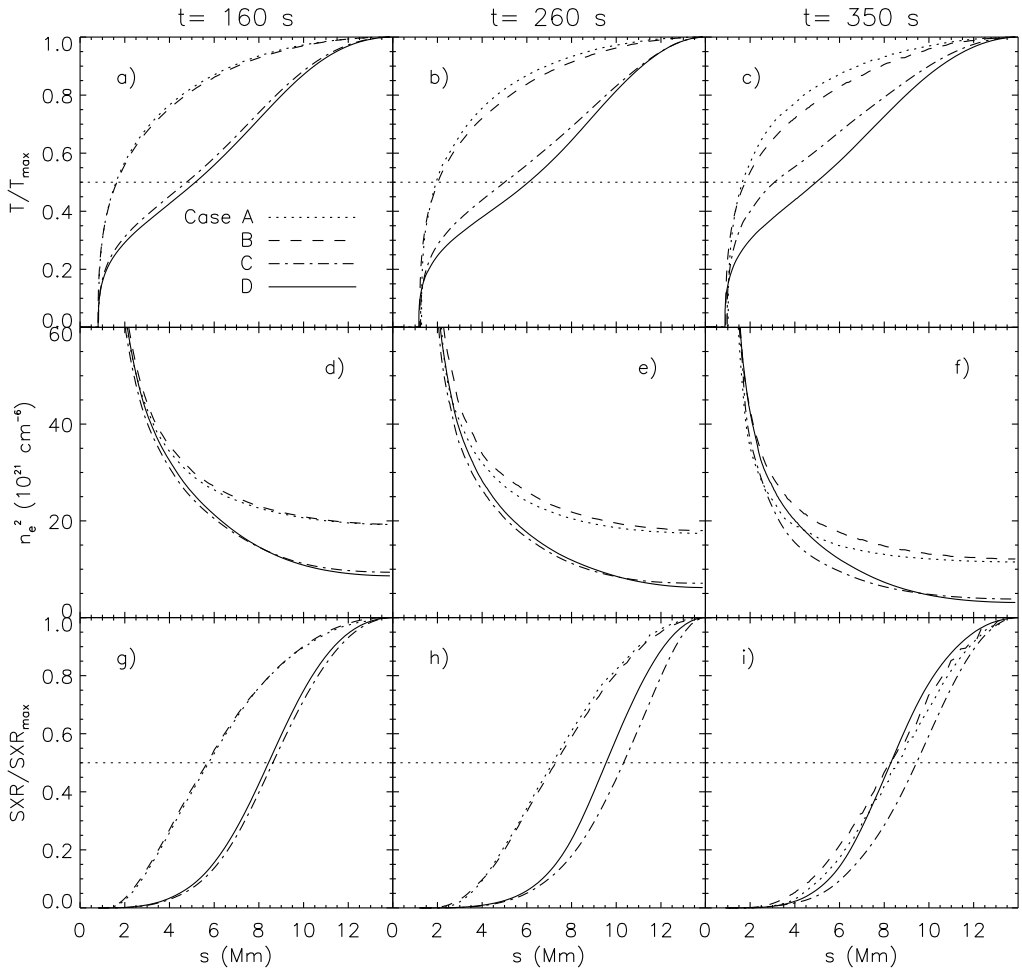

Figure 9.8: Comparison of temperature, density squared n_e^2, and thermal bremsstrahlung emission (at 6 keV) profiles among Cases A-D at selected times. Each of the temperature and emission profiles are normalized to its individual maximum. Each column is of the same time. The dotted horizontal lines in the top and bottom rows mark the 50% levels.

We now compare the four simulation cases more directly. Figure 9.8 shows the normalized temperature (*top*) and thermal bremsstrahlung emission (*bottom*, at 6 keV) profiles, together with the density squared n_e (*middle*) at selected times for all the cases. In general, the curves of Cases A and B form one group (called Group 1), and those of Cases C and D form another (Group 2), exhibiting the expected shapes due to different conduction suppression and/or heating imposed.

Case B has a temperature profile very close to that of Case A, despite its localized heating near the LT. This is because heat conduction (without suppression) is so efficient (Jiang et al., 2006) that the energy addition by localized heating is quickly conducted away from the LT and this makes the coronal temperature close to a uniform distribution. Cases C and D have a more confined high temperature region near the LT, due to their suppressed conduction. They also have a lower coronal density because their higher coronal temperature requires less material to produce sufficient pressure.

The thermal emission profiles, in general, follow the shape of the corresponding temperature profiles. Cases C and D have narrower emission profiles, same as their temperature profiles, particularly early during the decay phase. This is consistent with that found by Jiang et al. (2006). At some other times (e.g., $t = 360$ s), this pattern does not always hold. This is because thermal emission (eq. [8.7]) is an increasing function of both T (nonlinear) and n_e^2 (or emission measure, linear). In our simulation, T increases with distance (from FP to LT), while n_e^2 behaves oppositely. The interplay of these two quantities determines the resulting thermal emission profile. It is thus not surprising that the emission profile does not necessarily follow the shape of the corresponding temperature curve exactly. Sometimes, a hump[4] (not shown) in the thermal emission can be produced and it shifts back and forth along the loop, which is due to the enhanced local density and temperature by traveling waves (see discussions above). These new features were not present in the hydrostatic solutions of Jiang et al. (2006).

Figures 9.9*a* and 9.9*b* show the history of density squared n_e^2 and temperature, respectively, at the loop apex. Again, we see that Group 1 (Cases A and B) has similar values of n_e^2, and so do Group 2 (Cases C and D) whose values are less than that of Case A by up to a factor of four. Group 1 have an increasing density at early times before its decreasing phase, while the density of Group 2 has a generally decreasing trend. This happens because in Group 1 chromospheric evaporation continues to bring material to the corona early into the decay phase, as can be seen in the large upward velocity values in Figures 9.1 and 9.4. Group 2, on the other hand, has a higher coronal temperature due to suppression and thus a higher LT pressure (see Figs. 9.5 and 9.6) that produces a downward pressure gradient force to counteracts the evaporation upflow. This results in lower upflow velocities and decreasing (and lower) LT densities in Group 2.

As to the temperature, from Case A to D, we generally have increasing values at a given time, except on the very late stage when the curves of Cases B and C cross each other. This is expected because we have increasing suppression and/or heating applied. For example, Case D combines these effects of Cases B and C together, so it has the highest LT temperature. After $t \sim 500$ s, its LT temperature even slightly increases. This comes about because of the decreasing LT density and constant continuous heating and suppression of conduction.

Figures 9.9*c* and 9.9*d* show the spatially integrated total energy and thermal XR emission flux. They also exhibit similar patterns as the LT temperature. As is evident, the n_e^2, T, and XR emission curves of Group 2 all show similar fluctuations, which are caused by the traveling waves mentioned above.

We note that the average energy decay rate (Fig. 9.9*c)* of Case D (with combined

[4]The bright feature in X-rays moving along the loop is similar to the *TRACE* observation of the bright EUV blob that travels back and forth from one end of the loop to the other (Ryutova & Shine, 2006).

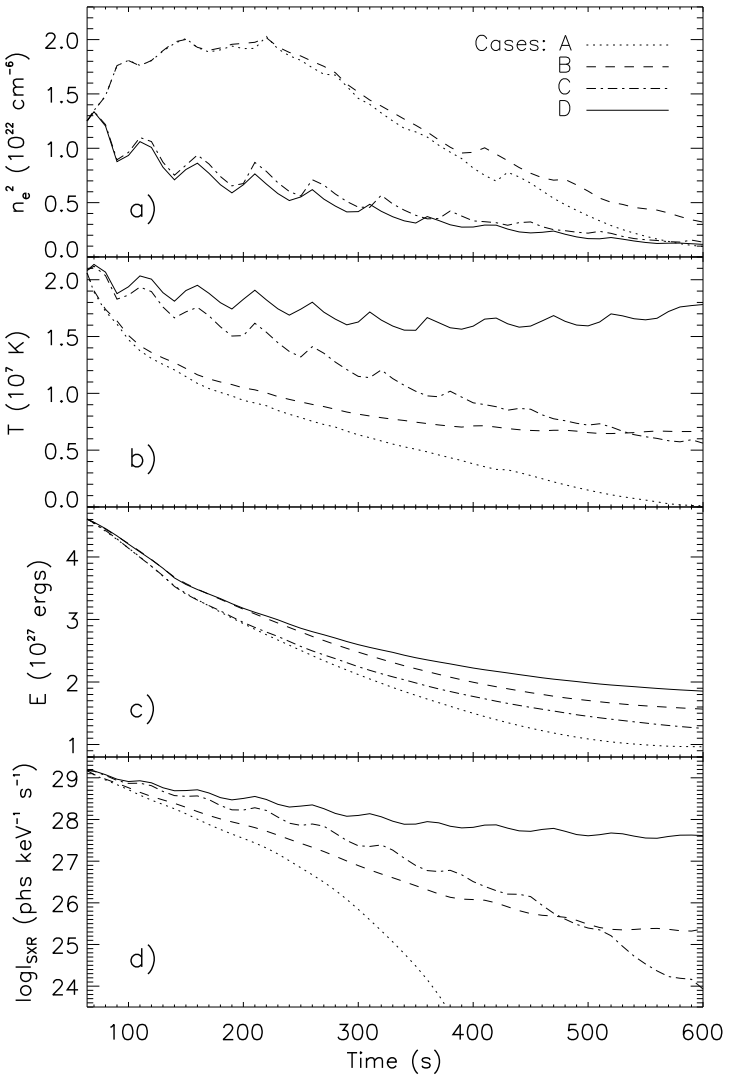

Figure 9.9: Comparison of decay of various quantities for Cases A-D. (*a*) and (*b*) Evolution of density squared n_e^2 and temperature, respectively, at the loop apex. (*c*) and (*d*) Total energy and thermal bremsstrahlung (at 6 keV) intensity $I_{\rm SXR}$, respectively, both integrated over the volume of the whole loop.

suppression and heating) is about 3/4 of that of Case A. Such a difference is much less than that of Jiang et al. (2006, see Fig. 13 there), with otherwise comparable parameters. This is because they assumed hydrostatic solutions and the calculation was restricted to the hot, coronal portion of the loop, so radiative loss is small. Therefore, the only effective energy loss channel in their model is through conduction to transfer energy to the FPs. Contrastingly, here, we have plasma flow and traveling HD waves that act as another energy carrier. The energy input from the LT can be carried by plasma down to the transition region and the chromosphere and then be efficiently radiated away there.

9.4 Summary and Discussion

We have performed a HD simulation for the decay phase of solar flares, by inclusion of the fluid dynamics calculation and the chromosphere in the computational domain. This work improves on the previous work by Jiang et al. (2006) who assumed a hydrostatic condition and that by Antiochos & Sturrock (1978) who neglected radiative loss. In general, our result confirms the conclusions by Jiang et al. (2006):

1. Heating at/near the LT alone is not able to confine the LT source in a small region as seen in SXRs, although it could be invoked to explain observed energy decay rates.

2. Suppression of conduction localized near the LT is needed to produce a narrow temperature profile and thus a compact SXR source near the LT.

3. A combined heating and suppression of conduction is suggested to be present and to be localized near the LT region. Such a coexistence can explain both the reduced energy decay rates and spatially confined LT source.

Our calculation has also uncovered some new information not present in Jiang et al. (2006):

1. Different density profiles can modify the thermal XR emission profiles based on the corresponding temperature profile. Even in the presence of a compact temperature profile, a somewhat broad XR emission profile could be produced due to the interplay of the density and temperature distributions.

2. Plasma flow and/or waves can carry energy away from the hot LT region, and thus counteract the effects of heating and suppression of conduction. Therefore, an even larger factor of suppression would be required to explain the XR observations.

In this simple simulation study, the parameter space has not been fully explored. The width w for the Gaussian suppression profile, for example, is important in determining the effects of suppression, and in particular, the existence/growth of the traveling HD waves. The radiative loss calculation can also be improved, say, using the newly released CHIANTI package. We look forward to a future modeling development to carry out such tasks.

Chapter 10

Concluding Remarks

Now it is time to step back and review this work. Here we recapitulate our motivation and highlight our conclusions. We then comment on directions for future investigations.

10.1 Summary and Conclusions

We have carried out an investigation of acceleration and transport of particles in solar flares, and their thermal and nonthermal radiative signatures, using both HXR data analysis and combined Fokker-Planck and hydrodynamic (HD) modeling. This research focuses on solar flares because they provide a unique laboratory for us to understand particle acceleration mechanisms which have far-reaching implications, not only for solar and space physics in particular, but also for astrophysics in general. We summarize here our conclusions and their implications in the context of contemporary flare research as follows.

10.1.1 Hard X-ray Observations

Our observational efforts utilized HXR data obtained by the currently active *RHESSI* mission and focused on spatial, temporal, and spectral variations of the LT and FP emissions.

1. In the stochastic acceleration (SA) model, the LT emission comes directly from the accelerated electrons and the FP emission is produced by escaping electrons. The emissions of the two sources are related and can thus be used to constrain the SA model parameters. We have carried out a preliminary **statistical study** of 29 limb flares, which have minimal projection effects, and obtained the relative spectra and fluxes of the LT and FP sources. As presented in *Chapter 2*, for the LT and FP sources, respectively, we find an average spectral index of $\bar{\gamma}_{\rm LT} = 6.84$ and $\bar{\gamma}_{\rm FP} = 3.35$, with a large difference which could, in principle, be explained by the SA model. However, the spectral indexes (of a given flare and from flare to flare) do not seem to be correlated. This is not expected, but not surprising either because of the complexity of the exact physical processes involved. This statistical study has also led us to identify four flares of special interest for further investigations, each of which presents *evidence* of particular aspects as well as imposes *challenges* for the classical reconnection model of solar flares.

2. In the classical flare model, magnetic reconnection takes place at lower altitudes first and then progresses to higher overlying loops. In this picture, one would expect that the

FPs separate while the LT source moves up with time. However, such a **correlated motion** of the different sources was rarely observed *simultaneously* in the past, although either a rising LT or two separating FP sources have been reported. We have shown in *Chapter 3* an excellent example of such a picture. The 2003 November 03 X3.9 flare, unlike many other complex X-class flares, shows a very simple morphology with a well-defined LT and two FP sources. The almost monotonic upward motion of the LT source and the increase of separation between the two FPs at comparable speeds are exactly what are expected. In addition, we find that the source motions are relatively slower during the more active phases of HXR emission; the emission centroid of the LT source shifts toward higher altitudes with increasing energy; the separation between the LT emission centroids at two different photon energies is anti-correlated with the FP flux. Non-uniformity of the reconnecting magnetic fields could be a possible explanation of these features.

3. Outflow jets of high speed plasmas and associated turbulence, in the classical 2-D picture of magnetic reconnection, is present in opposite directions along the current sheet. Accelerated particles and heated plasmas are expected to be present in both directions as well. During the impulsive phase, we have commonly observed *one* LT source. A **double-coronal-source** structure has only been observed recently by *RHESSI* in a few flares (Sui & Holman, 2003; Sui et al., 2004; Veronig et al., 2006; Li & Gan, 2007) which show an additional, weaker source above the common LT source. Due to the faintness of the additional source, its spectrum has not been studied in these flares. We discovered another yet stronger case of such a double-source morphology in the 2002 April 30 flare, in which the upper source is relatively bright and long-lived, and imaging spectroscopy can be obtained to infer its spectrum and light curve. Another advantage of this event is that the FPs are occulted and thus they do not contaminate the LT emission at high energies. Analysis of this flare has been presented in *Chapter 4*. We find that the two coronal sources, observed over the 6–30 keV range, appear at different altitudes and show energy-dependent structures with the higher energy emission being closer together (also see Sui & Holman, 2003; Sui et al., 2004). Spectral analysis implies that the emission at higher energies in the inner region between the two sources is mainly *nonthermal*, while the emission at lower energies in the outer region is primarily *thermal*. The two sources are both visible for about 12 minutes and have similar light curves and power-law spectra above about 20 keV. These observations suggest that the magnetic reconnection site lies between the two sources. Bi-directional outflows of the released energy in the form of turbulence and/or particles from the reconnection site could be the source of the observed radiation. The spatially resolved thermal emission below about 15 keV, on the other hand, indicates that the lower source has a larger emission measure but a lower temperature than the upper source. This is likely the result of the differences in the magnetic field and plasma density of the two sources. For the lower source, the separation between the centroids of the emission at different energies seems to be anti-correlated with the HXR light curve, which is consistent with our earlier finding mentioned above (see Chapter 3).

4. Magnetic field measurement in a flare region, in general, can provide clues of magnetic reconnection, while HXR data contains useful information of accelerated particles. Both types of observations, if available, can be combined and used to uncover the relationship between particle acceleration and magnetic reconnection development. In *Chapter 5*, we have examined the FP HXR emission together with the associated magnetic field in the

2003 October 29 X10 flare. This event occurred close to the disc center and thus had minimal projection effects for the line-of-sight magnetic field which can be obtained from *SOHO*/MDI. We find that there are two well-defined conjugate FPs showing **unshearing motions**, **various correlations**, **asymmetric characteristics**. (1) The double FPs first move toward and then away from each other, mainly parallel and perpendicular to the magnetic neutral line, respectively. The transition of these two phases of FP *unshearing motions* coincides with the direction reversal of the motion of the LT source, and with the minima of the estimated loop length and LT height. (2) The FPs show temporal *correlations* in HXR flux, spectral index, and magnetic field strength. The HXR flux exponentially correlates with the magnetic field strength which also anti-correlates with the spectral index before the second HXR peak's maximum, suggesting that particle acceleration sensitively depends on the magnetic field strength and/or reconnection rate. (3) *Asymmetries* are observed between the FPs: on average, the eastern FP is 2.2 times brighter in HXR flux and 1.8 times weaker in magnetic field strength, and moves 2.8 times faster away from the neutral line than the western FP; the estimated coronal column density to the eastern FP from the LT source is 1.7 times smaller. The two FPs have marginally different spectral indexes with their mean values of $\langle\gamma\rangle = 3.63 \pm 0.06$ vs. 3.79 ± 0.11. The eastern-to-western FP HXR flux ratio and magnetic field strength ratio are anti-correlated only before the second HXR peak's maximum. Neither magnetic mirroring nor column density *alone* can explain these observations when taken together, but their combination, together with other transport effects (including non-uniform target ionization, relativistic beaming, albedo, and return currents), may play a role.

5. **Chromospheric evaporation** is a consequence of energy deposition by electrons in the lower atmospheres and it is usually observed by blue-shifted line emissions. Such observations, in a sense, are indirect evidence of chromospheric evaporation, because the mass motion is not directly imaged. The superior capabilities of *RHESSI* enabled us to remedy this shortcoming with the observation of the M1.7 flare of 2003 November 13, which shows some unusual spatial evolution and provides direct evidence for chromospheric evaporation. Analysis of this flare is presented in *Chapter 6*. We find that, as expected, the LT source dominates at low energies, while the FP sources dominate the high-energy emission. At intermediate energies, both the LT and FPs may be seen, but during certain intervals emission from the legs of the loop dominates, in contrast to the commonly observed LT and FP emission. The HXR emission tends to rise above the FPs and eventually merge into a single LT source. This evolution starts at low energies and proceeds to higher energies. The spectrum of the resultant LT source becomes more and more dominated by a thermal component with an increasing emission measure as the flare proceeds. The SXRs and HXRs show a Neupert-type behavior. With a nonthermal bremsstrahlung model, the brightness profile along the loop is used to determine the density profile and its evolution, which reveals a gradual increase of the gas density in the loop. These results are evidence for chromospheric evaporation and are consistent with the qualitative features of hydrodynamic simulations of this phenomenon. However, some observed source morphologies, such as the leg emission, and their evolution cannot be accounted for by previous models. This motivated us to carry out the following modeling efforts.

10.1.2 Combined Fokker-Planck and Hydrodynamic Modeling

We have started an investigation of combining our Fokker-Planck *$\mathcal{F}$lare* code (Petrosian et al., 2001) with the NRL flux tube HD code (Mariska, Emslie, & Li 1989). The motivation is two-folded, one from the aforementioned new *RHESSI* observations and the other from theoretical demands which we describe as follows.

In solar flares, there are two important processes, one of which is the acceleration and transport of energetic particles, and the other of which is the HD response of the atmosphere heated via the particle energy deposition. The two processes are coupled together and can affect each other in a circular way. Variations of the acceleration rate and thus the spectrum of particles, for example, can alter the electron heating rate and thus affect the HD evolution. The chromospheric evaporation, as one form of the atmospheric response, can modify the density and temperature in the loop and possibly in the acceleration region as well. This, in turn, will change the acceleration process. The *circular nature* of the problem requires that the two processes should be studied together in a self-consistent way. However, because of the complexity of the subject, people in the past tended to separate them and focused on one process at a time, while making some simplified, yet not entirely accurate assumptions for the other. As progresses have been made on both sides over the past two decades, we are now in a position ready to break through previous imitations and conduct a combined study of both processes more accurately.

As described in *Chapter 7*, we use the Fokker-Planck code to calculate the electron distribution at each depth along the loop and thus obtain the spatial distribution of the electron energy loss rate (due to Coulomb collisions). Such energy loss is used as the heating function in the HD code and it drives the HD evolution. The updated density distribution is then fed back to the Fokker-Planck code to calculate the new heating rate. In this way, the two codes communicate in real time and keep track of the temporal evolution of the system. The heating rate calculated here is more accurate than the approximate, analytical ones (e.g., Emslie 1978) used in previous models. We also use more realistic electron spectra obtained from the recent SA model by Petrosian & Liu, S. (2004), which has a smooth transition from the quasi-thermal component at low energies to the nonthermal tail at high energies. Such a spectrum shape is consistent with that inferred from observed X-ray spectra, which can usually be fitted with a thermal plus power-law model. The previous models (e.g., Fisher et al., 1985a; Mariska et al., 1989), however, assumed a power-law spectrum with a low-energy cutoff (say 15 keV), thus essentially eliminating low-energy electrons from the distribution.

We now summarize our results from this newly combined Fokker-Planck and HD simulation. (1) One of the main findings is that inclusion of the more realistic electron spectrum from the SA model affects the spatial distribution of energy deposition and thus influences the HD evolution. The low-energy electrons in the quasi-thermal portion of the distribution produce more heating in the corona than the previous models (Mariska et al., 1989) which have more heating in the chromosphere. Because the radiative loss function has its peak in the upper chromosphere, direct chromospheric heating results in a significant portion of the energy being radiated away and less energy left available to evaporate the plasma. Therefore, our new model generally drives chromospheric evaporation more efficiently than previous models. (2) Another finding is that variations of the acceleration rate are actually

coupled with variations of the escape time $T_{\rm esc}$ and both factors can modify the escaping electron spectrum and thus the resulting HD response. In general, a higher acceleration rate produces a harder electron spectrum but smaller escaping electron flux, because stronger turbulence scatters particles more and traps them longer in the acceleration region. These two factors combine to produce less coronal heating and relatively more chromospheric heating. Therefore, for the same reason mentioned above, this results in comparably weaker chromospheric evaporation for a harder electron spectrum.

From the same simulations, we have checked the empirical Neupert effect, as presented in *Chapter 8*. Here we use more rigorous calculations of the energy contents and thermal and nonthermal X-ray radiation than previous works, e.g., by Veronig et al. (2005). We find that a correlation of the SXR derivative and the HXR flux indeed exists. A better linear correlation is found between the SXR derivative and the more physically related thermal energy variation rate. We point out that a simple *linear* correlation between the SXR derivative and the HXR flux is not expected, due to the many nonlinear processes involved.

As an extension of our studies on the flare impulsive phase, we have also carried out a simulation of the decay phase (*Chapter 9*). The motivation here is to test the effects of heating and suppression of conduction, presumably produced by turbulence (at a lower level during the decay phase), in the presence of HD flows. Our result confirms our earlier conclusion (Jiang et al., 2006) that suppression of conduction and/or heating is required to produce the observed low energy decay rate and the compact LT source seen in SXRs. The new conclusions include that plasma flows and waves can carry energy away from the hot LT region, and thus counteract the effects of heating and suppression of conduction. Therefore, an even larger factor of suppression would be required to explain the SXR observations.

10.2 Future Work

Now it is time to take a look into the future. As progress was made in this work, we realized that many aspects of this research can be improved and we briefly discuss several important ones as follows.

1. Time-dependent Transport Code: The current particle transport code finds a steady state solution, while time-dependent solutions can be obtained with the particle acceleration and HD codes. One can upgrade the transport code to a time-dependent version and then the combined codes can make time advances in a more self-consistent manner. The upgrade can be done based on the time-dependent code of Hamilton, Lu, & Petrosian (1990). Once a fully time-dependent version is available, we can drop the constraints set by the current assumption of semi-time-dependent approach in which the heating rate is a function of column depth. These constraints include: (1) the loop must be uniform, i.e., no magnetic convergence or divergence; (2) synchrotron loss and diffusion must be neglected.

2. Warm-target Coulomb Collisions in the Transport Code: The current transport code assumes a cold ambient plasma, whose electron thermal velocities are negligibly small compared with those of the accelerated high-energy electrons. This is true for the chromospheric materials, as well as for the coronal plasma during the early stage of a flare. However, as the flare proceeds and as the chromospheric evaporation takes place, the plasma in the flaring loop is significantly heated and the thermal energy of the ambient electrons

could be comparable to the kinetic energy of the accelerated electrons, particularly those in the low-energy portion of the spectrum. A modification to the Coulomb loss rate by taking into account the thermal energy of the background electrons is thus needed (e.g., Miller et al., 1996; Benz, 2002; Emslie, 2003). This has been done in the acceleration code, but has not yet been implemented into the transport code due to some technical difficulties. As an intermediate fix to this problem, one can stop the Fokker-Planck calculation once the energy of the beaming electrons degrades to the level of the thermal energy of background electrons. This is equivalent to the argument that such beaming electrons leave the nonthermal particle population and merge into the thermal background.

3. Angle-dependent Radiation Code: At present, the bremsstrahlung radiation is calculated using an angle-averaged cross-section for simplicity. A fully angle-dependent radiation code is available (McTiernan, 1989), but has not been implemented in the code yet. This would be included in the future development plan.

4. Momentum Deposition of Accelerated Particles: In the current model, momentum exchange between the accelerated particles and the background particles is not included in the HD equations. That is, the only contribution from the particles is the heating rate term in the energy equation. This is a valid approximation for electrons because of their small mass compared with that of the background protons. However, for accelerated protons (although less important in population than electrons), their momentum loss to the background plasma could be a significant portion of the system's momentum budget. This momentum, in addition to that produced by electron beam heating and the resulting overpressure, could be responsible for flaring seismic waves observed by helioseismological techniques (Kosovichev & Zharkova 1998). One of our future improvement would include the moment exchange term in the HD equation and we hope to combine this with the proton acceleration model (Petrosian & Liu, 2004).

5. Asymmetric Loops: The current HD model assumes a symmetric loop geometry and only calculates the evolution of one half of the loop. In reality, an asymmetric (to various extents) loop geometry is more general, which is indicated by commonly observed asymmetric HXR FP emissions (see *Chapter 5*). In such a configuration, on the side of the loop with a weaker magnetic field, the smaller convergence of the magnetic field results in a larger loss cone; this would allow more electrons to precipitate to the chromosphere, producing more heating and probably a stronger chromospheric evaporation upflow as well as a higher coronal density. However, such effects are counteracted by the larger cross-sectional area of the loop on this side and the energy deposited by electrons in a unit area may not be quite different from that on the other side. Another effect of an asymmetric loop geometry is that the evaporation upflow will not be symmetrically reflected at the loop apex and rather a stronger flow (higher velocity or density) on the one side will push a weaker flow on the other. The exact hydrodynamics will depend on the outcome of the interplay of such many factors and processes. A future direction would thus be to include the full loop in the combined HD and Fokker-Planck simulation. The NRL HD code is capable of a full-loop calculation, but the main challenge may come from making the acceleration and transport code work simultaneously in this manner and from setting proper boundary conditions. The simulation results can be checked against available HXR observations, particularly of those flares showing asymmetric FP emissions.

6. Auroras on (Extrasolar) Planets are produced by energetic particles bombarding and heating the planetary atmosphere, giving rise to emission in EUV and other wavelengths. These particles are accelerated as a result of interactions between the solar (stellar) wind and the planetary magnetosphere at the magnetopause or in the magnetotail. Auroras have been observed on magnetized solar-system planets, including the Earth, Jupiter, and Saturn. A number of Jupiter-like planets have recently been detected around giant stars. We (Liu, W. & Airapetian, 2008) argued that the massive winds from the hosting giants can produce strong and detectable auroral emission on those planets, despite their remote distances. We proposed to apply our combined Fokker-Planck and hydrodynamic code to an investigation of auroral processes in an evaporation scenario caused by injection of energetic electrons into the outer atmospheres of an extrasolar planet. Refinements to the existing solar-flare oriented code will be made to accommodate different physical conditions, such as collisional losses in a background plasma of various chemical compositions and ionizations. The model will be able to predict expected fluxes in UV continuum and emission lines, and new observations that can be used to search for evaporating planets around stars with high mass-loss rates.

Appendix A

RHESSI Data Analysis Procedures and Tools

Since *RHESSI* is a relatively new mission, there is currently no comprehensive guidelines published in the literature for necessary steps to take when analyzing *RHESSI* data of a selected flare. Unlike many other missions, *RHESSI* provides time-tagged count rate data and image reconstruction is performed on the ground by individual users. This offers the users more freedom in choosing his/her own parameters (e.g., time and energy bins), but requires a higher level of proficiency of the data analysis software. It is thus necessary to document steps and related caveats for analyzing *RHESSI* data.

Here we present a comprehensive account of *RHESSI* data analysis procedures used for previous chapters in this book. There are some overlaps among the following sections, which we choose to keep for completeness of each section. These procedures are refinements to the standard *RHESSI* image reconstruction (Hurford et al., 2002) and spectral fitting (Smith et al., 2002) techniques that are implemented in the Interactive Data Language (IDL) routines available in the SolarSoftWare (SSW; Freeland & Handy, 1998). Specific analysis routines are described by Schwartz et al. (2002), in various documents on the *RHESSI* Web site,[1] and in the author's personal library (available upon request). The procedures described here can be readily adopted for other *RHESSI* data analysis tasks.

A.1 Flow Chart for Statistical Study of Imaging Spectroscopy (Chapter 2)

We summarize here the steps taken for the statistical study of imaging spectroscopy of limb flares presented in Chapter 2, which includes the following four parts:

I. Initial Screening: In the very first step, we scan the online flare list and narrow down our search range gradually as follows.

1. We use the two criteria (as stated in Chapter 2), longitude $\geq 70^\circ$ and peak count rate $\geq 30\,\mathrm{s}^{-1}\,\mathrm{detector}^{-1}$ in the 12–25 keV channel, to perform the initial selection. We

[1] See http://hesperia.gsfc.nasa.gov/rhessidatacenter/.

also require the highest energy band showing flare counts to be greater than 12 keV, in order to allow a sufficiently wide energy range for spectrum fitting.

2. Next we check various plots available online at the *RHESSI* data center to obtain a general impression for each selected flare. The *Quicklook Browser*[2] offers *RHESSI* light curves, images, spectrograms, and monitor rates. The spectrogram (by S. Krucker) shows the history of photon spectrum and can help distinguish between counts produced by flare photons and by radiation-belt particles, the latter of which usually appear as a blob at high energies. When checking the images, one should pay attention to the flare location, source morphology, and the highest imageable energy band. Note that this browser only provides *quicklook images* (by J. McTiernan) of a single time interval in broad energy bands and may miss the HXR peak(s) and thus FP emissions. The energy-by-time image array of a flare at the HESSI Experimental Data Center (HEDC) at ETH Zurich,[3] if available, is particularly useful for detailed inspection of images at separate times and energies. By examining these quicklook data sets, we can narrow down our focus to a sample of flares that show well-defined source structures (e.g., with clear LT and FP sources).

II. Preliminary Checking: Now we are ready to download the real flight data and conduct some more customized checks for each flare in the sample.

1. We can plot light curves through the *RHESSI* GUI widget and check various flags, including attenuator states, decimation (can be corrected since 2003/09/12), spacecraft night (eclipse), and South Atlantic Anomaly (SAA).

2. Some important information not shown in GUI can be obtained through J. McTiernan's quicklook flags (by get_flist_flag.pro and get_flag.pro from the author's personal library): (*a*) particle events; (*b*) upper energy limit and weight of decimation; (*c*) SC Transmitter (when it is on, detector 8 becomes noisy and should not be used); (*d*) NMZ and SMZ flags (which are on when *RHESSI* is at high magnetic latitudes, where the background is higher and the rear segments are decimated — 3 out of 4 counts are discarded below 150 keV. For energies $\lesssim$ 200 keV, one should use front segments only in this case.)

3. One can also check the spin period, aspect solutions, and suspected roll solutions (using chk_spin_aspect.pro and pmtras_analysis.pro). In the early stage of the mission, images should be integrated over a integer number of the spacecraft rotation period, but now this requirement is not necessary as long as the integration time is sufficiently long (at least half a spin, G. Hurford, 2005, private communication). However, bad aspect or roll solutions would affect the accuracy of positioning of images, and thus flares with this defect should generally not be included in our sample.

4. Pileup effects (see §A.4 for details) can be checked with hsi_check_pileup.pro (originally written by S. Krucker, using D. Smith's preliminary pileup correction). If the fraction of piled-up photons exceeds the 10% level of the total photons in energy band where

[2]http://sprg.ssl.berkeley.edu/~tohban/browser, by A. Y. Shih.
[3]http://www.hedc.ethz.ch/www/quick_dp_search.html

imaging spectroscopy will be conducted, the flare should be removed from our sample, as pileup corrections for imaging are not yet available. The above steps 2–4 can all be done with pre_chk_batch.pro.

III. Imaging: For the flares remaining in the sample after passing all the above selections, one must first reconstruct images from which spectra of individual sources can then be extracted.

1. Preliminary images of wide time intervals, broad energy bins, large pixel sizes, and large field of views can be made with the Back-projection or CLEAN algorithm which is computationally fast. The purpose here is to obtain the flare morphology at different energies and its general evolution. This step can be skipped if such images are available online (*Quicklook Browser* or HEDC) as mentioned above.

2. By checking the resulting images, one can identify ranges in time, energy, and space in which there are well-define X-ray sources. Within these ranges, one may make more CLEAN images with finer time and energy bins. Another way to determine the upper limit of the energy range for imaging is to check the spatially integrated spectrum, and identify the energy where the spectrum turns flat toward higher energies (dominated by the background) or becomes noisy with large fluctuations.

3. Based on the above experience with the flare under study, the user now needs to determine the control parameters for the final images which will be used for imaging spectroscopy. There are no universal rules here, but the general considerations (particularly regarding photon statistics) of time and energy bins can be found in §2.2. We shall emphasize that the number of energy bins should be large enough for spectral fitting, especially in the 10–30 keV range, in which the conjunction between thermal and nonthermal components appears. For example, one may take 16-20 logarithmically spaced energy bins in the 10–100 kev range. Note that the selected image dimension (field of view) can be as small as possible to save computational time, but must be large enough to enclose *all* the sources (Hurford et al., 2002).

4. Now one is ready to use the above selected control parameters to make the final images. We used the PIXON algorithm because of its superior photometry, but we must tolerate its computational expense. An error map, based on χ^2 estimates, can be obtained afterwards for each image. In instances when PIXON is computationally non-affordable, we used the CLEAN algorithm and saved the component and residual maps, the latter of which can be used for error estimates (see §A.2).

IV. Imaging Spectroscopy: Once the images are reconstructed, we can proceed to obtain the spectra of individual sources.

1. We need to first identify individual LT and/or FP sources in the images. It is useful to superimpose *RHESSI* images on *TRACE* and *SOHO* EIT EUV images, *SOHO* MDI[4] magnetograms and/or white-light images, and *GOES* Soft X-ray Imager (SXI)

[4]Conjugate FPs are usually located in magnetic fields of opposite polarities. For limb flares, large inclination angles (from line-of-sight) of magnetic field lines make it not very reliable to determine polarities from MDI magnetograms alone. However, if one overplots magnetograms and white-light maps together, one can identify individual sunspots and better estimate the polarities.

images, which help to identify the loop structure. However, oftentimes, we find a complex morphology and it is thus difficult to determine the source types (LT or FP) from images alone. Then, we will need to obtain additional information from the spectrum of each source (see below).

2. Once individual sources are identified, we can draw a box (or a circle or polygon) around each source and integrate the photon flux enclosed. It is advised (Hurford et al., 2002) that one must integrate a *whole* source to obtain its spectrum, and a spectrum inferred from a portion of a spatially unresolved source is not meaningful due to *RHESSI*'s limited spatial resolution. The uncertainties (see §A.2) of the integrated flux should be calculated as well for each box.

3. Now that we have obtained the spectrum and its uncertainty of each source, one can fit a model (e.g., thermal plus power-law or double power-law) to the data using Spectral Executive (SPEX) package (replaced by its object version since 2004). Note that the energy range that seriously suffers from pileup effects (§A.4) should be excluded (Emslie et al., 2003) from spectral fitting.

4. From the spectral fitting result, together with morphological information obtained above (step 1), we can now determine the source types with more confidence, because a LT source usually has a softer spectrum and a stronger thermal component than the corresponding FP sources. This step marks the end of the imaging spectroscopic analysis of one flare in the sample.

A.2 Notes for Imaging Spectroscopy

1. Detector Selection: For spectroscopic images, the front segments of detectors 3, 4, 5, 6, and 8 were used as default. For broad band images (for inferring light curves of individual sources), detectors 3–8 were usually used. Detector 2 was deselected due to its threshold of ∼25 keV and poor energy resolution of ∼9 keV. Detector 7 was generally not included for spectroscopy either because of its threshold of 7 keV and resolution of ∼3 keV. We did not use detector 1 because its $2.3''$ spatial resolution is smaller than most of the smallest features in our sample. Detector 9, due to its large FWHM resolution ($3'$ pitch), should be excluded for flares (especially those on the solar disk) that are located too close to the spin axis, because it is required that, for imaging purposes, any X-ray source must be away from the spin axis at a distance at least twice the FWHM resolution of any detector used (G. Hurford, Aug. 07, 2003, private communication).

2. Background Estimate: Since *RHESSI* is non-shielded spacecraft, the background level in the data is high (Smith et al., 2002). Various components contribute to *RHESSI* image background, falling into two categories (Aschwanden et al., 2004): (1) Non-flare photon flux neither modulated by the grids nor by the spacecraft rotation, including cosmic diffuse X-ray background, secondary photons from cosmic ray interactions with Earth's atmosphere and the spacecraft, spacecraft radioactivity, and bremsstrahlung in the Earth's atmosphere and the spacecraft from electrons precipitating from the radiation belts, etc. These background components appear as an overall DC offset, to the extent that they remain uniform over

the spin period, in the modulation pattern (Hurford et al., 2002) and in the reconstructed images. This background category constitutes on the order of 1% of the total flare photons (T. Metcalf, 2003, private communication). (2) Flare-related flux not modulated by the grids but modulated by the spacecraft spin, i.e., flare photons that *bypass* the grids by Compton scattering at the spacecraft or Earth albedo, and flare photons that *pass* the grids but originate from large sources which are larger than the FWHM resolution of the coarsest grid used, including photons coming from outside the imaging field-of-view (FOV) or albedo photons reflected in the solar atmosphere and spread in a large FOV (G. Hurford, 2003, private communication). These fluxes form another category in image background which exhibit spatial structures and constitute on the order of 15% of the total flare flux (Aschwanden et al., 2004). A background model included in the PIXON (T. Metcalf, 2003, private communication) and forward-fitting algorithms (Aschwanden et al. 2002) attempts to remove the background flux of Category 2 from images. The way such a model works is to fit a sinusoidal function with a period of one and one half spacecraft spin period, respectively, to the modulation pattern and subtract the resulting fits from the count rate data. This background model was used for our PIXON images. We also took one more step in order to subtract the DC background flux of Category 1. To do this, we simply selected a sufficiently large box to enclose all flare sources. We then defined the rest of the image (excluding the selected box) as the background region, from which we obtained an average pixel value. For a given source with N pixels, the background flux (in units of photons cm^{-2} s^{-1} keV^{-1}) can be estimated as

$$b = \frac{a^2 N}{w} \times \frac{1}{M} \sum_{i=1}^{M} p_i \ , \tag{A.1}$$

where p_i is the individual pixel values (photons cm^{-2} s^{-1} arcsec^{-2}) in the background region, M is the corresponding number of pixels, a^2 (arcsec^2) is the area of a pixel, and w (keV) is the width of the energy bin. This DC background was then subtracted from the source flux.

3. Error Estimate: Error estimate for *RHESSI* images is currently a research topic (as of May 2008). Our first attempt involves two different approaches for CLEAN and PIXON images.

(1) For CLEAN images, we use the RMS of the residual map, σ_{rms}, as the uncertainty of each pixel value. If the pixels were all independent, the flux error or uncertainty (in units of photons cm^{-2} s^{-1} keV^{-1}) for a source with N pixels and energy bin width w would be

$$\sigma = \frac{a^2}{w} \sqrt{\sum_{i=1}^{N} \sigma_{\mathrm{rms}}^2} = \frac{a^2}{w} \sqrt{N} \sigma_{\mathrm{rms}} \ , \tag{A.2}$$

where a is the size (in units of arcsecs) of each square pixel. However, the pixels inside a resolution element are dependent (spatially unresolved). We assume each resolution element to be a square with a size of the equivalent FWHM (arcsecs) of the detector combination used (e.g., FWHM=9.8″ for detectors 3–8) and thus with a number of pixels of $N_0 = (\mathrm{FWHM}/a)^2$. We further assume that the pixels inside an element have the same error,

and therefore the flux error for each resolution element is $\sigma_1 = \frac{a^2}{w} N_0 \sigma_{\rm rms}$ rather than $\frac{a^2}{w}\sqrt{N_0}\sigma_{\rm rms}$. Since separate resolution elements inside a source are independent (spatially resolved), the resulting error for the whole source is

$$\sigma_* = \sqrt{N_1}\sigma_1 = \frac{a^2}{w}\sqrt{N_0}\sqrt{N}\sigma_{\rm rms} = \sqrt{N_0}\sigma = \left(\frac{\rm FWHM}{a}\right)\frac{a^2}{w}\sqrt{N}\sigma_{\rm rms} \ , \qquad \text{(A.3)}$$

where $N_1 = N/N_0$ is the number of resolution elements inside the source. The factor $\sqrt{N_0} = {\rm FWHM}/a$ corrects for oversampling of choosing pixels smaller than the resolution element.

(2) For PIXON images, we use the hsi_calc_image_error.pro routine (by T. Metcalf) in the SSW package to get an error map that contains the pixel by pixel error, σ_i, of an image. Given the reconstructed model image, these errors are intended to provide a measure of how well each pixel is constrained by the data. This IDL routine determines how large a change in the image is required to produce a one sigma variation (based on χ^2) in the fit. A revision of the routine was made in December 2003 by T. Metcalf to take into account oversampling when determining the pixel error σ_i. Like that for CLEAN images, the error of the spatially integrated flux of a source is

$$\sigma_* = \left(\frac{\rm FWHM}{a}\right)\frac{a^2}{w}\sqrt{\sum_{i=1}^{N}\sigma_i^2} \ . \qquad \text{(A.4)}$$

The resulting errors from these estimates are usually on the order of 10% at low energies (say, ∼10 keV) and larger at high energies, which are comparable to the values obtained by the currently default error estimate algorithm in the *RHESSI* spectral analysis software called Object Spectral Executive (OSPEX). That algorithm uses $\frac{1}{3}$ of the maximum brightness outside the source region, presumably mainly contributed by the residual map in case of a CLEAN image, multiplied by the number of pixels in the source of interest (without correcting for oversampling). Saint-Hilaire et al. (2008, see their Appendix B) recently suggested that such errors are overestimated, and recommended $\frac{1}{6}$ in place of the scaling factor $\frac{1}{3}$.

A.3 Spectral Analysis for the 2002-04-30 M1.4 Flare with a Double Coronal Source (Chapter 4)

We document in this section the specific procedures adopted in Chapter 4 to obtain the spatially integrated spectra throughout the 2002 April 30 M1.4 flare and the spatially resolved spectra of the two individual coronal sources during the first HXR peak.

A.3.1 Spatially Integrated Spectra

For the spatially integrated spectra we used the standard forward-fitting method implemented in the object-oriented routine called OSPEX and described in Brown et al. (2006). OSPEX uses an assumed parametric form of the photon spectrum and finds parameter

values that provide the best fit in a χ^2 sense to the measured count-rate spectrum in each time interval.

In analyzing the *RHESSI* spatially integrated count-rate spectra we took advantage of the fact that *RHESSI* makes nine statistically independent measurements of the same incident photon spectrum with its nine nominally identical detectors. By analyzing the data from each detector separately, up to nine values can be obtained for each spectral parameter. The scatter of these values about the mean then gives a more realistic measure of the uncertainty than can be obtained from the best fit to the spectrum summed over all detectors. In addition, treating each detector separately allows us to use the $\frac{1}{3}$ keV wide "native" energy bins of the on-board pulse-height analyzers for each detector. This avoids the energy smearing inherent in averaging together counts from different detectors that have different energy bin edges and sensitivities. We limited the total number of energy bins by using the $\frac{1}{3}$ keV native bins only where they are needed, i.e., between 3 and 15 keV. This provides the best possible energy resolution that is important in measuring the iron and iron-nickel line features at ∼6.7 and ∼8 keV, respectively (Phillips, 2004), and the instrumental lines at ∼8 and ∼10 keV. We used 1 keV wide energy bins (three native bins wide) at energies between 15 and 100 keV, where the highest resolution was not needed to determine the parameters of the continuum emission in this range.

We recommend the following sequential steps, which we generally followed, to obtain the "best-fit" values of the spectral parameters and their uncertainties in each time interval throughout the flare.

1. Select a time interval that covers all of the *RHESSI* observations for the flare of interest. Also include times during the neighboring *RHESSI* nighttime just before and/or just after the flare for use in determining the nonsolar background spectrum.

2. Accumulate count-rate spectra corrected for livetime, decimation, and pulse pileup (Smith et al. 2002; although it is best to correct pileup in step 6 below) for each of the nine detectors in 4 s time bins (about one spacecraft spin period) for the full duration selected in step 1 above. A full response matrix, including off-diagonal elements, is generated for each detector to relate the photon flux to the measured count rates in each energy bin.

3. Import the count-rate spectrum and the corresponding response matrix for one of the detectors into the *RHESSI* spectral analysis routine, OSPEX. We used detector 4, since it has close to the best energy resolution of all the detectors.

4. Select time intervals to be used in estimating the background spectrum and its possible variation during the flare. In general, nighttime data must be used if the attenuator state changes during the flare; otherwise pre- and/or postflare spectra can be used. Account can be taken of orbital background variations during the flare by using a polynomial fit to the background time history in selectable energy ranges or by using the variations at energies above those influenced by the flare. For this event, since the thin attenuator was in place for the whole duration of the flare, a preflare interval was used for background estimation.

5. Select multiples of the 4 s time intervals used in step 2 that are long enough to provide sufficient counts and short enough to show the expected variations in the spectra as the flare progresses. Be sure that no time interval includes an attenuator change. For this event, we selected the seven time intervals marked in Figure 4.1 covering the first HXR peak.

6. Fit the spectrum for the interval near the peak of the event to the desired functional form. Spectra can be fitted to the algebraic sum of a variety of functional forms, ranging from simple isothermal and power-law functions to more sophisticated models, such as various multi-thermal models and thin- and thick-target models with a power-law electron spectrum having sharp low- and high-energy cutoffs. In our case, we assumed that an isothermal component plus a double power law provides acceptable fits to the measured count-rate spectra in most cases. This simple two-component model is sufficient to capture the key physics for this flare, i.e., to estimate the relative contributions of the thermal and nonthermal components of the X-ray emission.

   The isothermal spectrum was based on the predictions using the CHIANTI package (ver. 5.2, Dere et al., 1997; Young et al., 2003) in SSW with Mazzotta et al. (1998) ionization balance. The iron and nickel abundances were allowed to vary about their coronal values to give the best fit to the iron features in the spectra.

   For simplicity, we set the power-law index below the variable break energy to be fixed at $\gamma = 2$ to approximate a flat (constant) electron flux below a cutoff energy. The value of γ above the break energy and the break energy itself were both treated as free parameters in the fitting process.

   We also included several other functions to accommodate various instrumental effects. These included two narrow Gaussians near 8 and 10 keV, respectively, to account for two instrumental features that may be L-shell lines from the tungsten grids. The thin attenuator was in place during the entire course of the flare, thus restricting us from fitting the spectra below ∼6 keV.

   Another routine available in OSPEX was used to both offset the energy calibration and change the detector resolution to better fit the iron-line feature at ∼6.7 keV. This is important at high counting rates when the energy scale can change by up to ∼0.3 keV.

   Pulse pileup can best be corrected for at this stage by using a separate routine with count-rate–dependent parameters, although this is still in the developmental stage and was not used for this chapter. However, the average livetime (between data gaps) during the impulsive peak (interval 1, 08:20:27–08:20:56 UT) of this M1.4 flare was 93.4%. This is to be compared with the values of 55% and 94% for the 2002 July 23 X4.8 flare and the 2002 February 20 C7.5 flare, respectively. In addition, the estimated ratio of piled-up counts to the total counts is below 10% at all energies, indicating very minor pileup effects on the spectra of this event. A more detailed account on estimating pileup severity can be found in §A.4.1 (also Liu, W. et al., 2006, their §2.1) in general and in §A.4.2 (also Liu, W. et al., 2008a) for imaging spectroscopy in particularly.

It is important to use good starting values of the parameters to ensure that the minimization routine converges on the best-fit values. These were obtained for detector 4 in the interval at the peak of the flare by experienced trial and error.

7. Once an acceptable fit (reduced $\chi^2 \lesssim 2$, with the systematic uncertainties set to zero) is obtained to the spectrum for the peak interval, OSPEX has the capability to proceed either forwards or backwards in time to fit the count-rate spectra in other intervals using the best-fit parameters obtained for one interval as the starting parameters to fit the spectrum in the next interval. This reduces the time taken to fit each time interval, but various manual adjustments are usually required to the fitted energy range, the required functions, etc., in specific intervals to ensure adequate fits in each case with acceptable values of χ^2.

8. The best-fit parameters found for each time interval for the one detector chosen in step 3 are now used as the starting parameters in OSPEX for the other detectors. In this way, acceptable fits can be obtained in each time interval for all nine detectors. In practice, it is usually not possible to include detectors 2, 5, or 7 in this automatic procedure, since they have higher energy thresholds and/or poorer resolution compared to the other detectors.

9. The different best-fit values (in practice, only six were obtained) of each spectral parameter can now be combined to give a mean and standard deviation. These values then constitute the results of this spectral analysis and can be used for further interpretation as indicated in Chapter 4. For display purposes, it is important to show the best-fit photon spectrum computed using these mean parameters with some indication of the photon fluxes determined in each energy bin from the measured count rates. For this purpose, we have chosen to display the photon fluxes averaged over all detectors used in the analysis (all but detectors 2, 5, and 7). The photon flux of each detector was determined by taking the count rate and folding it through the corresponding response matrix with the assumed photon spectrum having the best-fit parameters. This gives a reasonable representation but it is well known that data points determined in this way are "obliging" and follow the assumed spectrum (Fenimore et al., 1983, 1988). Hence, such plots (Fig. 4.6) should be viewed with caution. Also note that the χ^2 values of the averaged photon fluxes are not necessarily representative of the independent fits to the data of individual detectors.

A.3.2 Spatially Resolved (Imaged) Spectra

In order to determine the photon spectra of the two distinct sources seen in the X-ray images, we used *RHESSI* 's imaging spectroscopy capability and carried out the following steps.

1. We selected the same seven intervals (marked in Fig. 4.1) as those used for the spatially integrated spectra.

2. For each selected time interval, images in narrow energy bins ranging from 1 keV wide at 6 keV to 11 keV wide at 50 keV were constructed using the computationally

expensive PIXON algorithm (Metcalf et al., 1996), which gives the best photometry and spatial resolution (Aschwanden et al., 2004) among the currently available imaging algorithms. Detectors 3, 4, 5, 6, and 8 covering angular scales between 6.8″ and 106″ were used to allow the two sources to be clearly resolved. No modulation was evident in the detector 1 and 2 count rates, showing that the sources had no structure finer than the 3.9″ FWHM resolution of detector 2.

3. The PIXON images were imported into OSPEX for extracting fluxes of individual sources. Note that the images are provided in units of photons $\mathrm{cm}^{-2}\ \mathrm{s}^{-1}\ \mathrm{keV}^{-1}\ \mathrm{arcsec}^{-2}$, using only the *diagonal* elements of the detector response matrix to convert from the measured count rates to photon fluxes. OSPEX converts the images back to units of counts $\mathrm{cm}^{-2}\ \mathrm{s}^{-1}\ \mathrm{keV}^{-1}\ \mathrm{arcsec}^{-2}$, using the same diagonal elements and then uses the *full* detector response matrix, including all off-diagonal elements, to compute the best-fit photon spectrum (photons $\mathrm{cm}^{-2}\ \mathrm{s}^{-1}\ \mathrm{keV}^{-1}$) for each source separately. The summed count rates in the two boxes shown in the middle panel of Figure 4.2 around the average positions of the two sources were accumulated separately for each image in each energy bin. The boxes were adjusted accordingly for each time interval if the sources moved. (Note that only a single box was used for interval 1 when only the lower source was detected.)

4. The uncertainties in the count rates were calculated from the PIXON error map based on χ^2 variations of the reconstructed image (see Appendix §A.2). The errors were originally obtained in photon space and then converted in the same way described above to count space where the actual fitting was performed.

5. The two independent count-rate spectra, one for each source, were then fitted independently to the same functions used for the spatially integrated spectra as described earlier. We further demand that the iron abundance of the thermal component and the break energy of the double power law be fixed at the values given by the fit to the corresponding spatially integrated spectrum in the same time interval. This makes the spectra directly comparable for our purposes. Note that the error bars of the imaging spectral parameters are obtained from the χ^2 variation during the fitting procedure. At times when such an error is smaller than that of the corresponding spatially integrated spectrum, the latter value is used instead.

Finally, for a self-consistency check, we have compared the sum of the imaging spectra of the two sources with the spatially integrated spectrum and found that they are consistent. The only exception is at the low energies ($\lesssim$10 keV) where the imaging spectra do not have enough resolution for us to see the iron-line feature.

A.4 Effects of Pulse Pileup

Pulse pileup refers to the phenomenon that two or more photons close in time are detected as one photon with their energies summed (Smith et al., 2002). When count rates are high, as happens in large flares, an artifact appears in the measured spectrum at twice or a larger multiple of the energy of the peak of the count rate spectrum that is at ∼6 keV in

the *RHESSI* attenuator A0 state, ∼10 keV in the A1 state, and ∼18 keV in the A3 state. Unfortunately, due to the nonlinear complexity of the problem, there is currently no 100% reliable pileup correction algorithm available in the *RHESSI* software, especially for imaging spectroscopy. For spatially integrated spectra, the only available correction algorithm is the preliminary one of Smith et al. (2002), while another one is under development by R. Schwartz as of May 2008; for imaging spectroscopy, there is no existing correction at all. Below we discuss pileup effects in greater detail for two individual flares addressed in the main body of this book.

A.4.1 Pileup Effects for the 2003-11-13 M1.7 Flare (Chapter 6)

It is necessary to check if pulse pileup is important in the 2003 November 13 M1.7 flare (Chapter 6) before we can make a more quantitative interpretation of the data. There are several ways to do the check, the first and simplest of which is the detector livetime, i.e., the complement of the deadtime during which the detector is not able to distinguish among different incident photons. We first accumulated spatially integrated spectra for every 1 s time bin during the interval of 04:58:01-04:59:49 UT,[5] using the front segments of all nine detectors except detectors 2 and 7, which have degraded energy resolution (Smith et al., 2002). We then obtained the fractional livetime (between data gaps) from the spectrum object data and averaged it over the seven detectors being used. The resulting livetime generally decreases with time, ranging from 96% to 89%, with a small modulation produced by the spacecraft spin. In this M1.7 flare, such a livetime is comparably high (cf. the livetime of ∼ 55% during the 2002 July 23 X4.8 flare and of ∼ 94% during the 2002 February 20 C7.5 flare) and indicates minor pileup severity.

Another approach involves inspecting the change of the spectrum due to pileup. We accumulated spectra over each spacecraft spin period (∼ 4 s, with the same set of detectors mentioned above) and used the pileup correction to obtain the relative fraction of the pileup counts among the total counts as a function of energy (Smith et al., 2002). We find that the pileup counts amount to less than ∼ 10% of the total counts at all energies until 04:59:01 UT, when the livetime drops to 91%. After that, the relative importance of the pileup counts continues to increase, but remains below ∼ 20% of the total counts before 04:59:17 UT. Toward the end of the first HXR pulse (04:59:45-04:59:49 UT, livetime of ∼ 90%), the ratio of pileup counts to total counts exceeds 10% in the entire 20-40 keV range and humps up to 43% near 28 keV. We integrate both the pileup counts and total counts over the 20-40 keV band and plot their ratio versus time as a general indicator of pileup severity (see Fig. A.1). Clearly this ratio is $\lesssim$ 15% during the first two-thirds of the interval shown and does not reach the moderate ∼ 25% level until the very end.

We therefore conclude that pileup effects are generally not very significant for this flare, especially during the first minute of the impulsive phase, because the count rate is not too high and the thin shutter is in during the time interval of interest, which further attenuates the count rate. It should be noted that the two piled-up photons (that result in a single photon seen in the image) most probably originate from the same location on the Sun, and pileup of photons across different sources is relatively unimportant (G. Hurford, 2006,

[5]This time interval is also used in studying the evolution of the source morphology in §6.2.1 (see text about Fig. 6.5), which covers the bulk of the first HXR pulse.

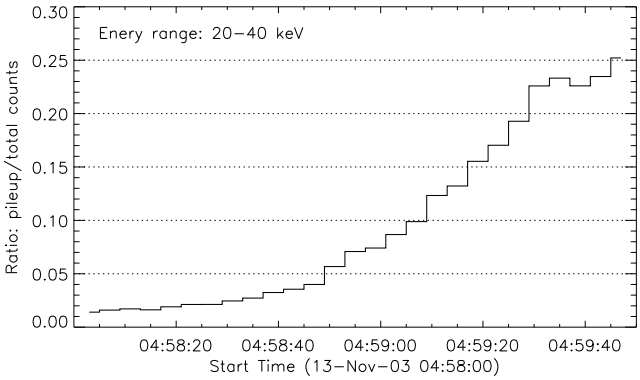

Figure A.1: Ratio of pileup counts to total counts, both integrated over the 20-40 keV range in time bins of one spacecraft spin for the 2003 November 13 M1.7 flare [from Liu, W. et al. 2006].

private communication). Therefore, the source geometry would not be significantly affected by pileup, except that there could be a "ghost" of a low-energy source appearing in a high-energy image for very large (e.g. X-class) flares (see, e.g., §A.4.2). However, the spectra of individual sources derived from images are distorted, which is relatively more significant at the LT than at the FPs. This is because low-energy photons dominate over high-energy photons in population, and have the highest probability to produce pileup, and generally most of the low-energy photons are emitted by the LT source.

A.4.2 Pileup Effects on Imaging Spectroscopy for the 2003-10-29 X10 Flare (Chapter 5)

It is necessary to assess the importance of pileup and its effects on our interpretation of *RHESSI* data for the 2003 October 29 X10 flare (Chapter 5). We have adopted and improved upon the several ways to estimate the pileup severity and minimize its effects described above (§A.4.1).

Figure A.2*a* shows the history of the fractional livetime (*thin line*), as a general indicator of pileup severity, averaged over detectors 3–9 and over 4 s intervals, which generally anti-correlates with the detector count rate. It decreases (from 96%) as the flare progresses toward its impulsive peak and reaches its minimum of 24% at 20:46:10 UT. This value is very small compared with the livetime minima of 55% during the 2002 July 23 X4.8 flare and 94% during the 2002 February 20 C7.5 flare, and thus indicates severe pileup effects. We can further check the detailed livetime variation on a 0.1 s cadence, as shown in Figure A.2*b* for detector 9. The modulation caused by the coarse grids (FWHM of 183″) above detector 9 during the spacecraft rotation with a ∼4 s period is clearly seen. That is, during each modulation period, the livetime cycles between its minimum and maximum values in anti-correlation with the count rate. The fractional livetime varies between about 5% and 70%. Knowing the way *RHESSI* makes images (Hurford et al., 2002), this fine temporal variation makes pileup correction for imaging spectroscopy even more difficult than for the spatially integrated spectra.

In addition to livetime, it is more informative to examine how pileup affects the shape of

the spectrum. We thus performed pileup corrections to the spatially integrated spectra using the preliminary algorithm of Smith et al. (2002). Figures A.2*c* and A.2*d* show an example of the measured and pileup-corrected count-rate spectra, the first- and second-order pileup spectra, and the ratio of the piled-up to total counts. As is evident (Fig. A.2*d*), the fraction of the piled-up counts is negligibly small at low energies, which amounts to less than 1% (below 18 keV) and less than 10% (below 26 keV). The most obvious alteration of the spectrum shape occurs in the 30–40 keV range in which 36 keV is twice the energy (18 keV) of the peak in the count-rate spectrum (in the A3 attenuator state) and thus the peak of the first order (two photons counted as one) piled-up spectrum. In this energy range pileup produces a small artificial hump in the measured spectrum, which results from a corresponding reduction of counts at low energies (15–20 keV). Above 50 keV, although the

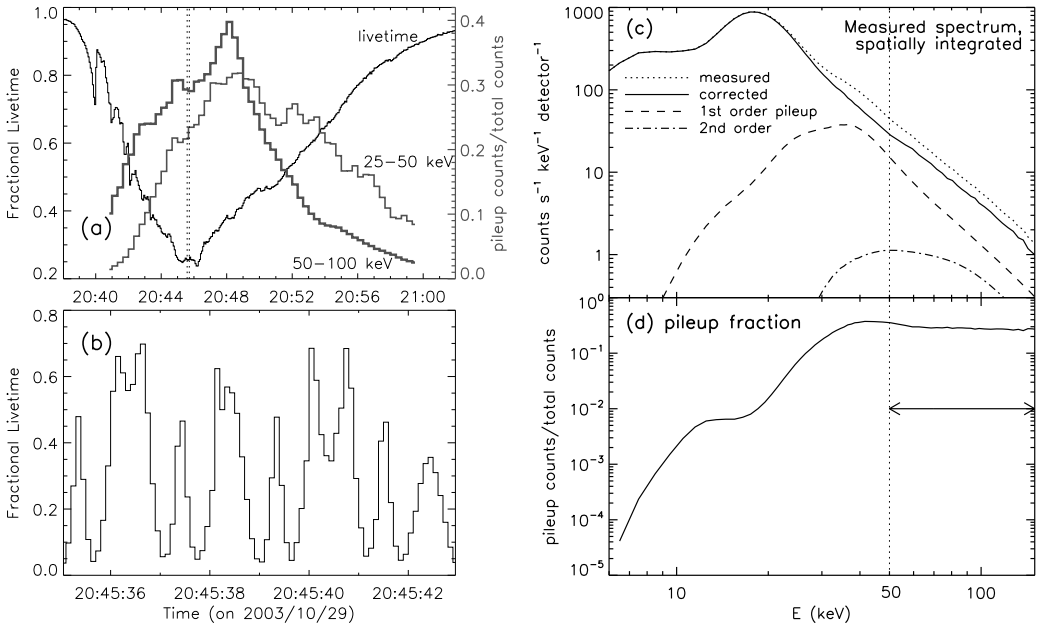

Figure A.2: Assessment of pileup severity for the 2003 October 29 X10 flare. (*a*) Fractional livetime (excluding data gaps, *thin line, left scale*) averaged among detectors 3–9 (used for the images presented in Chapter 5) over 4 s intervals as a function of time. Overlaid are the fractions of the counts recorded in the two energy bins of 25–50 and 50–100 keV that are piled up (*thick lines, right scale*), estimated with the algorithm of Smith et al. (2002). (*b*) Fractional livetime of detector 9 with a 0.1 s cadence during an 8 s interval marked by the two vertical dotted lines in (*a*). The modulation is caused by the changing count rate produced by the grids above the detector as the spacecraft rotates. (*c*) Count rate spectrum averaged over detectors 3–9 for interval 20:46:00–20:46:20 UT covering the livetime minimum in (*a*). The dotted and solid lines are the measured and pileup corrected spectra (Smith et al., 2002), respectively. The dashed and dot-dashed lines are the first- (two photons) and second-order (three photons) piled-up spectra estimated from the measured spectrum, with their peaks marked by the vertical dotted lines at 36 and 54 keV, respectively. (*d*) The fraction of the total recorded counts as a function of energy that are piled up (including first- and second-order pileup) [from Liu, W. et al. 2008a].

they are different in absolute values, the pileup corrected and measured spectra are almost parallel (Fig. A.2*c*), and the pileup fraction is almost constant with a relative variation

<30% (Fig. A.2*d*). We also integrated the piled-up counts and obtained their ratios to the total counts in the 25–50 and 50–100 keV bands, which are shown in Figure A.2*a* vs. time as a another general indicator of pileup importance.

In Chapter 5 we are specifically interested in the spatially resolved spectra of the LT and FP sources. Because of the rotational modulation nature of *RHESSI* image reconstruction (Hurford et al., 2002), pileup has quite different effects on imaging spectroscopy compared with effects on the spatially integrated spectrum discussed above. Such effects can be avoided or alleviated in various ways, which can make imaging spectroscopy less affected by pileup than spatially integrated spectroscopy (R. Schwartz, private communication). The specific effects are as follows: (1) As noted above (§A.4.1), pileup of photons from two or more spatially resolved sources is generally insignificant in images. This is more true for finer grids because two photons must come from the same region within the FWHM resolution of the grid in order to pileup as one photon in the underlying detector. We used uniform weighting (Hurford et al., 2002) for image reconstruction, which assigns higher weights for finer grids and thus de-emphasizes pileup of photons originating from within a large source area that is included in the FWHM of coarser grids. (2) Among all the sources, LT suffers the most from pileup compared to the FPs. This is because pileup depends on count rates. Most of the detected photons in the A3 state have energies below ∼20 keV where the LT source dominates, while the FPs dominate at higher energies where the photon flux is much lower. (3) As noted above, the peak of the count-rate spectrum of this flare (in the A3 attenuator state) is ∼18 keV. The majority of pileup results from photons around this energy and appears as a ghost LT source (e.g., Fig. 5.3*i*) at energies around 36 keV (see Fig. A.2*c*). Therefore, below ∼25 keV, pileup at the LT source is negligible; above ∼50 keV, the shape of the FP spectrum is most likely not affected by pileup, and only the flux is elevated by a constant factor independent of energy up to 150 keV because of second and higher order pileup due to high count rates in this flare. (4) In addition, we are mainly concerned with the similarities and differences of HXR fluxes and spectral shapes (power-law indexes) between the two FP sources, which may be even more insensitive to pileup. This is because the percentage of piled-up counts among the measured counts of the two FPs are likely to be very similar and thus the two FPs are affected to similar extents. In our imaging spectroscopic analysis, we have thus fitted the LT spectra only below 20 keV and the FP spectra only above 50 keV in order to minimize pileup effects. This 50 keV was also used by Emslie et al. (2003) and Saldanha et al. (2008) as the lower limit of the energy range for fitting the (FP) spectra of X-class flares in which pileup is important.

A.5 *RHESSI* Simulation Tool and Its Applications

One of the advantages of the *RHESSI* software is the inclusion of the simulation tool, developed and maintained by J. McTiernan. A user can specify a model source morphology together with a photon spectrum, and use this model as an input to the simulation software. Then the software will generate images based on a user-specified image reconstruction algorithm (Hurford et al., 2002), taking into account the real instrument response, as if they were seen through the "eyes" of *RHESSI*. This can help user better understand observed flare morphology and distinguish reality from artifacts.

We have frequently used this simulation tool in our *RHESSI* data analysis. One of the

examples was to simulate the emission profile along a loop in which thermal conduction is or is not suppressed and compare the results with the observed profile. Details of this study can be found in Jiang et al. (2006).

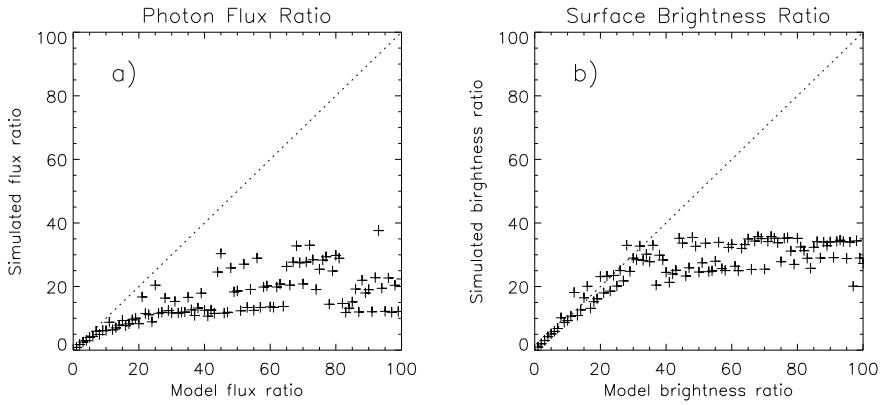

Figure A.3: (*a*) Simulated HXR photon flux ratio vs. input model flux ratio, obtained from the *RHESSI* simulation software. The dotted diagonal line indicates a perfect instrument response. (*b*) Same as (*a*) but for surface brightness.

Another example of simulation is testing the *RHESSI* dynamic range. Here we input an image with a size of $64'' \times 64''$ ($1''$ pixel), in which two $3'' \times 3''$ uniform sources were placed along the diagonal line, with their centers located at $x = 21''$ and $x = 46''$, respectively. We then fixed the surface brightness of one source at 1 unit (arbitrary scale) and varied that of the other from 1 to 100 units, for each of which we ran the simulation software with the CLEAN algorithm to obtain an output image. Afterwards we calculated the ratio of the spatially integrated flux as well as the maximum surface brightness of the two sources. The simulated ratios (as of August 2003) are plotted against the corresponding input (model) ratios in Figure A.3. As we can see, the surface brightness ratio can preserve the model input value up to about 30, beyond which the simulated ratio becomes flat. This simulation suggests a dynamic range of $\sim$30 for surface brightness, higher than the nominal value of 10 as of 2003. The dynamic range for the integrated flux is slightly less than 10, because there are photons registered beyond the finite integration area in the image due the point spread function of the instrument.

Appendix B

Techniques for Analyzing Footpoint Asymmetries in the 2003-10-29 X10 Flare (Chapter 5)

In this appendix we describe the techniques used in Chapter 5 to analyze the footpoint asymmetries in the 2003 October 29 X10 flare, including coalignment of images obtained by different instruments (§B.1), a mathematical treatment of column density asymmetry (§B.2), and an estimate of the density in the legs of the loop (§B.3).

B.1 Coalignment of Images from Different Instruments

We describe in this section the procedures that were taken to coalign images[1] obtained by different instruments shown in §5.2.3. It was assumed that images from all instruments had accurate plate scales and roll angles were corrected for the solar P-angle, but had different absolute origins for the x and y coordinates. *RHESSI*'s images are located on the Sun to sub-arcsecond accuracy thanks to its solar limb sensing aspect system and star based roll angle measurements (Fivian et al., 2002). Thus all other images were corrected to match the *RHESSI* features using the following procedures.

(1) We first obtained an accurate coalignment of *SOHO* MDI with *RHESSI*, which is important for our purpose to find the magnetic field strength at the HXR FPs.

(1.1) The first step is to identify specific features on the MDI map that have *RHESSI* counterparts. Qiu & Gary (2003) found good spatial agreement between HXR FPs and MDI magnetic anomaly features with an apparent sign reversal in a white-light flare. This was interpreted as HXR-producing nonthermal electrons being responsible for heating the lower atmosphere, which consequently altered the Ni I 6768 Å line profile that is used by MDI to measure the magnetic field.

We selected two neighboring magnetograms at 20:41:35 and 20:42:35 UT when the magnetic anomaly features were most pronounced, and subtracted the former from the latter. This running-differenced map (which we call map_0, Fig. B.1) highlights regions of the newest

[1] See P. Gallagher's tutorial for coaligning images at http://hesperia.gsfc.nasa.gov/∼ptg/trace-align

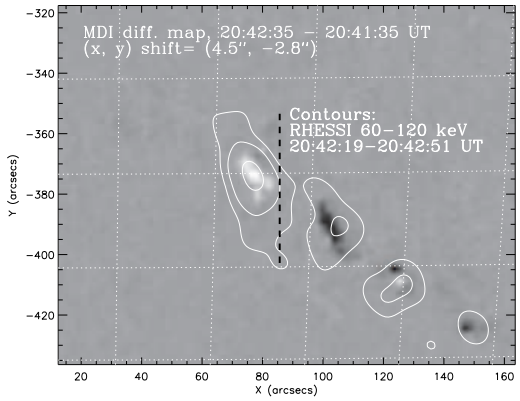

Figure B.1: Difference (*gray background*) between two MDI magnetograms at 20:42:35 and 20:41:35 UT, overlaid with a *RHESSI* 60–120 keV image at 20:42:19–20:42:51 UT (white contours at 15%, 30%, & 80% of the maximum brightness). The MDI differenced magnetogram has been corrected to an Earth-centered view and shifted in x and y to give the best fit to the four *RHESSI* HXR sources (see text). For display purposes only, we also did the solar rotation correction to the fiducial *TRACE* time of 20:50:42 UT as we did for Fig. 5.6*a*, and the vertical dark dashed line shows the same general magnetic neutral line as shown there [from Liu, W. et al. 2008a].

changes, which are presumably caused by precipitation of nonthermal electrons and are expected to appear cospatial with HXR sources. As evident, there is one (three) apparent increase (decrease) feature(s) mainly in the negative (positive) polarity (cf., Fig. 5.6), which appear as *white* (*dark*) patches in Figure B.1. Meanwhile, we reconstructed a *RHESSI* image (called map_1) at 60–120 keV integrated in the interval of 20:42:19–20:42:51 UT (a multiple of the *RHESSI* spin period, ∼4 s, and closest to the corresponding integration time of the second MDI magnetogram, 20:42:20–20:42:50 UT). We found an one-to-one correspondence between the four major HXR FP sources (Fig. B.1, *contours*) and the magnetic anomalies.

(1.2) The second step is to convert *SOHO*'s L1 view to the appearance as viewed from an Earth orbit. In principle, for the best accuracy, one could use a routine called *mk_soho_map_earth.pro* developed by T. Metcalf in the Solar SoftWare (SSW) package, which reads *SOHO* orbital data and involves complicated trigonometry and warping. Its results, however, were unstable and introduced artificial pointing jumps. Thus, we used a simpler, but less accurate, routine called *map2earth.pro* developed by D. Zarro, which only corrects for the pixel size of the map according to different distances from the Sun to the L1 point and to the Earth. We call the resulting Earth-viewed differenced MDI magnetogram $map_{0,\,\mathrm{Earth}}$.

(1.3) Finally, we took the absolute values of MDI $map_{0,\,\mathrm{Earth}}$ to make a new map called $map'_{0,\,\mathrm{Earth}}$ and coregister it with the corresponding *RHESSI* map_1 by cross-correlation. The required pointing shifts for MDI are $\Delta x = 4.5'' \pm 2.0''$ and $\Delta y = -2.8'' \pm 2.0''$. This practical approach yielded the best coalignment between MDI and *RHESSI*, and also resolved the inaccuracy caused by negligence of *SOHO* orbital data in the *map2earth.pro* routine. Here we estimate the uncertainty with the $2.0''$ MDI pixel size and use error propagation with the corresponding pixel sizes for the following coalignments with other instruments.

(2) Following a similar practice, we cross-correlated the *TRACE* white light image at

20:49:49 UT (Fig. 5.6*c*) with an MDI magnetogram[2] at 20:49:35 UT and found that the *TRACE* image (pixel size 0.5″) must be shifted by $\Delta x = 2.2''$ and $\Delta y = 0.0''$. Considering the MDI offset estimated above, this translates to a required shift of $\Delta x = 2.2 + 4.5 = 6.7'' \pm 2.1''$ and $\Delta y = 0.0 - 2.8 = -2.8'' \pm 2.1''$ for *TRACE* to match *RHESSI*'s pointing. These shifts were applied to all the *TRACE* images shown in Figure 5.6, assuming they shared a common pointing that did not change during the flare.

(3) To find the correct pointing for the OSPAN Hα image (pixel size 2.2″) at 20:42:11 UT (Fig. 5.6*b*), we used the concurrent *TRACE* 1600 Å image (20:42:11 UT) as the reference. Cross-correlation between the two images indicated that the former must be shifted by $\Delta x = -1.0''$ and $\Delta y = 6.6''$. Using the above relative *TRACE* pointing, we found the shifts of $\Delta x = -1 + 6.7 = 5.7'' \pm 3.0''$ and $\Delta y = 6.6 - 2.8 = 3.8'' \pm 3.0''$ required for this Hα image.

B.2 Derivation of Footpoint HXR Fluxes Resulting from Asymmetric Coronal Column Densities

Here we derive the numerical expressions for the HXR fluxes of the two FPs and their ratio as a function of energy resulting from column density asymmetry addressed in §5.5.2. We adopted the empirical expression of Leach & Petrosian (1983, their eq. (11)) for nonthermal bremsstrahlung X-ray emission as a function of column density, which has also been used in Chapter 6 [see eq. (6.5)]. This expression well approximates the Fokker-Planck calculation of particle transport under the influence of Coulomb collisions that includes energy losses and pitch-angle scattering, the latter of which was neglected in other forms of X-ray profiles based on approximate analytical solutions (e.g., Emslie & Machado, 1987). For an injected power-law (index δ) electron flux, the resulting fractional bremsstrahlung emission intensity per unit dimensionless column density τ at photon energy k (in units of rest electron energy $m_e c^2 = 511$ keV, m_e being the electron mass) can be written as

$$I_0(\tau, k) = \left(\frac{\delta}{2} - 1\right) \left(\frac{k+1}{gk^2}\right) \left(1 + \tau \frac{k+1}{gk^2}\right)^{-\delta/2} , \tag{B.1}$$

where $\tau = N[4\pi r_0^2 \ln \Lambda] = N/[5 \times 10^{22}\,\mathrm{cm}^{-2}]$ is the dimensionless column density, for the classical electron radius $r_0 = e^2/m_e c^2 = 2.8 \times 10^{-13}$ cm and the Coulomb logarithm $\ln \Lambda = 20$; g is a factor determined by the pitch-angle distribution of the injected electron spectrum, which we assumed to be isotropic and thus $g = 0.37$ (Leach, 1984). This emission profile is normalized to unity, $\int_0^\infty I_0(\tau, k) d\tau = 1$. Integrating equation (B.1) yields the cumulative photon emission from the injection site ($\tau = 0$) to the transition region ($\tau = \tau_{\rm tr} \equiv N_{\rm tr}/[5 \times 10^{22}\ \mathrm{cm}^{-2}]$, where $N_{\rm tr} = \int_0^{s_{\rm tr}} n[s] ds$ and $s_{\rm tr}$ are the coronal column density and distance to the transition region),

$$F_{\rm Corona}(\tau_{\rm tr}) = \int_0^{\tau_{\rm tr}} I_0(\tau, k) d\tau = 1 - \left(1 + \tau_{\rm tr} \frac{k+1}{gk^2}\right)^{1-\delta/2} , \tag{B.2}$$

[2]It would have been preferable to use an MDI white-light image, but none was recorded during the flare.

whose complement gives the emission accumulated below the transition region, i.e., the HXR flux of the FP,

$$F_{\rm FP}(\tau_{\rm tr}) = \int_{\tau_{\rm tr}}^{\infty} I_0(\tau,k)d\tau = 1 - F_{\rm Corona}(\tau_{\rm tr}) = \left(1+\tau_{\rm tr}\frac{k+1}{gk^2}\right)^{1-\delta/2}. \quad \text{(B.3)}$$

Note that at large photon energies (tens to hundreds of keV), $F_{\rm Corona}(\tau_{\rm tr})$ is usually much smaller than $F_{\rm FP}(\tau_{\rm tr})$. In addition, $F_{\rm Corona}(\tau_{\rm tr})$ is distributed in a large volume in the leg of the loop in the relatively *tenuous* plasma, while $F_{\rm FP}(\tau_{\rm tr})$ is concentrated at the FP in the *dense* transition region and chromosphere. This results in an even smaller surface brightness in the leg than at the FP, which may well exceed the dynamic range of HXR telescopes (e.g., $\gtrsim$10:1 for *RHESSI*). This is why leg emission is so rarely observed (Liu, W. et al., 2006; Sui et al., 2006).

As we know, a power-law electron flux (index=δ) produces a thick-target (integrated from $\tau = 0$ to $\tau = \infty$) photon spectrum of approximately a power-law, $I_{\rm thick} = A_0 k^{-\gamma}$, where $\gamma = \delta - 1$ (Brown, 1971; Petrosian, 1973) for an isotropically injected electron spectrum, and A_0 is the normalization factor [in units of photons $\rm s^{-1}$ $\rm cm^{-2}$ $(511\,\rm keV)^{-1}$]. Since I_0 gives the fractional spatial photon distribution at a given energy, the physical photon spectrum at energy k and at a depth where the overlying column density is τ can be written as $I(\tau,k) = I_{\rm thick} I_0(\tau,k) = A_0 k^{-\gamma} I_0(\tau,k)$. It follows that the X-ray flux of the FP is

$$I_{\rm FP}(\tau_{\rm tr},k) = \int_{\tau_{\rm tr}}^{\infty} I(\tau,k)d\tau = I_{\rm thick} F_{\rm FP}(\tau_{\rm tr}) = A_0 k^{-\gamma}\left(1+\tau_{\rm tr}\frac{k+1}{gk^2}\right)^{1-\delta/2}, \quad \text{(B.4)}$$

and the photon flux ratio of the two FPs (1 and 2),

$$R_I = \frac{I_{\rm FP}(\tau_{\rm tr,2},k)}{I_{\rm FP}(\tau_{\rm tr,1},k)} = \left(1+\tau_{\rm tr,2}\frac{k+1}{gk^2}\right)^{1-\delta/2}\left(1+\tau_{\rm tr,1}\frac{k+1}{gk^2}\right)^{-(1-\delta/2)}. \quad \text{(B.5)}$$

The above two equations were used in §5.5.2 to calculate the FP fluxes and their ratio resulting from different coronal column densities.

B.3 Estimation of Column Densities in Loop Legs

We describe below the approach to estimate the coronal column densities $N_{\rm tr}$ in the legs of the loop, which is defined and used in §5.5.2 as the density integrated along the loop from the acceleration region to the transition region at the FPs. In the stochastic acceleration model of Petrosian & Liu (2004), the LT source is the region where particle acceleration takes place (Liu, W. et al., 2008b; Xu et al., 2008). We thus subtracted[3] the estimated LT size (i.e., the radius r of the *equivalent sphere*; see Fig. 5.5*c*) from the distances along the loop from the LT centroid to the FP centroids obtained in §5.4.2 (i.e., l_i, where i=1 for E-FP and 2 for W-FP; see Fig. 5.7*c*), to obtain the path lengths in the legs $s_{{\rm tr},i} = l_i - r$.

[3]In some other models (e.g., Masuda et al., 1994), the acceleration region is assumed to be located above the "LT" source and a distance needs to be added to l_i. Such a practice was not attempted here, and as we can see from §5.5.2, will not change our conclusions.

Here the FP centroids are assumed to be situated at negligibly small distances below the transition region. To give the desired column densities $N_{\mathrm{tr},\,i}$, the path lengths $s_{\mathrm{tr},\,i}$ (i=1, 2) were then multiplied by the density n_{leg} (assumed to be uniform) in the legs of the loop, which was estimated as follows.

The density of the LT source n_{LT} inferred in §5.2.2 (see Fig. 5.5*d*) provides our first guess for the leg density n_{leg} as assumed by Falewicz & Siarkowski (2007). The relative brightness of *nonthermal* bremsstrahlung emission the leg and FP provides another important clue. This is because, for the same reason of collisional losses mentioned in §5.5.2, the ratio of the leg to FP brightness, particularly at low energies, is an increasing function of the leg density. This predicted ratio cannot exceed the observed LT-to-FP brightness ratio, because the LT source is where the maximum loop brightness is located, and it includes additional contributions from *thermal* emission, piled-up photons, and/or electrons trapped in the acceleration region (Petrosian & Liu, 2004). This imposes an upper limit for the leg density n_{leg}.

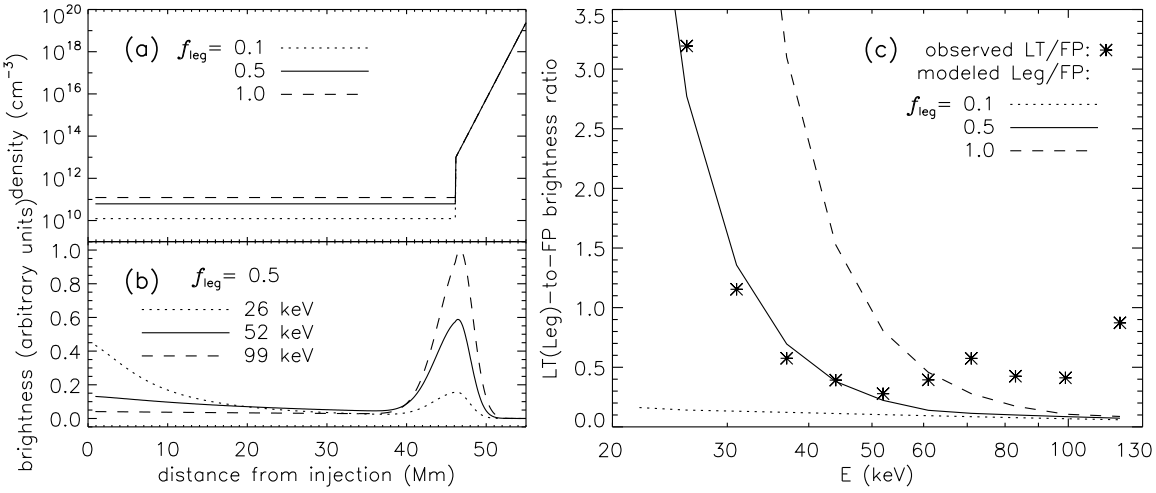

Figure B.2: (*a*) Density vs./ distance s along the loop for different values of the scaling factor f_{leg}, which is applied to the LT density $n_{\mathrm{LT}} = 1.2 \times 10^{11}\,\mathrm{cm}^{-3}$ to give the leg density $n_{\mathrm{leg}} = f_{\mathrm{leg}} n_{\mathrm{LT}}$ (see text). The distance starts at the injection from the acceleration region, and the transition region is located at $s = 46$ Mm. (*b*) Nonthermal emission profiles as seen by *RHESSI* at selected energies. These are produced by a power-law electron flux (index $\delta = 4.96$) injected into the loop with the density profile shown in (*a*) for the case of $f_{\mathrm{leg}} = 0.5$. The humps on the right are the FP emission. (*c*) Observed ratio of the LT-to-FP maximum brightness (*asterisk*) as a function of energy, overlaid with the modeled leg-to-FP ratio (*lines*) for different density profiles shown in (*a*). Above ∼50 keV the abnormal increase of the observed ratio with energy is unreal due to increasing noise at higher energies.

To estimate this upper limit for n_{leg}, we selected the second last long integration interval (20:54:40–20:56:40 UT) shown in Figure 5.8*d* when the loop column density has become large late in the flare and yet the HXR flux is not too low to give sufficient count statistics for images. (1) From images at different energies we obtained the *observed* ratio of the maximum brightness of the LT source to that of the dimmer W-FP source, which is a decreasing function of energy as shown in Figure B.2*c*. (2) The next step was to calculate

the *modeled* leg to FP brightness ratio: (*a*) We assumed a piecewise density profile $n(s)$ consisting of an l_2 long leg with a uniform density of $n_{\rm leg} = f_{\rm leg} n_{\rm LT}$ (where $f_{\rm leg}$ is a scaling factor to be determined), a jump to $10^{13}\,{\rm cm}^{-3}$ at the transition region ($s = l_2$), and an exponential increase with a scale height of 0.6 Mm (given by an assumed temperature of 10^4 K) in the chromosphere (see Fig. B.2*a*). (*b*) Assuming a power-law electron flux with a spectral index of δ injected at the upper end of the leg ($s = 0$), the modeled nonthermal HXR profile was given by $n(s) I_0(\tau, k; \delta)$, where I_0 is defined by equation (B.1). Here we have used the values of $l_2 = 46$ Mm, $n_{\rm LT} = 1.2 \times 10^{11}\,{\rm cm}^{-3}$, and $\delta = 4.96$ from the observation at 20:54:40–20:56:40 UT. (*c*) The modeled emission profile was then convolved with a Gaussian of FWHM=9.8″ corresponding to the CLEAN beam size used for detectors 3–9. A sample of the emission profiles is shown in Figure B.2*b*. (*d*) From the resulting profile, the modeled ratio of the leg-to-FP maximum brightnesses was obtained and compared with the observed ratio (see, e.g., Fig. B.2*c*). (3) To find the upper limit for the scaling factor $f_{\rm leg}$, we started with $f_{\rm leg} = 1$ and iterated the above steps (*a*)–(*d*) with decreasing values at a step of 0.05, until the modeled ratio best fits the the observed ratio as a function of energy in a least-squares sense. This gave us $f_{\rm leg,\,max} = 0.5$, which was then used for the upper limits of the leg density $n_{\rm leg,\,max} = f_{\rm leg,\,max} n_{\rm LT}$ and column densities $N_{{\rm tr},\,i} = n_{\rm leg,\,max}(l_i - r)$ shown in Figure 5.8*e* throughout the flare. This scaling means that the average density in the legs must be smaller than the estimated LT density. Another possibility is that the LT density inferred is an overestimate due to an underestimate of the volume, because of the choice of the 50% contour level (see §5.2.2) which may be too high, or because of the lack of knowledge of the source size in the third dimension along the line of sight.

Appendix C

Energy Loss and Diffusion due to Coulomb Collisions With Warm Plasmas

C.1 Coulomb Loss in Warm Plasmas

In the previous SA model, the energy loss rate due to Coulomb collisions with the ambient plasma is calculated by assuming a cold-target scenario, in which the nonthermal electron velocity $v \gg v_{\rm th}$, where $v_{\rm th} = \sqrt{2kT/m_e}$ is the thermal velocity of the background electrons. This is a valid assumption in the high-energy regime, but it is not necessarily true for low-energy electrons whose velocity is comparable to or even less than those of the ambient electrons. In the latter case, the electrons may even gain energy from the ambient, rather than lose energy as is always the case in the cold-target scenario. More general treatment of Coulomb loss is therefore desired. Miller et al. (1996) has included such calculations in their electron acceleration model. Emslie (2003) also considered this effect when calculating particle transport and found that it can significantly reduce the inferred energy content of the injected electron distribution.

Here we briefly document how we improve on this in our current SA model. Since nonthermal electrons almost do not lose energy by collision with background protons or heavier ions, here we restrict ourselves to electron-electron collision only. The Coulomb energy loss rate for cold plasmas is:

$$\dot{E}^{\rm cold}_{\rm Coul} = 4\pi r_0^2 \ln\Lambda c n/\beta\,, \tag{C.1}$$

where $r_0 = e^2/(m_e c^2) = 2.8\times10^{-13}$ cm is the classical electron radius and $\ln\Lambda = 20$ (Leach, 1984) is a reasonable value for solar flares. Following Miller et al. (1996, eq. (2.5a))[1], we rewrite the general Coulomb loss rate (see also Benz, 2002, eq. (2.6.28); Spitzer, 1962, p. 128–129) as

$$\dot{E}_{\rm Coul} = \dot{E}^{\rm cold}_{\rm Coul}[\psi(x) - \psi'(x)], \tag{C.2}$$

[1]Note E in Miller et al. (1996) should be replaced with $\frac{1}{2}m_e v^2/(m_e c^2)$, *not* $\gamma - 1$, to make it valid in both non-relativistic and relativistic regimes, where $m_e c^2$ is used to make energy dimensionless. The same notation should be taken for Miller's eq. (2.5b); see below.

where we redefine $x = Em_ec^2/(kT)$, which is reduced to the definition of $\tilde{x} = (v/v_{\rm th})^2$ of Miller et al. (1996) at non-relativistic energies. In the relativistic regime, $x(\propto E)$ can approach ∞, which is mathematically more convenient than $\tilde{x}$ that has a finite upper limit of $(c/v_{\rm th})^2$.

$$\psi(x) = P(3/2, x) = \frac{1}{\Gamma(3/2)} \int_0^x t^{3/2-1} e^{-t} dt \tag{C.3}$$

is the incomplete gamma function (see Press et al., 1992, p. 160), where $\Gamma(a) = \int_0^\infty e^{-t} t^{a-1} dt$ is the common gamma function. Figure C.1 shows $\psi(x)$ and $\psi'(x)$, which approaches 1 and 0 very quickly, respectively, when x increases. Since

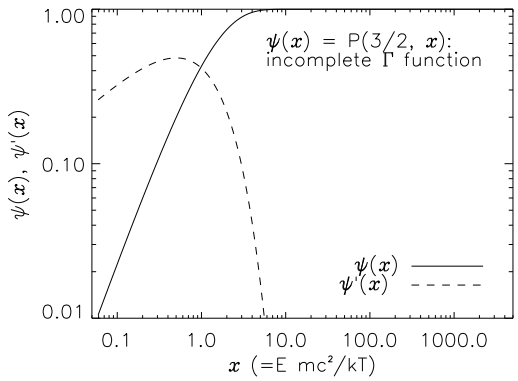

Figure C.1: Incomplete gamma function $\psi(x)$ and its derivative.

$$P(a+1, x) = P(a, x) - \frac{x^a e^{-x}}{a\Gamma(a)},$$

one can rewrite

$$\psi(x) = P(3/2, x) = P(1/2, x) - 2\sqrt{\frac{x}{\pi}} e^{-x} = \mathrm{erf}(\sqrt{x}) - 2\sqrt{\frac{x}{\pi}} e^{-x}, \tag{C.4}$$

where

$$\mathrm{erf}(\sqrt{x}) = \frac{2}{\sqrt{\pi}} \int_0^x e^{-t^2} dt \tag{C.5}$$

is the error function. One can also readily obtain

$$\psi'(x) = 2\sqrt{\frac{x}{\pi}} e^{-x}. \tag{C.6}$$

Substituting equations C.4 and C.6 to C.2, we have

$$\dot{E}_{\rm Coul} = \dot{E}^{\rm cold}_{\rm Coul} \left[\mathrm{erf}(\sqrt{x}) - 4\sqrt{\frac{x}{\pi}} e^{-x} \right], \tag{C.7}$$

in terms of more commonly used error function. The absolute value of the Coulomb loss

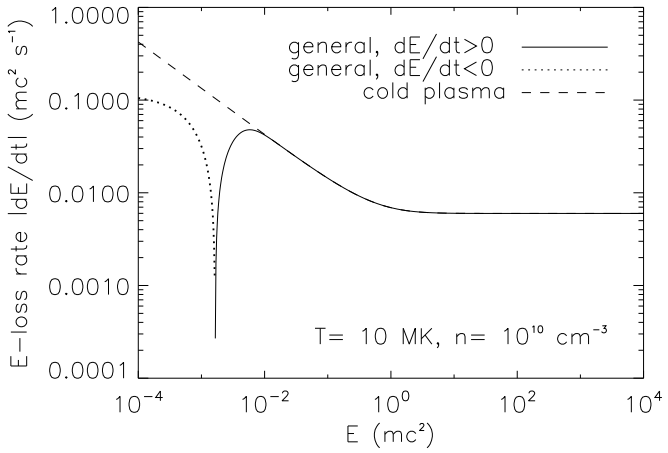

Figure C.2: Absolute value of Coulomb loss rate $\dot{E}_{\rm Coul}$ (*solid* and *dotted*) calculated for a typical background plasma condition for solar flares, $T = 10^7\,{\rm K}, n = 10^{10}\,{\rm cm}^{-3}$. Below the energy corresponding to the sharp "spike", $\dot{E}_{\rm Coul}$ turns to negative (*dotted*), meaning particle gaining energy. The cold-plasma loss rate $\dot{E}^{\rm cold}_{\rm Coul}$ (*dashed*) is shown for comparison.

rate is shown in Figure C.2, together with its counterpart of cold-target approximation. As energy decreases, this Coulomb loss rate (solid line) first increases; it then decreases and becomes negative (gaining energy). The energy at which it turns negative is very close to (but slightly less than) the thermal energy of background electrons. As expected, the cold-target Coulomb loss rate (dashed line) deviates from the general loss rate at low energies but the two agree well at high energies.

C.2 Coulomb Diffusion in Warm Plasmas

Similarly, Coulomb collision also contributes to diffusion in energy. In general, one can split the diffusion coefficient $D(E)$ into two parts:

$$D(E) = D_{\rm turb}(E) + D_{\rm Coul}(E), \tag{C.8}$$

where $D_{\rm turb}(E)$ and $D_{\rm Coul}(E)$ are contributions by turbulence and by Coulomb collisions, respectively. At low energies, energy diffusion due to Coulomb collisions becomes important, while at high energies, diffusion would be dominated by the contribution from turbulence. However, the $D_{\rm Coul}(E)$ term was not included in the previous SA mode.

Following Miller et al. (1996, eq. (2.5b))[2], we rewrite the Coulomb diffusion coefficient (see also Spitzer, 1962, p. 132)

$$D_{\rm Coul}(E) = \dot{E}^{\rm cold}_{\rm Coul}\left(\frac{kT}{m_e c^2}\right)\psi(x) = \dot{E}^{\rm cold}_{\rm Coul}\left(\frac{kT}{m_e c^2}\right)\left[{\rm erf}(\sqrt{x}) - 2\sqrt{\frac{x}{\pi}}e^{-x}\right]. \tag{C.9}$$

[2]Note $D(E)$ in eq. (C.10) here is equivalent to $D_C(E)/2$ in eq. (2.5b) of Miller et al. (1996).

C.3 Implementation of Coulomb Loss and Diffusion

The Fokker-Planck equation in some early works (Miller et al., 1996; Petrosian & Liu, 2004) was written as,

$$\frac{\partial f}{\partial t} = \frac{\partial^2}{\partial E^2}[D(E)f] - \frac{\partial}{\partial E}\{[A_1(E) - \dot{E}_{L1}]f\} - \frac{f}{T_{\rm esc}(E)} + Q(E)\,, \tag{C.10}$$

in a way which is slightly different from that of equation (1.1) used here. By substituting equation (C.8) one can rewrite this equation as

$$\frac{\partial f}{\partial t} = \frac{\partial}{\partial E}\left[D\frac{\partial f}{\partial E}\right] - \frac{\partial}{\partial E}\left\{\left[\left(A_1 - \frac{dD_{\rm turb}}{dE}\right) - \left(\dot{E}_{L1} + \frac{dD_{\rm Coul}}{dE}\right)\right] f\right\} - \frac{f}{T_{\rm esc}} + Q, \tag{C.11}$$

which can be directly compared with equation (1.1). We then identify the following relationship between the two ways of writing the Fokker-Planck equation:

$$A = A_1 - \frac{dD_{\rm turb}}{dE},^{3} \tag{C.12}$$

$$\dot{E}_L = \dot{E}_{L1} + \frac{dD_{\rm Coul}}{dE} = \dot{E}^{\rm eff}_{\rm Coul} + \dot{E}_{\rm synch}, \tag{C.13}$$

where we substitute equation (C.13) and define the effective Coulomb loss rate

$$\dot{E}^{\rm eff}_{\rm Coul} = \dot{E}_{\rm Coul} + \frac{dD_{\rm Coul}}{dE}. \tag{C.14}$$

We must modify the energy loss rate accordingly using the above two equations, when we include Coulomb diffusion using equations (C.9) and (C.8).

Let us now derive $dD_{\rm Coul}/dE$ and $\dot{E}^{\rm eff}_{\rm Coul}$. Using equation (C.9), we have

$$\frac{dD_{\rm Coul}}{dE} = D_{\rm Coul}\frac{d}{dE}\ln D_{\rm Coul} = D_{\rm Coul}\left[\frac{d}{dE}\ln \dot{E}^{\rm cold}_{\rm Coul} + \frac{d}{dE}\ln\psi(x)\right], \tag{C.15}$$

in which by equation (C.1) and $E = \gamma - 1$ we note

$$\frac{d}{dE}\ln \dot{E}^{\rm cold}_{\rm Coul} = -\frac{d\ln\beta}{dE} = -\frac{1}{\beta}\frac{d\beta}{d\gamma} = -\frac{1}{\beta^2\gamma^3} = -\frac{1}{\gamma(\gamma^2-1)} = -\frac{1}{\gamma(\gamma+1)E},$$

and by $x = Em_ec^2/kT$ we have

$$\frac{d}{dE}\ln\psi(x) = \frac{\psi'(x)}{\psi(x)}\frac{dx}{dE} = \frac{\psi'(x)}{\psi(x)}\frac{m_ec^2}{kT}.$$

Plugging the above two expressions to equation (C.15) and noting equation (C.9), we obtain

$$\frac{dD_{\rm Coul}}{dE} = \dot{E}^{\rm cold}_{\rm Coul}\left[\psi'(x) - \frac{\psi(x)}{x}\frac{1}{\gamma(\gamma+1)}\right], \tag{C.16}$$

[3] This notation conversion has already been taken care of in the code properly.

and, by using equation (C.2), the effective Coulomb loss rate

$$\dot{E}^{\rm eff}_{\rm Coul} = \dot{E}_{\rm Coul} + \frac{dD_{\rm Coul}}{dE} = \dot{E}^{\rm cold}_{\rm Coul}\psi(x)\left[1 - \frac{1}{x}\frac{1}{\gamma(\gamma+1)}\right]$$
$$= \dot{E}^{\rm cold}_{\rm Coul}\left[{\rm erf}(\sqrt{x}) - 2\sqrt{\frac{x}{\pi}}e^{-x}\right]\left[1 - \frac{1}{x}\frac{1}{\gamma(\gamma+1)}\right]. \qquad \text{(C.17)}$$

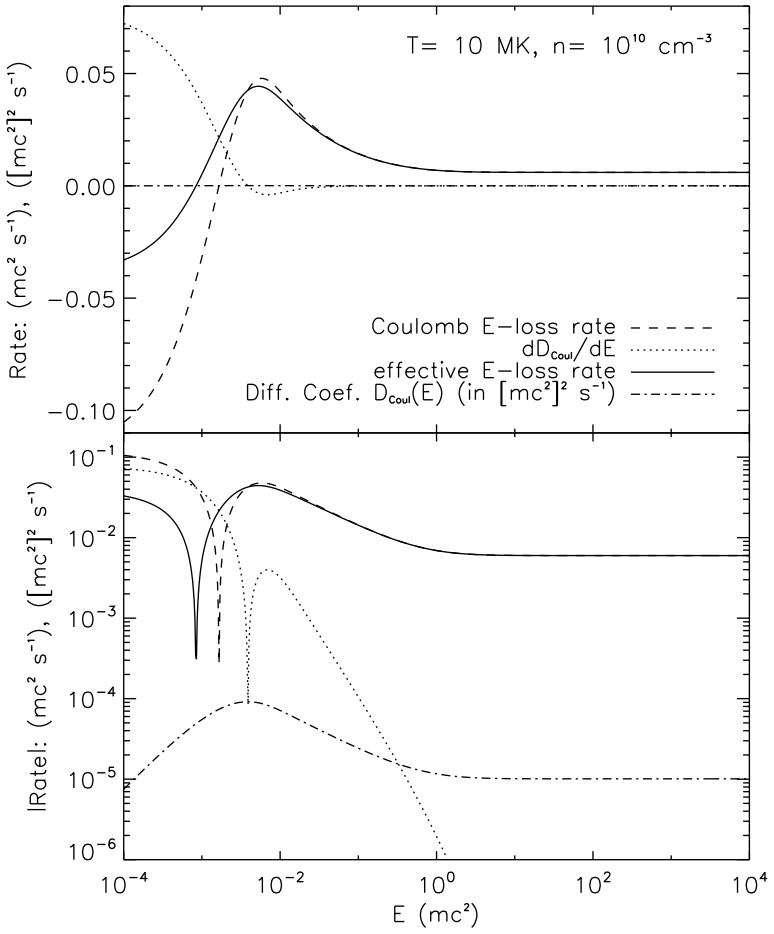

Figure C.3: Energy loss and diffusion rates due Coulomb collisions. *Top:* Coulomb energy loss rate $\dot{E}_{\rm Coul}$, diffusion coefficient $D_{\rm Coul}(E)$ and its derivative $dD_{\rm Coul}/dE$, and effective Coulomb energy loss rate $\dot{E}^{\rm eff}_{\rm Coul} = \dot{E}_{\rm Coul} + dD_{\rm Coul}/dE$. $D_{\rm Coul}(E)$ is in units of $(mc^2)^2\,{\rm s}^{-1}$ and the others are in units of $mc^2\,{\rm s}^{-1}$. *Bottom:* same as the top panel but for the absolute values plotted in a logarithmic scale.

Figure C.3 shows the energy loss or diffusion rates calculated for the same background plasma condition as in Figure C.2. As can be seen, with decreasing energy, the Coulomb energy loss rate $\dot{E}_{\rm Coul}$ changes its sign from positive to negative at about the energy of the background electron thermal energy, while the Coulomb diffusion derivative $dD_{\rm Coul}/dE$

does the opposite. The addition of the two gives the effective Coulomb loss rate $\tau_{\rm Coul}^{\rm eff}$, which is mainly dominated by $\dot{E}_{\rm Coul}$ except at low energies. The energy at which $\tau_{\rm Coul}^{\rm eff}$ flips its sign is slightly (by a half decade) lower than that of $\dot{E}_{\rm Coul}$.

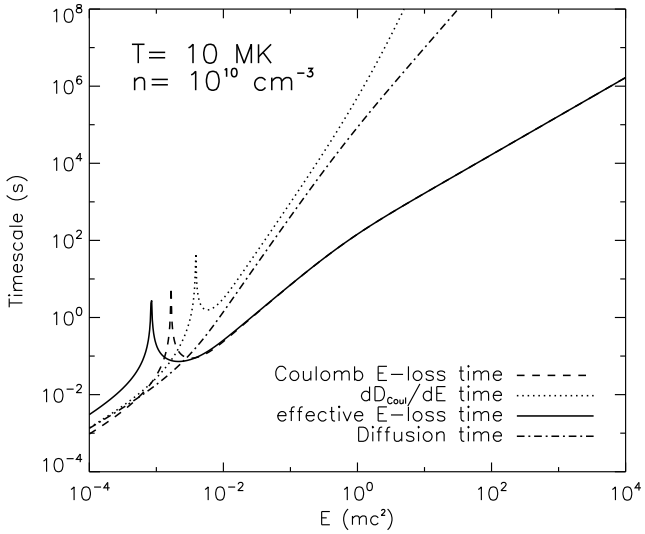

Figure C.4: Coulomb loss and diffusion timescales: $\tau_{\rm Coul}$, $\tau_{D'_{\rm Coul}}$, $\tau_{\rm Coul}^{\rm eff}(=[1/\tau_{\rm Coul}+1/\tau_{D'_{\rm Coul}}]^{-1})$, and $\tau_{D_{\rm Coul}}$ (see text for definitions), corresponding to the rates plotted in Fig. C.3. Note the spikes indicate infinite time and are located at the energy where the corresponding rate changes its sign (i.e., the rate equals zero). See the top panel of Fig. C.3 for their signs.

It is convenient to define various timescales based on the above obtained coefficients:

$$\tau_{\rm Coul}^{\rm cold} = E/\dot{E}_{\rm Coul}^{\rm cold} = (\gamma-1)\beta(4\pi r_0^2 \ln\Lambda cn)^{-1}, \tag{C.18}$$

$$\tau_{\rm Coul} = E/|\dot{E}_{\rm Coul}| = \tau_{\rm Coul}^{\rm cold}|\psi(x)-\psi'(x)|^{-1}, \tag{C.19}$$

$$\tau_{\rm Coul}^{\rm eff} = E/|\dot{E}_{\rm Coul}^{\rm eff}| = \tau_{\rm Coul}^{\rm cold}\left|1-\frac{1}{x}\frac{1}{\gamma(\gamma+1)}\right|^{-1}/|\psi(x)|, \tag{C.20}$$

$$\tau_{D'_{\rm Coul}} = \frac{E}{|dD_{\rm Coul}/dE|} = \tau_{\rm Coul}^{\rm cold}\left|\psi'(x)-\frac{\psi(x)}{x}\frac{1}{\gamma(\gamma+1)}\right|^{-1}, \tag{C.21}$$

$$\tau_{D_{\rm Coul}} = E^2/D_{\rm Coul} = E^2[\dot{E}_{\rm Coul}^{\rm cold}(kT/m_ec^2)\psi(x)]^{-1} = \tau_{\rm Coul}^{\rm cold}x/\psi(x), \tag{C.22}$$

Figure C.4 shows these timescales, which is proportional to the inverse of the bottom panel of Figure C.3. We note that above $\sim$ 10 keV (about 10 times higher than the thermal energy of background electrons), both Coulomb diffusion time and the $dD_{\rm Coul}/dE$ time are sufficiently large that Coulomb diffusion can be neglected in the Fokker-Planck calculation, as the previous SA model does.

C.4 Thermalization Test of Injected Distribution

We have tested the implementation of the new Coulomb loss and diffusion. We turned off acceleration by turbulence, but left Coulomb loss and diffusion on in the code. We injected a narrow Gaussian (δ-function like) distribution of electrons with a mean energy of 1 keV into a background plasma of Maxwellian distribution with a temperature of 1 keV and a density of $n_e = 1.5 \times 10^{10}\,\mathrm{cm}^{-3}$. We then calculated the time-dependent spectrum of these electrons. Figure C.5 shows the evolution of the electron distribution in separate time intervals (*left*: 0–0.01 s, *middle*: 0.01–0.1 s, *right*: 0.1-1 s). The injected Gaussian (*black*) and the background Maxwellian (*gray*) distribution are plotted in all the panels as a reference. As can be seen, the distribution quickly thermalizes and approaches the background Maxwellian distribution (overlapping with the final distribution at $t = 1\,\mathrm{s}$). From Figure C.4, we note that the Coulomb diffusion timescale $\tau_{D_{\mathrm{Coul}}}$ is about 0.1 s at $E = 1\,\mathrm{keV}$ in a plasma of $n_e = 1 \times 10^{10}\,\mathrm{cm}^{-3}$ (similar to the density here). The duration of 1 s in this calculation is thus about 10 times longer than the diffusion timescale, which allows sufficient time for the thermalization to happen.

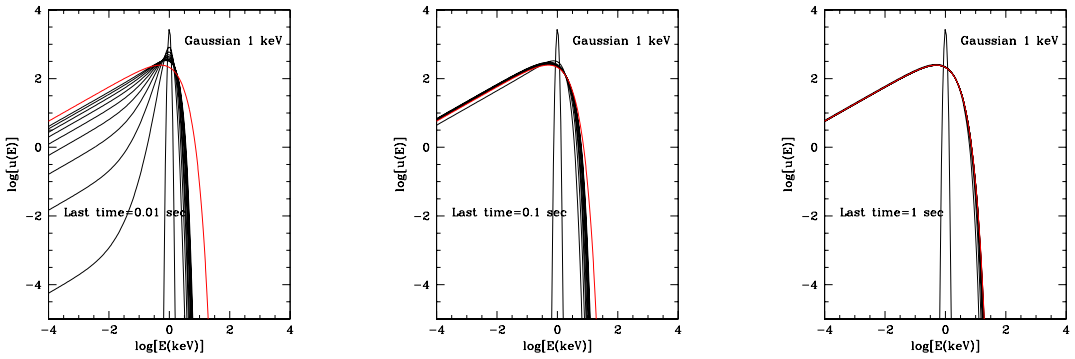

Figure C.5: Test against thermal distribution for injected Gaussian distribution when Coulomb diffusion is included. The injected narrow Gaussian (*black*) and the background Maxwellian (*gray scale*) distributions are fixed in each panel as a reference. The other curves (*black*, evenly spaced in time) in each panel show the temporal evolution on different stages *left*: 0–0.01 s, *middle*: 0.01–0.1 s, *right*: 0.1-1 s [Courtesy of William East].

List of Tables

2.1 List of 29 limb flares in the sample for the statistical study of imaging spectroscopy 10

3.1 Loop-top velocity and footpoint separation speed in the 2003-11-03 X3.9 flare 27

5.1 Correlations between various parameters of the conjugate footpoints in the 2003-10-29 X10 flare 67

5.2 Asymmetric characteristics of the conjugate footpoints in the 2003-10-29 X10 flare 73

7.1 Summary of cases in the combined Fokker-Planck & hydrodynamic simulation 145

8.1 Neupert effect test of simulation cases 164

9.1 Summary of cases in the decay phase simulation 168

List of Figures

1 Artistic view of *RHESSI* observing the Sun . . . iii

1.1 Schematic of a stochastic acceleration model and two examples from the 2003-11-03 X3.9 & 2002-04-30 M1.4 flare . . . 3

2.1 Distribution of heliographic location and peak count rate of the selected flares . . . 10
2.2 *RHESSI* light curves of flare 2092002 (2002-09-20, M1.8) . . . 12
2.3 PIXON images of flare 2092002 at different energies . . . 13
2.4 νf_ν spectra of the loop-top and footpoint sources of flare 2092002 . . . 13
2.5 Light curves of the individual loop-top and footpoint sources in flare 2092002 . . . 14
2.6 *RHESSI* Light curves and source morphology of flare 2080327 (2002-08-03, X1.0) . . . 15
2.7 HXR contours at different energies on a *TRACE* EUV image for flare 2080327 . . . 16
2.8 Light curves of individual loop-top and footpoint sources in flare 2080327 . . . 17
2.9 Images of flares 2082809 (2002-08-28, C6.6) and 2111410 (2002-11-14, C5.5) . . . 18
2.10 Statistics of loop-top and footpoint spectral indexes . . . 18
2.11 Histograms of footpoint to loop-top flux ratios at different times and energies . . . 19
2.12 Statistics of *RHESSI* peak count rates . . . 21

3.1 Flare (X3.9) of 2003-11-03: *RHESSI* and *GOES* light curves . . . 24
3.2 Evolution of loop-top and footpoint source positions overlaid on *SOHO* MDI magnetogram . . . 26
3.3 History of positions and spectral indexes of the loop-top and footpoint sources . . . 28
3.4 Energy-dependent loop-top source structure and its correlation with HXR flux . . . 29

4.1 Flare (M1.4) of 2002-04-30: *RHESSI* & *GOES* light curves . . . 35
4.2 PIXON images in different energy bands near the maximum of the main HXR peak . . . 36
4.3 Energy-dependent *RHESSI* source structure, together with *SOHO* EIT & MDI images . . . 38
4.4 Temporal evolution of the source structure at different energies . . . 40
4.5 History of the centroid heights and X-ray fluxes of the two coronal sources . . . 41
4.6 Imaged spectra of the two coronal sources . . . 43
4.7 Evolution of various spectroscopic quantities of the two coronal sources . . . 45
4.8 Schematic of the spatial variation of photon spectra hardness . . . 47
4.9 Scenario of magnetic reconnection and particle acceleration suggested by observations . . . 48

5.1 Flare (X10) of 2003-10-29: *RHESSI* and *GOES* light curves . . . 55
5.2 *RHESSI* 12-25 and 60-100 keV images at selected times . . . 57
5.3 CLEAN images in different energy bins . . . 58
5.4 Imaged spectra of the loop-top and two footpoint sources . . . 60
5.5 Evolution of spectroscopic parameters of the loop-top source . . . 61
5.6 Multiwavelength images overlaid with *RHESSI* contours and centroids . . . 63
5.7 Motions of *RHESSI* centroids of the loop-top and two footpoint sources . . . 65
5.8 History of HXR and magnetic field parameters of the two footpoints . . . 68
5.9 Correlations between the HXR and magnetic field parameters of the two footpoints. . . . 69
5.10 Effects of asymmetric column densities on footpoint HXR asymmetry . . . 76
5.11 Footpoint HXR flux asymmetry vs. energy for the 2003-10-29 X10 flare and others . . . 81

6.1 Flare (M1.7) of 2003-11-13: *RHESSI* and *GOES* light curves . . . 87
6.2 Mosaic (energy-by-time) of CLEAN images . . . 88
6.3 *RHESSI* images overlaid on *SOHO* EIT and MDI maps . . . 90
6.4 Loop model and profiles of X-ray surface brightness ($\parallel, \perp$ to the loop) . . . 91
6.5 Evolution of X-ray profiles $\parallel$ to the loop in three different energy bands . . . 93
6.6 PIXON images at the impulsive peak in four different energy bands . . . 94
6.7 Energy-dependent X-ray profiles ($\parallel$ to the loop) in three 24 s time intervals . . . 95
6.8 Centroids of two halves of the loop at different energies . . . 96
6.9 Centroid positions of the northern half loop, $\parallel$ and $\perp$ to the loop . . . 97
6.10 History of source compactness and spectral parameters . . . 99
6.11 Bremsstrahlung yield vs. electron spectral index for a low-energy cutoff at $E_1 = 20$ keV . . . 100
6.12 Test of the Neupert effect: various correlations . . . 102
6.13 Spatially integrated spectra (νF_ν) for at three times . . . 106
6.14 Averaged density profiles inferred along the loop at three times . . . 107

7.1 Task flow chart for Particle (Fokker-Planck) and Hydrodynamic (HD) code communication . . . 121
7.2 Initial state of the flare loop for the HD simulation . . . 122
7.3 HD evolution of various quantities for reference Case R . . . 124
7.4 History of various quantities at 1 Mm from the acceleration region for Case R . . . 125
7.5 Evolution of electron spectra at different locations for Case A . . . 126
7.6 HD evolution of various quantities for Case A . . . 128
7.7 Evolution of electron flux vs. depth at different energies for Case A . . . 129
7.8 Evolution of photon spectra at different locations for Case A . . . 131
7.9 Evolution of photon fluxes vs. depth at different energies for Case A . . . 133
7.10 Evolution of electron spectra at different locations for Case B . . . 135
7.11 Evolution of photon spectra at different locations for Case B . . . 136
7.12 Evolution of electron & photon fluxes vs. depth at different energies for Case B . . . 137
7.13 HD evolution of Case B . . . 138
7.14 Evolution of electron & photon spectra at different locations for Case C . . . 140
7.15 Evolution of electron & photon fluxes vs. depth at different energies for Case C . . . 141
7.16 HD evolution of Case C . . . 142
7.17 HD evolution of various quantities for Case D . . . 143
7.18 Electron & photon spectra and fluxes vs. depth for Case D . . . 144
7.19 Comparison of history of various quantities for the five cases . . . 146

8.1 Thermal bremsstrahlung emissivity vs. temperature . . . 151
8.2 History of energy budget and X-ray emission for Case R . . . 152
8.3 Consistency check of energy conservation for Case R . . . 153
8.4 Neupert effect test for Case R at photon energy 1.6 keV . . . 154
8.5 Neupert effect test for Case R at photon energy 6 keV . . . 155
8.6 History of energy budget and X-ray emission for Case A . . . 156
8.7 Neupert effect test for Case A at 1.6 keV . . . 157
8.8 Neupert effect test for Case A at 6 keV . . . 158
8.9 History of energy budget and X-ray emission for Case B . . . 159
8.10 Neupert effect test for Case B at 1.6 keV . . . 160
8.11 History of energy budget and X-ray emission for Case C . . . 161
8.12 Neupert effect test for Case C at 1.6 keV . . . 161
8.13 History of energy budget and X-ray emission for Case D . . . 162
8.14 Neupert effect test for Case D at 1.6 keV . . . 163

9.1 HD evolution of Case A . . . 169
9.2 Energy budget evolution of Case A . . . 170
9.3 Energy budget evolution of Case A: coronal and chromospheric portions . . . 171
9.4 HD evolution of Case B . . . 172
9.5 HD evolution of Case C . . . 173
9.6 HD evolution of Case D . . . 174

9.7 Energy budget evolution of Case D: full loop and coronal portion 175
9.8 Comparison of temperature, density, and X-ray emission profiles among Cases A-D 176
9.9 Comparison of decay of various quantities for Cases A-D 178

A.1 Ratio of piled-up to total counts during the 2003-11-13 M1.7 flare 198
A.2 Pileup severity during the 2003-10-29 X10 flare 199
A.3 Simulated *RHESSI* dynamic range 201

B.1 Cospatial of MDI magnetic anomaly and HXR footpoints in the 2003-10-29 X10 flare 203
B.2 Estimate of the loop leg density in the 2003-10-29 X10 flare 206

C.1 Incomplete gamma function $\psi(x)$ and its derivative. 209
C.2 Energy loss rate due to Coulomb collisions in a warm background plasma 210
C.3 Energy loss and diffusion rates due to Coulomb collisions in a warm background plasma . . . 212
C.4 Timescales of Coulomb energy loss and diffusion 213
C.5 Thermalization test of an injected Gaussian distribution of electrons 214

NOTE — Color versions of some figures can be found online at:
http://sun.stanford.edu/∼weiliu or
http://hesperia.gsfc.nasa.gov/∼weiliu

Bibliography

Abbett, W. P. & Hawley, S. L. 1999, ApJ, 521, 906

Alexander, D. & Metcalf, T. R. 2002, Sol. Phys., 210, 323

Allred, J. C., Hawley, S. L., Abbett, W. P., & Carlsson, M. 2005, ApJ, 630, 573

Antiochos, S. K. & Sturrock, P. A. 1978, ApJ, 220, 1137

Antonucci, E., Alexander, D., Culhane, J. L., de Jager, C., MacNeice, P., Somov, B. V., & Zarro, D. M. 1999, in The Many Faces of the Sun: A Summary of the Results from NASA's Solar Maximum Mission, ed. K. T. Strong et al. (New York: Springer-Verlag), 345

Antonucci, E., Dodero, M. A., & Martin, R. 1990, ApJS, 73, 137

Antonucci, E., Gabriel, A. H., Acton, L. W., Leibacher, J. W., Culhane, J. L., Rapley, C. G., Doyle, J. G., Machado, M. E., et al. 1982, Sol. Phys., 78, 107

Antonucci, E., Gabriel, A. H., & Dennis, B. R. 1984, ApJ, 287, 917

Asai, A., Ishii, T. T., Kurokawa, H., Yokoyama, T., & Shimojo, M. 2003, ApJ, 586, 624

Aschwanden, M. J. 2002, Space Science Reviews, 101, 1

—. 2004, Physics of the Solar Corona: An Introduction (Springer-Verlag)

Aschwanden, M. J., Brown, J. C., & Kontar, E. P. 2002, Sol. Phys., 210, 383

Aschwanden, M. J., Fletcher, L., Sakao, T., Kosugi, T., & Hudson, H. 1999, ApJ, 517, 977

Aschwanden, M. J., Metcalf, T. R., Krucker, S., Sato, J., Conway, A. J., Hurford, G. J., & Schmahl, E. J. 2004, Sol. Phys., 219, 149

Aschwanden, M. J., Schwartz, R. A., & Alt, D. M. 1995, ApJ, 447, 923

Bai, T. & Ramaty, R. 1978, ApJ, 219, 705

Battaglia, M. & Benz, A. O. 2006, A&A, 456, 751

Benka, S. G. & Holman, G. D. 1994, ApJ, 435, 469

Benz, A. 2002, Plasma Astrophysics: Kinetic Processes in Solar and Stellar Coronae, second edition (Dordrecht: Kluwer Academic Publishers, Astrophysics and Space Science Library, Vol. 279)

Brosius, J. W. 2003, ApJ, 586, 1417

Brosius, J. W. & Phillips, K. J. H. 2004, ApJ, 613, 580

Brown, J. C. 1971, Sol. Phys., 18, 489

—. 1973a, Sol. Phys., 31, 143

—. 1973b, Sol. Phys., 28, 151

Brown, J. C., Emslie, A. G., Holman, G. D., Johns-Krull, C. M., Kontar, E. P., Lin, R. P., Massone, A. M., & Piana, M. 2006, ApJ, 643, 523

Canfield, R. C., de La Beaujardiere, J.-F., Fan, Y., Leka, K. D., McClymont, A. N., Metcalf, T. R., Mickey, D. L., Wuelser, J.-P., & Lites, B. W. 1993, ApJ, 411, 362

Carmichael, H. 1964, in The Physics of Solar Flares, ed. W. N. Hess, 451

Chandran, B. D. G. & Cowley, S. C. 1998, Physical Review Letters, 80, 3077

Chernov, G. P., Yan, Y. H., Fu, Q. J., & Tan, C. M. 2005, A&A, 437, 1047

Cox, A. N. 2000, Allen's Astrophysical Quantities (4th ed. Publisher: New York: AIP Press; Springer, 2000. ISBN: 0387987460)

Crosby, N. B., Aschwanden, M. J., & Dennis, B. R. 1993, Sol. Phys., 143, 275

Culhane, J. L. & Acton, L. W. 1970, MNRAS, 151, 141

Dauphin, C., Vilmer, N., & Krucker, S. 2006, A&A, 455, 339

Dennis, B. R. 1985, Sol. Phys., 100, 465

Dennis, B. R., Emslie, A. G., Hudson, H. S., & Lin, R. P., eds. 2008, Solar Flares at High Energy: A RHESSI-inspired Monograph

Dennis, B. R., Veronig, A., Schwartz, R. A., Sui, L., Tolbert, A. K., Zarro, D. M., & Rhessi Team. 2003, Advances in Space Research, 32, 2459

Dennis, B. R. & Zarro, D. M. 1993, Sol. Phys., 146, 177

Dere, K. P., Landi, E., Mason, H. E., Monsignori Fossi, B. C., & Young, P. R. 1997, A&AS, 125, 149

Dere, K. P., Moses, J. D., Delaboudinière, J.-P., Brunaud, J., Carabetian, C., Hochedez, J.-F., Song, X. Y., Catura, R. C., et al. 2000, Sol. Phys., 195, 13

Donea, A.-C. & Lindsey, C. 2005, ApJ, 630, 1168

Doschek, G. A., Feldman, U., Kreplin, R. W., & Cohen, L. 1980, ApJ, 239, 725

Doschek, G. A., Mariska, J. T., Strong, K. T., Bentley, R. D., Brown, C. M., Culhane, J. L., Lang, J., Sterling, A. C., et al. 1994, ApJ, 431, 888

Dung, R. & Petrosian, V. 1994, ApJ, 421, 550

Efron, B. & Petrosian, V. 1992, ApJ, 399, 345

—. 1995, ApJ, 449, 216

Emslie, A. G. 1978, ApJ, 224, 241

—. 2003, ApJ, 595, L119

Emslie, A. G., Kontar, E. P., Krucker, S., & Lin, R. P. 2003, ApJ, 595, L107

Emslie, A. G. & Machado, M. E. 1987, Sol. Phys., 107, 263

Falewicz, R. & Siarkowski, M. 2007, A&A, 461, 285

Feldman, U., Doschek, G. A., Kreplin, R. W., & Mariska, J. T. 1980, ApJ, 241, 1175

Fenimore, E. E., Conner, J. P., Epstein, R. I., Klebesadel, R. W., Laros, J. G., Yoshida, A., Fujii, M., Hayashida, K., & et al. 1988, ApJ, 335, L71

Fenimore, E. E., Klebesadel, R. W., & Laros, J. G. 1983, Advances in Space Research, 3, 207

Fisher, G. H., Canfield, R. C., & McClymont, A. N. 1985a, ApJ, 289, 434

—. 1985b, ApJ, 289, 425

—. 1985c, ApJ, 289, 414

Fivian, M., Hemmeck, R., McHedlishvili, A., & Zehnder, A. 2002, Sol. Phys., 210, 87

Fletcher, L. & Hudson, H. 2001, Sol. Phys., 204, 69

Fletcher, L. & Hudson, H. S. 2002, Sol. Phys., 210, 307

—. 2008, ApJ, 675, 1645

Forbes, T. G. & Acton, L. W. 1996, ApJ, 459, 330

Forbes, T. G. & Lin, J. 2000, Journal of Atmospheric and Terrestrial Physics, 62, 1499

Freeland, S. L. & Handy, B. N. 1998, Sol. Phys., 182, 497

Gallagher, P. T., Dennis, B. R., Krucker, S., Schwartz, R. A., & Tolbert, A. K. 2002, Sol. Phys., 210, 341

Gan, W. Q., Cheng, C. C., & Fang, C. 1995, ApJ, 452, 445

Gan, W. Q. & Fang, C. 1990, ApJ, 358, 328

Goff, C. P., Matthews, S. A., van Driel-Gesztelyi, L., & Harra, L. K. 2004, A&A, 423, 363

Gopalswamy, N., Barbieri, L., Cliver, E. W., Lu, G., Plunkett, S. P., & Skoug, R. M. 2005, J. Geophys. Res., 110, 9

Grigis, P. C. & Benz, A. O. 2004, A&A, 426, 1093

Hamilton, R. J. 1990, Ph.D. Thesis, Stanford University

Hamilton, R. J., Lu, E. T., & Petrosian, V. 1990, ApJ, 354, 726

Hamilton, R. J. & Petrosian, V. 1992, ApJ, 398, 350

Hawley, S. L. & Fisher, G. H. 1994, ApJ, 426, 387

Hirayama, T. 1974, Sol. Phys., 34, 323

Holman, G. D. 1985, ApJ, 293, 584

—. 2003, ApJ, 586, 606

Holman, G. D., Sui, L., Brosius, D. G., & Dennis, B. R. 2005, AGU Fall Meeting Abstracts, A288

Holman, G. D., Sui, L., Schwartz, R. A., & Emslie, A. G. 2003, ApJ, 595, L97

Hoyng, P., Duijveman, A., Machado, M. E., Rust, D. M., Svestka, Z., Boelee, A., de Jager, C., Frost, K. T., Lafleur, H., Simnett, G. M., van Beek, H. F., & Woodgate, B. E. 1981, ApJ, 246, L155

Hudson, H. S. 1991, BAAS, 23, 1064

Hudson, H. S., Wolfson, C. J., & Metcalf, T. R. 2006, Sol. Phys., 234, 79

Hurford, G. J., Krucker, S., Lin, R. P., Schwartz, R. A., Share, G. H., & Smith, D. M. 2006, ApJ, 644, L93

Hurford, G. J., Schmahl, E. J., Schwartz, R. A., Conway, A. J., Aschwanden, M. J., Csillaghy, A., Dennis, B. R., Johns-Krull, C., et al. 2002, Sol. Phys., 210, 61

Hurford, G. J., Schwartz, R. A., Krucker, S., Lin, R. P., Smith, D. M., & Vilmer, N. 2003, ApJ, 595, L77

Ji, H., Huang, G., & Wang, H. 2007, ApJ, 660, 893

Ji, H., Huang, G., Wang, H., Zhou, T., Li, Y., Zhang, Y., & Song, M. 2006, ApJ, 636, L173

Ji, H., Wang, H., Goode, P. R., Jiang, Y., & Yurchyshyn, V. 2004, ApJ, 607, L55

Ji, H., Wang, H., Liu, C., & Dennis, B. R. 2008, ApJ, 680, 734

Jiang, Y. W., Liu, S., Liu, W., & Petrosian, V. 2006, ApJ, 638, 1140

Jiang, Y. W., Liu, W., Petrosian, V., & McTiernan, J. 2003, in Bulletin of the American Astronomical Society, 840

Jin, M. & Ding, M. D. 2007, A&A, 471, 705

Kiplinger, A. L. 1995, ApJ, 453, 973

Koch, H. W. & Motz, J. W. 1959, Reviews of Modern Physics, 31, 920

Kontar, E. P., Brown, J. C., & McArthur, G. K. 2002, Sol. Phys., 210, 419

Kontar, E. P., Piana, M., Massone, A. M., Emslie, A. G., & Brown, J. C. 2004, Sol. Phys., 225, 293

Kopp, R. A. & Pneuman, G. W. 1976, Sol. Phys., 50, 85

Kosovichev, A. G. 2006, Sol. Phys., 33

Kosovichev, A. G. & Zharkova, V. V. 1998, Nature, 393, 317

Krucker, S., Christe, S., Lin, R. P., Hurford, G. J., & Schwartz, R. A. 2002, Sol. Phys., 210, 445

Krucker, S., Fivian, M. D., & Lin, R. P. 2005, Advances in Space Research, 35, 1707

Krucker, S., Hurford, G. J., & Lin, R. P. 2003, ApJ, 595, L103

Krucker, S., Kontar, E. P., Christe, S., & Lin, R. P. 2007, ApJ, 663, L109

Krucker, S. & Lin, R. P. 2000, ApJ, 542, L61

Kundu, M. & Woodgate, B., eds. 1986, Energetic Phenomena on the Sun: The Solar Maximum Mission Flare Workshop. Proceedings

Kundu, M. R., Nitta, N., White, S. M., Shibasaki, K., Enome, S., Sakao, T., Kosugi, T., & Sakurai, T. 1995, ApJ, 454, 522

Langer, S. H. & Petrosian, V. 1977, ApJ, 215, 666

Leach, J. 1984, Ph.D. Thesis, Stanford University

Leach, J. & Petrosian, V. 1981, ApJ, 251, 781

—. 1983, ApJ, 269, 715

Lee, T. T., Petrosian, V., & McTiernan, J. M. 1993, ApJ, 412, 401

—. 1995, ApJ, 448, 915

Li, J., Metcalf, T. R., Canfield, R. C., Wuelser, J.-P., & Kosugi, T. 1997, ApJ, 482, 490

Li, J. P. & Ding, M. D. 2004, ApJ, 606, 583

Li, P., Emslie, A. G., & Mariska, J. T. 1993, ApJ, 417, 313

Li, Y. P. & Gan, W. Q. 2007, Advances in Space Research, 39, 1389

Lin, R. P., Dennis, B. R., Hurford, G. J., Smith, D. M., Zehnder, A., Harvey, P. R., Curtis, D. W., Pankow, D., et al. 2002, Sol. Phys., 210, 3

Lin, R. P., Krucker, S., Hurford, G. J., Smith, D. M., Hudson, H. S., Holman, G. D., Schwartz, R. A., Dennis, B. R., et al. 2003, ApJ, 595, L69

Liu, C., Lee, J., Deng, N., Gary, D. E., & Wang, H. 2006a, ApJ, 642, 1205

Liu, S., Melia, F., & Petrosian, V. 2006b, ApJ, 636, 798

Liu, S., Petrosian, V., & Mason, G. M. 2004a, ApJ, 613, L81

—. 2006c, ApJ, 636, 462

Liu, S., Petrosian, V., & Melia, F. 2004b, ApJ, 611, L101

Liu, Y. & Hayashi, K. 2006, ApJ, 640, 1135

Liu, Y., Kurokawa, H., Liu, C., Brooks, D. H., Dun, J., Ishii, T. T., & Zhang, H. 2007, Sol. Phys., 240, 253

Liu, W. 2006, PhD thesis, Stanford University

Liu, W. & Airapetian, V. 2008, in American Astronomical Society Meeting 211, 159.01

Liu, W., Jiang, Y. W., Liu, S., & Petrosian, V. 2004a, ApJ, 611, L53

Liu, W., Jiang, Y. W., Liu, S., & Petrosian, V. 2004b, in Bulletin of the American Astronomical Society, 739

Liu, W., Liu, S., Jiang, Y. W., & Petrosian, V. 2006, ApJ, 649, 1124

Liu, W., Petrosian, V., Dennis, B. R., & Holman, G. D. 2008a, submitted to ApJ

Liu, W., Petrosian, V., Dennis, B. R., & Jiang, Y. W. 2008b, ApJ, 676, 704

Lu, E. T. 1989, Ph.D. Thesis, Stanford University

MacKinnon, A. L. & Craig, I. J. D. 1991, A&A, 251, 693

Mariska, J. T., Doschek, G. A., Boris, J. P., Oran, E. S., & Young, Jr., T. R. 1982, ApJ, 255, 783

Mariska, J. T., Emslie, A. G., & Li, P. 1989, ApJ, 341, 1067

Masuda, S. 1994, PhD thesis, University of Tokyo

Masuda, S., Kosugi, T., Hara, H., Tsuneta, S., & Ogawara, Y. 1994, Nature, 371, 495

Masuda, S., Kosugi, T., & Hudson, H. S. 2001, Sol. Phys., 204, 55

Mazzotta, P., Mazzitelli, G., Colafrancesco, S., & Vittorio, N. 1998, A&AS, 133, 403

McClements, K. G. 1992, A&A, 258, 542

McClements, K. G. & Alexander, D. 2005, ApJ, 619, 1153

McTiernan, J. M. 1989, Ph.D. Thesis, Stanford University

McTiernan, J. M., Hudson, H. S., & Metcalf, T. R. 2004, in Bulletin of the American Astronomical Society, Vol. 36, 668

McTiernan, J. M. & Petrosian, V. 1990, ApJ, 359, 524

—. 1991, ApJ, 379, 381

Melrose, D. B. & White, S. M. 1981, J. Geophys. Res., 86, 2183

Metcalf, T. R., Hudson, H. S., Kosugi, T., Puetter, R. C., & Pina, R. K. 1996, ApJ, 466, 585

Metcalf, T. R., Leka, K. D., & Mickey, D. L. 2005, ApJ, 623, L53

Miller, J. A., Cargill, P. J., Emslie, A. G., Holman, G. D., Dennis, B. R., LaRosa, T. N., Winglee, R. M., Benka, S. G., et al. 1997, J. Geophys. Res., 102, 14631

Miller, J. A., Larosa, T. N., & Moore, R. L. 1996, ApJ, 461, 445

Miller, J. A. & Mariska, J. T. 2005, AGU Spring Meeting Abstracts, C2+

Milligan, R. O., Gallagher, P. T., Mathioudakis, M., Bloomfield, D. S., Keenan, F. P., & Schwartz, R. A. 2006, ApJ, 638, L117

Minoshima, T., Yokoyama, T., & Mitani, N. 2008, ApJ, 673, 598

Nagai, F. & Emslie, A. G. 1984, ApJ, 279, 896

Neupert, W. M. 1968, ApJ, 153, L59

Park, B. T. 1996, Ph.D. Thesis, Stanford University

Park, B. T. & Petrosian, V. 1995, ApJ, 446, 699

—. 1996, ApJS, 103, 255

Park, B. T., Petrosian, V., & Schwartz, R. A. 1997, ApJ, 489, 358

Parker, E. N. 1963, ApJS, 8, 177

Peres, G. & Reale, F. 1993, A&A, 275, L13

Petrosian, V. 1973, ApJ, 186, 291

Petrosian, V. 1994, in Proceedings of Kofu Symposium, 239–242

Petrosian, V. 1996, in American Institute of Physics Conference Series, ed. R. Ramaty, N. Mandzhavidze, & X.-M. Hua, 445

—. 2001, ApJ, 557, 560

Petrosian, V. & Donaghy, T. Q. 1999, ApJ, 527, 945

Petrosian, V., Donaghy, T. Q., & Llyod, N. M. 2001

Petrosian, V., Donaghy, T. Q., & McTiernan, J. M. 2002, ApJ, 569, 459

Petrosian, V. & Liu, S. 2004, ApJ, 610, 550

Petschek, H. E. 1964, in The Physics of Solar Flares, ed. W. N. Hess, 425

Phillips, K. J. H. 2004, ApJ, 605, 921

Pick, M., Démoulin, P., Krucker, S., Malandraki, O., & Maia, D. 2005, ApJ, 625, 1019

Press, W. H., Teukolsky, S. A., Vetterling, W. T., & Flannery, B. P. 1992, Numerical recipes in FORTRAN. The art of scientific computing (Cambridge University Press, 1992, 2nd ed.)

Qiu, J., Ding, M. D., Wang, H., Gallagher, P. T., Sato, J., Denker, C., & Goode, P. R. 2001, ApJ, 554, 445

Qiu, J. & Gary, D. E. 2003, ApJ, 599, 615

Qiu, J., Lee, J., & Gary, D. E. 2004, ApJ, 603, 335

Qiu, J., Lee, J., Gary, D. E., & Wang, H. 2002, ApJ, 565, 1335

Ramaty, R. 1979, in AIP Conf. Proc. 56: Particle Acceleration Mechanisms in Astrophysics, ed. J. Arons, C. McKee, & C. Max, 135–154

Ramaty, R. & Murphy, R. J. 1987, Space Science Reviews, 45, 213

Ryutova, M. & Shine, R. 2006, J. Geophys. Res., 111, 3101

Saint-Hilaire, P., Krucker, S., & Lin, R. P. 2008, Sol. Phys., in press

Sakao, T. 1994, PhD thesis, University of Tokyo

Sakao, T., Kosugi, T., & Masuda, S. 1998, in ASSL Vol. 229: Observational Plasma Astrophysics : Five Years of YOHKOH and Beyond, ed. T. Watanabe & T. Kosugi (Boston: Kluwer), 273

Saldanha, R., Krucker, S., & Lin, R. P. 2008, ApJ, 673, 1169

Sato, J. 2001, ApJ, 558, L137

Scherrer, P. H., Bogart, R. S., Bush, R. I., Hoeksema, J. T., Kosovichev, A. G., Schou, J., Rosenberg, W., Springer, L., et al., & MDI Engineering Team. 1995, Sol. Phys., 162, 129

Schlickeiser, R. 1989, ApJ, 336, 243

Schmahl, E. J. & Hurford, G. J. 2002, Sol. Phys., 210, 273

—. 2003, Advances in Space Research, 32, 2477

Schmahl, E. J., Kundu, M. R., & Garaimov, V. I. 2006, ApJ, 643, 1271

Schmieder, B., Hagyard, M. J., Guoxiang, A., Hongqi, Z., Kalman, B., Gyori, L., Rompolt, B., Demoulin, P., et al. 1994, Sol. Phys., 150, 199

Schwartz, R. A., Csillaghy, A., Tolbert, A. K., Hurford, G. J., Mc Tiernan, J., & Zarro, D. 2002, Sol. Phys., 210, 165

Siarkowski, M. & Falewicz, R. 2004, A&A, 428, 219

Silva, A. V. R., Wang, H., Gary, D. E., Nitta, N., & Zirin, H. 1997, ApJ, 481, 978

Smith, D. M., Lin, R. P., Turin, P., Curtis, D. W., Primbsch, J. H., Campbell, R. D., Abiad, R., Schroeder, P., et al. 2002, Sol. Phys., 210, 33

Spicer, D. S. 1979, Sol. Phys., 62, 269

Spitzer, L. 1962, Physics of Fully Ionized Gases (New York: Interscience, 2nd ed., 1962)

Sturrock, P. A. 1966, Nature, 211, 695

Sturrock, P. A., ed. 1980, Solar flares: A monograph from SKYLAB Solar Workshop II

Su, Y., Gan, W. Q., & Li, Y. P. 2006, Sol. Phys., 51

Su, Y., Golub, L., & Van Ballegooijen, A. A. 2007, ApJ, 655, 606

Sui, L. & Holman, G. D. 2003, ApJ, 596, L251

Sui, L., Holman, G. D., & Dennis, B. R. 2004, ApJ, 612, 546

—. 2005, ApJ, 626, 1102

—. 2006, ApJ, 645, L157

—. 2007, ApJ, 670, 862

Sui, L., Holman, G. D., Dennis, B. R., Krucker, S., Schwartz, R. A., & Tolbert, K. 2002, Sol. Phys., 210, 245

Švestka, Z. 1976, Solar Flares (Berlin, Heidelberg: Springer-Verlag, ISBN 90-277-0662-X, 415 p.)

Švestka, Z. F., Fontenla, J. M., Machado, M. E., Martin, S. F., & Neidig, D. F. 1987, Sol. Phys., 108, 237

Sweet, P. A. 1958, in IAU Symp. 6: Electromagnetic Phenomena in Cosmical Physics, ed. B. Lehnert, 123

Syniavskii, D. V. & Zharkova, V. V. 1994, ApJS, 90, 729

Tandberg-Hanssen, E. & Emslie, A. G. 1988, The physics of solar flares (Cambridge and New York: Cambridge University Press, 286 p.)

Tomczak, M. & Ciborski, T. 2007, A&A

Tsuneta, S. 1996, ApJ, 456, 840

Tsuneta, S., Hara, H., Shimizu, T., Acton, L. W., Strong, K. T., Hudson, H. S., & Ogawara, Y. 1992, PASJ, 44, L63

Tsuneta, S., Masuda, S., Kosugi, T., & Sato, J. 1997, ApJ, 478, 787

Tsuneta, S. & Naito, T. 1998, ApJ, 495, L67

Veronig, A. M. & Brown, J. C. 2004, ApJ, 603, L117

Veronig, A. M., Brown, J. C., Dennis, B. R., Schwartz, R. A., Sui, L., & Tolbert, A. K. 2005, ApJ, 621, 482

Veronig, A. M., Karlický, M., Vršnak, B., Temmer, M., Magdalenić, J., Dennis, B. R., Otruba, W., & Pötzi, W. 2006, A&A, 446, 675

Vestuto, J. G., Ostriker, E. C., & Stone, J. M. 2003, ApJ, 590, 858

Wang, H., Gary, D. E., Zirin, H., Schwartz, R. A., Sakao, T., Kosugi, T., & Shibata, K. 1995, ApJ, 453, 505

Wang, L., Lin, R. P., Krucker, S., & Gosling, J. T. 2006, Geophys. Res. Lett., 33, 3106

Wang, T., Sui, L., & Qiu, J. 2007, ApJ, 661, L207

Watanabe, T. 1990, Sol. Phys., 126, 351

Winter, III, H. D. & Martens, P. C. 2006, AAS/Solar Physics Division Meeting, 37, 13.13

Wuelser, J.-P., Canfield, R. C., Acton, L. W., Culhane, J. L., Phillips, A., Fludra, A., Sakao, T., Masuda, S., et al. 1994, ApJ, 424, 459

Xu, Y., Cao, W., Liu, C., Yang, G., Jing, J., Denker, C., Emslie, A. G., & Wang, H. 2006, ApJ, 641, 1210

Xu, Y., Cao, W., Liu, C., Yang, G., Qiu, J., Jing, J., Denker, C., & Wang, H. 2004, ApJ, 607, L131

Xu, Y., Emslie, A. G., & Hurford, G. J. 2008, ApJ, 673, 576

Yang, G., Xu, Y., Cao, W., Wang, H., Denker, C., & Rimmele, T. R. 2004, ApJ, 617, L151

Yokoyama, T. & Shibata, K. 2001, ApJ, 549, 1160

Young, P. R., Del Zanna, G., Landi, E., Dere, K. P., Mason, H. E., & Landini, M. 2003, ApJS, 144, 135

Zharkova, V. V., Brown, J. C., & Syniavskii, D. V. 1995, A&A, 304, 284

Zharkova, V. V. & Gordovskyy, M. 2004, ApJ, 604, 884

—. 2006, ApJ, 651, 553

Author Index

Abbett, W. P., 110
Alexander, D., 23, 54, 74, 82
Allred, J. C., 85, 110
Antiochos, S. K., 166, 179
Antonucci, E., 85, 86, 93
Asai, A., 66
Aschwanden, M. J., vii, 4, 23, 36, 54, 73, 82, 104, 190, 191, 196

Bai, T., 80
Battaglia, M., 33
Benka, S. G., 2, 52, 72
Benz, A., 185, 208
Brosius, J. W., 86
Brown, J. C., 2, 5, 51, 79, 110, 192, 205

Canfield, R. C., 72
Carmichael, H., 1
Chandran, B. D. G., 166
Chernov, G. P., 94
Cox, A. N., 150
Crosby, N. B., 20
Culhane, J. L., 151

Dauphin, C., 34
Dennis, B. R., vii, 2, 20, 36, 85, 98
Dere, K. P., 89, 194
Ding, M. D., 54
Donaghy, T. Q., 4, 8, 30, 104, 115
Donea, A.-C., 56, 62
Doschek, G. A., 85, 93
Dung, R., 112

Efron, B., 20, 21
Emslie, A. G., vii, 5, 6, 30, 54, 75, 110, 145, 150, 183, 185, 190, 200, 204, 208

Falewicz, R., 54, 75, 77, 78
Fang, C., 110
Feldman, U., 85
Fenimore, E. E., 195
Fisher, G. H., 110
Fisher, G. H., 7, 85, 86, 103, 104, 107, 110, 144, 145, 183
Fivian, M., 62, 202
Fletcher, L., 30, 53, 71, 82
Forbes, T. G., 23, 31, 72
Freeland, S. L., 187

Gallagher, P. T., 23, 27, 31
Gan, W. Q., 21, 34, 49, 51, 85, 110, 181
Gary, D. E., 30, 202
Goff, C. P., 54
Gopalswamy, N., 56
Gordovskyy, M., 80, 82
Grigis, P. C., 67, 134

Hamilton, R. J., 3–5, 33, 46, 50, 108, 109, 184
Handy, B. N., 187
Hawley, S. L., 110
Hirayama, T., 1
Holman, G. D., 2, 25, 27, 29, 30, 33, 39, 46, 49, 51–53, 66, 72, 83, 98, 110, 181
Hoyng, P., 2, 33
Hudson, H. S., vii, 2, 30, 53, 71, 82, 85
Hurford, G. J., 2, 5, 11, 25, 30, 37, 56, 57, 59, 70, 89, 92, 96, 108, 187, 189–191, 198, 200

Ji, Haisheng, 53, 55–57, 64, 66, 83
Jiang, Y. W., 7, 12, 13, 33, 34, 52, 100, 166–168, 170, 177, 179, 184, 201
Jin, M., 54

Kiplinger, A. L., 70, 83
Koch, H. W., 116
Kontar, E. P., 44, 79
Kopp, R. A, 1, 23
Kosovichev, A. G., 123, 185
Kosugi, T., 30
Krucker, S., 1, 23, 25, 26, 30, 54, 70, 73, 188, 200
Kundu, M., vii, 54, 56

Langer, S. H., 80
Leach, J., 4, 7, 78, 79, 84, 104, 109, 111, 204, 208
Lee, J., 30
Lee, T. T., 20–22
Li, J. P., 54
Li, Jing, 54
Li, Peng, 5, 6, 101, 110, 150, 183
Li, You-Ping, 21, 34, 49, 51, 181
Lin, Jun, 72
Lin, R. P., vii, 4, 8, 23, 25, 86
Liu, Chang, 56

Liu, Siming, 3, 7, 18, 20, 30, 31, 46, 50, 52, 67, 72, 80, 83, 100, 101, 108–111, 113, 114, 185, 205, 206, 211
Liu, Wei, 5, 23, 33, 34, 36, 39, 42, 48, 51–54, 59, 60, 66, 67, 73, 75, 82, 83, 85–87, 194, 198, 199, 203, 205
Liu, Yang, 56
Liu, Yu, 56, 72
Lu, E. T., 4

MacKinnon, A. L., 109
Mariska, J. T., 5, 6, 85, 110, 118, 167, 171, 172, 183
Mason, G. M., 3, 114
Masuda, S., 3, 5, 8, 9, 12, 30, 33, 46, 52, 66, 205
Mazzotta, P., 194
McClements, K. G., 54, 82, 109
McTiernan, J. M., 4, 7, 30, 72, 80, 109, 115, 185, 188, 200
Melrose, D. B., 74
Metcalf, T. R., 23, 37, 56, 66, 86, 92, 192, 196, 203
Miller, J. A., 3, 33, 46, 108–110, 185, 208–211
Milligan, R. O., 104, 145
Minoshima, T., 80
Motz, J. W., 116

Nagai, F., 110
Neupert, W. M., 2, 36, 85, 110, 149

Park, B. T., 3, 4, 8, 33, 108, 109, 114
Parker, E. N., 1
Peres, G., 86
Petrosian, V., 2–5, 7–9, 14, 18–21, 30, 31, 33, 46, 50–52, 54, 67, 72, 78–80, 83, 84, 98, 100, 101, 103, 104, 108–112, 114, 115, 120, 184, 185, 204–206, 211
Petschek, H. E., 1, 33
Phillips, K. J. H., 193
Pick, M., 34
Pneuman, G. W., 1, 23
Press, W. H., 209

Qiu, Jiong, 30, 54, 202

Ramaty, R., 2, 3, 33, 80
Ryutova, M., 177

Saint-Hilaire, P., 33, 54, 77
Sakao, T., 2, 5, 8, 30, 33, 54, 66
Saldanha, R., 70
Sato, J., 25
Scherrer, P. H., 71
Schlickeiser, R., 168
Schmahl, E. J., 25, 30, 66, 96
Schmieder, B., 23
Schwartz, R. A., 187
Siarkowski, M., 54, 75, 77, 78
Silva, A. V. R., 86, 104
Smith, D. M., 4, 11, 25, 55, 59, 86, 92, 97, 187, 188, 190, 193, 196, 197, 199
Spicer, D. S., 167
Spitzer, L., 166, 208, 210
Sturrock, P. A., 1, 166, 179
Su, Yang, 21
Su, Yingna, 66
Sui, Linhui, 5, 23, 25, 27, 33, 34, 39, 42, 46, 48, 49, 51–53, 66, 77, 83, 87, 103, 111, 181, 205
Švestka, Z. F., vii, 31
Sweet, P. A., 1
Syniavskii, D. V., 109, 115

Tandberg-Hanssen, E., vii, 150
Tomczak, M., 8
Tsuneta, S., 2, 23, 31, 52

Veronig, A. M., 7, 34, 36, 49, 51, 53, 85, 86, 100, 103, 149, 181
Vestuto, J. G., 113

Wang, Haiming, 54
Wang, Linghua, 1
Wang, Tongjiang, 34
Watanabe, T., 85
White, S. M., 74
Winter, III, H. D., 110
Wuelser, J.-P., 85

Xu, Yan, 51, 54, 56, 70, 73, 86, 205

Yang, Guo, 56, 66
Yokoyama, T., 85
Young, P. R., 194

Zharkova, V. V., 80, 82, 109, 115, 123, 185

Subject Index

^{4}He abundance, 112
RHESSI
  design and capabilities, 4
  dynamic range, 17, 42, 59, 62, 87, 201
  imaging algorithms, 11
    CLEAN, 26, 57, 58, 88, 189, 191
    PIXON, 13, 18, 36, 40, 94, 189, 192
    visibility forward-fitting, 39
  imaging spectroscopy, 11, 27, 42, 59, 189, 190, 195, *see* X-rays, spectroscopy for results
    background, 190
    data analysis flow chart, 187
    detector selection, 190
    energy bins, 11
    error/uncertainties, 191
    integration time, 11
    pulse pileup, 198
  pulse pileup, 9, 30, 59, 60, 62, 86, 92, 196
    detector livetime, 194, 197, 199
  simulation tools, 200
  spatial resolution, 29, 36, 57, 88, 190
  spectroscopy, 192, *see* X-rays, spectroscopy for results
    spectral fitting, 27, 42, 59, 97, 194

Acceleration of particles, 1
  DC electric field, 2, 52, 72
  shock, 2, 52
  stochastic, viii, 2, 4, 8, 18, 30, 31, 46, 48–52, 72, 82, 100, 108, 110, 111, 180, 205
    schematic of, 3
Acceleration region, 3, 48, 54, 67, 74, 111, 114, 119, 120, 125, 148, 205, 206
  spatial extent, 51
Auroras, 186
  numerical simulation, 148, 186
  on extrasolar planet, 186

Bremsstrahlung, 132, *see* X-rays for diagnostics
  angle-dependent, 185
  cross-section, 116
  nonthermal, 46–49, 78, 95, 98, 104, 108, 116, 132
    spatial distribution (profile), 104, 105, 133, 137, 204, 206, 207
    spectra, 13, 31, 43, 44, 60, 99, 106, 189, 194
  photon spectrum, 131, 136
  relativistic beaming, 80
  thermal, 46–49, 78, 95, 98, 108, 132, 150, 151, 154, 177, 206
    emissivity, 151
    spatial distribution (profile), 176, 177
    spectra, 13, 27, 43, 44, 60, 99, 106, 189, 190, 194, 196
  thick-target, 76, 117, 205
    equivalent electron flux, 115
  thin-target, 116
  yield, 98, 100, 139, 148

Chromospheric evaporation, 2, 37, 49, 60, 85, 139, 144, 147, *see* also Flare (individual), 2003-11-13 M1.7
  dependence on electron spectrum, 148
  Doppler shifts, 86
  driven by
    collisional heating, 110, 123
    conduction, 127, 145
  evaporation front, 123, 125, 127, 130, 132
  hydrodynamic simulation, 85, 109
  imaging, 86, 93, 96, 97
  loop density resulting from, 107, 131
  Neupert effect, *see* Neupert effect
  upflow velocity, 93, 103, 139, 144
Chromospheric oscillation, 171
Column density/depth, 47, 70, 75, 79, 121
  asymmetry, 75, 78, 83
  dimensionless, 76, 104, 204
  effective, 75, 79
Conduction, 46, 48, 49
  electron conductivity, 117
  ion conductivity, 117
  Spitzer, 119
  suppression of, 100, 166
    simulation model, 167, 173
    simulation results, 168, 175, 179
Coronal mass ejections (CMEs), 1, 24, 56
Coulomb collision, 52, 74, 75, 78, 80, 109, 167, 204
  energy diffusion, 115, 210
  energy loss, 2, 4, 8, 111, 115, 119, 120, 130
    effective Coulomb loss rate, 211, 212

to cold targets, 208
to warm targets, 184, 208–210
pitch-angle scattering/diffusion, *see* Electron, pitch angle
Coulomb logarithm, 98, 111, 115, 204
Current helicity, 56, 72
Current sheet, 2, 33, 34, 82
Currents, vertical, 72

Electron
classical radius, 111
energy distribution, 76, 126, 135, 204, 207
high-energy cutoff, 72, 194
low-energy cutoff, 45, 80, 98, 99, 102, 110, 126, 127, 144, 145, 183, 194
nonthermal, 36, 46, 49, 67, 94, 104, 110, 118, 126, 144, 202, 203, 208
thermal (Maxwellian), 50, 110, 112, 144, 167, 214
energy flux, 103, 144
gyrofrequency, 72, 112
number flux, 115, 119
angle-integrated, 116, 126
equivalent thick-target flux, 115, 130
escaping from acceleration region, 115, 127, 139, 146, 147
precipitating to footpoints, 74, 80
spatial distribution, 129, 134
spectrum, *see* energy distribution
pitch angle
distribution, 74–76, 80, 112, 114, 115, 204
scattering/diffusion, 4, 74, 75, 77–79, 109, 204
plasma frequency, 72, 112
power, 103
runaway, 51
stopping distance/column density, 75, 104
Energy contents, 149, 151, 152
conversion of, 171
gravitational, 149, 170, 171
kinetic, 149, 153, 164, 171, 172
thermal, 149, 151, 153, 154, 165, 168, 170, 171
Neupert effect, *see* Neupert effect
variation rate, 155, 162, 165, 175

Flare
gamma-ray, 56
microflares, 23
phases
decay, 12, 20, 22, 34, 44, 87, 100, 101, 103, 119, 123, 154, 166, 175–177
impulsive, 4, 5, 12, 31, 35, 44, 48, 54, 66, 86, 100, 101, 107–109, 111, 119, 123, 166, 181, 197
statistics, 18
correction for selection biases, 20
imaging spectroscopy, 18
size distribution, 20
two-ribbon, 2, 56
white-light, 1, 2, 56, 62, 70
Flare (individual)
2002-04-30 M1.4, 33
double coronal source, 34
magnetic reconnection site, 47
2002-08-03 X1.0 (multiple loops), 14, 16, 17
2002-09-20 M1.8 (single loop), 12
imaging spectroscopy, 13
2003-10-29 X10, 53
footpoint unshearing motions, correlations, asymmetries, *see* Footpoint sources
2003-11-03 X3.9, 23
correlated motions of loop-top and footpoint sources, 25
2003-11-13 M1.7, 85
chromospheric evaporation, 91, 93, 96, 97, 106
Neupert effect, 98
Fokker-Planck
equation, 4, 111, 211
equation coefficients, 114
acceleration, 114
diffusion, 114
numerical code, 6, 110, 111
Footpoint sources, 8, 12, 13, 89, 202
asymmetries, 73
acceleration-induced anisotropy, 80
column density, 75
energy dependence, 82
magnetic mirroring, 74
non-uniform target ionization, 79
photospheric albedo, 80
relativistic beaming, 80
correlations, 66
images, 26, 29, 57
magnetic field, 70, 202
motion, 26, 65
approaching, 64
relative, 25, 64
separation, 25, 64

unshearing, 62, 65
pulse pileup, 200
shear angle, 64
spectra, 13, 60, 76
spectral index, 13, 18, 28, 60, 67, 68, 77
thick-target, *see* Bremsstrahlung

Gamma-rays, 2, 23, 70, 100

Hα emission, 2, 53, 63, 86, 204
Helioseismic (Sunquake) signals, 56, 62, 123
Hydrodynamics
equations, 117
simulation, 85, 108
collisional heating rate, 119, 121
temporal evolution, 127

Iron
abundance, 59, 194, 196
X-ray line emission, 60, 194

Loop-top sources, 8, 12, 13, 52
altitude
ascent, 25, 28, 40
descent, 25, 28, 40, 66
energy dependence, 28, 29, 38
emission measure, 45, 49, 61
images, 26, 29, 57, 89
motion, 26, 40, 65
pulse pileup, 200
spectra, 13, 43, 60
spectral index, 18, 28, 43
temperature, 13, 45, 49, 61
thin-target, *see* Bremsstrahlung

Magnetic field
chromospheric, 56
coronal, 72
extrapolation
force-free, 72
potential, 56
magnetogram
line-of-sight, 56
photospheric, 56
vector, 56, 72
shear, 64
Magnetic free energy, 56, 66
Magnetic mirroring, 4, 13, 74, 78, 109
asymmetric, 74, 78, 79, 83
pitch-angle distribution asymmetry, 80
return current asymmetry, 80
loss cone, 74
trapping, *see* Trapping of particles
Magnetic reconnection, 1, 51, 56
geometry, 1, 23
model of solar flares, 1, 23
outflow, 2, 33, 34
rate, 27, 71, 72, 101
schematic of, 3
site/region, 2, 32, 33, 46–48, 50, 75
motion, 2, 25, 66, 87

Neupert effect, 2, 36, 85, 98, 165
energy budget, *see* Energy contents
temporal correlation, 104
test of, 98, 100, 108, 149, 153
Non-uniform target ionization, 79

Opacity minimum, 56

Plasma waves, 94, *see* also Turbulence
dispersion relation, 112
modes, 112
wave-particle resonance interaction, 3, 112
Proton
acceleration, 185
momentum, 185

Radiative loss, 48, 117, 123, 150, 152, 158, 166, 170, 171, 179
spatial distribution, 124, 127
wavelength dependence, 165
Radio emission, 1, 24
double coronal source, 34
footpoint asymmetry, 54
microwave images, 56
zebra pattern, 94
Return current, 80, 115

Separatrix, 72
Shearing flows, photospheric, 56, 66
Software packages
CHIANTI, 59, 179, 194
OSPEX, 22, 59, 192–196
Solar SoftWare (SSW), x, 187, 192, 194, 203
SPEX, 190
Solar energetic particles (SEPs), 56, 70
^{3}He rich events, 3
Space instruments
ACE, 3, 56
CGRO, 4
GOES, 24, 35, 55, 56, 86, 87, 97, 99, 100, 102, 151, 154

SXI, 189
Hinode, 84
Hinotori, 4, 5, 85
ISEE-3, 4
OSO-5 & -7, 4
RHESSI, *see RHESSI*
SDO, 84
SMM, 4, 5, 86
SOHO, 24, 86, 189, 203
CDS, 104
EIT, 38, 90
LASCO, 24
MDI, 26, 38, 56, 63, 70, 90, 202
SUMER, 34
TRACE, 10, 11, 15, 16, 62–64, 177, 189, 203
Yohkoh, 3–5, 8, 19, 54, 85, 110, 116
BCS, 86
HXT, 54, 78, 82
SXT, 86
Synchrotron
energy loss, 111
pitch-angle diffusion, 115

Transition region, 2, 68, 75, 79, 84, 116, 120, 123, 127, 130, 132, 139, 149, 152, 170, 171, 179, 205, 207
Trapping of particles, 206
by magnetic mirroring, 52, 53, 84
by turbulence, 3, 52, 148
Turbulence, 2, 49, 100, 108, 125, 210, *see* also Plasma waves
cascade, 3
level, 31, 46, 50, 51, 72, 147, 167
particle acceleration by, 109
particle scattering by, 80, 112
plasma heating by, 119, 165–167
resonance interaction, *see* Plasma waves
spatial distribution, 31, 48, 51
spectrum, 4, 49, 113
suppression of conduction by, *see* Conduction
trapping, *see* Trapping of particles

X-ray sources (spatially resolved)
centroids
energy dependence, 28, 29, 38, 41, 96
temporal evolution, 26, 28, 40, 41, 65
light curves, 14, 17, 41, 68
spatial gradient of spectral hardness, 46
spectra, 43, *see* also Loop-top/Footpoint sources
nonthermal, *see* Bremsstrahlung
thermal, *see* Bremsstrahlung
types
coronal (above loop-top), 33, 36, 49
footpoint, *see* Footpoint sources
leg, 89, 90
loop-top, *see* Loop-top sources
X-rays
albedo, 80
nonthermal, *see* Bremsstrahlung
observing instruments, 4
spectral evolution
soft-hard-hard(er) (SHH), 67, 79
soft-hard-soft (SHS), 20, 67, 69, 71, 79, 98, 104, 134, 159
spectroscopy
imaging, 13, 18, 28, 43, 60, *see RHESSI*, imaging spectroscopy for technicalities
spatially integrated, 28, 43, 60, 99, 106, 199
thermal, *see* Bremsstrahlung
thick-target, *see* Bremsstrahlung
thin-target, *see* Bremsstrahlung